2013

Bioactive glass scaffolds for the regeneration of load-bearing bone

Xin Liu

BIOACTIVE GLASS SCAFFOLDS FOR THE REGENERATION OF LOAD-BEARING BONE

by

XIN LIU

A DISSERTATION

Presented to the Faculty of the Graduate School of the

MISSOURI UNIVERSITY OF SCIENCE AND TECHNOLOGY

In Partial Fulfillment of the Requirements for the Degree

DOCTOR OF PHILOSOPHY

in

CERAMIC ENGINEERING

2013

Approved by

Mohamed N. Rahaman, Advisor

B. Sonny Bal

Richard K. Brow

Roger F. Brown

Delbert E. Day

PUBLICATION DISSERTATION OPTION

The body of this dissertation has been compiled in the format for publication in peer-reviewed journals. Five papers have been included in the following order. The first paper, "Oriented Bioactive Glass (13-93) Scaffolds with Controllable Pore Size by Unidirectional Freezing of Camphene-based Suspensions: Microstructure and Mechanical Response," was published in Acta Biomaterialia in 2011, in Volume 7, Issue 1, pages 406-416. The second paper, "Porous and Strong Bioactive Glass (13-93) Scaffolds Prepared by Unidirectional Freezing of Camphene-based Suspensions" was published in Acta Biomaterialia in 2012, in Volume 8, Issue 1, pages 415-423. The third paper "Bone Regeneration in Strong Porous Bioactive Glass (13-93) Scaffolds with an Oriented Microstructure Implanted in Rat Calvarial Defects" was published in Acta Biomaterialia in 2013, in Volume 9, Issue 1, pages 4889-4898. The forth paper, "Mechanical Properties of Bioactive Glass (13-93) Scaffolds Fabricated by Robotic Deposition for Structural Bone Repair " was published in Acta Biomaterialia in 2013. The fifth paper, "Enhanced Bone Regeneration in Rat Calvarial Defects Implanted with Surface-modified and BMP-loaded Bioactive Glass (13-93) Scaffolds" was accepted for publication in Acta Biomaterialia in 2013.

A sixth paper given in the appendix, titled "Conversion of Melt-derived Microfibrous Borate (13-93B3) and Silicate (45S5) Bioactive Glass in a Simulated Body Fluid", was published in Journal of Materials Science: Materials in Medicine in 2013 in Volume 24, Issue 3, pages 583-595.

ABSTRACT

Biocompatible scaffolds that replicate the structure and function of bone would be ideal bone substitutes for structural bone loss, provided they have the requisite mechanical properties for reliable long-term loading. In this dissertation, strong porous scaffolds of silicate 13-93 bioactive glass, created with two different microstructures, were evaluated to determine their mechanical properties and their capacity to regenerate bone in a rat calvarial defect model. Scaffolds with an oriented microstructure of columnar pores were prepared by unidirectional freezing of camphene-based suspensions, followed by thermal annealing and sintering. By optimizing the freezing conditions, annealing time, and sintering temperature, constructs (porosity = 50 ± 4%; average pore diameter = 100 μm) were created with a compressive strength of 47 ± 5 MPa and an elastic modulus of 11 ± 3 GPa (in the orientation direction). New bone formation in the pore space of the scaffolds increased from 37% at 12 weeks to 55% at 24 weeks in vivo. Scaffolds with grid-like microstructure (porosity= 47 ± 1%; pore width = 300 μm), prepared by a robotic deposition (robocasting) technique, had a compressive strength (86 ± 9 MPa) and an elastic modulus (13 ± 2 GPa) comparable to human cortical bone, a Weibull modulus of 12, and excellent fatigue resistance in compression. Bone regeneration in the as-fabricated scaffolds in vivo (32% at 6 weeks) was significantly enhanced (to ~60%) by a surface treatment in an aqueous phosphate solution or loading the surface-treated scaffolds with bone morphogenetic protein-2 (1 μg/defect), prior to implantation. Scaffolds of 13-93 bioactive glass with a grid-like microstructure prepared by robocasting, showing better mechanical properties and a greater capacity to support bone formation, are more promising in structural bone repair.

ACKNOWLEDGMENTS

I am grateful to my advisor, Dr. Mohamed N. Rahaman, who has supported me in many ways during the past four years. He has provided numerous valuable suggestions and discussions to make this dissertation possible. His great enthusiasm and meticulous attitude towards research have inspired me to work for excellence.

I sincerely appreciate the assistance of Dr. Roger F. Brown for his assistance with the in vitro and in vivo experiments in my research. I am also grateful to Dr. B. Sonny Bal, Dr. Richard K. Brow and Dr. Delbert E. Day, who provided valuable comments and constructive suggestions throughout my PhD education. I want to thank Dr. Qiang Fu (Corning Inc.), Dr. Yongxing Liu, Dr. Gregory E. Hilmas and Dr. Lynda F. Bonewald (UMKC) for helpful discussion on my research work. I would also like to thank Dr. Wenhai Huang (Tongji, China) for introducing me to the idea of studying in the USA.

Several persons provided assistance to enable me to complete my research or provided guidance with the direction of my research, and I would like to express my sincere thanks to them: Dr. Ted Day (Mo-Sci Corp.), Dr. Lianxiang Bi (UMKC), Dr. Jeremy Watts, Clarissa Wisner, Dr. Kai Song, Dr. Eric Bohannan, and Xiaoming Cheng.

All of my colleagues and friends deserve many thanks as well. Dr. Tieshu Huang, Dr. Shichang Zhang, Dr. Hailuo Fu, Yifei Gu, Xiao Wei, Yinan Lin, Dr. Liying Zhang, and Lina Ma, I greatly appreciated working and learning with you.

Last but not least, I would like to thank those who made this possible: my parents, Yongshou Liu and Meihua Zeng, and my husband, Wei Yuan. Their love, belief, and encouragement kept me moving forward in the journey of graduate study.

TABLE OF CONTENTS

LIST OF ILLUSTRATIONS

PAPER I **Page**

PAPER III

PAPER IV

PAPER V

LIST OF TABLES

1. PURPOSE OF THIS DISSERTATION

The main purpose of this Ph.D. research was to create and evaluate strong porous scaffolds of bioactive glass with controlled architectures for potential applications in loaded bone repair.

Bioactive glass and ceramics have been widely investigated for healing bone defects, because of their ability to enhance bone formation and to bond with surrounding tissue. The glass designated 13-93 (53 SiO_2, 6 Na_2O, 12 K_2O; 5 MgO, 20 CaO and 4 P_2O_5, wt%) is a silicate-based bioactive glass with a modified 45S5 composition, which has better processing characteristics by viscous flow sintering than the 45S5 bioactive glass. When fabricated into 3D scaffolds, the 13-93 bioactive glass can be sintered to high density without crystallization, which leads to optimum scaffold strength. Previous research in our research group (Fu, Huang et al) showed that the 13-93 bioactive scaffolds with an oriented microstructure, prepared by unidirectional freezing of suspensions, and scaffolds with a grid-like microstructure, prepared by a solid freeform fabrication (SFF) technique, had higher mechanical properties than scaffolds prepared by more conventional methods, such as the polymer foam replication technique, which make them potential candidates for loaded bone repair.

In this work, the oriented 13-93 bioactive glass scaffolds were fabricated by a unidirectional freezing method and their ability to support bone regeneration were evaluated in osseous defects. The 13-93 bioactive glass scaffolds with grid-like microstructure were prepared by a robotic deposition method. The mechanical properties and the ability to support bone regeneration of the scaffolds were studied and compared with those of the oriented scaffolds.

PAPER

I. ORIENTED BIOACTIVE GLASS (13-93) SCAFFOLDS WITH CONTROLLABLE PORE SIZE BY UNIDIRECTIONAL FREEZING OF CAMPHENE-BASED SUSPENSIONS: MICROSTRUCTURE AND MECHANICAL RESPONSE

Xin Liu, Mohamed N. Rahaman, Qiang Fu
Department of Materials Science and Engineering and Center for Bone and Tissue Repair and Regeneration, Missouri University of Science and Technology, Rolla, MO, 65409, USA

ABSTRACT

Scaffolds of 13-93 bioactive glass (composition 6.0 Na_2O, 7.9 K_2O, 7.7 MgO, 22.1 CaO, 1.7 P_2O_5, 54.6 SiO_2 (mol.%)) containing oriented pores of controllable diameter were prepared by unidirectional freezing of camphene-based suspensions (10 vol.% particles) on a cold substrate (-196 ^oC or 3 ^oC). By varying the annealing time (0–72 h) to coarsen the camphene phase, constructs with the same porosity (86 ± 1%) but with controllable pore diameters (15–160 μm) were obtained after sublimation of the camphene. The pore diameters had a self-similar distribution that could be fitted by a diffusion-controlled coalescence model. Sintering (1 h at 690 ^oC) was accompanied by a decrease in porosity and pore diameter, the magnitude of which depended on the pore size of the green constructs, giving scaffolds with a porosity of 20–60% and average pore diameter of 6–120 μm. The compressive stress vs. deformation response of the sintered scaffolds in the orientation direction was linear, followed by failure. The compressive strength and elastic modulus in the orientation direction varied from 180 MPa and 25 GPa (porosity = 20%) to 16 MPa and 4 GPa (porosity = 60%), respectively, which were 2–3 times larger than the values in the direction perpendicular to the orientation. The potential use of these 13-93 bioactive glass scaffolds for the repair of large defects in load-bearing bones, such as segmental defects in long bones, is discussed.

1. Introduction

There is a need to develop new scaffolds to repair segmental defects in long bones, using a method that is biocompatible and durable during the patient's lifetime. At present, bone allografts and custom metal augments are used to address segmental skeletal deficiency, but treatments are limited by concerns related to high costs, limited availability, unpredictable long-term durability, uncertain healing to host bone, and other variables. Biocompatible scaffolds that replicate the structure and function of bone would be ideal bone substitutes, provided they have the requisite mechanical properties for reliable long-term cyclical loading during weight-bearing. Ideally, the scaffold should have mechanical properties (e.g., elastic modulus and compressive strength) comparable to those of the tissue to be replaced. The scaffolds should also have a microstructure suitable for tissue growth into the porous scaffolds, to allow strong bonding and facile integration with apposing host bone and surrounding soft tissues. A porosity of ~50% and an interconnected pore size (diameter or width of the openings between adjoining pores) of 100 μm are considered to be the minimum requirements to permit tissue ingrowth and function [1].

The use of biodegradable polymers for replacing large defects in load-bearing bones (such as segmental defects in long bones) is challenging because of their very low mechanical strength and elastic modulus [2, 3]. Bioactive glasses and bioactive ceramics are attractive materials for filling bone defects because of their widely recognized ability to support the growth of bone cells [4, 5], and to bond strongly with hard and soft tissue [6, 7]. However, porous three-dimensional scaffolds of these bioactive materials prepared by conventional methods often lack the requisite mechanical properties for repairing segmental defects in bone.

Unidirectional freezing of suspensions has been shown to provide a method for preparing oriented scaffolds with far higher mechanical properties (in the orientation direction) when compared to scaffolds prepared by more conventional methods [8]. Hydroxyapatite (HA) scaffolds prepared by unidirectional freezing of aqueous suspensions were found to have a compressive strength of 65 MPa (porosity = 56%) [9]. However, the lamellar pores obtained after sublimation of the frozen liquid had pore widths of only 10–40 μm, far smaller than the minimum pore size known to favor tissue

ingrowth. Fu et al. [10, 11] found that the use of binary mixtures of solvents, consisting of water and dioxane (60 wt% dioxane), produced a marked change from the lamellar microstructure, giving a columnar microstructure with far larger pore widths (pore diameter = 90–110 μm). Columnar scaffolds of silicate bioactive glass (13-93) had a compressive strength of 25 ± 3 MPa (porosity = 55–60%) in the orientation direction, and provided a more favorable substrate than the lamellar scaffolds for supporting cell proliferation and function, and cell infiltration into the interior pores of the scaffolds [8]. When implanted into subcutaneous pockets in the dorsum of rats, columnar scaffolds of 13-93 bioactive glass also showed the ability to support tissue infiltration into the interior pores of the scaffold [12].

The use of aqueous-based suspensions is limited by concerns about the degradation of the bioactive glass during processing, particularly for the more recently developed bioactive glass compositions, such as borate and borosilicate bioactive glass, which react faster than silicate bioactive glass [13, 14]. Furthermore, our previous work showed that only a limited range of pore diameters (10–100 μm) were obtained in HA and bioactive glass scaffolds prepared by unidirectional freezing of aqueous suspensions [8, 10]. For the intended application of bioactive glass scaffolds in bone repair, it would be useful to achieve a wider range of controllable pore diameters.

Camphene ($C_{10}H_{16}$) has been shown to have favorable characteristics for use as a sublimable vehicle in the preparation of constructs by freezing of suspensions [15]. Camphene-based suspensions can be frozen at room temperature, higher than the temperatures used for freezing aqueous suspensions [15-17]. Examples of previous work (summarized in Table 1) showed that constructs prepared by freeze casting of camphene-based suspensions had pore sizes in the range 10–300 μm, far larger than the pore size range for scaffolds prepared from aqueous suspensions.

Recent work has shown that oriented constructs of Al_2O_3 with pore sizes >100 μm can be prepared using a two-step process consisting of unidirectional freezing of camphene-based suspensions, followed by annealing the frozen constructs for 24 hours at 35°C [18]. It was suggested that the larger pore sizes achieved using this two-step process resulted from growth of the camphene crystals during the annealing step. However, a

clear understanding of the kinetics and mechanisms of the camphene growth process during this annealing step is lacking.

The objective of the present work was to investigate the use of a two-step process, involving unidirectional freezing and thermal annealing of camphene-based suspensions, for creating oriented bioactive glass scaffolds with controllable pore sizes. The present work has two major differences when compared to our previous work on the preparation of oriented scaffolds by unidirectional freezing of aqueous suspensions [8, 10, 11]. First, organic (camphene)-based suspensions are used in this work, which are advantageous for limiting the degradation of the bioactive glass, particularly for future work in which more reactive glass compositions will be used. Second, a two-step process (freezing and thermal annealing) is investigated in this work for the creation of scaffolds with a wider range of pore diameters than those obtained from aqueous suspensions. In contrast to previous work [18], the kinetics and mechanism of the camphene phase coarsening during the annealing step were studied to provide a clearer understanding of the microstructure development. Silicate 13-93 glass was used as the scaffold material in this work because of its attractive bioactive properties and our extensive previous experience with its preparation and evaluation. This glass is based on the well-researched 45S5 composition, but it has a higher SiO_2 content, plus additional network modifiers, such as K_2O and MgO [7]. Products of 13-93 glass are also approved for *in vivo* use by the U.S. Food and Drug Administration (FDA). Relationships among the processing conditions, microstructure, and mechanical properties of the fabricated scaffolds were investigated.

2. Materials and methods

2.1. Preparation of oriented 13-93 bioactive glass scaffolds

Bioactive glass (13-93) scaffolds with oriented pores were prepared in a set of sequential steps: preparation of camphene-based suspensions, unidirectional freezing of the suspensions, thermal annealing of the frozen constructs at a temperature near the solidification temperature of the suspension, sublimation of the camphene crystals, and heat treatment (sintering) to densify the glass network.

Glass with the 13-93 (composition: $6Na_2O$, $7.9K_2O$, 7.7MgO, 22.1CaO, $1.7P_2O_5$, $54.6SiO_2$ (mol.%), $6Na_2O$, $12K_2O$, 5MgO, 20CaO, $4P_2O_5$, $53SiO_2$ (wt.%)) was prepared

by melting a mixture of analytical grade Na_2CO_3, K_2CO_3, $MgCO_3$, $CaCO_3$, SiO_2 and NaH_2PO_4 $2H_2O$ (Sigma-Aldrich, St. Louis, MO) in a platinum crucible for 1 h at 1300°C and quenching between cold stainless steel plates. The glass (density = 2.50 g/cm^3) was crushed, ground in a hardened steel shatterbox (8500 Shatterbox®, Spex SamplePrep LLC., Metuchen, NJ, USA), and attrition-milled for 2 h in water with ZrO_2 grinding media. The size of the resulting glass particles was 1.0 ± 0.5 μm, as measured by a laser diffraction particle size analyzer (Model LS 13 320, Beckman Coulter Inc., CA). Camphene ($C_{10}H_{16}$; CAS 5794-04-7; Alfa Aesar, Ward Hill, MA, USA), with a melting temperature = 35 °C and a solid density = 0.85 g/cm^3 (according to manufacturer's specifications) was used as the dispersion medium. Isostearic acid ($C_{18}H_{36}O_2$; MP Biomedicals LLC, Solon, OH, USA) was selected as the dispersant because of its use in previous work [26].

The optimum concentration of isostearic acid required for stabilizing the glass particles in liquid camphene at 55°C was determined by measuring the viscosity of the suspension (10 vol% particles) as a function of dispersant concentration using a rotating cylinder viscometer (VT500; Haake Inc., Paramus NJ). Suspensions containing 5–40 vol% glass particles and the optimum concentration of isostearic acid (2 wt% based on the dry mass of the glass particles) were prepared by ball milling for 24 h at 55°C in sealed polyethylene bottles. The viscosity of each suspension was measured as a function of shear rate at 55°C using a rotating cylinder viscometer (Haake VT500). The data were used to determine the effect of particle concentration on the viscosity of the suspension.

Suspensions for unidirectional freezing, consisting of 10 vol% glass particles, 2 wt% isostearic acid, and camphene, were prepared by ball milling the mixture for 24 h at 55°C in a sealed polypropylene bottle. Suspensions containing 5 and 15 vol% particles were also used but they resulted in weak constructs (5 vol% particles) or low porosity constructs (15 vol% particles). The solidification of the slurry was monitored using differential scanning calorimetry, DSC (Model 2010; TA Instruments, City, State, USA) at a heating rate of 2 °C/min. Unidirectional freezing was performed by pouring the slurry into cylindrical rubber molds (11 mm in diameter × 20 mm, or 18 mm in diameter × 15 mm) placed on a copper plate kept at 3°C using an ice–water mixture or at −196°C using liquid nitrogen. In order to optimize the unidirectional solidification, the rubber

molds were warmed at 55°C prior to placing them on the cold copper plate and, after the slurry was poured, the molds were covered with rubber caps previously warmed to 55°C. For comparison, more randomly solidified samples were prepared by pouring the suspension into a cylindrical copper mold, sealing the mold, and immersing it in an ice–water mixture.

After solidification, the samples were transferred individually into polyvinyl chloride (PVC) tubes, and sealed with PVC caps to avoid camphene loss. The samples were then annealed at 34°C for up to 72 h in an incubator (Model CCC 0.5d; Boekel Industries Inc., Feasterville, PA, USA). This annealing temperature was chosen because the DSC experiments described above showed a peak in the solidification profile of the slurry at 36°C. After the annealing step, the samples were cooled to room temperature, and the camphene was removed by sublimation (24 h at room temperature). The porous constructs were sintered in air for 1 h at 690°C (heating and cooling rate = 5°C/min) to densify the glass phase. The use of this sintering temperature was based on previous work.

2.2. Microstructural characterization of porous constructs

After sublimation of the camphene (and before the sintering step), the porous constructs were too weak to be manipulated and characterized by microscopy. In order to develop adequate strength without significantly altering the pore characteristics, the porous constructs were lightly pre-sintered for 5 h at 600°C, well below the sintering temperature. The porosity of these pre-sintered constructs was determined from their mass and external dimensions. The pre-sintered samples were mounted in epoxy resin, sectioned in planes parallel and perpendicular to the freezing direction, polished, coated with Au/Pd, and examined using scanning electron microscopy, SEM (S-4700; Hitachi, Tokyo, Japan) at an accelerating voltage of 15 kV and a working distance of 18 mm. The sintered constructs were prepared and examined in the SEM using a similar method. In order to better characterize the pore network in three dimensions, the sintered scaffolds were examined using synchrotron X-ray tomography. Scanning was carried out at the Advanced Light Source (ALS, Lawrence Berkeley National Lab., Berkeley, CA) using 22 keV monochromatic X-rays and a resolution size of 1.7 μm voxel.

The porosity and pore diameters (or widths) in the cross-sections were analyzed using imaging software (Image J). At least 150 pores per cross-section were analyzed for each sample. Polished cross-sections of the constructs in the directions perpendicular and parallel to the freezing direction were observed by optical microscopy (Optiphot-POL, Nikon Corp., Tokyo, Japan) to confirm the microstructural homogeneity along the length of the samples. The porosity of the sintered constructs was measured by the Archimedes method and the values were compared with those obtained by image analysis.

2.3. Evaluation of pore connectivity of oriented scaffolds

The connectivity of the oriented pores in the sintered scaffolds was evaluated by a capillary suction test using a blood-like solution which had a viscosity equal to that of human blood. The blood-like solution consisted of 34 wt% glycerol, 65 wt% deionized water and 1 wt% Alizarin red. The composition of the solution was based on the viscosity data of water–glycerol mixtures [27] which had a viscosity equal to that of human blood [28]. The flat surface and the circumferential surface of the porous constructs were dipped slightly (to a depth of < 1mm) into the surface of the solution. After the liquid was drawn up into the pores by capillary pressure, the constructs were allowed to dry. Both the external surface and the cross-section of the constructs were visually examined to assess the infiltration of the liquid.

2.4. Mechanical response of sintered scaffolds

The mechanical response of the sintered constructs in the directions parallel and perpendicular to the freezing (orientation) direction was measured in compression using an Instron testing machine (Model 5881; Norwood, MA, USA). Cylindrical constructs (7 mm in diameter $\times$ 7 mm) and cubic constructs (7 mm $\times$ 7 mm $\times$ 7 mm) were deformed in the directions parallel and perpendicular to the orientation direction, respectively, at a rate of 0.5 mm/min. The contact surfaces of the constructs were machined flat, to provide parallel surfaces for the tests. At least 8 samples were tested for each group, and the compressive strength and elastic modulus were determined as an average $\pm$ standard deviation. For comparison, cylindrical constructs (7 mm in diameter $\times$ 7 mm) with a more random microstructure prepared as described earlier were tested under the same conditions.

3. Results

3.1. Viscosity of camphene-based suspensions

The viscosity of the camphene-based suspensions (10 vol% glass particles) as a function of the dispersant (isostearic acid) concentration at a constant shear rate (100 s^{-1}) (Fig. 1), showed that 1−2 wt% isostearic acid gave the lowest viscosity of the suspension, presumably corresponding to the most stable suspension. These viscosity data confirmed qualitative sedimentation tests which showed that suspensions containing ~2 wt% isostearic acid had the slowest particle sedimentation rate. Henceforth, suspensions used in the experiments were stabilized with 2 wt% isostearic acid.

For particle concentrations of 5–40 vol% used in these experiments, the viscosity of the suspension initially decreased with increasing shear rate, but became almost independent of shear rate above 50–100 s^{-1}. The results are omitted for the sake of brevity. Figure 2 shows results for the relative viscosity of the suspension (shear rate = 100 s^{-1}) as a function of the glass particle concentration. The data can be fitted by a modified Krieger-Dougherty equation [29, 30]:

$$\eta_r = \left(1 - \frac{\phi}{\phi_m}\right)^{-n} \tag{1}$$

where η_r, the relative viscosity, is defined as the viscosity of the suspension, η, divided by the viscosity of the solvent (camphene) η_L, ϕ is the volume fraction of particles, ϕ_m is the volume fraction of particles at which the viscosity becomes practically infinite, and n is a fitting parameter. The maximum solids loading predicted by this model is ϕ_m = 43 vol%, with n = 3.2.

3.2. Microstructure of frozen constructs

After sublimation of the camphene, pre-sintering of the constructs resulted in a linear shrinkage of <5% in the directions perpendicular and parallel to the freezing direction, regardless of the freezing temperature and annealing time used in the freeze casting process. Therefore, the microstructure of the pre-sintered constructs could be taken as a good approximation to the microstructure of the constructs after sublimation of the camphene. Furthermore, the morphology of the pores resulting from the sublimation

of the camphene was well replicated by the epoxy resin used for mounting the samples for microscopy.

SEM images of the cross-sections in the directions perpendicular and parallel to the freezing direction are shown in Fig. 3 for the constructs prepared by freezing on copper substrates at 3°C and –196°C (annealing time = 0 h). Apart from a size difference, the overall pore morphology of the two groups of constructs frozen at the two different temperatures was similar. The pores appeared to show an interconnected cellular morphology in the cross-section perpendicular to the freezing direction (Figs. 3a, 3c). The average diameter (or width) of the pores increased from ~15 μm for the constructs frozen at –196°C to ~40 μm for the constructs frozen at 3°C. The sections parallel to the freezing direction (Figs. 3b, 3d) showed that while the pores were oriented, they did not have a regular cylindrical shape. Instead, the pores appeared to have a dendritic-like morphology.

3.3. Effect of thermal annealing on microstructure of frozen constructs

Figure 4 shows SEM images of the cross-sections of constructs frozen at 3°C and annealed at 34°C for 6, 12, and 72 h. The annealing step resulted in a change of the pore cross-section from a cellular morphology to a nearly circular shape within 6 h (Fig. 4a). With increasing annealing time, the pore cross-section remained circular and the average pore diameter increased (Figs. 4c, 4e). SEM images of the cross-section parallel to the freezing direction (Figs. 4b, 4d, 4f) showed that after an annealing time of 6 h, the pores still had a somewhat dendritic shape. However, the pores developed a nearly cylindrical shape with smoother pore walls within an annealing time of 12 h. Furthermore, the pores remained oriented during the annealing process. Despite the wide difference in the average pore width of the constructs frozen at 3°C (40 μm) and at –196°C (15 μm), the temperature of freezing had little effect on the average pore diameter after an annealing time of 6 h. The microstructures of the annealed constructs for a freezing temperature of –196°C are therefore omitted for brevity.

The average pore diameter of the constructs frozen at 3°C or –196°C and annealed for 0–72 h at 34°C increased rapidly within the first 12 h of annealing, but then increased more slowly thereafter (Fig. 5). Starting from a pore width of 40 μm (freezing temperature = 3°C) or 15 μm (freezing temperature = –196°C), the average pore diameter

increased to ~80 μm and ~125 μm after annealing times of 6 h and 12 h respectively. Annealing for 72 h resulted in a further increase in the average pore diameter to ~160 μm.

Analysis of SEM images of the cross-sections of the constructs showed that the fractional area of the porous region was 67 ± 4% in the planes parallel and perpendicular to the freezing direction, and that this value was independent of the annealing time. Taken together with the results described above, this means that with increasing annealing time, the number of pores decreased, the average pore diameter increased, the thickness of the pore walls increased, but the overall pore volume remained almost constant during the annealing process.

Based on the mass and dimensions of the frozen or annealed constructs, the porosity of the constructs was found to be 86 ± 1 %, which is in good agreement with the expected value of 90% for constructs formed from suspensions with 10 vol% particles. On the other hand, as indicated above, the porosity determined from image analysis of SEM micrographs was 67 ± 4% in the planes perpendicular or parallel to the freezing direction. This difference in porosity determined by the two methods is due to the presence of fine pores between the glass particles in the walls of the construct. Furthermore, the annealing process caused a coarsening of the camphene phase (and the large pores resulting from the sublimation of the camphene), but apparently had little effect on the packing of the glass particles in the walls of the construct.

3.4. Microstructure of sintered constructs

Optical images of the cross-sections of the sintered constructs (formed by freezing at 3°C and annealing for 72 h at 34°C) showed no marked difference in microstructure along the length of the sample (20 mm long) (data not included). Neglecting a thin surface layer, the microstructure of the constructs can be taken as homogeneous and independent of distance from the top and bottom of the construct. Figure 6 shows SEM images of the cross-sections (perpendicular and parallel to the freezing direction) of the sintered constructs which were formed by freezing at 3°C and annealing at 34°C for the times indicated. The sections perpendicular to the freezing direction (Figs. 6a, 6c, 6e) showed a microstructure consisting of a dense glass matrix containing pores with a nearly circular cross-section. The open porosity and average pore width (or diameter) of the

sintered constructs increased markedly with the duration of the annealing step. When compared to the microstructure of the constructs after the freezing and annealing steps, the fine pores between the glass particles in the walls of the construct were essentially eliminated by viscous flow sintering, giving a dense glass network. The larger oriented pores resulting from the camphene sublimation also shrank (i.e. became smaller in diameter) and, if below a certain diameter, were completely eliminated.

Since shorter annealing times resulted in pores with smaller diameters, the porosity of the sintered constructs, in turn, decreased with decreasing annealing time. Images of the sections parallel to the freezing direction showed that for the frozen construct without the annealing treatment (Fig. 6b), the elongated pores resulting from the camphene sublimation shrank during sintering, leading to fine, presumably isolated pores. On the other hand, while the oriented pores in the annealed constructs became smaller in diameter, they apparently remained continuous (Figs. 6d, 6f). Constructs annealed for longer times, as outlined above, had larger pore diameters, so the corresponding sintered constructs also had larger pore diameters.

X-ray tomography images of constructs prepared by annealing for 24 h and sintering showed an oriented, columnar microstructure (Fig. 7). Although the pores are not perfectly aligned along the direction of freezing, a high degree of orientation is evident. The images also showed that the oriented pores were not discontinuous in the direction perpendicular to the freezing direction. Neighboring pores appeared to be connected at several positions along their length. In addition to showing microstructural features that were compatible with those observed by SEM, the X-ray tomography images provided a clearer view of the pore orientation.

The average pore diameter (or width) and porosity determined by image analysis are shown in Fig. 8 for the sintered constructs formed by freezing at 3°C followed by annealing at 34 °C for 0–72 h. Both the pore diameter and the porosity increased with annealing time. Without annealing, the sintered construct had a porosity of $19 \pm 4\%$ and a pore width of 6 ± 2 μm. The sintering shrinkage was approximately isotropic, equal to 46-48% in the axial direction (parallel to the freezing direction) and in the radial direction (perpendicular to the freezing direction). For an annealing time of 24 h, the porosity and pore diameter of the sintered constructs were $52 \pm 3\%$ and 90 ± 30 μm, respectively,

while annealing for 72 h resulted in a porosity of 59 ± 3 % and a pore diameter of 110 ± 50 μm. The sintering shrinkage decreased with annealing time became more anisotropic; for an annealing time of 72 h, the shrinkage was 31% and 38% in the axial and radial direction, respectively.

As outlined earlier, to test the interconnectivity of the pores, the planar or circumferential surface of the sintered constructs was dipped lightly (to a distance <1 mm) into a blood-like solution. All the constructs annealed for 6 h or longer were rapidly filled with the blood-like solution (within 5 s) as a result of capillary pressure of the pores, regardless of whether the planar or circumferential surface was dipped into the solution. Figure 9 shows the cross-sections of the sintered constructs, prepared by freezing at 3°C and annealing for 6 h or 72 h at 34°C, after the constructs were dipped in the solution and dried. The infiltration of the solution completely throughout the constructs indicated that pores were interconnected in both the axial and radial directions.

3.5. Mechanical response of sintered constructs

The stress vs. deformation response of the sintered constructs in compression, in the freezing (orientation) direction, is shown in Fig. 10. The data are shown for the sintered constructs formed by freezing at 3°C and annealing for varying times in the range 0–72 h. The stress shown is the engineering stress, equal to the load divided by the initial cross-sectional area of the construct, while the deformation is the change in length divided by the initial length. The stress increased linearly with deformation, followed by a sharp decrease due to failure. The constructs failed in a brittle manner, fracturing into several pieces. However, the constructs annealed for 72 h (with the highest porosity) showed some degree of compaction following failure, resulting in a series of small decreases in stress with higher deformation. The compressive strength of the sintered constructs, taken as the highest stress in the stress vs. deformation response, varied from 180 ± 70 MPa (0 h annealing; porosity = 20%) to 16 ± 2 MPa (72 h annealing; porosity = 60%) (Table 2). The elastic modulus, determined from the slope, varied from 25 ± 5 GPa (0 h annealing) to 4 ± 1 GPa (72 h).

When tested in the direction perpendicular to the orientation direction, the constructs showed a response which was qualitatively similar to that in the orientation direction, but they were markedly weaker (Fig. 11). For the constructs prepared by

annealing for 24 h and sintering, the compressive strength and elastic modulus in the perpendicular direction (13 ± 3 MPa and 2 ± 1 GPa, respectively), were 2–3 times smaller than those in the orientation direction (27 ± 8 MPa and 7 ± 3 GPa, respectively). For comparison, constructs with a random microstructure showed mechanical response that was somewhat intermediate between those for the oriented scaffolds in the directions parallel and perpendicular to the freezing (orientation) direction (Fig. 11).

4. Discussion

4.1. Colloidal stability and viscosity of camphene-based suspensions

The viscosity of the suspension is an important processing parameter in the freeze casting process. For a given particle size, it determines the sedimentation velocity of the particles in the suspension [31], as well as the critical solidification front velocity for particle engulfment in the growing camphene crystal front. In the freezing process, the particles are rejected from the growing camphene crystals, and the interaction of the particles with the growing camphene crystal front determines the engulfment or rejection of the particles by the solidification front. For a given particle size, the critical solidification front velocity has been shown to vary inversely as the viscosity of the suspension [32, 33].

The colloid stability of the suspension is also important in that it determines the flocculation rate of the suspension as well as the viscosity of the suspension. The use of 2 wt% isostearic acid as a dispersant resulted in the formation of suspensions with approximately the lowest viscosity (Fig. 1). For this dispersant concentration, the maximum particle loading ϕ_m in the suspension, predicted on the basis of the Krieger–Dougherty equation (Fig. 2) was only 43%. In comparison, aqueous suspensions of 13-93 glass, with a similar particle size, stabilized with 0.5 wt% EasySperse, were found to have a ϕ_m of 55% [34]. The effectiveness of other dispersants for stabilizing bioactive glass particles in liquid camphene will be investigated in future work.

4.2. Solidification of camphene-based suspensions

In comparison with the unidirectional freezing of aqueous suspensions where the strongly anisotropic growth of hexagonal ice crystals leads to a lamellar structure [35], the tendency of camphene to form dendrites when solidified under appropriate

temperature conditions resulted in a more dendritic structure upon freezing camphene-based suspensions [36]. While camphene has been reported to have a cubic crystal structure, some studies indicated that the structure was tetragonal [36]. An anisotropy of ~3% was found in the ⟨001⟩ or *c*-direction, while the *a*- and *b*-directions are equivalent in a tetragonal unit cell. Camphene dendrites therefore grow preferentially in the c-direction, with side-branching or secondary dendritic growth in the orthogonal *a*- and *b*-directions.

Unidirectional freezing of camphene-based suspensions on a cold substrate starts with nucleation of camphene on the surface of the substrate. The imposed temperature gradient favors the growth of camphene crystals whose ⟨001⟩ or *c*-direction coincides with the temperature gradient, leading to growth of primary dendrites down the temperature gradient. As illustrated in Fig. 12, as the primary dendrites grow, the particles are expelled. This, coupled with side-branching or secondary dendritic growth, leads to the accumulation of the particles between the secondary dendrites emanating from the primary dendrites. Therefore, after sublimation of the camphene from the frozen constructs, the oriented pores should have a rough surface, due to the camphene removed from the side-branches or secondary dendrites, as observed in Fig. 3.

Camphene can be solidified at room temperature, and the solidification of camphene-based suspensions at room temperature resulted in the formation of larger camphene dendrites (larger pores upon sublimation of the camphene) because of low dendrite velocity. However, the tendency for unidirectional growth of the primary dendrites was reduced. Therefore, in the present work, freezing on a cold substrate at 3°C or −196°C was used to provide a steep vertical temperature gradient, which favored crystal growth preferentially down the temperature gradient. The size (width) of the primary camphene dendrites (or the size of the pores resulting from their sublimation) can be controlled by manipulating the freezing rate. In the case of unidirectional freezing of aqueous suspensions of hydroxyapatite, an increase in the freezing rate from 2°C/min to 10°C/min resulted in a decrease in the lamellar pore width from ~40 μm to ~10 μm [9]. In the present system, the cooling rate cannot be accurately measured. However, a decrease in the cold substrate temperature from 3°C to −196°C (the boiling point of liquid nitrogen), which is equivalent to an increase in the cooling rate, resulted in a

decrease in the pore widths from ~40 μm to ~15 μm. However, these pore widths obtained by manipulating the freezing rate only are much smaller than the pore sizes (>100 μm) found to be favorable for promoting tissue infiltration into the interior of porous constructs [1].

4.3. Coarsening of camphene phase during thermal annealing

The thermodynamic driving force for the coarsening of the camphene phase and the attainment of a nearly circular cross-section during annealing of the frozen constructs at 34°C (Fig. 4) is the reduction of the high surface area of the camphene dendrites. The microstructural observations and image analysis described earlier showed that the diameter (width) of the camphene in the frozen constructs and, hence, the diameter of the pores resulting from the camphene sublimation, increased with increasing annealing time (Figs. 4, 5). In order to provide information on the mechanism of the camphene phase coarsening, the growth kinetics of the pores resulting from sublimation of the camphene were compared with the predictions of theoretical models.

The coarsening of a dilute concentration of spherical particles (or precipitates) in a solid or liquid medium has been analyzed by Lifshitz and Slyozov [37], and by Wagner [38], commonly referred to as the LSW theory. Coarsening is assumed to be controlled by diffusion through the medium (diffusion control) or by the interface reaction (dissolution of the particles in the medium or deposition of solute onto the particle surfaces). For a time-invariant (self-similar) particle size distribution, the theoretical distribution function for interface reaction-controlled coarsening has the form:

$$f(s,t) = \frac{3}{4} s \left(\frac{2}{2-s} \right)^5 \exp\left(\frac{-3s}{2-s} \right) \qquad (0 < s < 2) \tag{2}$$

where $s = d / d^*$, d = particle radius, d^* = radius of particle that neither grows nor shrinks, and d^* is related to the average particle radius $\bar{d}$ by $\bar{d} = (8/9)d^*$. In the case of diffusion-controlled coarsening, the distribution function has the form:

$$f(s,t) = \frac{4}{9} s^2 \left(\frac{3}{3+s} \right)^{7/3} \left(\frac{3/2}{3/2-s} \right)^{1/3} \exp\left(\frac{-s}{3/2-s} \right) \qquad (0 < s < 3/2) \tag{3}$$

and $\bar{d} = d^*$. The average radius of the particles increases with time according to:

$$\bar{d}^n - d_o^n = Kt \tag{4}$$

where n = 2 for interface reaction-controlled coarsening, and n = 3 for diffusion-controlled coarsening. While corrections have been made to the LSW theory to account for the effect of more concentrated systems, in the present work the LSW theory for a dilute concentration of particles is used.

Direct coalescence of particles has also been proposed as a mechanism for coarsening [39]. In this case, two or more particles interconnected by solid necks are assumed to coarsen by diffusive transport of matter occurring essentially in the neck regions. A statistical theory [40] for particle coarsening by coalescence also predicts a self-similar, time-invariant, particle size distribution function, but the distribution function has the form:

$$F(s,t) = 2.136s^2 \exp(-0.712s^3) \quad (5)$$

The average particle size, $\bar{d}$, is predicted to increase with time, *t*, according to Equation (4) with the exponent *n* = 3.

For the frozen constructs annealed for varying times at 34°C, Fig. 13a shows that a plot of the cumulative fraction of pores with diameters smaller than a certain size vs. the reduced pore size, *s*, falls on a single curve regardless of the annealing time, indicating a self-similar distribution for all annealing times (6–72 h). Furthermore, a comparison of the data for the pore size distribution with the predictions of the LSW theory (diffusion or reaction control) and the coalescence model shows that the coalescence model provides the best fit to the data (Fig. 13b), indicating that direct coalescence of the interconnected camphene phase is the predominant mechanism of coarsening. Figure 14 shows that after a threshold annealing time (6 h), the growth of the pore diameters can be fitted by Equation (4), but a clear distinction between n = 2 and n = 3 cannot be made from the present data.

4.4. Microstructure and mechanical response of sintered scaffolds

The porosity and average pore diameter of the sintered scaffolds prepared from suspensions frozen at 3°C and annealed for 0–72 h at 34°C are summarized in Table 2. Although all the constructs had a starting porosity of ~86% after the annealing step, sintering resulted in a markedly lower porosity, in the range 20–60% for annealing times of 0–72 h. The fine pores between the particles in the glass network sintered rapidly by viscous flow sintering to produce a dense glass network. Later, viscous flow sintering

also resulted in some reduction of the pore diameter of the large oriented pores and, hence, to further shrinkage of the scaffold. Since the rate of viscous flow sintering varies inversely as the pore radius, the constructs that were annealed for shorter times sintered faster because of their smaller pores, so the porosity of the sintered scaffolds decreased with shorter annealing time (Table 2).

When tested in the directions parallel and perpendicular to the freezing (orientation) direction, the sintered scaffolds showed a brittle response characteristic of dense ceramics and glass, in which the compressive stress increased linearly with deformation, followed by catastrophic failure (Fig. 11). This response is markedly different from that of oriented hydroxyapatite and 13-93 bioactive glass scaffolds prepared by unidirectional freezing of aqueous-based suspensions which showed an 'elastic-plastic' response and a large strain for failure (>20%) [8, 11]. The response is also qualitatively different from that of 13-93 bioactive glass scaffolds prepared by a polymer foam replication technique, in which numerous peaks and valleys were observed in the stress vs. deformation response after the initial elastic deformation [34].

4.5. Scaffolds for bone repair

The present study shows promising results for the potential use of these oriented bioactive glass scaffolds in the repair of large defects in load-bearing bones, such as segmental defects in long bones. Bone is generally composed of two types: cortical (or compact) bone, and trabecular (cancellous or spongy) bone. Cortical bone, found primarily in the shaft of long bones and as the outer shell around cancellous bone, has a porosity of 5–10%; the compressive strength and elastic modulus in the direction parallel to the orientation (long axis) has been reported in the range 120–150 MPa and 10–20 GPa, respectively. A wide range has been reported for the elastic modulus (0.1–5 GPa) and compressive strength (2–12 MPa) of cancellous bone [41, 42]. In particular, sintered constructs prepared in this work for annealing times of 12–24 h, with a porosity of ~50% and an average pore diameter of 60–90 μm have a compressive strength of 25–50 MPa, and elastic modulus of 7–10 GPa.

In another study [16], scaffolds of silicate 45S5 bioactive glass were prepared by freezing camphene-bases suspensions in a random manner at room temperature. The frozen constructs were not annealed, so pore sizes resulting from the camphene

sublimation were <50 μm. Sintering for 3 h at 700 ^{o}C-1100 ^{o}C resulted in crystallization of the glass, with the formation of a crystalline $Na_2O \cdot 2CaO \cdot 3SiO_2$ phase, and limited densification of the resulting glass-ceramic phase below 1000 ^{o}C. While a devitrified 45S5 glass is still bioactive, the rate of conversion to a hydroxyapatite-type material (i.e., its bioactive potential) is markedly reduced [7].

These constructs prepared in this work have the requisite pore characteristics for supporting tissue infiltration, as well as adequate mechanical properties for replacing load-bearing bones. A detailed study of the *in vitro* and *in vivo* biological performance of these scaffolds is in progress, and the results will be described in a subsequent publication.

5. Conclusion

Oriented bioactive glass (13-93) scaffolds with promising microstructure and mechanical response for potential use in the repair of load-bearing bones were created using a method based on unidirectional freezing of camphene-based suspensions. Annealing the frozen constructs for 0-72 h at 34 ^{o}C (slightly below the solidification temperature of the suspension) resulted in coarsening of the camphene crystals, which provided a method for controlling the pore diameter of the constructs (in the range 15-160 μm after sublimation of the camphene). Coarsening of the camphene crystals during the annealing step can be described by a diffusion-controlled coalescence model. Sintering resulted in a decrease in the porosity and the pore diameter, giving scaffolds with porosities of 20–60% and pore diameters of 6–120 μm for annealing times of 0–72 h. The sintered scaffolds had compressive strength and elastic modulus values in the freezing (orientation) direction which varied from 180 MPa and 25 GPa (porosity = 20%), respectively, to 16 MPa and 4 GPa (porosity = 60 %) which were 2-3 times larger than those measured in the direction perpendicular to the orientation direction.

Acknowledgement

This work was supported by the U.S. Army Medical Research Acquisition Activity, under Contract No. W81XWH-08-1-0765, and by the National Institute of Health, NIAMS, Grant # 1R15AR056119-01. The authors would like to thank Dr. D. E.

Day for use of glass preparation facilities and the Advanced Light Source (ALS), Lawrence Berkeley National Laboratory, funded by the Department of Energy under Contract No. DE-AC02-05CH11231, for use of the dedicated X-ray tomography beam-line.

References

[1] Hulbert SF, Young FA, Mathews RS, Klawitter JJ, Talbert CD, Stelling FH. Potential of ceramic materials as permanently implantable skeletal prostheses. J Biomed Mater Res 1970; 4:433–456.

[2] Goldstein SA, Patil PV, Moalli MR, Perspectives on tissue engineering of bone, Clin Orthop Rel Res 1999; 367S: 419 – 423.

[3] Kneser U, Schaefer DJ, Munder B, Klemt C, Andree C, Stark GB. Tissue engineering of bone. Min Invas Ther & Allied Technol 2002; 11: 107–116.

[4] Wheeler DL, Stokes KE, Park HE, Hollinger JO. Evaluation of particulate Bioglass® in a rabbit radius ostectomy model. J Biomed Mater Res 1997; 35A: 249–254.

[5] Wheeler DL, Stokes KE, Hoellrich RG, Chamberland DL, McLoughlin SW. Effect of bioactive glass particle size on osseous regeneration of cancellous defects. J Biomed Mater Res 1998; 41A: 527–533.

[6] Hench LL, Splinter RJ, Allen WC, Greenlee TK. Bonding mechanism at the interface of ceramic prosthetic materials. J Biomed Mater Res 1971; 5: 117–141.

[7] Hench LL. Bioceramics. J Am Ceram Soc 1998; 81:1705–1728.

[8] Fu Q, Rahaman MN, Bal BS, Brown RF. Preparation and *in vitro* evaluation of bioactive glass (13-93) scaffolds with oriented microstructures for repair and regeneration of load-bearing bones. J Biomed Mater Res Part A 2010; 94A: 1380-90.

[9] Deville S, Saiz E, Tomsia AP. Freeze casting of hydroxyapatite scaffolds for bone tissue engineering. Biomaterials 2006; 27:5480–5489.

[10] Fu Q, Rahaman MN, Dogan F, Bal BS, Freeze casting of porous hydroxyapatite scaffolds - I. Processing and general microstructure. J Biomed Mater Res 2008; 86B: 125–135.

[11] Fu Q, Rahaman MN, Dogan F, Bal BS, Freeze casting of porous hydroxyapatite scaffolds - II. Sintering, microstructure, and mechanical behavior. J Biomed Mater Res 2008; 86B: 514–522.

[12] Fu Q, Rahaman MN, Bal BS, Kuroki K, Brown RF. *In vivo* evaluation of 13-93 bioactive glass scaffolds with trabecular and oriented microstructures in a subcutaneous rat implantation model. J Biomed Mater.Res Part A 2010; 95A: 235-44.

[13] Huang W, Day DE, Kittiratanapiboon K, Rahaman MN. Kinetics and mechanisms of the conversion of silicate (45S5), borate and borosilicate glasses to hydroxyapatite in diluate phosphate solutions. J Mater Sci: Mater Med 2006; 17:583–596.

[14] Fu Q, Rahaman MN, Fu H, Liu X. Bioactive glass scaffolds with controllable degradation rates for bone tissue engineering applications, I: preparation and *in vitro* degradation. J Biomed Mater Res Part A 2010; 95A: 164-71.

[15] Araki K, Halloran JW. New freeze-casting technique for ceramics with sublimable vehicles, J Am Ceram Soc 2004; 87:1859–1863.

[16] Song JH, Koh YH, Kim HE. Fabrication of a porous bioactive glass-ceramic using room-temperature freeze casting. J Am Ceram Soc 2006; 89: 2649–2653.

[17] Koh YH, Lee EJ, Yoon BH, Song JH, Kim HE. Effect of polystyrene addition on freeze casting of ceramic/camphene slurry for ultra-high porosity ceramics with aligned pore channels. J Am Ceram Soc 2006; 89: 3646–3653.

[18] Yoon BH, Choi WY, Kim HE, Kim JH, Koh YH. Aligned porous alumina ceramics with high compressive strengths for bone tissue engineering. Scripta Mater 2008; 58: 537-540.

[19] Soon YM, Shin KH, Koh YH, Lee JH, Kim HE. Compressive strength and processing of camphene-based freeze cast calcium phosphate scaffold with aligned pores. Mater Lett 2009; 63: 1548–1550.

[20] Lee EJ, Koh YH, Yoon BH, Kim HE, Kim HW. Highly porous hydroxyapatite bioceramics with interconnected pore channels using camphene-based freeze casting. Mater Lett 2007; 61:2270–2273.

[21] Yoon BH, Koh YH, Park CS, Kim HE. Generation of large pore channels for bone tissue engineering using camphene-based freeze casting, J Am Ceram Soc 2007; 90: 1744–1752

[22] Yook SW, Kim YE, Yoon BH, Soon YM, Koh YH. Improvement of compressive strength of porous hydroxyapatite scaffolds by adding polystyrene to camphene-based slurries, Mater Lett 2009; 63:955–958.

[23] Macchetta A, Turner IG, Bowen CR. Fabrication of HA/TCP scaffolds with a graded and porous structure using a camphene-based freeze-casting method. Acta Biomater 2009; 5:1319–1327.

[24] Yook SW, Yoon BH, Kim HE, Koh YH, Kim YS. Porous titanium (Ti) scaffolds by freezing TiH2/camphene slurries. Mater Lett 2008; 62:4506–4508.

[25] Han J, Hong C, Zhang X, Du J, Zhang W. Highly porous ZrO2 ceramics fabricated by a camphene-based freeze-casting route: Microstructure and properties. J Euro Ceram Soc 2010; 30:53–60.

[26] Tadros TF. Colloids in Cosmetics and Personal Care. Winheim, Germany; Wiley-VCH Verlag Gmbh & Co. KGaA, 2008; p.68.

[27] Dean JA, Lange's Handbook of Chemistry (15th Edition), McGraw-Hill, 1999.

[28] Pirofsky B, The determination of blood viscosity in man by a method based on Poseuille's law, J Clin Invest 1953; 32:292–298.

[29] Krieger IM, Dougherty M. A mechanism for non-newtonian flow in suspensions of rigid spheres. Trans Soc Rheol 1959; 3: 137–152.

[30] Bergstrom L. Shear thinning and shear thickening of concentrated ceramic suspensions. Colloids Surf A: Physicochem Eng Aspects 1998; 133: 151–155.

[31] Rahaman MN. Ceramic Processing. Boca Raton, FL; Taylor & Francis/CRC Press, 2006; p. 109.

[32] Uhlmann DR, Chalmers B, Jackson KA. Interaction between particles and a moving ice–liquid interface. J Appl Phys 1964; 35: 2986–2993.

[33] Körber C, Rau G, Cosman MD, Cravahlo EG. Interaction of particles and a moving ice–liquid interface. J Cryst Growth 1985; 72: 649–62.

[34] Fu Q, Rahaman MN, Bal BS, Brown RF, Day DE. Mechanical and *in vitro* performance of 13-93 bioactive glass scaffolds prepared by a polymer foam replication technique. Acta Biomater 2008; 4: 1854–1864.

[35] Deville S, Saiz E, Tomisa AP. Ice-templated porous alumina structures. Acta Mater 2007; 55:1965–1974.

[36] Rubinstein ER, Glicksman ME. Dendritic growth kinetics and structure II. Camphene. J Crystal Growth 1991;112:97–110.

[37] Lifshitz IM, Slyozov VV. The kinetics of precipitation from supersaturated solutions. Phys Chem Solids 1961;19:35–50.

[38] Wagner C. Theory of ostwald ripening. Z Electrochem 1961;65:581–591.

[39] Takajo S, Kaysser WA, Petzow G, Analysis of particle growth by coalescence during liquid phase sintering, Acta Metall 1984;32:107–113.

[40] Kaysser WA, Takajo S, Petzow G. Particle growth by coalescence during liquid phase sintering of Fe-Cu. Acta Metall 1984;32:114–122.

[41] Rho JY, Hobatho MC, Ashman RB. Relations of density and CT numbers to mechanical properties for human cortical and cancellous bone. Med Eng Phys 1995:17:347–355.

[42] An YH, Draughn RA. Mechanical Testing of Bone and the Bone-implant Interface. CRC Press, Boca Raton, FL, 2000; p. 51.

Table 1 Summary of porous constructs fabricated by freezing of camphene-based suspensions

Material	Particle size (μm)	Freezing/annealing conditions	Freezing directionality	Pore size (μm)	Porosity (%)	Ref.
13-93 glass	1–2	3°C; –196°C/ 34°C (0–72 h)	Unidirectional	10–160	20–60	Present work
45S5 glass	—	20 °C	No	10–40	53	[16]
Al_2O_3	0.4	25°C; 0 °C	No/Yes	—	20–50	[15]
Al_2O_3	0.3	20°C	No	50	>88	[17]
Al_2O_3	0.3	3°C/35°C (24 h)	Unidirectional	102–210	57–83	[18]
CaP	—	3°C/32°C (1–3 days)	Unidirectional	122–166	62–65	[19]
HA	—	20°C	No	20–40	56–75	[20]
HA	—	0–35 °C	No	80–250	55–76	[21]
HA	—	34°C	No	141–324	71–73	[22]
HA/TCP	—	4–30 °C	No	40–200	31–73	[23]
Ti	1–3	33°C	No	>100	49–63	[24]
ZrO_2	0.4	0°C; –196°C	Unidirectional	15–30	65–83	[25]

Table 2 Microstructural characteristics and mechanical properties in compression for 13-93 bioactive glass scaffolds prepared by unidirectional freezing of camphene-based suspensions at 3°C, annealing at 34°C for the times shown, and sintering for 1 h at 690°C.

Annealing time (h)	Annealed construct		Sintered construct			
	Porosity (%)	Pore diameter or width (μm)	Porosity (%)	Pore diameter or width (μm)	Compressive strength (MPa)	Elastic modulus (GPa)
0	86 ± 1	40 ± 5	19 ± 4	6 ± 2	180 ± 70	25 ± 5
6	86 ± 1	75 ± 25	37 ± 7	38 ± 10	66 ± 32	10 ± 3
12	86 ± 1	130 ± 40	46 ± 6	60 ± 20	53 ± 10	9 ± 3
24	86 ± 1	150 ± 50	52 ± 3	90 ± 30	27 ± 8[1]	7 ± 3[1]
					16 ± 3[2]	3 ± 1[2]
					13 ± 3[3]	2 ± 1[3]
72	86 ± 1	160 ± 50	59 ± 3	115 ± 50	16 ± 2	4 ± 1

[1]Parallel to the orientation direction; [2]Scaffold with more random microstructure; [3]Perpendicular to the orientation direction.

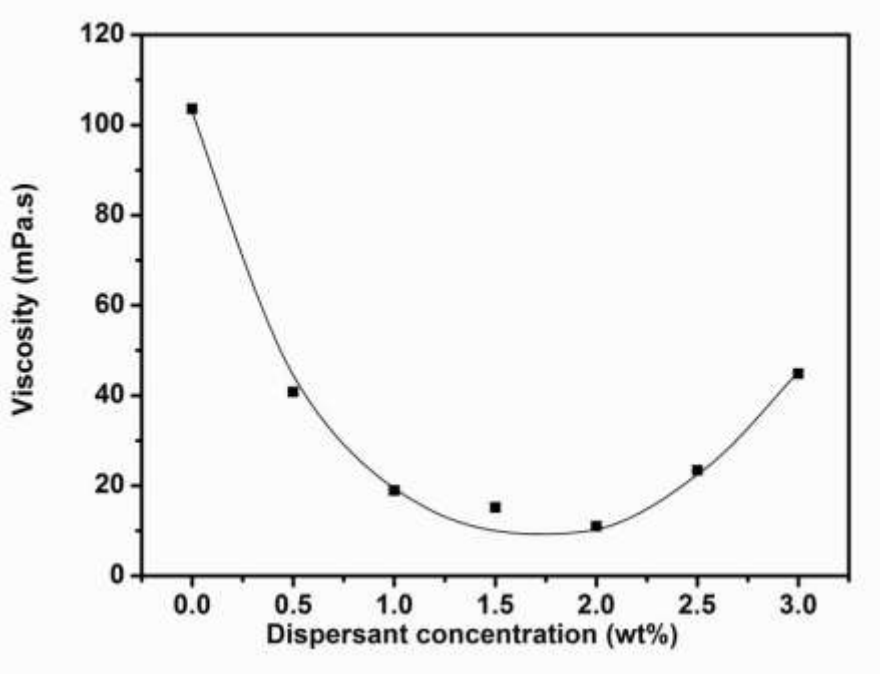

Fig. 1. Viscosity of camphene-based suspensions containing 10 vol% 13-93 bioactive glass particles vs. isostearic acid (dispersant) concentration (shear rate = 100 s^{-1}).

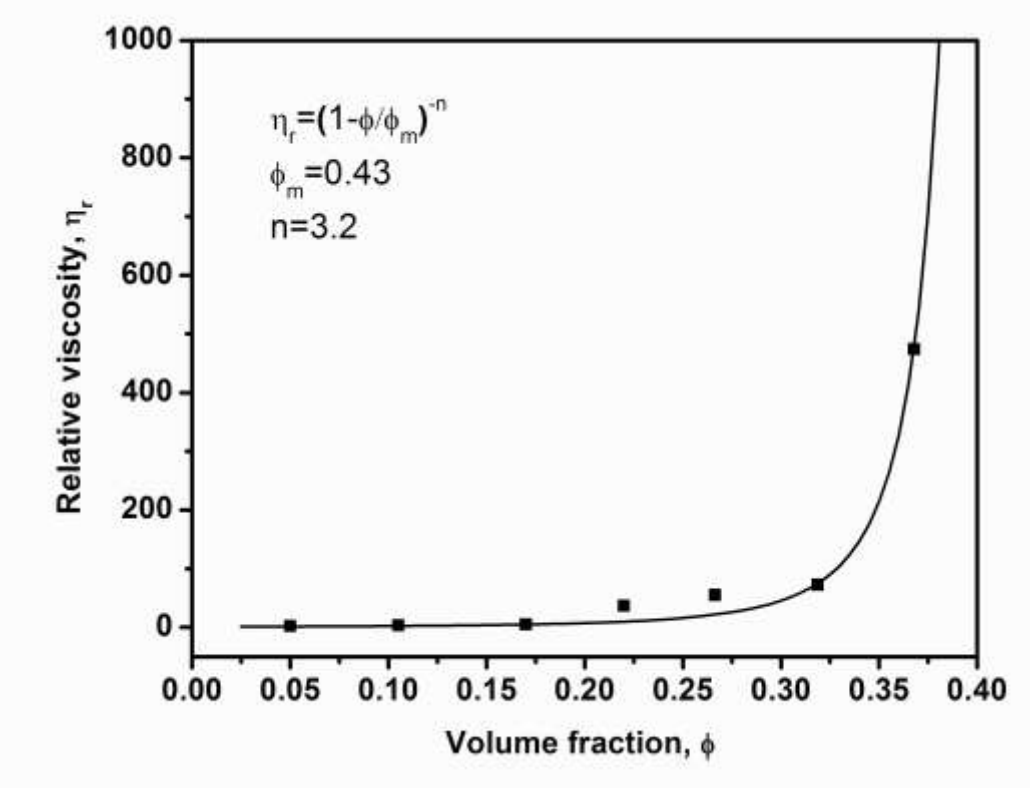

Fig. 2. Relative viscosity vs. volume fraction of 13-93 bioactive glass particles in camphene-based suspensions stabilized with 2 wt% isostearic acid (shear rate = 100 s^{-1}).

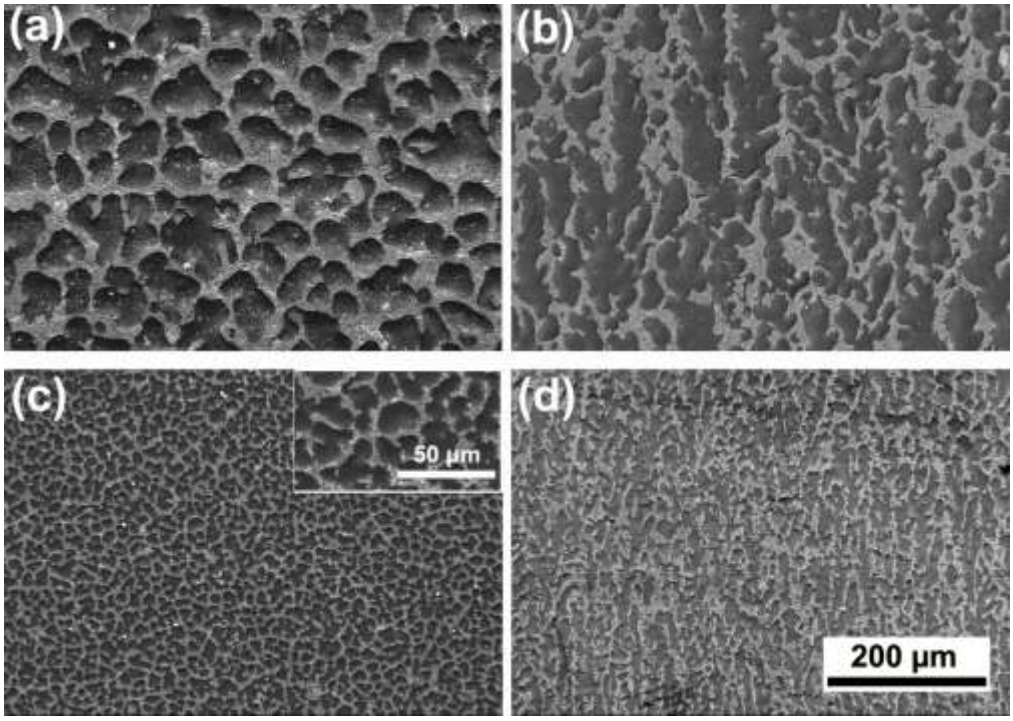

Fig.3. SEM images of 13-93 bioactive glass constructs prepared by unidirectional freezing of camphene-based suspensions (10 vol% particles) on a copper substrate at 3°C (a, b), and at –196°C (c, d). The sections are perpendicular (a, c) and parallel (b, d) to the freezing direction.

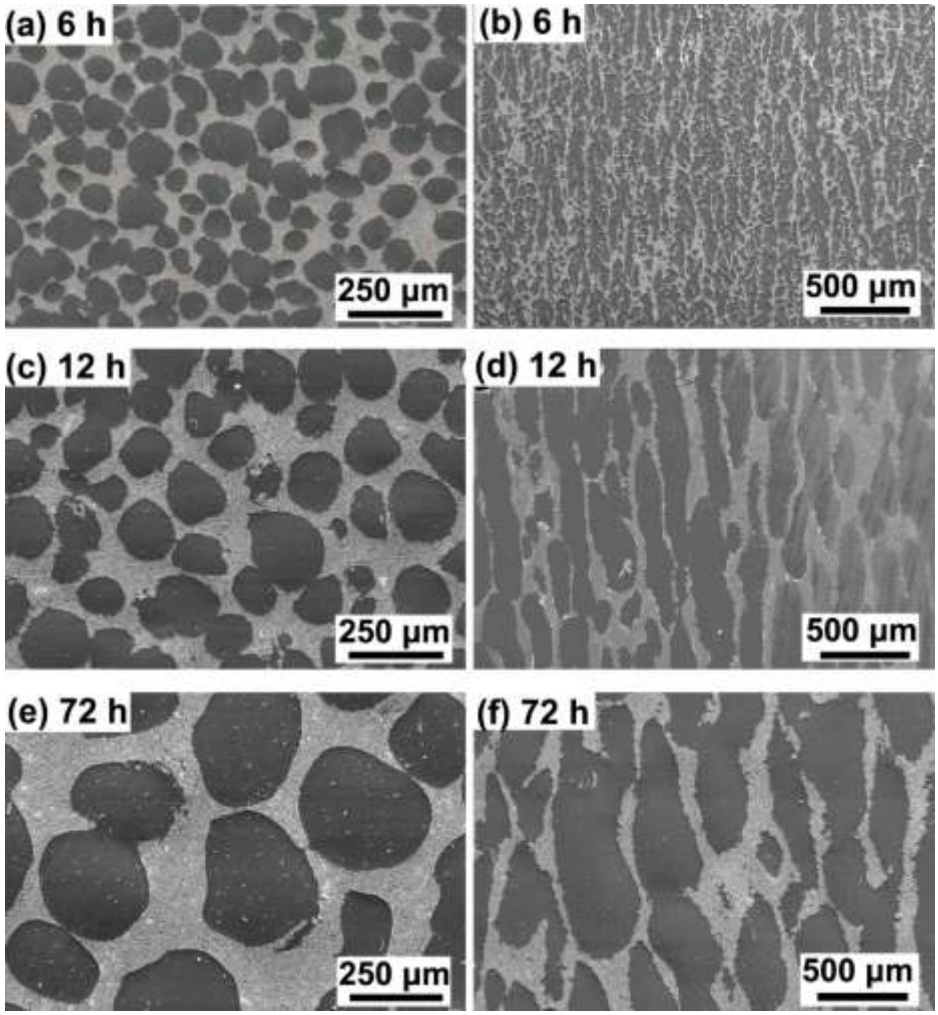

Fig. 4. SEM images of the cross-sections perpendicular (a, c, e) and parallel (b, d, f) to the freezing direction, for 13-93 bioactive glass constructs prepared by unidirectional freezing of camphene-based suspensions (10 vol% particles) at 3°C, and thermal annealing at 34°C for the times shown.

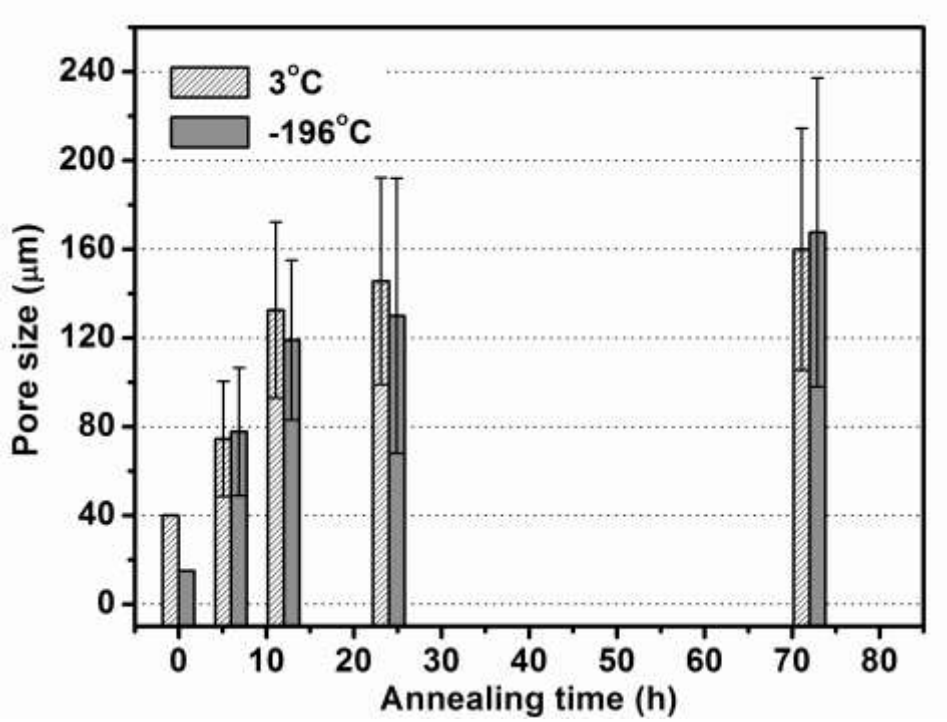

Fig.5. Average pore size (diameter) vs. annealing time for 13-93 bioactive glass constructs prepared by freezing camphene-based suspensions (10 vol% particles) at 3°C and thermal annealing at 34°C.

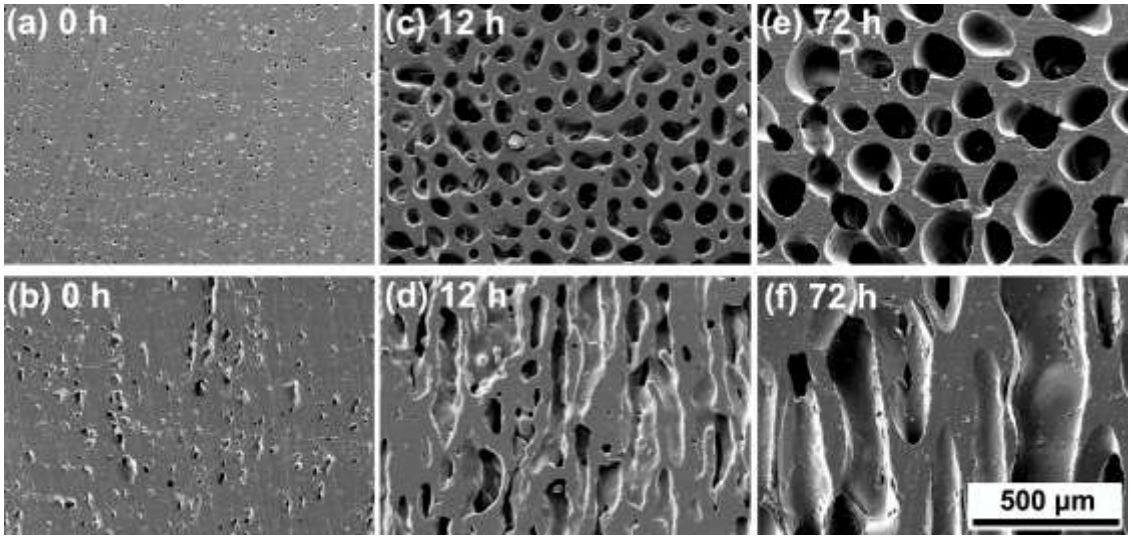

Fig. 6. SEM images of the cross-sections perpendicular (a, c, e) and parallel (b, d, f) to the freezing direction, for 13-93 bioactive glass constructs prepared by unidirectional freezing of camphene-based suspensions at 3°C, thermal annealing at 34°C for the times shown, and sintering for 1 h at 690°C.

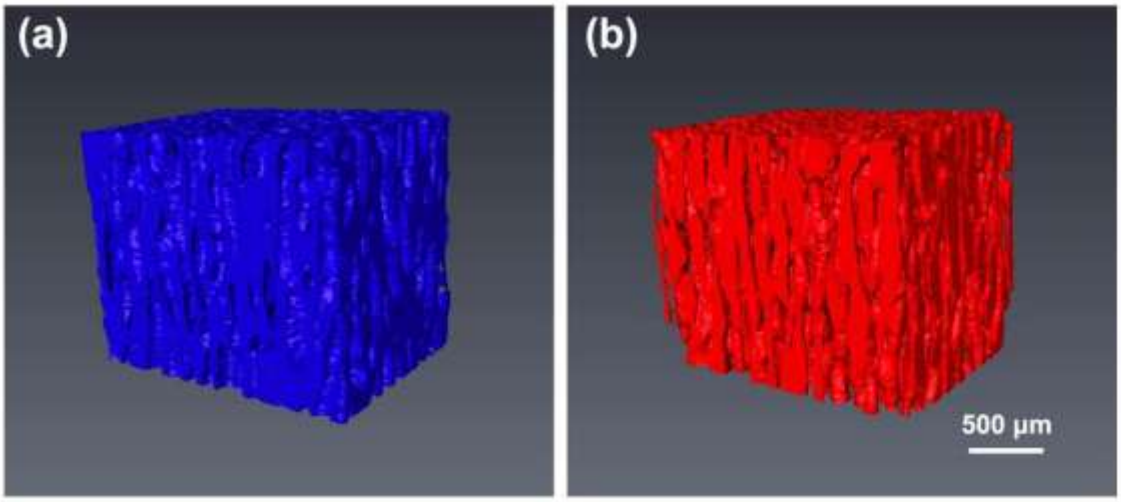

Fig. 7.X-ray tomography images of sintered 13-93 bioactive glass constructs prepared by unidirectional freezing camphene-based suspension at 3^{o}C, annealing for 24 h (glass phase in blue color; pore phase in red color).

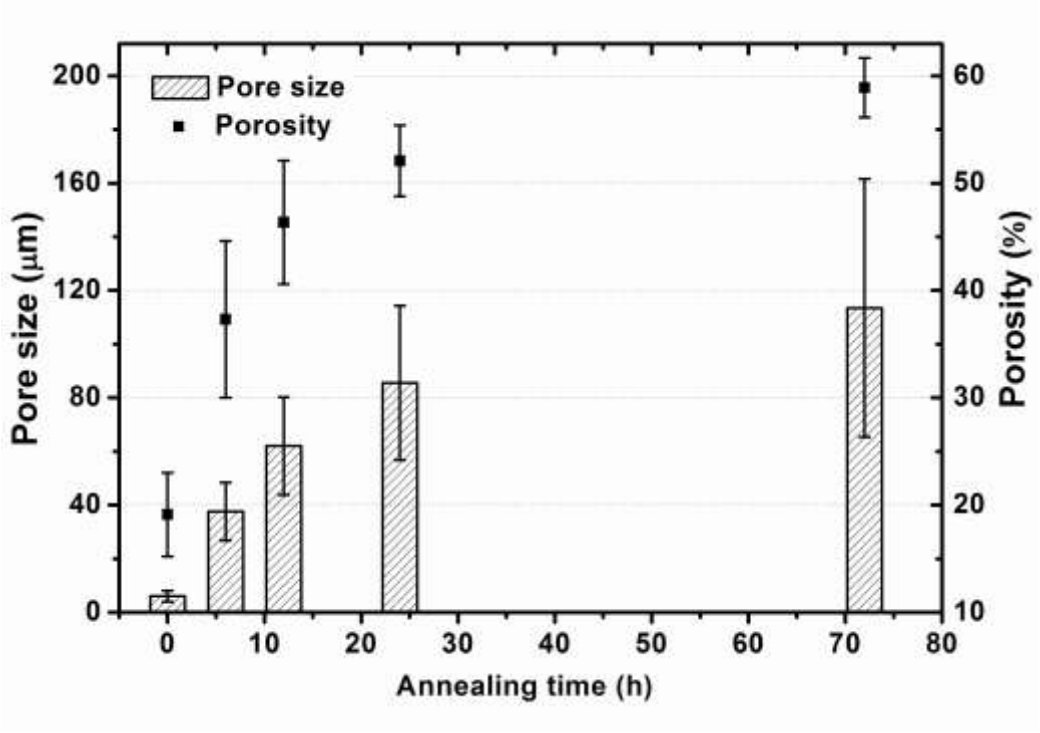

Fig. 8. Porosity and pore size vs. annealing time for sintered constructs of 13-93 bioactive glass prepared by unidirectional freezing of camphene-based suspensions at 3°C, thermal annealing at 34°C, and sintering for 1 h at 690°C.

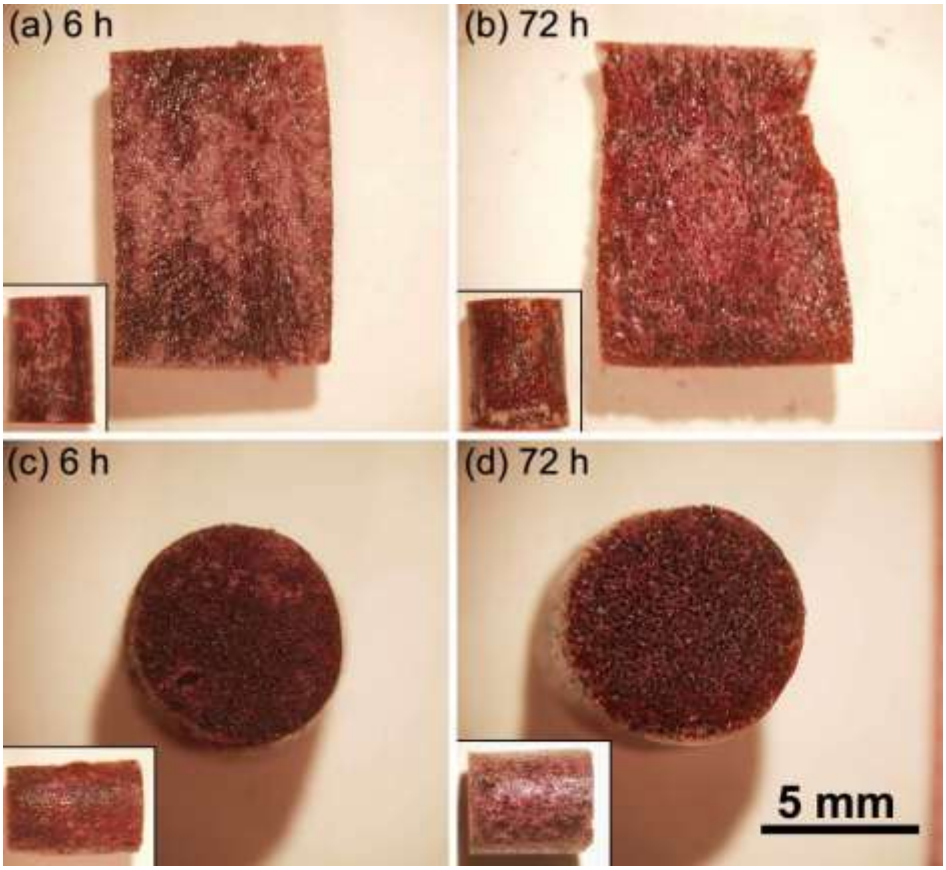

Fig. 9. Optical images of the cross-sections of sintered 13-93 bioactive glass constructs, showing the interconnectivity of the pores. The constructs were prepared by unidirectional freezing of camphene-based suspensions at 3°C, annealing at 34°C for 6 h or 72 h, and sintering for 1 h at 690°C. The flat surface (a, c) and the circumferential surface (b, d) of cylindrical constructs were lightly dipped into a blood-like solution, dried, and sectioned. (Inset: surface of the cylindrical constructs after drying).

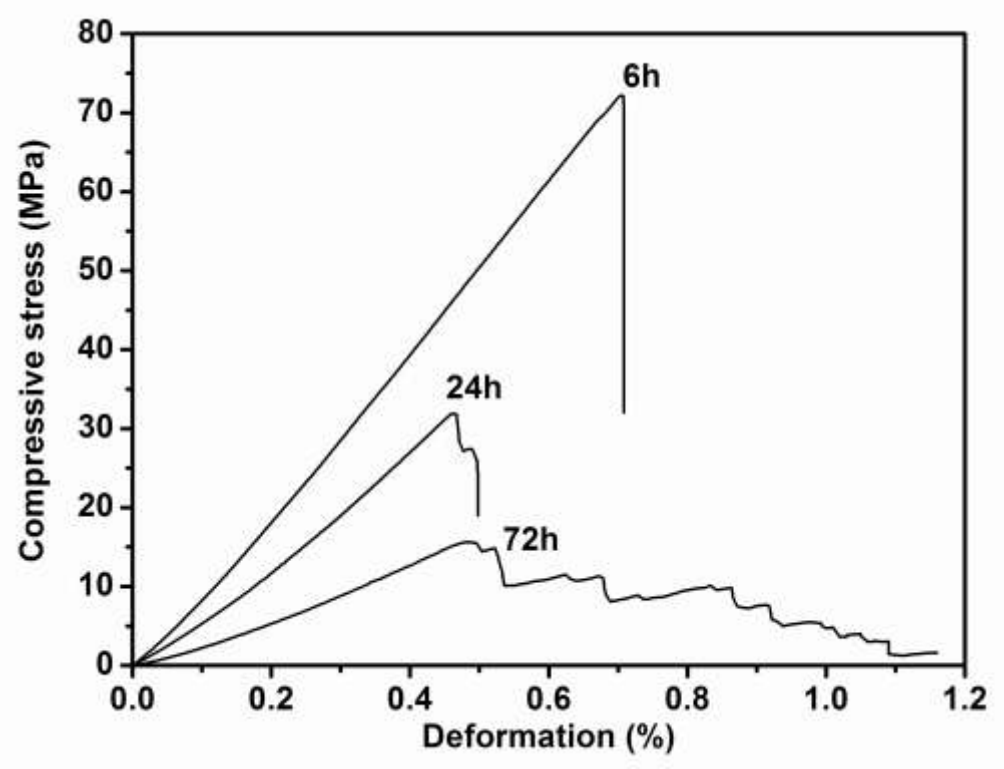

Fig. 10. Compressive stress vs. deformation in the orientation direction (direction of freezing) for sintered 13-93 bioactive glass constructs prepared by unidirectional freezing of camphene-based suspensions (10 vol% particles) at 3°C, annealing at 34°C for the times shown, and sintering for 1 h at 690°C.

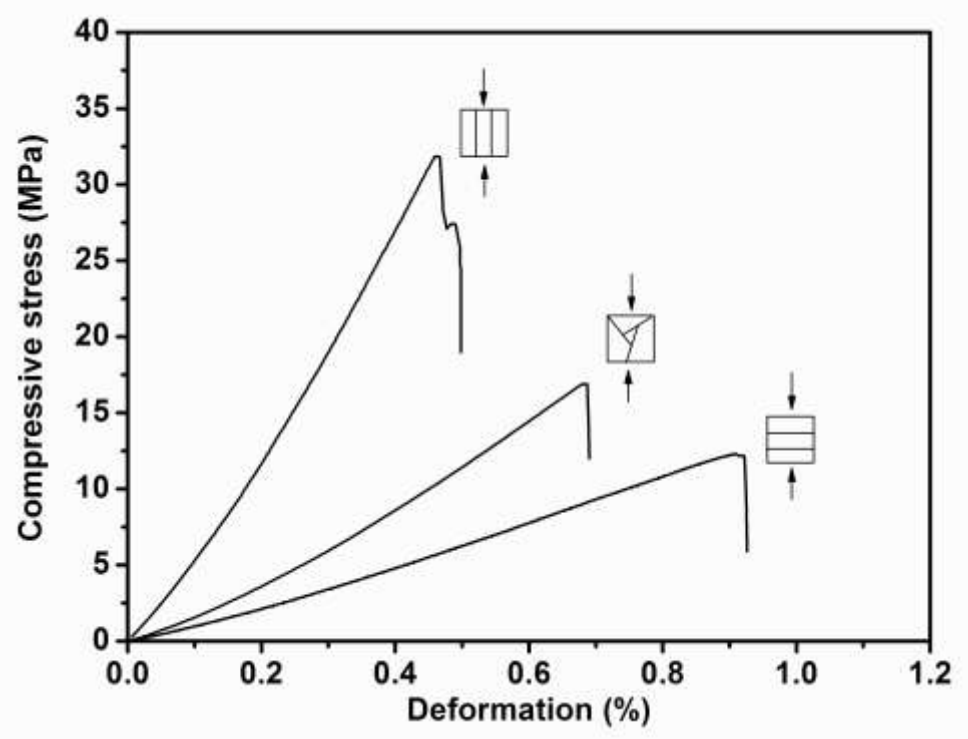

Fig. 11. Compressive stress vs. deformation for oriented scaffolds in the longitudinal direction and transverse direction as well as non-oriented scaffold prepared by freezing camphene-based suspension at 3^{o}C, annealing for 24 h.

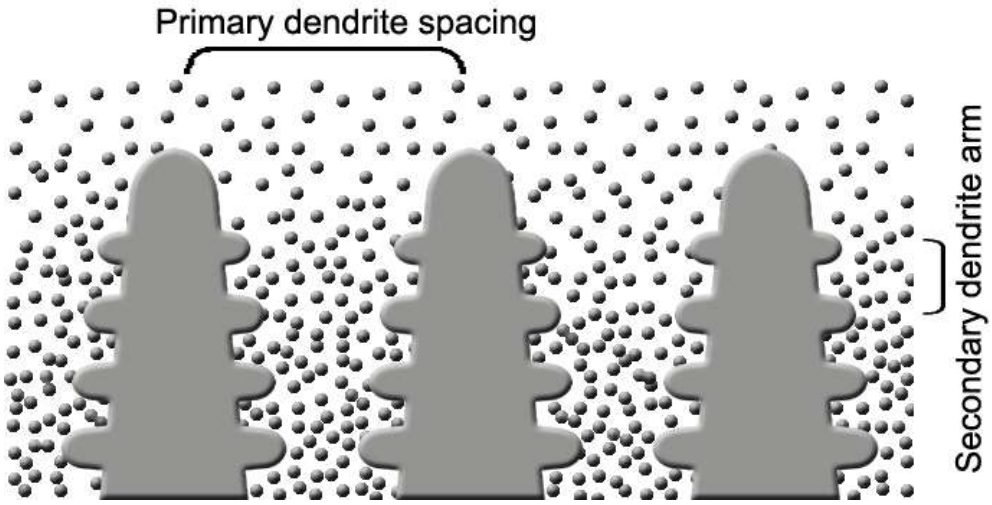

Fig. 12. Schematic of the growth of camphene dendrites during unidirectional freezing of camphene-based suspensions.

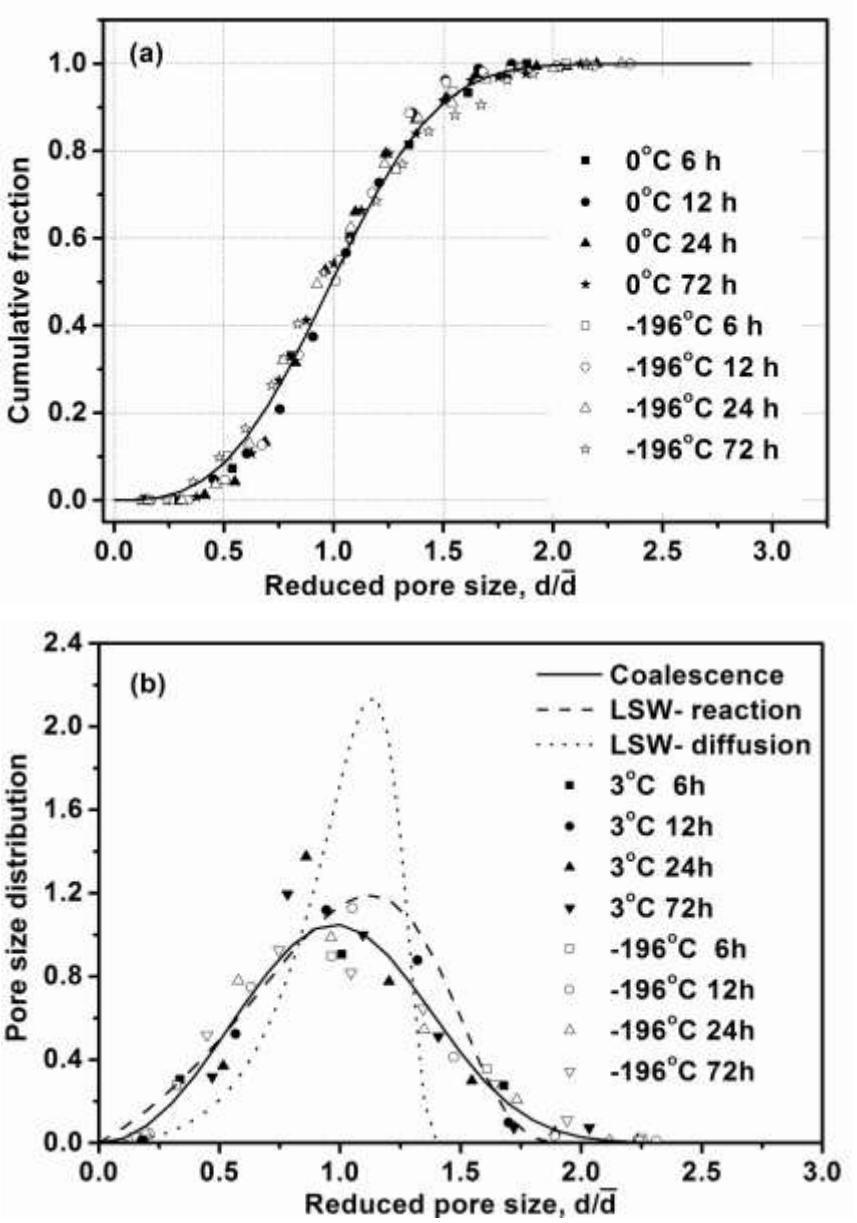

Fig.13. (a) Cumulative fraction of pores vs. normalized pore diameter, for constructs prepared by freezing at 0°C and −196°C, and annealed at 34°C for 6, 12, 24, and 72 h. (b) Pore size distribution data vs. normalized pore diameter for the constructs described in (a), compared with the predictions of the LSW model for interface- and diffusion-controlled coarsening and a coalescence model.

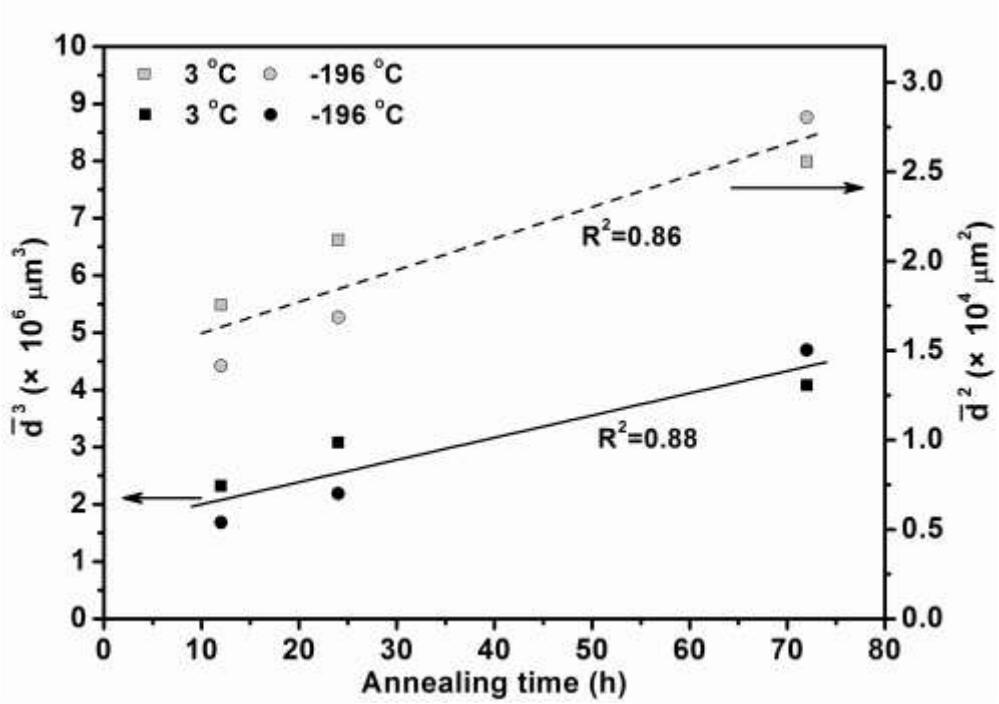

Fig. 14. Data for the average pore diameter vs. annealing time at 34°C for constructs prepared by freezing at 0°C and –196°C, and annealed at 34°C for 12, 24, and 72 h. The data are fitted using Equation (3) for n = 3 and n = 2.

II. POROUS AND STRONG BIOACTIVE GLASS (13-93) SCAFFOLDS PREPARED BY UNIDIRECTIONAL FREEZING OF CAMPHENE-BASED SUSPENSIONS

Xin Liu[1], Mohamed N. Rahaman[1], Qiang Fu[2]

[1]Department of Materials Science and Engineering and Center for Bone and Tissue Repair and Regeneration, Missouri University of Science and Technology, Rolla, MO 65409, USA

[2]Materials Sciences Division, Lawrence Berkeley National Laboratory, Berkeley, CA 94720, USA

ABSTRACT

Scaffolds of 13-93 bioactive glass (6Na_2O, 12K_2O, 5MgO, 20CaO, 4P_2O_5, 53SiO_2; wt.%) with an oriented pore architecture were formed by unidirectional freezing of camphene-based suspensions, followed by thermal annealing of the frozen constructs to grow the camphene crystals. After sublimation of the camphene, the constructs were sintered (1 h at 700 ^oC) to produce a dense glass phase with oriented macropores. The objective of this work was to study how constant freezing rates (1–7 $^oC\ min^{-1}$) during the freezing step influenced the pore orientation and mechanical response of the scaffolds. When compared to scaffolds prepared by freezing the suspensions on a substrate kept at a constant temperature of 3 ^oC (time-dependent freezing rate), higher freezing rates resulted in better pore orientation, a more homogeneous microstructure and a marked improvement in the mechanical response of the scaffolds in compression. Scaffolds fabricated using a constant freezing rate of 7 $^oC\ min^{-1}$ (porosity = 50 $\pm$4%; average pore diameter = 100 μm), had a compressive strength of 47 $\pm$5 MPa and an elastic modulus of 11 $\pm$3 GPa (in the orientation direction). In comparison, scaffolds prepared by freezing on the constant-temperature substrate had strength and modulus values of 35 $\pm$11 MPa and 8 $\pm$3 GPa, respectively. These oriented bioactive glass scaffolds prepared by the constant freezing rate route could potentially be used for the repair of defects in load-bearing bones, such as segmental defects in the long bones.

1. Introduction

There is a need to develop new scaffolds to repair large defects in load-bearing bones using materials that are biocompatible and durable during the patient's lifetime [1]. Treatment methods based on the use of bone autografts and allografts are effective for the repair of contained defects in non-loaded bone which do not require a significant amount of graft material. However, they suffer from limitations (e.g., donor site morbidity; limited supply; possible transmission of diseases; high costs). Synthetic biocompatible scaffolds that replicate the structure and function of bone would be ideal bone substitutes, provided they have the requisite mechanical properties for reliable long-term cyclical loading during weight bearing.

Scaffolds should have a porous microstructure suitable for supporting tissue ingrowth, and mechanical properties comparable to those of the tissue to be replaced. An interconnected pore size (diameter or width of the openings between adjoining pores) of 100 μm is considered to be the minimum requirement to permit tissue ingrowth and function [2]. The repair of segmental defects in load-bearing bones such as the long bones often involves the substitution of defects larger than a few centimeters [3]. Therefore it is essential that processing methods provide control of the microstructure over the entire dimensions of the scaffold in order to achieve the requisite mechanical reliability of the scaffold.

The mechanical response of porous materials with an anisotropic microstructure is strongly dependent on the pore orientation [4-6]. Commonly, the mechanical response in the pore orientation direction is often far superior to that in the perpendicular direction, and superior to that for scaffolds with a random microstructure. For example, the compressive strength and elastic modulus of human cortical bone in the orientation direction are almost twice those in the perpendicular direction [7]. The formation of scaffolds with oriented pore architectures could provide an approach for creating porous and strong three-dimensional scaffolds for applications in the repair of loaded bone.

Unidirectional freezing of aqueous suspensions has been used recently to produce oriented scaffolds of bioceramics and bioactive glass [8, 9]. The process commonly results in the formation of porous constructs with a lamellar microstructure. However, the width of the slot-like pores (10–40 μm) is considered to be too small to support tissue

ingrowth. A variety of techniques has been used to control the width and morphology of the pores, such as the use of different freezing rates [10], modification of the solvent composition [11−13], patterning of the cold substrate [14], application of an electric field [15], and coarsening of the crystals [16]. In addition, control of the freezing rate has been shown to lower the variation in the pore width along the freezing direction [17, 18], and to provide a homogenous lamellar microstructure over several centimeters [19]. However, in addition to the narrow pore width of the scaffolds mentioned above, another limitation in the use of aqueous solvents is the chemical degradation of the bioactive glass, particularly for more reactive borosilicate and borate bioactive glasses.

Our previous work showed that the use of organic (camphene)-based suspensions, coupled with a two-step forming process, can alleviate the above-mentioned limitations of aqueous suspensions [16]. Bioactive glass scaffolds prepared from camphene-based suspensions had a columnar microstructure with average pore diameters larger than 100 μm. The two-step process consisted of unidirectional freezing of the suspension on a substrate kept at a constant temperature (3 °C) followed by thermal annealing, typically for ~24 h at ~35 °C (near the softening point of the frozen mixture). In the freezing step, solid camphene dendrites form in the suspension of bioactive glass particles in liquid camphene, starting at the interface with the cold substrate and growing down the temperature gradient (Fig. 1). The dendrites redistribute the particles, which are concentrated in the inter-dendritic spaces. The result is a frozen construct consisting of particle-free solid dendrites and inter-dendritic material of bioactive glass particles in fine-scale frozen camphene. Upon sublimation of the camphene, the primary dendrites become macropores which are separated by concentrated glass particulate regions in the shape of the inter-dendritic spaces. Sintering results in the preferential removal of the fine pores in the particulate regions, giving a cellular scaffold with dense glass struts approximating the shape of the inter-dendritic regions and macropores in the shape of the primary dendrites. Annealing the frozen construct near the solidification temperature of the suspension leads to coarsening of the primary dendrites and removal of the secondary dendrite arms. As a result, the annealed construct has uniaxially-aligned primary dendrites with larger diameter than the frozen construct, which are better for long bone scaffolds.

In our previous work [16], unidirectional freezing on a constant-temperature substrate did not provide a constant freezing rate. Instead, the freezing rate was time-dependent, decreasing with time as the solidification front moved from the cold substrate to the top of the sample. Because of this time-dependent freezing rate, the achievement of uniaxially-aligned camphene dendrites and homogeneity of the dendrite diameter was limited to only ~1 cm.

In the present work, an apparatus was assembled to study unidirectional freezing of camphene-based suspensions at constant freezing rates. We hypothesized that the use of constant freezing rates could create constructs with more spatially uniform dendrites, resulting in the production of bioactive glass scaffolds with improved mechanical properties (in the orientation direction). Constructs of silicate 13-93 glass were formed using the two-step freezing and annealing process described previously. In the freezing step, constant freezing rates in the range 1–7 °C/min were used. The effect of the freezing rate on the pore orientation, microstructural homogeneity, and mechanical response of the fabricated scaffolds was studied. For comparison, scaffolds were prepared using the same process but with the freezing step carried out on a substrate held at a constant temperature, as described in our previous work [16].

Silicate 13-93 bioactive glass was used in this work because of our previous experience with forming scaffolds of this glass using other techniques [9, 20-22]. In addition, 13-93 bioactive glass has better processing characteristics by viscous flow sintering than the more widely researched 45S5 glass. While it is based on the 45S5 composition, 13-93 glass has a higher SiO_2 content, plus additional network modifiers, such as K_2O and MgO [23], which provides a larger window between the glass transition temperature and the onset of crystallization. As a result, the glass phase in porous constructs formed from 13-93 glass particles can be sintered to high density without crystallization, which often leads to an improvement in the mechanical strength of the scaffolds. Furthermore, *in vitro* cell culture showed no marked difference between the ability of 13-93 and 45S5 glass to support the proliferation and function of osteoblastic cells [24].

2. Materials and methods

2.1. Preparation of oriented 13-93 bioactive glass scaffolds

The fabrication of bioactive glass (13-93) scaffolds with oriented pores by unidirectional freezing of camphene-based suspensions was performed using a sequence of steps [16]: preparation of a homogeneous suspension; unidirectional freezing of the suspension; isothermal annealing of the frozen constructs near the softening point of the mixture to coarsen the camphene crystals; sublimation of the camphene crystals to replicate the macropores; and sintering to densify the glass phase in the macropore walls.

The procedure for preparing camphene-based suspensions is described in detail elsewhere [16]. Briefly, bioactive glass with the 13-93 composition ($6Na_2O$, $12K_2O$, 5MgO, 20CaO, $4P_2O_5$, $53SiO_2$; wt %) (kindly provided by Mo-Sci Corp., Rolla, Missouri), was ground to produce particles with an average size of ~1 μm. Suspensions were prepared by ball milling a mixture of the glass particles (10 vol%), camphene ($C_{10}H_{16}$; CAS 5794-04-7; Alfa Aesar, Ward Hill, MA, USA), and 2 wt% of isostearic acid ($C_{18}H_{36}O_2$; MP Biomedicals LLC, Solon, OH, USA) for 24 h at 55 °C in a closed polypropylene bottle.

Unidirectional freezing of the suspensions was performed at selected constant freezing rates in the range 1–7 °C/min using a specially assembled apparatus, described in detail elsewhere [25]. Briefly, the suspension was poured into a polytetrafluoroethylene mold which was surrounded by a heating jacket and placed on a cold copper rod (cold finger). Since camphene could freeze at room temperature, a constant output was applied to the heating jacket which kept the mold temperature at around 35 ^{o}C in order to minimize the heat transfer through the mold. The mold was also covered with a rubber cap to prevent heat transfer from the top. The cold finger was cooled by liquid nitrogen. The temperature of the cold finger was controlled by another heating jacket, a thermocouple within the cold finger, and a proportional–integral–derivative (PID) controller. Frozen constructs with a diameter of ~10 mm and a length of ~20 mm were prepared. For comparison, unidirectional freezing was also performed by freezing the suspensions on a copper substrate kept at a constant temperature of 3 °C, as described in our previous work [16].

After freezing, each construct was placed in a closed poly (vinyl chloride) (PVC) container to avoid camphene loss, and annealed for 24 h at 34 ^{o}C in an incubator to coarsen the camphene dendrites. The samples were cooled to room temperature, removed from the PVC containers, and kept for 24 h at room temperature in a fume hood to sublime the camphene phase. Finally, the porous constructs were sintered in air for 1 h at 700 °C (heating rate = 5°C/min) to remove the fine pores between the bioactive glass particles in the walls of the oriented macropores.

2.2. Microstructural characterization of porous constructs

After sublimation of the camphene, the porous constructs were pre-sintered (5 h at 600 °C) in order to develop adequate strength for handling but to maintain the as-formed porous microstructure. These pre-sintered constructs were sectioned in planes parallel and perpendicular to the freezing direction, infiltrated with epoxy resin, ground and polished. The polished sections were coated with Au/Pd, and examined by scanning electron microscopy (SEM) using an S-4700 microscope (Hitachi, Tokyo, Japan) at an accelerating voltage of 15 kV and a working distance of 18 mm. Sections of the sintered constructs (1 h at 700 °C) were also prepared and examined using a similar procedure.

The line intercept method was used to determine the average pore diameter of the constructs from sections perpendicular to the freezing direction. More than 100 intersections were counted. The open porosity of the sintered constructs was measured using the Archimedes method. The pore size distribution was determined using a liquid extrusion porosimeter (LEP-1100 AX, Porous Materials Inc., NY), with water used as the wetting liquid.

2.3. Mechanical response of sintered scaffolds

The mechanical response of the sintered constructs in the direction of freezing was measured in compression using an Instron testing machine (Model 4204; Norwood, MA, USA). Cylindrical constructs (7 mm in diameter $\times$ 7 mm) were deformed at a rate of 0.5 mm/min. Six samples were tested for each group, and the compressive strength and elastic modulus were determined as an average $\pm$ standard deviation. Statistical analysis was performed using one-way analysis of variance. After testing, the fractured surfaces of the scaffolds were examined using SEM.

3. RESULTS

3.1. Freezing rate of suspensions

Figure 2 shows the temperature of the cold finger (copper rod) as a function of time for the freezing process at three different freezing rates (1, 4, and 7 °C/min). Higher cooling rates were limited by the conductivity and the lowest achievable temperature of the copper rod. In order to maintain the required freezing rate, the temperature of the copper rod was lowered continuously with the aid of the PID controller. The average solidification rates, 4, 10, and 16 μm/s, for the freezing rates of 1, 4, and 7 °C/min, respectively, were determined from the length of the frozen construct and the time required to completely freeze the construct. For comparison, the time for complete freezing is also shown for the suspensions frozen on the constant-temperature substrate (3 °C).

3.2. Microstructure of frozen constructs

Figure 3 shows SEM images of the cross-sections parallel to the freezing direction for constructs prepared at constant freezing rates of 1 and 7 °C/min after sublimation of the camphene; for comparison, SEM images of constructs prepared by freezing on a constant-temperature substrate (3 °C) are also shown. Images for constructs frozen at 4 °C/min are not shown for the sake of brevity. The images were taken at the top, middle, and bottom region along the length of the construct. Generally, the pores showed a dendritic morphology, resulting from the growth of primary camphene dendrites down the imposed temperature gradient, and side-branching or secondary camphene dendrites emanating from the primary dendrites. However, the spatial homogeneity of the pore diameter was dependent on the freezing method and the rate of freezing.

The constructs frozen on the constant-temperature substrate (Figs. 3A1-A3) had a vastly different microstructure from bottom to top. Starting with fine oriented pores at the bottom of the construct, the diameter of the pores increased with distance along the freezing direction. For the constructs frozen at constant rates, the lowest rate (1 °C/min) resulted in an improvement in the homogeneity of the pore diameter between the bottom and top of the construct (Figs. 3B1−B3). The spatial homogeneity of the pore diameter continued to increase with increasing freezing rate, until at the highest rate used (7

°C/min), there was little difference in the homogeneity of the pore diameter from the bottom to the top of the construct, a length of ~20 mm (Figs. 3C1−C3).

Using the cross-sections perpendicular to the freezing direction, the average pore diameter was determined at the bottom, middle, and top regions of the constructs (Fig. 4a). As shown, there were significant differences in pore diameter between the three regions for all the constructs except for those frozen at the highest rate of 7 °C/min, for which there was a significant difference between the middle and top regions only. The average pore diameter, normalized to the pore diameter at the bottom of the construct is shown in Fig. 4b as a function of distance from the bottom of the construct. For the construct frozen on the constant-temperature substrate (3 ^{o}C), the average pore diameter at the top was ~3 times the value at the bottom. In comparison, for the construct prepared by freezing at a constant rate of 7 °C/min, the difference in average pore size along the length was markedly smaller.

3.3. Microstructure of constructs after annealing and sintering

SEM images of the cross-sections parallel to freezing direction are shown in Fig. 5 for the constructs after the freezing and thermal annealing (24 h at 34 °C) steps, and after sublimation of the camphene. The images are shown for the bottom, middle, and top regions of the samples frozen on the constant-temperature substrate (3 °C) and under constant freezing rates of 7 °C/min. When compared to the microstructures of the constructs after the freezing step only (no thermal annealing) (Fig. 3), the diameter of the pores resulting from the primary camphene dendrites has increased markedly. There is also an absence of pores from the secondary dendrite arms in the construct frozen at 7 °C/min (Fig. 5B1−B3). In the case of the constructs frozen on the constant-temperature substrate, the absence of pores from the secondary dendrite arms is not clearly evident (Fig. 5A1−5A3).

In general, the orientation of the pores was more evident after the annealing step, and the average pore diameter showed little dependence on the freezing rates used in this work. However, there was some difference in the pore morphology. The constructs prepared by freezing on the constant-temperature substrate showed some difference in the thickness of the macropore walls from the bottom to the top of the construct (Figs. 5A1–5A3). For this group, no clear orientation of the pores was observed at the top of the

constructs. In comparison, the constructs frozen at constant rates showed better homogeneity in the thickness of the struts (macropore walls) and the pore diameter along the length of the construct. Constructs frozen under the fastest rate (7°C/min) showed well-aligned pores along the freezing direction, and channel-like pores can be observed along the freezing direction (Fig. 5B1–5B3).

After sintering, the scaffolds had approximately the same porosity of 50 ± 4%, regardless of the conditions used in the freezing step. For the scaffolds prepared by freezing on the constant-temperature substrate (3 °C), SEM images of the cross-sections parallel to the freezing direction showed differences in pore alignment along the length of the construct (Fig. 6a). The pores were well oriented from the bottom to the middle of the scaffolds, but were poorly aligned above the middle region. In comparison, the constructs prepared by freezing at a constant rate of 7 °C/min showed good pore alignment and a homogeneous microstructure from the bottom to the top of the construct (Fig. 6b). SEM images of sections perpendicular to the freezing direction showed macropores with an approximately circular cross-section (Fig. 6c, d) and an almost fully dense glass struts (Fig. 6e).

The distributions of pore diameters for the sintered constructs formed by freezing on the constant-temperature substrate and under constant freezing rates of 1 °C/min and 7 °C/min are shown in Fig. 7. For all three groups, the pore sizes were mostly in the range 50–150 μm, with a peak value of ~100 μm. For the construct prepared by freezing at 7 °C/min, the pore size data followed an approximately bell-shaped curve, typical of a normal distribution. However, the data for the constructs prepared by freezing on the constant-temperature substrate or freezing at 1 °C/min showed a tail in the distribution curve at pore sizes larger than ~150 μm.

3.4. Mechanical response of sintered constructs

Figure 8a shows examples of the stress vs. deformation response in compression for the sintered constructs formed by freezing on the constant-temperature substrate (3 °C) and under a constant freezing rate of 7 °C/min. Both constructs showed an elastic response, in which the stress increased approximately linearly with deformation, followed by failure in which the samples fractured into several pieces, typical of dense brittle

solids. The fracture planes were almost vertical, along the orientation direction; mirror area and hackle lines were found on the fractured surfaces of the glass struts, which are common features accompanying the failure of a dense glass. As shown in Fig. 8a, the construct formed by freezing at a constant rate had a higher compressive strength (stress at failure) than the construct formed by freezing on the constant-temperature substrate.

The compressive strength and elastic modulus (slope of the stress vs. deformation response) of the sintered constructs are shown in Fig. 8b. Constructs formed by freezing at the lowest rate (1 °C/min) had a compressive strength (37 ± 7 MPa) and an elastic modulus (8 ± 3 GPa) (data not shown) that were not significantly different from those for the construct formed by freezing on the constant-temperature substrate (strength = 35 ± 11 MPa; elastic modulus = 8 ± 3 GPa). In comparison, the construct formed by freezing at the highest rate (7 °C/min) had a significantly higher compressive strength (47 ± 5 MPa) (p<0.05) and a higher elastic modulus (11 ± 3 GPa) (p<0.08).

4. Discussion

The results of the present work show that controlled unidirectional freezing of camphene-based suspensions, under an imposed constant freezing rate, resulted in the formation of 13-93 bioactive glass constructs with a more homogeneous microstructure and better pore alignment, when compared to constructs formed under a time-dependent freezing rate (freezing on a constant-temperature substrate). The microstructural improvement resulted in an enhancement of the compressive strength and elastic modulus of the sintered constructs. Bioactive glass scaffolds (porosity = 50 ± 4%; average pore width ≈ 100 μm) formed by freezing at a constant rate of 7 °C/min (the highest freezing rate available in this work) showed a compressive strength of 47 ± 5 MPa and an elastic modulus of 11 ± 3 GPa. These scaffolds could have potential application in the repair of load-bearing bones, such as segmental defects in the long bones.

The results showed that after the freezing step, the homogeneity of the primary dendrite diameter over the length of the frozen construct was dependent on the method of freezing and the freezing rate (Figs. 3 and 4). As described previously, freezing at constant rates of 1, 4, and 7 °C/min resulted in average solidification rates of approximately 4, 10, and 16 μm/s, respectively (Fig. 2). Therefore, the results also

showed that the spatial homogeneity of the dendrite diameters improved with increasing values of the solidification rate. In contrast, the solidification rate decreased with time for the constructs frozen on the constant-temperature substrate, resulting in a reduction in the homogeneity of the primary dendrite diameter over the length of the construct. In the present work, homogeneity of the camphene dendrite diameter was achieved over a sample length of ~30 mm for the highest solidification rate (16 μm/s) achievable with the equipment. In contrast, for constructs prepared by freezing on the constant temperature substrate (3 °C), homogeneity of the dendrite diameter was achieved over a distance of only ~10 mm.

The results (Figs. 3 and 4) also showed a dependence of the diameter of the primary camphene dendrite on the solidification rate. Based on previous studies [8, 11, 19, 25, 26], the dependence of the average dendrite diameter d on the average solidification rate v was assumed to follow a power law relation

$$d = kv^{-m} \tag{1}$$

where k is a constant and m is an exponent. A plot of the data for d (taken from Fig. 3a) vs. v (taken from Fig. 2) showed that the exponent m varied from ~0.3 for the bottom region of the construct to ~0.6 for the top region (Fig. 9).

The pore channel size (width or diameter) in constructs prepared by the unidirectional freezing of suspensions has been found to depend on factors such as the solidification rate, the solvent, and the particles in the suspension. For suspensions of Al_2O_3 particles in camphene, Shanti et al. [26] did not measure the solidification rate directly, but assumed that the rate varied inversely with distance from the cold substrate. They plotted the pore channel size as a function of the relative solidification rate and found that $m = 0.33$. In comparison, for aqueous Al_2O_3 suspensions, the results from Deville et al. [25] and Waschkies et al. [19] for the average pore channel spacing as a function of the solidification rate give $m \approx 0.9$ and $m \approx 0.8$, respectively. The data from Zhang et al. [11] for the average pore spacing of constructs formed from aqueous solutions of poly(vinyl alcohol) give $m \approx 0.6$. The m values in the present work fall within the range of values described above for previous studies. The reason for the increase in the m values (0.3−0.6) from the bottom to the top of the construct (Fig. 9) is

not clear. However, a possible reason might be a decrease in the solidification velocity with distance from the cold substrate.

As described previously, interconnected pores with a diameter or width between neighboring pores of ~100 μm are considered to be the minimum requirement for supporting tissue ingrowth and function [2]. Our previous work on unidirectional freezing of camphene-based suspensions on a constant-temperature substrate showed that this minimum pore diameter can be achieved or exceeded by using a two-step process (freezing followed by thermal annealing) [16]. That study also showed that the annealing step resulted in coarsening of the primary camphene dendrites, typical of an Ostwald ripening process. As a consequence, despite large differences in the diameter of the primary camphene dendrites formed after the freezing step, the annealing step resulted in a self-similar distribution of dendrite diameters with approximately the same average diameter. That trend was also observed in the present work. Constructs prepared by freezing on a constant-temperature substrate and under constant freezing rates (1–7 °C/min) had approximately the same average primary dendrite diameter after the annealing process (Fig. 5). After sintering, the constructs had approximately the same average pore diameter, and the distribution of pore diameters approximated a bell-shaped curve (Fig. 7). However, the construct formed by freezing at a constant rate of 7 °C/min showed a narrower distribution of pore sizes, which could result from the better homogeneity of the primary dendrite diameter achieved in the freezing step. In comparison, for the sample frozen on a constant-temperature substrate (3 °C), differences in the orientation and morphology of the pores (or crystals) resulting from the freezing step remained after the annealing and sintering steps (Figs. 5 and 6).

The mechanical strength of the constructs is determined by their microstructure. In the present work, the sintered constructs can be approximated by a uniaxial composite consisting dense glass struts and channel voids. In this case, the compressive strength and elastic modulus can be described by a rule of mixtures. However, off-axis pores will reduce the strength and modulus. As discussed previously, higher freezing rates lead to better alignment of the pores and to fewer off-axis void channels, resulting in a higher strength and modulus (Fig. 8).

The repair of defects in load-bearing bones is a challenging clinical problem. Bioactive glass scaffolds with a more random microstructure, prepared by methods such as sintering of particles or short fibers (porosity = 40−50%), as well as polymer foam replication and sol-gel processing (porosity = 75−90%), often have compressive strength and stiffness in the range of those reported for trabecular bone [20, 21, 27–29]. Consequently, they are limited to the repair of non-loaded bone. In comparison, bioactive glass scaffolds with an oriented microstructure prepared recently by unidirectional freezing of suspensions (porosity = 50%; average pore diameter = 100 μm) have shown average compressive strength (25–35 MPa) and elastic modulus (5–10 GPa), values far higher than those reported for trabecular bone [9, 16]. More recently, bioactive glass scaffolds (13-93 or 6P53B) with a grid-like microstructure prepared by solid freeform fabrication methods (porosity = 50−60%; pore width = 200−500 μm) have shown a compressive strength (~140 MPa), comparable to the values reported for cortical bone [22, 30, 31]. Although the guidelines for the requisite mechanical properties of scaffolds intended for loaded bone repair are currently unclear, the present method could provide bioactive glass scaffolds with a favorable combination of mechanical strength and pore characteristics for potential applications in the repair of loaded bone. The ability of these oriented scaffolds to substitute for bone defects is currently being evaluated *in vivo* in animal models.

5. Conclusion

Silicate 13-93 bioactive glass scaffolds with an oriented pore architecture were formed using a two-step process consisting of unidirectional freezing of camphene-based suspensions followed by thermal annealing near the softening point of the frozen mixture. The pore orientation and homogeneity of the microstructure were dependent primarily on the freezing conditions, whereas the pore diameter was controlled by the annealing step. A higher freezing rate (7 °C/min) resulted in improved pore alignment and a more homogeneous microstructure over a larger length of the sample. Constructs frozen on a cold substrate or at constant freezing rates of 1–7 °C/min had approximately the same average pore diameter after the annealing step. After sintering, constructs prepared by freezing at 7 °C/min (porosity = 50%; pore diameter = 100 μm) had a compressive

strength of 47 ± 5 MPa and an elastic modulus of 11 ± 3 GPa. These bioactive glass scaffolds have a favorable combination of strength, stiffness, and pore characteristics for potential application in the repair of loaded bone.

Acknowledgement

This work was supported by the U.S. Army Medical Research Acquisition Activity, under Contract No. W81XWH-08-1-0765, and by the National Institutes of Health, National Institute of Arthritis, Musculoskeletal and Skin Diseases (NIH/NIAMS), Grant No. 1R15AR056119-01. Q.F. and A.P.T. are grateful for the support from the National Institutes of Health, National Institute of Dental and Craniofacial Research (NIH/NIDCR), Grant No. 1R01DE015633.The authors would like to thank Dr. D. E. Day and Mo-Sci Corp, Rolla, Missouri, for providing the bioactive glass used in this work, and C. Gilbert for assistance with setting up the controlled freezing rate apparatus.

References

[1] U.S. Census Bureau. Health and nutrition. U.S. Census Bureau statistical abstracts of the United States, Washington, DC, 117 (2009).

[2] Hulbert SF, Young FA, Mathews RS, Klawitter JJ, Talbert CD, Stelling FH. Potential of ceramic materials as permanently implantable skeletal prostheses. J Biomed Mater Res 1970;4:433–56.

[3] Reichert JC, Saifzadeh S, Wullschleger ME, Epari DR, Schütz MA, Duda GN, Schell H, van Griensven M, Redl H, Hutmacher DW. The challenge of establishing preclinical models for segmental bone defect research. Biomaterials 2009;30:2149–63.

[4] Ma PX, Zhang R. Microtubular architecture of biodegradable polymer scaffolds. J Biomed Mater Res 2001;56:469–77.

[5] Fu Q, Rahaman MN, Dogan F, Bal BS. Freeze casting of porous hydroxyapatite scaffolds. II. Sintering, Microstructure, and Mechanical Behavior. J Biomed Mater Res B 2008;86: 514–22.

[6] Shanjani Y, Hu Y, Pilliar RM, Toyserkani E. Mechanical characteristics of solid-freeform-fabricated porous calcium polyphosphate structures with oriented stacked layers. Acta Biomater 2011;7:1788–96.

[7] Wirtz DC, Schiffers N, Pandorf T, Radermacher K, Weichert D, Forst R. Critical evaluation of known bone materials properties to realize anisotropic FE-simulation of the proximal femur. J Biomech 2000;33:1325–30.

[8] Deville S, Saiz E, Tomsia AP. Freeze casting of hydroxyapatite scaffolds for bone tissue engineering. Biomaterials 2006;27:5480–9.

[9] Fu Q, Rahaman MN, Brown RF, Bal BS. Preparation and in vitro evaluation of bioactive glass (13-93) scaffolds with oriented microstructures for repair and regeneration of load-bearing bones. J Biomed Mater Res A 2010;93:1380–90.

[10] Hu L, Wang CA, Huang Y, Sun C, Lu S, Hu Z. Control of pore channel size during freeze casting of porous YSZ ceramics with unidirectionally aligned channels using different freezing temperatures. J Euro Ceram Soc 2010;30:3389–96.

[11] Zhang H, Hussain I, Brust M, Butler M, Rannard SP, Cooper AI. Aligned two- and three-dimensional structures by directional freezing of polymers and nanoparticles. Nat Mater 2005;4:787–93.

[12] Rahaman MN, Fu Q. Manipulation of porous bioceramics microstructures by freezing of suspensions containing binary mixtures of solvents. J Am Ceram Soc 2008; 9:4137–40.

[13] Araki K, Halloran JW. Room-temperature freeze casting for ceramics with nonaqueous sublimable vehicles in the naphthalene–camphor eutectic system. J Am Ceram Soc 2004; 87:2014–9.

[14] Munch E, Saiz E, Tomsia AP. Architectural control of freeze-cast ceramics through additives and templating. J Am Ceram Soc 2009;92:1534–9.

[15] Tang YF, Zhao K, Wei JQ, Qin YS. Fabrication of aligned lamellar porous alumina using directional solidification of aqueous slurries with an applied electrostatic field. J Euro Ceram Soc 2010; 30:1963–5.

[16] Liu X, Rahaman MN, Fu Q. Oriented bioactive glass (13-93) scaffolds with controllable pore size by unidirectional freezing of camphene-based suspensions: Microstructure and mechanical response. Acta Biomater 2011;7:406–16.

[17] Schoof H, Apel J., Heschel I, Rau G. Control of pore structure and size in freeze-dried collagen sponges. J Biomed Mater Res B 2001;58:352–7.

[18] O'Brien FJ, Harley BA, Yannas IV, Gibson L. Influence of freezing rate on pore structure in freeze-dried collagen-GAG scaffolds. Biomaterials 2004;25:1077–86.

[19] Waschkies T, Oberacker R, Hoffmann MJ. Control of lamellae spacing during freeze casting of ceramics using double-side cooling as a novel processing route. J Am Ceram Soc 2009;92:S79–84.

[20] Fu Q, Rahaman MN, Huang W, Day DE, Bal BS. Preparation and bioactive characteristics of a porous 13-93 Glass, and its fabrication into the articulating surface of a proximal tibia. J Biomed Mater Res A 2007;82:222–9.

[21] Fu Q, Rahaman MN, Bal BS, Brown RF, Day DE. Mechanical and in vitro performance of 13-93 bioactive glass scaffolds prepared by a polymer foam replication technique. Acta Biomater 2008;4:1854–64.

[22] Huang TS, Doiphode ND, Rahaman MN, Leu MC, Bal BS, Day DE. Porous and strong bioactive glass (13-93) scaffolds prepared by freeze extrusion fabrication. Mater Sci Eng C 2011; 31: 1482–89.

[23] Brink M. The influence of alkali and alkaline earths on the working range for bioactive glasses. J Biomed Mater Res 1997; 36:109–17.

[24] Brown RF, Day DE, Day TE, Jung S, Rahaman MN, Fu Q. Growth and differentiation of osteoblastic cells on 13-93 bioactive glass fibers and scaffolds. Acta Biomater 2008;4: 387-396.

[25] Deville S, Saiz E, Nalla RK, Tomsia AP. Freezing as a path to build complex composites. Science 2006;311:515−518.

[26] Shanti NO, Araki K, Halloran JW. Particle redistribution during dendritic solidification of particle suspensions. J Am Ceram Soc 2006;89:2444−7.

[27] Rahaman MN, Day DE, Brown RF, Fu Q, Jung SB. Nanostructured bioactive glass scaffolds for bone repair. Ceram Eng Sci Proc 2008;29:211−25.

[28] Liu X, Huang W, Fu H, Yao A, Wang D, Pan H, Lu WW. Bioactive borosilicate glass scaffolds: improvement on the strength of glass-based scaffolds for tissue engineering. J Mater Sci: Mater Med 2009;20:365–72.

[29] Jones JR, Ehrenfried LM, Hench LL. Optimising bioactive glass scaffolds for bone tissue engineering. Biomaterials 2006;27:964–73.

[30] Doiphode ND, Huang TS, Leu MC, Rahaman MN, Day DE. Freeze extrusion fabrication of 13-93 bioactive glass scaffolds for bone repair. J Mater Sci: Mater Med 2011; 22:515-23.

[31] Fu Q, Saiz E, Tomsia AP. Bio-inspired highly porous and strong glass scaffolds. Adv Funct Mater 2010;21:1058–63.

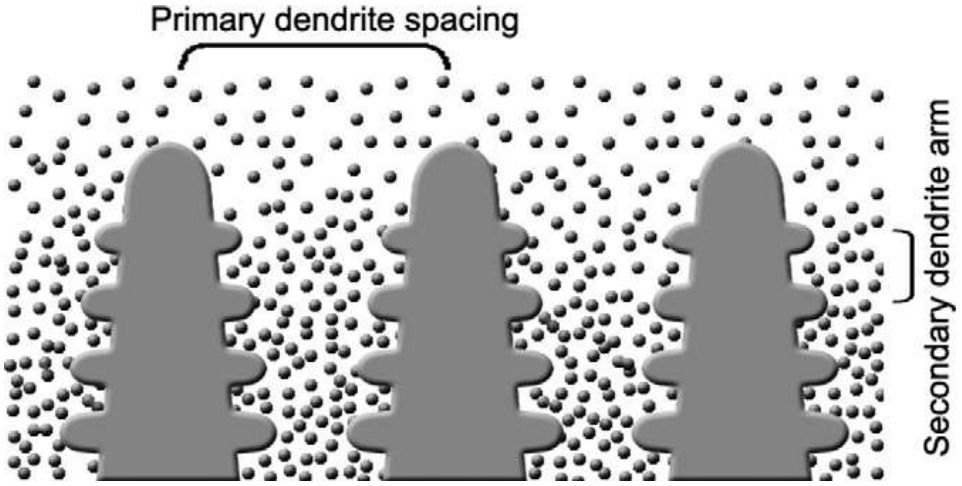

Fig. 1. Schematic of the growth of camphene dendrites during unidirectional freezing of camphene-based suspensions [16].

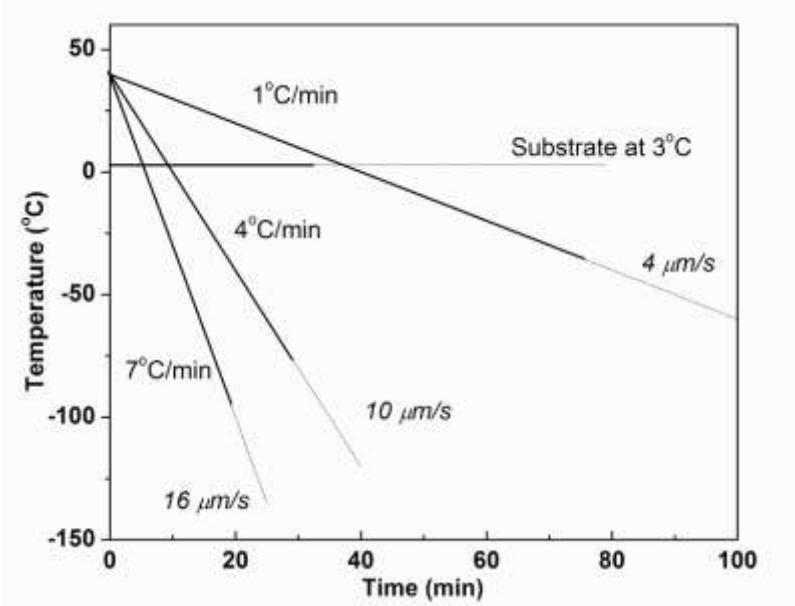

Fig. 2. Data for the substrate (cold finger) temperature vs. time during unidirectional freezing of camphene-based suspensions at constant rates (1–7 °C/min). The average velocity of the camphene solidification front is shown for each freezing rate. For comparison, suspensions were also frozen on a substrate kept at a constant temperature (3 °C). The solid lines show the time taken to completely freeze a construct 20 mm in height under the conditions shown.

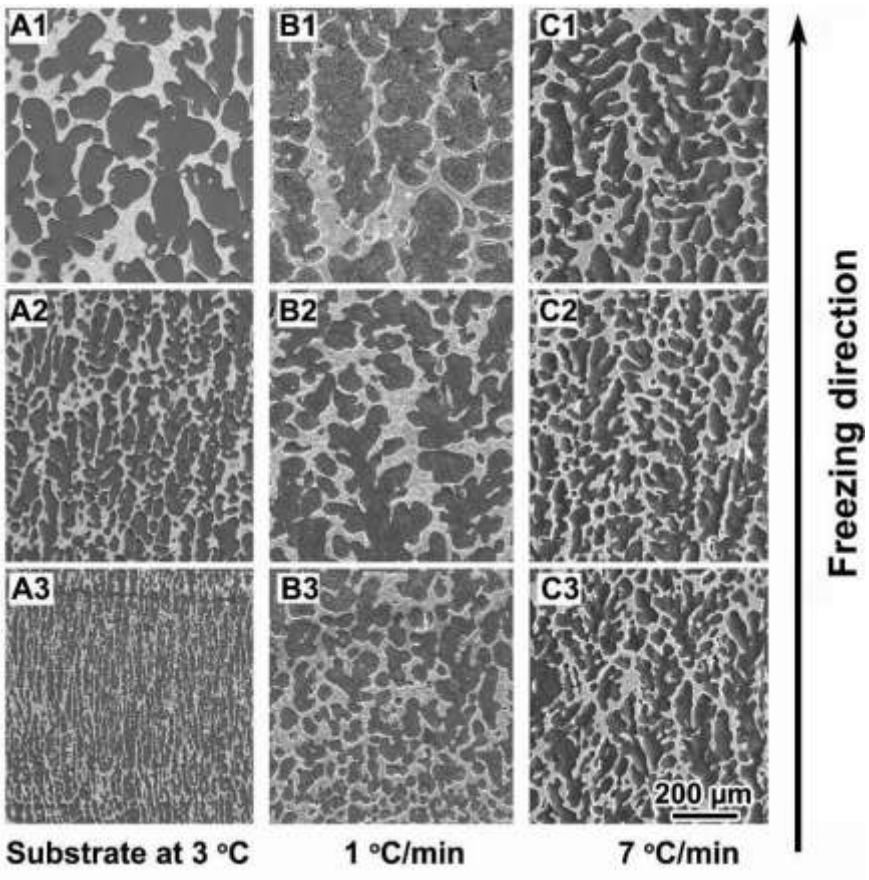

Fig. 3. SEM images of the cross-sections parallel to the freezing direction for as-solidified 13-93 bioactive glass constructs prepared by unidirectional freezing on a constant-temperature substrate (3°C) (A1–A3), or at constant freezing rates of 1 ^{o}C/min (B1–B3), and 7^{o}C/min(C1–C3). Images are shown for the bottom, middle, and top portions of the constructs along the freezing direction.

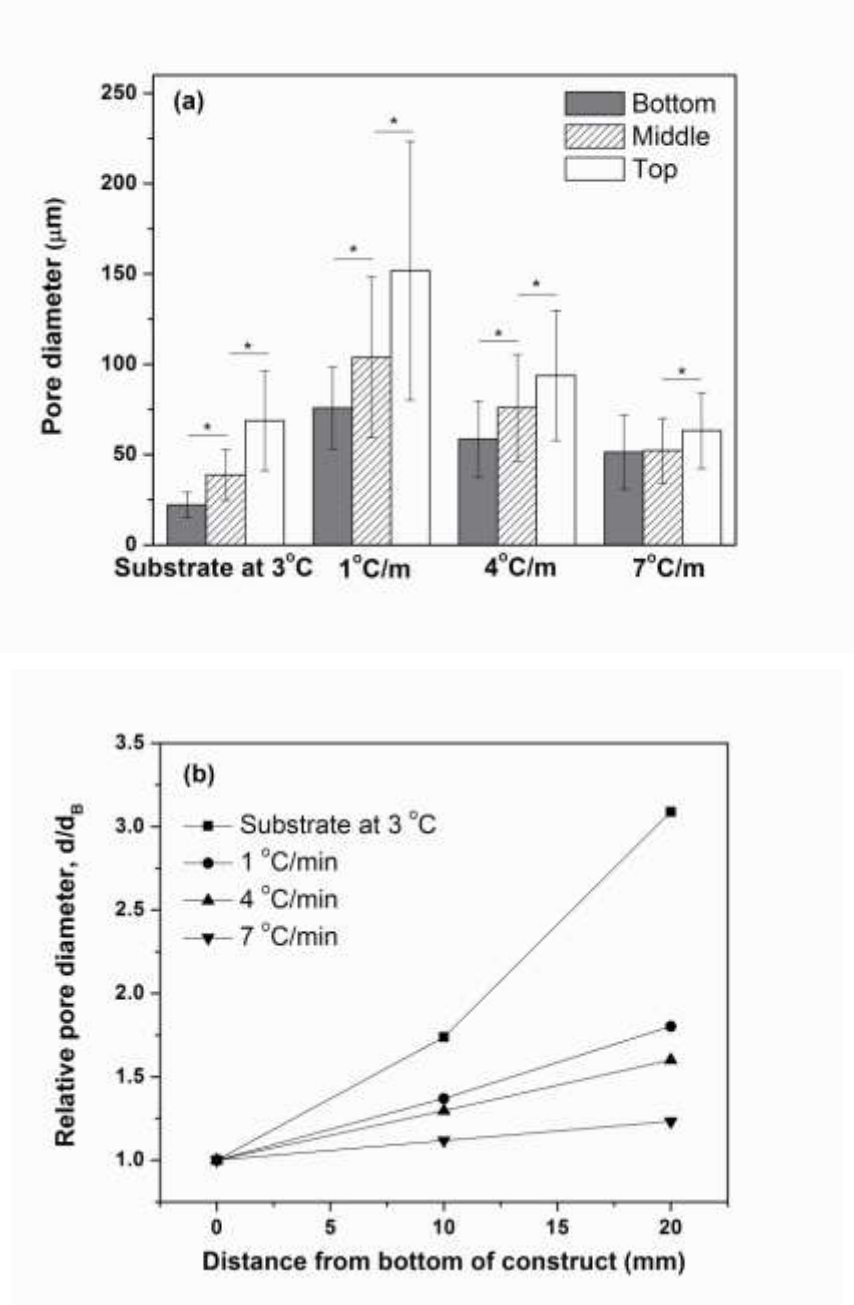

Fig. 4. (a) Pore diameter at the bottom, middle, and top portion of the construct after the freezing step and sublimation of the camphene, for constructs frozen unidirectionally on a constant-temperature substrate (3 °C) or at constant rates (1, 4, and 7 °C/min) (*p< 0.05); (b) Pore diameter (normalized to the pore diameter at the bottom portion of the construct) vs. distance from the bottom of the construct plotted from the data in (a).

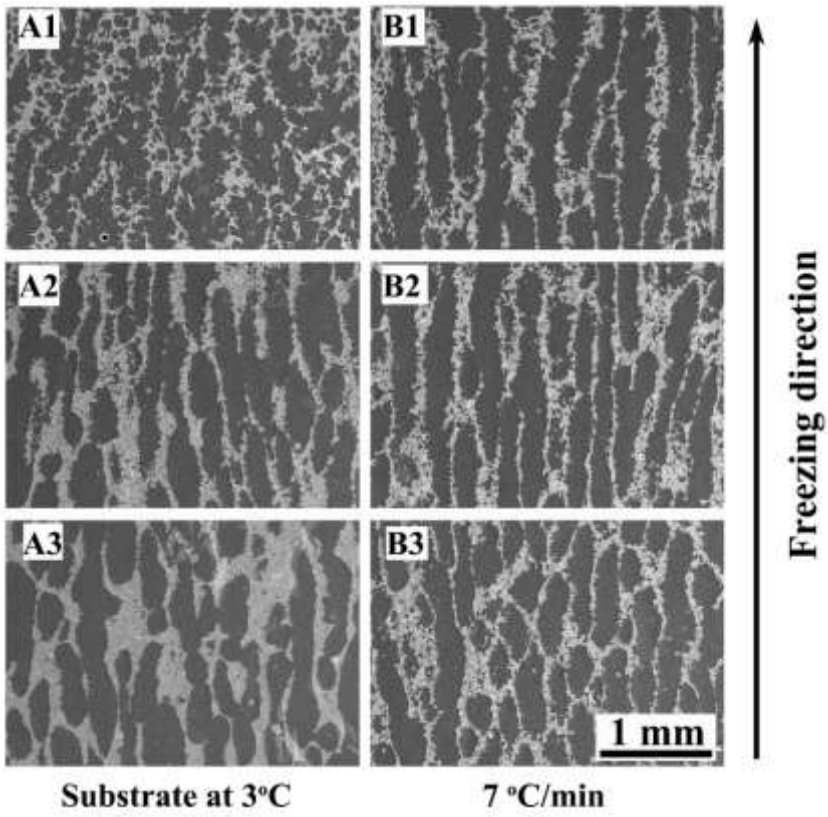

Fig. 5. SEM images of cross-sections parallel to the freezing direction for constructs after freezing, annealing for 24 h at 34 °C, and sublimation of the camphene. The freezing step was performed on a constant-temperature substrate (3 °C) (A1–A3) or at a constant freezing rate of 7 °C/min (B1–B3). Images are shown for the bottom, middle, and top portions of the constructs along the freezing direction.

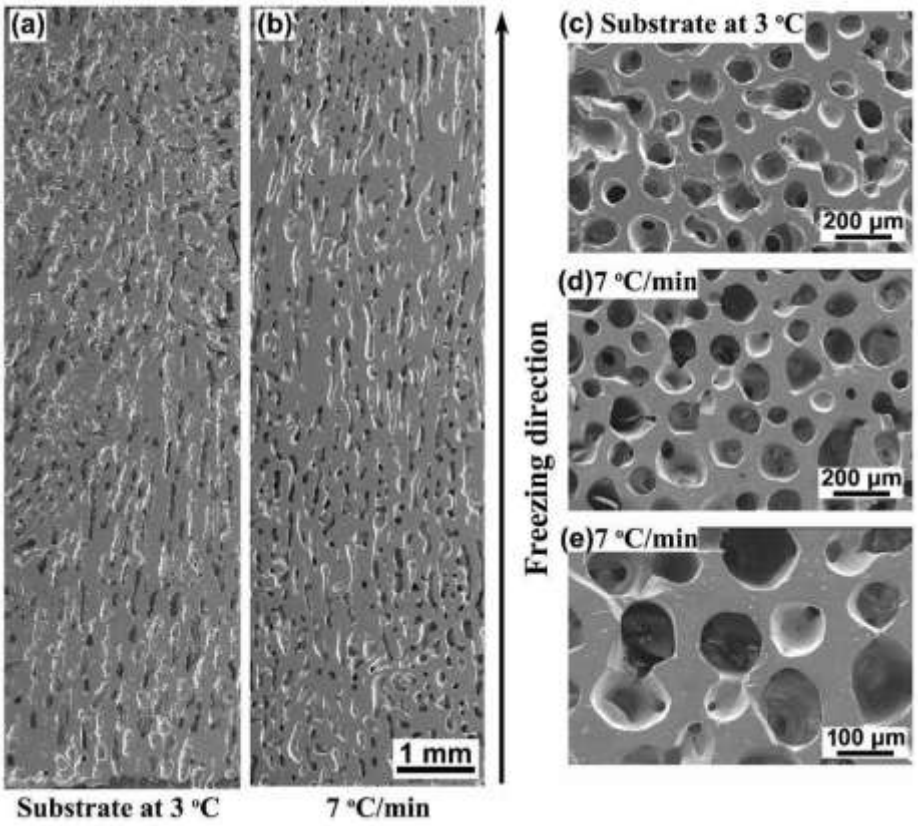

Fig.6. SEM images of cross-sections parallel and perpendicular to the freezing direction for sintered constructs prepared by freezing on a constant-temperature substrate (3 °C) (a, c), or at a constant rate of 7 ^{o}C /min (b, d, e). Sections parallel to the freezing direction (a, b) and perpendicular to the freezing direction (c, d, e) are shown.

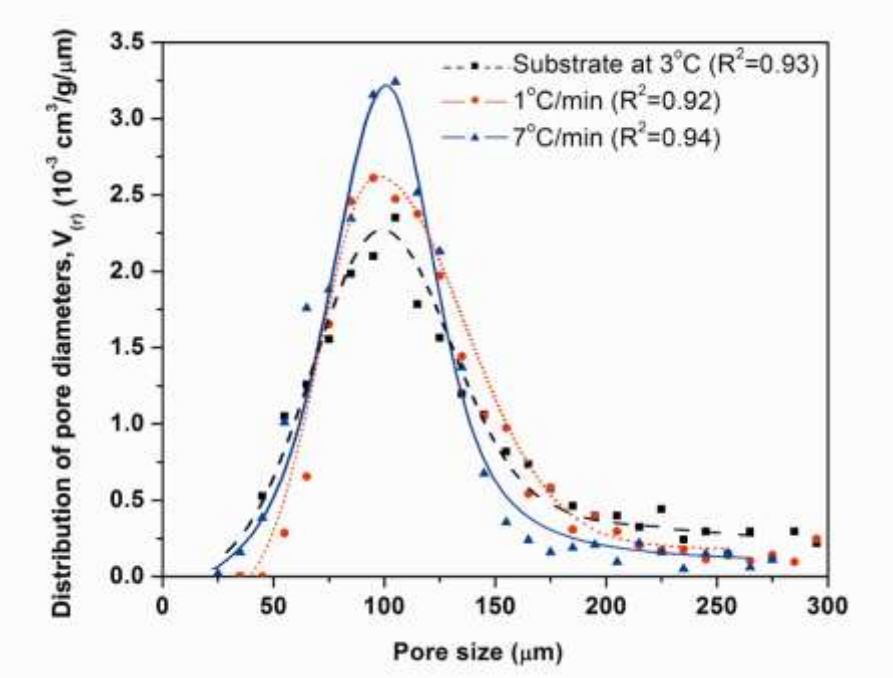

Fig. 7. Distribution of the pore diameters for sintered constructs (700 ^{o}C for 1 h) prepared by freezing on a constant-temperature substrate (3 °C), or at constant freezing rates of 1 and 7 ^{o}C /min. The data points for each sample were fitted by polynomial function, and the R^2 value for each curve is shown.

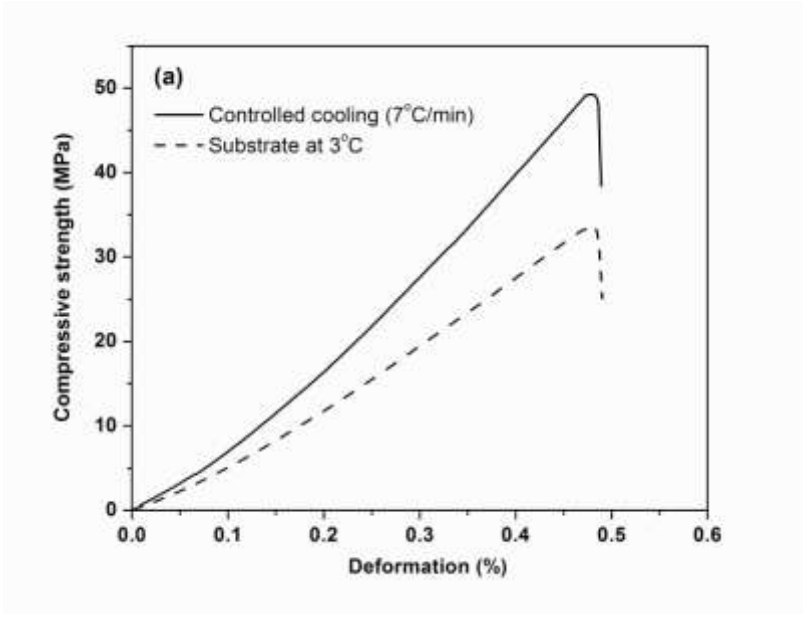

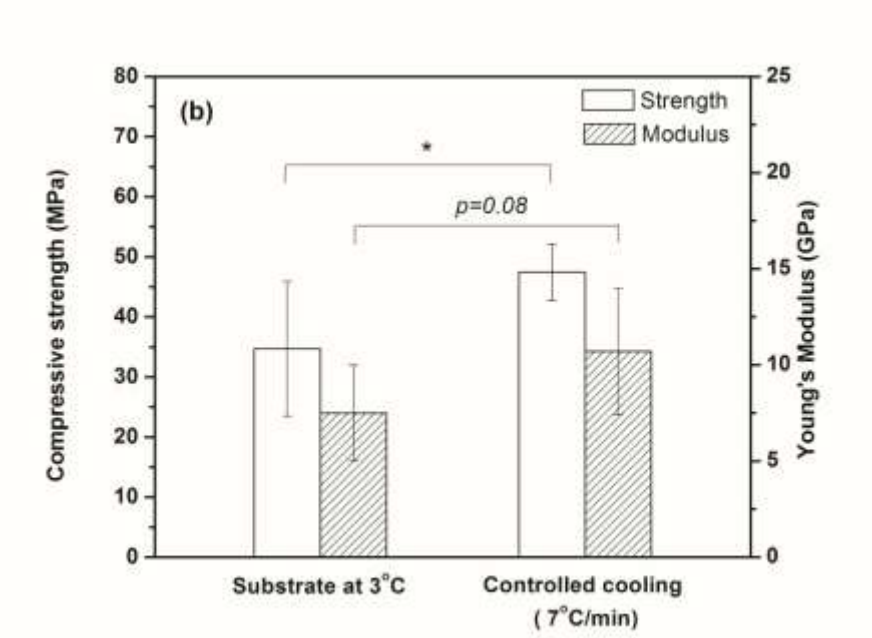

Fig. 8. (a) Examples of compressive stress vs. deformation response for sintered constructs tested parallel to the orientation direction. The constructs were prepared by freezing on a constant-temperature substrate (3 °C) or at a constant rate of 7 °C /min. (b) Compressive strength and elastic modulus determined from the stress vs. strain data. (*$p<$ 0.05).

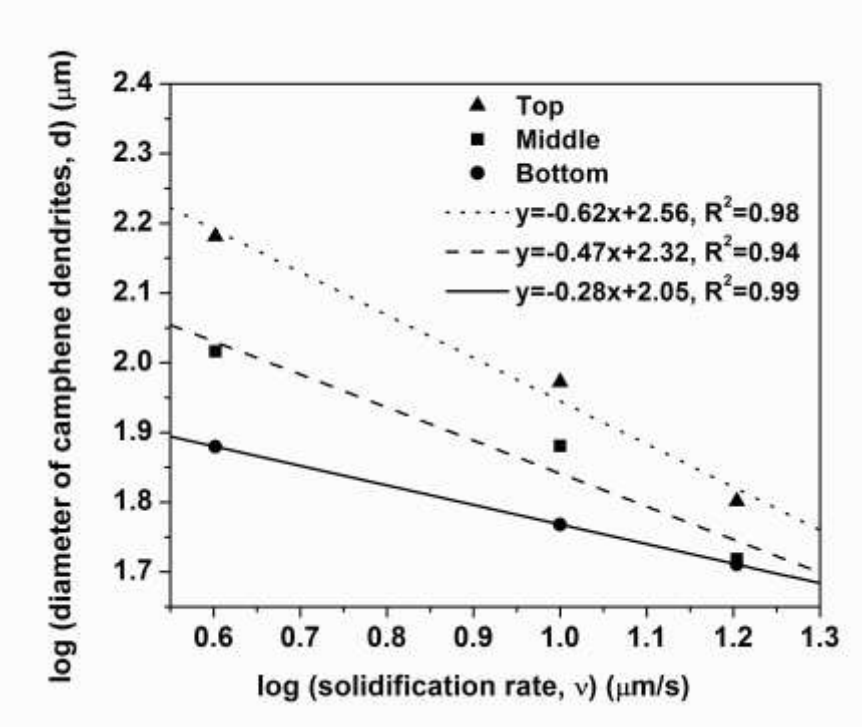

Fig. 9. Average diameter of primary camphene dendrites vs. average solidification rate for unidirectional freezing of camphene based suspensions at constant rates of freezing. The results are shown for the bottom, middle, and top portions of the construct (total length = 20 mm).

III. BONE REGENERATION IN STRONG POROUS BIOACTIVE (13-93) SCAFFOLDS WITH AN ORIENTED MICROSTRUCTURE IMPLANTED IN RAT CALVARIAL DEFECTS

Xin Liu[1], Mohamed N. Rahaman[1], Qiang Fu[2]

[1]Department of Materials Science and Engineering and Center for Bone and Tissue Repair and Regeneration, Missouri University of Science and Technology, Rolla, MO 65409, USA

[2]Materials Sciences Division, Lawrence Berkeley National Laboratory, Berkeley, CA 94720, USA

ABSTRACT

There is a need for synthetic bone graft substitutes to repair large bone defects resulting from trauma, malignancy, and congenital diseases. Bioactive glass has attractive properties as a scaffold material but factors that influence its ability to regenerate bone in vivo are not well understood. In the present work, the ability of strong porous scaffolds of 13-93 bioactive glass with an oriented microstructure to regenerate bone was evaluated in vivo using a rat calvarial defect model. Scaffolds with an oriented microstructure of columnar pores (porosity = 50%; pore diameter = 50−150 μm) showed mostly osteoconductive bone regeneration, and new bone formation, normalized to the available pore area (volume) of the scaffolds, increased from 37% at 12 weeks to 55% at 24 weeks. Scaffolds of the same glass with a trabecular microstructure (porosity = 80%; pore width = 100−500 μm), used as the positive control, showed bone regeneration in the pores of 25% and 46% at 12 and 24 weeks, respectively. The brittle mechanical response of the as-fabricated scaffolds changed markedly to an elasto-plastic response in vivo at both implantation times. These results indicate that both groups of 13-93 bioactive glass scaffolds could potentially be used to repair large bone defects, but scaffolds with the oriented microstructure could also be considered for the repair of loaded bone.

1. Introduction

There is a clinical need for the development of synthetic scaffolds to repair large bone defects. In particular, the replacement of structural bone loss remains a challenging clinical problem. Millions of patients in the United States alone suffer each year from considerable bone loss resulting from trauma, malignancy, and congenital diseases, and this number is expected to increase substantially with the doubling of the population over the age of 65 years [1, 2]. Autogenous bone grafts, the gold standard for treatment, suffer from problems such as limited supply and donor site morbidity. Bone allografts are alternatives but they are expensive, and carry the risk of disease transmission and adverse host immune reaction. The delivery of growth factors, such as bone morphogenetic protein-2 (BMP-2), from a biodegradable carrier matrix, such as collagen, is used clinically for fracture and spinal repair. However, growth factors are expensive, and concerns have been expressed about possible links of high levels of growth factors to cancer and other complications [3, 4]. These problems have increased the need for synthetic bone graft substitutes.

Bioactive glasses are promising scaffold materials for bone regeneration because of their ability to convert to hydroxyapatite (HA), the main mineral constituent of bone, as well as their proven osteoconductivity and their ability to form a strong bond with bone and soft tissues [5, 6]. However, three-dimensional (3D) scaffolds of bioactive glasses prepared by many conventional methods often lack the requisite combination of porosity and mechanical properties for the repair of load-bearing bones. The compressive strengths reported for bioactive glass scaffolds prepared by many conventional methods are often lower than or comparable to the values reported for human trabecular bone (2–12 MPa) [7−9].

In our previous work, a method based on unidirectional freezing of suspensions [10] was used to form strong porous scaffolds of silicate 13-93 glass with an oriented microstructure of columnar pores which might have potential application in loaded bone repair [11, 12]. Scaffolds (porosity = 50%; pore diameter = 50–150 μm), created by unidirectional freezing of organic (camphene)-based suspensions showed an elastic modulus of 11 ± 3 GPa, in the range of values reported for human cortical bone (5–15 GPa), and a compressive strength of 47 ± 5 MPa, compared to a value of 100- 150 MPa

for human cortical bone. Bioactive glass (13-93) scaffolds with a similar oriented microstructure have been shown to support the proliferation and function of osteogenic MLO-A5 cells in vitro [13] and the infiltration of soft (fibrous) tissue in a rat subcutaneous model [14]. However, the ability of those oriented scaffolds to support bone regeneration in vivo was not evaluated.

It is known that bone regeneration in implants cannot be well predicted from their ability to support soft tissue infiltration, and that the microstructure and mechanical properties of porous scaffolds have a marked effect on host response [15]. Based on the promising mechanical properties and favorable microstructure of the "oriented" 13-93 bioactive glass scaffolds observed in our previous work, one objective of the present study was to evaluate the ability of the scaffolds to support bone regeneration and integration in an animal model. Another objective was to test the mechanical response of the scaffolds after implantation in vivo. Implants were evaluated using histomorphometry, electron microscopy, and mechanical testing techniques 12 and 24 weeks postimplantation. A rat calvarial defect model was used because it is a standard, inexpensive assay to study new bone formation in an osseous defect. Scaffolds of the same glass (13-93) with a microstructure similar to dry human trabecular bone were selected as the positive control group in order to study microstructural effects on bone regeneration; untreated defects served as the negative control group.

2. Materials and methods

2.1. Preparation of bioactive glass (13-93) scaffolds

Scaffolds of 13-93 bioactive glass (composition 53SiO_2, 6Na_2O, 12K_2O, 5MgO, 20CaO, 4P_2O_5; wt %) with an oriented microstructure (referred to as "oriented" scaffolds) were prepared by unidirectional freezing of organic (camphene)-based suspensions using a method described in our previous work [11]. Scaffolds of the same bioactive glass with a microstructure similar to dry human trabecular bone (referred to as "trabecular" scaffolds), the positive control group, were prepared using a polymer foam replication technique, as described in detail elsewhere [14]. The open porosity and pore size distribution of the scaffolds were measured using the Archimedes method and liquid extrusion porosimetry, respectively, as described previously [11, 16]. Table 1 summarizes

the characteristics of the two groups of scaffolds. The as-fabricated constructs were sectioned and ground to form thin discs (4.6 mm in diameter × 1.5 mm), washed twice with deionized water and ethanol, dried, and dry-heat sterilized (12 h at 250 ^{o}C) prior to implantation.

2.2. Animals and surgical procedure

All animal experimental procedures were approved by the Animal Care and Use Committee, Missouri University of Science and Technology. Twenty-six male Sprague Dawley rats (3 months old; weight = 350–400 g) were maintained in the animal facility for 2 weeks to become acclimated to diet, water, and housing under a 12 hour/12 hour light/dark cycle. The rats were anesthetized with a combination of ketamine (72 mg/kg) and xylazine (6 mg/kg) and maintained under anesthesia with isoflurane gas in oxygen. The surgical site was shaved and scrubbed with iodine. Using sterile instruments and aseptic technique, a 2 cm cranial skin incision was made in an anterior to posterior direction along the midline. The subcutaneous tissue, musculature and periosteum were dissected and reflected to expose the calvaria. A full-thickness defect (4.6 mm in diameter) was created in the central area of each parietal bone using a saline-cooled trephine drill to prevent overheating of the bone margins and to remove the bone debris. The dura mater was not disturbed. The bone defects were randomly implanted with disc-shaped bioactive glass scaffolds (4.6 mm in diameter × 1.5 mm) from each group (oriented or trabecular microstructure) or left empty. The periosteum and skin were repositioned and closed using wound clips. All animals were intramuscularly given a dose of ketoprofen (3 mg/kg), and allowed to recover. The condition of the surgical wound, food intake, activity, and clinical signs of infection were monitored daily. After 12 and 24 weeks, the animals were sacrificed by CO_2 inhalation, and the calvarial defect sites with surrounding bone and soft tissue were harvested for subsequent evaluation.

2.3. Synchrotron X-ray microcomputed tomography analysis

Harvested samples from each group were analyzed using synchrotron X-ray microcomputed tomography (SR microCT) at the Advanced Light Source synchrotron facility at the Lawrence Berkeley National Laboratory, Berkeley, CA. The samples were analyzed in a monochromatic X-ray beam of 22 keV and a resolution size of 1.7 μm voxels. The transmitted X-rays were imaged via a scintillator, magnifying lens, and

digital camera. The samples were scanned in the absorption mode, and the images were obtained using a filtered back-projection algorithm. In this mode, the gray scale values of the reconstructed image are representative of the absorption coefficient.

2.4. Histology

The harvested samples were fixed in 10% buffered formaldehyde for 3 days, and then transferred into 70% ethyl alcohol. Each sample was cut in half using a diamond wire saw (Model 850, South Bay Technology Inc., San Clement, CA) for paraffin-embedding and poly(methylmethacrylate) (PMMA)-embedding respectively. Tissue samples for paraffin sections were decalcified in 14 % ethylenediaminetetraacetic acid (EDTA) solution for 8 weeks, dehydrated in a series of graded ethanol, and embedded in paraffin. Longitudinal sections cut at 5 μm were used for hematoxylin and eosin (H&E) staining.

The undecalcified samples were embedded in PMMA. The fixed samples were dehydrated using ethanol, infiltrated with MMA monomer and polymerized [17]. The samples were affixed to acrylic slides and ground down to 40 μm using a surface grinder (EXAKT 400CS, Norderstedt, Germany). The plastic sections were stained using the von Kossa technique [18]. Transmitted light images of the stained sections were taken with an Olympus BX 50 microscope connected with a CCD camera (DP70, Olympus, Japan).

2.5. Histomorphometric analysis

Light micrographs of H&E stained sections were used for histomorphometric analysis of bone regeneration within the defects. The entire defect area was measured, from one edge of the original calvarial bone, including the glass scaffold and tissue within, to the other edge of the host bone. Bone regeneration and the pore phase within this area were outlined and measured using NIH Image J software. Total bone regeneration was determined using 2 methods: (1) by normalizing the area of new bone to the total defect area, and (2) by normalizing the area of new bone to the available area of the pore phase in the scaffolds. Von Kossa positive area was determined from light micrographs of von Kossa stained sections. The dark area indicating mineralization was outlined and measured by NIH Image J, and the percent mineralization was normalized to the total defect area. For each implantation time, 5 samples for each group were evaluated, and the results are presented as a mean ± standard deviation.

2.6. Scanning electron microscopy and energy-dispersive X-ray analysis

Unstained sections of the implants in PMMA were coated with carbon and examined in a field-emission scanning electron microscope, FE-SEM (S-4700; Hitachi, Tokyo, Japan) equipped with an energy dispersive X-ray (EDS) spectrometer (Apollo X; EDAX, Inc.) to analyze morphological and compositional changes resulting from the bioactive glass conversion. The observations were performed at an accelerating voltage of 15 kV and a working distance of 12 mm. The Ca/P atomic ratio was determined using the EDAX Genesis program, with synthetic hydroxyapatite and 13-93 glass as standards. Three randomly selected regions were analyzed, and the results are presented as a mean ± standard deviation.

2.7. Mechanical testing

After the animals were sacrificed, the bioactive glass implants with a layer of surrounding bone were removed using a trephine drill (inner diameter = 5 mm). The host bone surrounding the implants was trimmed with dental burs, leaving a disc-shape sample ~4.6 mm in diameter and ~ 1.5 mm in thickness. The implants were wrapped in gauze previously soaked in phosphate-buffered saline (PBS) to limit drying, kept at –20^{o}C, and thawed to room temperature before testing [19]. The mechanical response of the implants was evaluated using a diametral compression test [20]. This test was used because of the small, disc-shaped geometry of the implants. The test is valid for determining the tensile strength of materials that show elastic deformation prior to failure. However, it has also been used to compare the response of materials that deform plastically [21−23] by considering the load to failure.

For each group, 5 samples were tested at each implantation time (deformation rate = 0.5 mm/min). After testing, the samples were freeze-dried (Freezezone 4.5, Labconco Corp., Kansas City, MO) to maintain the as-fractured morphology, mounted in epoxy resin, sectioned, and polished. The polished cross-sections were coated with carbon and examined in an FE-SEM (Hitachi; S-4700) using the backscattered electron (BSE) mode at an accelerating voltage of 15 kV and a working distance of 13 mm.

For comparison, as-fabricated bioactive glass scaffolds with the oriented microstructure and dimensions similar to those of the implants (5 mm in diameter × 1.5

mm) were immersed in simulated body fluid (SBF) [24] at 37^{o}C for 12 and 24 weeks, and tested under the same conditions. Five samples were tested for each immersion time.

2.8. Statistical analysis

The results are presented as a mean ± standard deviation. For each group of bioactive glass implants, analysis for differences in total bone regeneration and von Kossa positive area between implantation times was performed using one-way analysis of variance (ANOVA) with Tukey's post hoc test; differences were considered significant for $p < 0.05$.

3. Results

The microstructural and mechanical properties of the as-fabricated oriented and trabecular scaffolds used in the present study were similar to those described in our previous work [11, 16]. They are summarized in Table 1, and images of the cross-sections are shown in Fig. 1 for reference.

3.1. Bone regeneration and integration

SR microCT images of the scaffolds in the rat calvarial defects 12 and 24 weeks postimplantation (Fig. 2) allowed observation of bone regeneration and integration of the scaffolds with host bone. The images shown are for a plane half-way along the thickness of the implant. The differences in gray-scale in the images resulted from atomic mass and density differences of the elements in the material [25]. The unconverted bioactive glass, calcium phosphate material resulting from the glass conversion, and mineralized tissue have a higher calcium concentration and they showed a light-gray color. In comparison, soft tissue and calcium-depleted regions within the implants were dark-gray.

Twelve weeks postimplantation, new bone formation was found mainly within the oriented scaffold, with little new bone ingrowth and integration at the periphery (edge) of the implants (as revealed by the gaps at the interface between the implant and host bone) (Fig. 2a). Bone regeneration was higher at 24 weeks, and there was better integration between the scaffold and host bone (Fig. 2b). In comparison, the trabecular scaffolds showed new bone growth predominantly at the periphery of the scaffolds at 12 weeks, and there was good integration of the scaffold with host bone (Fig. 2c). At 24 weeks, bone regeneration was higher within the scaffolds and at the periphery (Fig. 2d).

Transmitted light images of H&E stained sections of the oriented and trabecular scaffolds implanted for 12 and 24 weeks in the rat calvarial defects are shown in Fig. 3. Twelve weeks postimplantation, new bone formation (B) and bridging of the defect occurred predominantly on the bottom (dural side) of the oriented implants (Fig. 3a, c). Bone regeneration in the implants and integration with host bone (O) was higher at 24 weeks (Fig. 3b, d). In comparison, the trabecular implants showed new bone growth (B) predominantly at the periphery of the implants, with little new bone formation on the dural side at 12 weeks (Fig. 3e). The amount of bone ingrowth was higher at 24 weeks, both at the periphery and on the dural side of the implants, and bony "islands" were present within the implants (Fig. 3f). In general, bone regeneration and integration observed from the H&E stained sections are compatible with the observations from the SR microCT images discussed previously. In the untreated defects, a thin layer of new bone was found at the defect margin after 12 weeks, and most of the defect was filled with compressed fibrous connective tissue. A thin layer of bone formed after 12 weeks failed to bridge the defect after 24 weeks (Fig. 3g, h).

Histomorphometric analysis showed that total bone regeneration in the implants increased significantly from 12 to 24 weeks (Fig. 4). For the oriented implants, total bone regeneration normalized to the total defect area was 18 ± 3% at 12 weeks and 24 ± 2% at 24 weeks. When normalized to the available pore area in the scaffolds, total bone regeneration was 37 ± 8% and 55 ± 5% at 12 and 24 weeks, respectively. Total bone regeneration in the trabecular implants was 19 ± 9% and 36 ± 12% at 12 and 24 weeks, respectively, when normalized to the total defect area; when normalized to the area of the pore phase, the values were 25 ± 12% and 46 ± 13% at 12 and 24 weeks, respectively.

3.2. Mineralization of bioactive glass implants

Conversion of the oriented bioactive glass implants to an HA-like material in the rat calvarial defects was examined in an FE-SEM using BSE imaging for differences in phase and EDS mapping for elemental distributions of Ca (K), P (K), and Si (K) (Fig. 5). Twelve weeks postimplantation, BSE images of planar sections of the implants showed 3 regions: a light-gray inner core, a darker transition region, and a light-gray outer layer (Fig. 5a). Based on the EDS mapping (Figs. 5b–d), the inner core, rich in Ca and Si, was presumably an unconverted glass core (denoted G). The transition layer was found to be a

Si-rich layer with low concentration of Ca and P (denoted S), while the outer layer, rich in Ca and P, was the converted layer, presumably an HA-like material (denoted H). At 24 weeks, the unconverted glass core had almost disappeared, leaving a Si-rich core (S), and the HA-like outer layer (H) was thicker.

The Ca/P atomic ratios in different regions of the implants are shown in Table 2. The Ca/P ratios in the regions of newly formed bone and the converted (HA-like) layer at 12 and 24 weeks were comparable to the value for stoichiometric HA (1.67). The glass region had a high Ca/P ratio (6.4 ± 0.4), comparable to the theoretical value for 13-93 glass (6.5). At 12 weeks, the Ca/P ratio of the Si-rich layer (2.6 ± 0.2) was between the values for HA and the glass. With an increase in the implantation time to 24 weeks, the Ca/P ratio of the Si-rich region decreased to 1.9 ± 0.1. For both implantation times, the tissue appeared to bond directly to the outer converted layer (H) of the implant. The presence of microcracks in the implant and the gap between the bone (B) and the surface of the implant (H) in Fig. 5a was presumably caused by capillary stresses during drying of the implant and by shrinkage stresses during embedding in PMMA.

Von Kossa stained images (Fig. 6) showed the mineralized phase in the defects. The positive stained areas indicated the presence of phosphate material [26]. Both the newly formed bone and the HA-like converted layer of the scaffold were stained dark whereas the unconverted glass (low in phosphate content) transmitted light. The regions of new bone formation were similar to those observed previously in the H&E stained sections. For both groups of implants, the total mineralized area, normalized to the total defect area, increased significantly with implantation time from 12 to 24 weeks (Fig. 7), as a result of the increase in bone regeneration and conversion of the bioactive glass implant to an HA-like material.

3.3. Mechanical response of bioactive glass implants

The response of the bioactive glass scaffolds (applied force vs. displacement) determined in the diametral compression test is shown in Fig. 8. The results are shown for the oriented scaffolds as fabricated and after immersion in SBF for 12 and 24 weeks, and for the oriented and trabecular scaffolds implanted in rat calvarial defects for 12 and 24 weeks. (The curves were arbitrarily shifted along the *x*-axis to maintain clarity.) As fabricated, the oriented scaffold showed a typical elastic response followed by failure: the

load increased almost linearly with deformation before fracture at a load of 88 ± 17 N. After immersion in SBF, an elastic response was still observed but the load at fracture decreased markedly, to 38 ± 5 N at 12 weeks and 34 ± 7 N at 24 weeks. As shown for trabecular scaffolds of 13-93 glass, the decrease in compressive strength as a function of immersion time in SBF can be modeled in terms of a reduction in the effective cross-sectional area of the glass struts for load bearing due to conversion of the surface layer of the glass to a mesoporous HA-like material [27]. However, additional factors, such as an increase in the critical flaw size resulting from corrosion in SBF, could also contribute to the decrease in failure load.

In comparison, the scaffolds showed a markedly different mechanical response after implantation in vivo. An elasto-plastic response was observed, in which the load initially increased approximately linearly with deformation (region 1), followed by region 2 in which the deformation showed a large increase with a small change in load, and finally region 3 in which the load increased more steeply, presumably due to compaction of the sample. For the oriented implants, the load at the yield point (taken as the load at approximately the elastic limit) was ~11 N at 12 weeks, and it showed little increase (to ~13 N) at 24 weeks. The trabecular scaffolds implanted for 12 weeks were too weak to be tested in the mechanical testing machine; 24 weeks postimplantation, the load at the yield point was ~4 N.

The load vs. displacement response of the scaffolds after implantation in vivo showed a large degree of scatter which is believed to result from two main sources. First, the size of the implants used in the rat calvarial defect model was small (4.6 mm × 1.5 mm); as a result, small variations in the overall geometry can have a marked effect on the mechanical response. Second, the distribution of new bone within the implants was not homogeneous; for the implantation times used, new bone infiltrated only the lower part of the oriented scaffolds.

The energy absorbed during the deformation of the scaffolds was estimated from the area under the force vs. displacement curve [28]. For the scaffolds implanted in vivo, the area was determined up to a deformation of 40%, which corresponded approximately to the deformation at which compaction of the sample started to occur. For the oriented scaffolds implanted for 12 and 24 weeks, the energy absorbed during the deformation (20

mJ) was 2–3 times the value of the as-fabricated scaffolds and ~20 times the values for the oriented scaffolds immersed in SBF for similar periods.

4. Discussion

The results of the present work provided new information for the potential use of strong porous bioactive glass (13-93) scaffolds with an oriented microstructure in bone repair. In particular, the results provided information on the ability of the oriented implants to regenerate bone and integrate with host bone, and on the mineralization and mechanical response of the implants in a bone defect model. While the animal model used was a non-loaded bone defect model, the results are useful for designing scaffolds to be used in the more demanding application of loaded bone regeneration.

4.1. Bone regeneration and integration

While the oriented and trabecular scaffolds were both capable of supporting bone regeneration in rat calvarial defects, the microstructure strongly influenced the way in which new bone infiltrated the implant and the integration of the implant with host bone (Figs. 2, 3). Twelve weeks postimplantation, new bone formed mainly on the dural (bottom) side of the oriented implants, with little bone ingrowth into the periphery (edge) of the implants. At 24 weeks, there was an improvement in total bone regeneration, bone infiltration into the periphery of the implants, and integration with host bone were higher. In comparison, the trabecular implants showed bone regeneration predominantly into the periphery of the implants and better integration with host bone than the oriented implants at 12 weeks (Figs. 2, 3).

The difference in bone infiltration in the two groups of scaffolds (at the periphery vs. the dural side) may result from differences in the scaffold architecture. Previous studies have shown that in addition to porosity and pore size, other factors such as pore interconnectivity, the size of the opening between adjacent pores, permeability, and microstructural anisotropy of the scaffolds can have an important effect on bone infiltration [29, 30]. Whereas the trabecular scaffolds had a larger porosity (~80%) and pore of larger size (100−500 μm), the more tortuous pore channels could limit bone ingrowth to the periphery. In comparison, the oriented scaffolds had a lower porosity (~50%), and the pore diameter (50−150 μm) was just comparable to the minimum pore

size shown to be favorable for bone ingrowth [31, 32]. However, the oriented pores were connected at several positions along their length, and the pore channels were less tortuous, which could facilitate bone ingrowth into the interior of the scaffolds. Despite the larger pore size, new bone formation in the trabecular scaffolds based on the available pore area (volume) was 46 ± 13%, compared to 55 ± 5% for the oriented scaffolds (Fig. 4b). This might be a further indication that the tortuosity of the pore channels played an important role in controlling bone infiltration in the scaffolds.

It has been observed that the dura mater, pericranium, and surrounding bone can each influence osteogenesis differently in rabbit calvarial defects [33]. The dura was more osteogenic than the pericardium, and it appeared to be the source of bone growth on the dural side and in the interior of implants, whereas the pericranium appeared to enhance bone growth into the periphery. Since the mechanism of bone growth at the periphery could be different from that into the interior of the scaffolds, the architecture of the scaffolds could also influence bone growth at the periphery relative to the interior. Apparently, the trabecular microstructure was more conducive to bone growth from the pericranium and surrounding bone, whereas the oriented microstructure was better at supporting bone ingrowth from the dura mater.

In practice, the method used to create the oriented scaffolds used in this study (unidirectional freezing of suspensions) has a limited ability for substantially increasing the pore diameter of the scaffolds. Furthermore, an increase in the pore diameter is achieved mainly at the expense of lowering the mechanical properties of the scaffolds [11]. Consequently, use of these oriented bioactive glass implants for the repair of loaded bone may require additional considerations for accelerating bone ingrowth and integration.

4.2. Mineralization of scaffolds in vivo

A distinctive property of bioactive glasses is their conversion to an HA-like material (mineralization) in vivo [5, 6]. The HA-like layer grows as conversion of the bioactive glass continues with time, leading to a continuous degradation of the scaffold mechanical properties. Conversion of a bioactive glass in vitro (in SBF) is sometimes used as a guide to its mineralization in vivo, but the in vitro kinetic data might not be very applicable to the in vivo environment. The results of this study showed that 13-93

glass converted faster in rat calvarial defects than in SBF in vitro. SEM showed that after immersion in SBF for 24 weeks, the oriented scaffolds consisted of a converted layer ~10 μm thick, a SiO_2-rich layer (~3 μm), and a considerable amount of unconverted glass (results not shown). In comparison, 24 weeks postimplantation, the oriented scaffolds were almost completely converted to an HA-like material (~30 μm thick) surrounding a SiO_2-rich core, with little unconverted glass (Fig. 5). The faster conversion of 13-93 bioactive glass in vivo presumably resulted from the more dynamic environment of the body (compared to the more static in vitro system), and the presence of electrolytes, proteins, and biological polymers in the body fluid [34, 35].

An interesting observation was that EDS analysis showed the presence of Si in the converted layer of the bioactive glass, with a concentration gradient from the SiO_2-rich interior to the surface of the implant (Fig. 5). Apart from a difference in rate, the conversion of 13-93 bioactive glass to HA appears to follow a mechanism similar to that of 45S5 bioactive glass [5], resulting in the formation of an HA-like material surrounding a SiO_2-rich core. Previous studies have suggested that degradation of the SiO_2-rich core occurred continuously by cellular resorption and Si transport through the HA-like material, followed by Si dissolution [35, 36]. The solubility of silica in water is ~0.015 wt% at 37 ^{o}C [37], and silicon substitution in HA is < 2 wt% [38]. The observed Si concentration in the implants may be due to the degradation of the SiO_2-rich core and transport from the high concentration at the interface with the HA-like material to the low concentration at the surface of the implant.

4.3. Mechanical response of scaffolds in vitro and in vivo

Another interesting finding of the present study was the marked difference in mechanical response between the scaffolds after immersion in SBF in vitro (elastic response in which the load to failure decreased with immersion time) and after implantation in vivo for 12 and 24 weeks (elasto-plastic response) (Fig. 8). This difference presumably resulted mainly from the infiltration of new bone and soft tissue into the scaffolds in vivo. A composite structure was formed, consisting of unconverted glass, HA-like material formed by partial conversion of the glass, and tissue (new bone and soft tissue) infiltrated into the pores of the scaffold (Fig. 5a, e). The infiltrated tissue presumably provided a deformable matrix for the brittle glass and HA-like material.

Scaffolds implanted for 12 and 24 weeks in rat calvarial defects maintained their external geometry following the diametral compression test. SEM examination of the implants after testing (Fig. 9) showed that while the glass phase had fractured into several pieces, it was held together by the matrix composed of new bone and soft tissue.

The mechanical response of the bioactive glass scaffolds observed in this study is compatible with the results of recent studies which showed that the brittle failure of porous ceramics can be altered after implantation in vivo or after infiltration with polymers in vitro. Porous HA scaffolds, with a brittle response as fabricated, showed an elasto-plastic response in compression after implantation for 8 weeks in an rhBMP-2 driven ectopic bone model in muscle [39]. Coating or infiltrating porous glass or ceramic scaffolds with a biodegradable polymer resulted in an improvement in toughness and an elasto-plastic response in compression [40−42]. The toughness of the scaffolds, determined from the energy adsorbed per unit volume during deformation, could be increased by 2−20 times after incorporation of the polymer phase [7, 40, 43]. Scaffolds with compressive strengths of ~0.1−0.5 MPa as fabricated , had toughness values of ~40−250 $kJ \cdot m^{-3}$ after coating or infiltrating with a polymer phase [43−45], while the toughness of scaffolds with higher compressive strengths (~10 MPa) had toughness values up to ~1000 $kJ \cdot m^{-3}$ [41]. In the present study, the energy absorbed during deformation of the oriented scaffolds (implantation time = 12 or 24 weeks) was ~800 $kJ \cdot m^{-3}$, which is in the higher range of values reported for bioactive glass scaffolds coated or infiltrated with a polymer phase.

The results of the present in vivo study showed the ability of oriented bioactive glass (13-93) scaffolds to support bone regeneration, almost complete conversion within 24 weeks, and development of a desirable elasto-plastic response. In general, upon implantation of a bioactive glass scaffold in a bone defect, the strength of the scaffold decreases with time due to conversion of the glass to an HA-like material, but this should be countered by an increase in strength due to bone ingrowth. A key issue for application of these oriented scaffolds in loaded bone repair is matching the conversion rate of the glass with the rate of bone regeneration to provide the requisite mechanical properties. This issue is being addressed in our current work.

5. Conclusion

Strong porous scaffolds of 13-93 bioactive glass with an oriented microstructure of columnar pores (porosity = 50%; pores diameter = 50–150 μm) showed the capacity to regenerate bone in rat calvarial defects. Bone regeneration in the oriented implants normalized to the available pore area (volume) increased from 37% at 12 weeks to 55% at 24 weeks. Scaffolds with a trabecular microstructure (porosity = 80%; pore width = 100−500 μm), used as the positive control, showed bone regeneration in the pores of 25% and 46% at 12 and 24 weeks, respectively. Conversion of the bioactive glass implants in vivo was more than 3 times faster than in vitro (immersion in simulated body fluid), resulting in almost complete conversion of the glass 24 weeks postimplantation. The mechanical response of the implants changed markedly from a brittle response in vitro (as fabricated or after immersion in simulated body fluid) to an elasto-plastic response after implantation in vivo for 12 or 24 weeks. Together, the results indicate promising potential for the use of these oriented bioactive glass scaffolds in the repair of loaded or non-loaded bone.

Acknowledgement

This work was supported by the National Institutes of Health, National Institute of Arthritis, Musculoskeletal and Skin Diseases (NIAMS), Grant # 1R15AR056119-01, and by the U.S. Army Medical Research Acquisition Activity, under Contract No. W81XWH-08-1-0765. The authors would like to thank Mo-Sci Corp., Rolla, MO for the bioactive glass used in this work, Dr. R. F. Brown for assistance with animal surgeries, and the Advanced Light Source, Lawrence Berkeley National Lab, for use of the dedicated X-ray tomography beamline.

References

[1] U.S. Census Bureau. Interim State Population Projections 2005.

[2] U.S. Census Bureau. Health and nutrition. U.S. Census Bureau statistical abstracts of the United States, Washington, DC, 2009; p. 117.

[3] Thawani JP, Wang AC, Than KD, Lin CY, La Marca F, Park P. Bone morphogenetic proteins and cancer: review of the literature. Neurosurgery 2010;66:233-46.

[4] Pasche B. Role of transforming growth factor beta in cancer. J Cell Physiol 2001;186:153-68.

[5] Hench LL. Bioceramics. J Am Ceram Soc 1998;81:1705-28.

[6] Rahaman MN, Day DE, Bal BS, Fu Q, Jung SB, Bonewald LF. Bioactive glass in tissue engineering. Acta Biomater 2011;7:2355-73.

[7] Fu Q, Saiz E, Rahaman MN, Tomsia AP. Bioactive glass scaffolds for bone tissue engineering: state of the art and future perspectives. Mater Sci Eng C 2011;31:1245-56.

[8] Baino F, Vitale-Brovarone C. Three-dimensional glass-derived scaffolds for bone tissue engineering: Current trends and forecasts for the future. J Biomed Mater Res A 2011;97:514-35.

[9] Gerhardt L-C, Boccaccini AR. Bioactive glass and glass-ceramic scaffolds for bone tissue engineering. Materials 2010;3:3867-910.

[10] Deville S, Saiz E, Nalla RK, Tomsia AP. Freezing as a path to build complex composites. Science 2006;311:515-8.

[11] Liu X, Rahaman MN, Fu Q, Tomsia AP. Porous and strong bioactive glass (13-93) scaffolds prepared by unidirectional freezing of camphene-based suspensions. Acta Biomater 2012;8:415-23.

[12] Liu X, Rahaman MN, Fu Q. Oriented bioactive glass (13-93) scaffolds with controllable pore size by unidirectional freezing of camphene-based suspensions: microstructure and mechanical response. Acta Biomater 2011;7:406-16.

[13] Fu Q, Rahaman MN, Bal BS, Brown RF. Preparation and in vitro evaluation of bioactive glass (13-93) scaffolds with oriented microstructures for repair and regeneration of load-bearing bones. J Biomed Mater Res A 2010;93:1380-90.

[14] [14] Fu Q, Rahaman MN, Bal BS, Kuroki K, Brown RF. In vivo evaluation of 13-93 bioactive glass scaffolds with trabecular and oriented microstructures in a subcutaneous rat implantation model. J Biomed Mater Res A 2010;95:235-44.

[15] Place ES, Evans ND, Stevens MM. Complexity in biomaterials for tissue engineering. Nat Mater 2009;8:457-70.

[16] Fu Q, Rahaman MN, Sonny Bal B, Brown RF, Day DE. Mechanical and in vitro performance of 13–93 bioactive glass scaffolds prepared by a polymer foam replication technique. Acta Biomater 2008;4:1854-64.

[17] Sanderson C, Kitabayashi LR. Parallel experience of two different laboratories with the initiator Perkadox 16 for polymerization of methylmethacrylates. J Histotechnology 1994;17:343-8.

[18] Sheehan D, Hrapchak B. Theory and Practice of Histotechnology. 2nd ed. St. Louis: CV Mosby Co.; 1980.

[19] An YH, Draughn RA. Mechanical Testing of Bone and the Bone-Implant Interface. Boca Raton, FL: CRC Press; 1999.

[20] Thomas MB, Doremus RH, Jarcho M, Salsbury RL. Dense hydroxylapatite: fatigue and fracture strength after various treatments, from diametral tests. J Mater Sci 1980;15:891-4.

[21] Xie D, Brantley WA, Culbertson BM, Wang G. Mechanical properties and microstructures of glass-ionomer cements. Dent Mater 2000;16:129-38.

[22] Womack WJ, Santoni BG, Puttlitz CM. Diametral compression of non-circular diaphyseal bone sections. J Biomech 2008;41:194-9.

[23] Sinka IC, Cunningham JC, Zavaliangos A. Analysis of tablet compaction. II. Finite element analysis of density distributions in convex tablets. J Pharm Sci 2004;93:2040-53.

[24] Kokubo T, Kushitani H, Sakka S, Kitsugi T, Yamamuro T. Solutions able to reproduce in vivo surface-structure changes in bioactive glass-ceramic A-W. J Biomed Mater Res 1990;24:721-34.

[25] Fu Q, Huang W, Jia W, Rahaman MN, Liu X, Tomsia AP. Three-dimensional visualization of bioactive glass-bone integration in a rabbit tibia model using synchrotron X-ray microcomputed tomography. Tissue Eng Part A 2011;17:3077-84.

[26] Bonewald LF, Harris SE, Rosser J, Dallas MR, Dallas SL, Camacho NP, Boyan B, Boskey A. Von Kossa staining alone is not sufficient to confirm that mineralization in vitro represents bone formation. Calcified Tissue Int 2003;72:537-47.

[27] Fu Q, Rahaman MN, Fu H, Liu X. Silicate, borosilicate, and borate bioactive glass scaffolds with controllable degradation rate for bone tissue engineering applications. I. Preparation and in vitro degradation. J Biomed Mater Res A 2010;95:164-71.

[28] Gibson LJ, Ashby MF. Cellular Solids: Structure and Properties. 2nd ed. Cambridge: Cambridge University Press; 1997.

[29] Jones AC, Arns CH, Hutmacher DW, Milthorpe BK, Sheppard AP, Knackstedt MA. The correlation of pore morphology, interconnectivity and physical properties of 3D ceramic scaffolds with bone ingrowth. Biomaterials 2009;30:1440-51.

[30] Otsuki B, Takemoto M, Fujibayashi S, Neo M, Kokubo T, Nakamura T. Pore throat size and connectivity determine bone and tissue ingrowth into porous implants: Three-dimensional micro-CT based structural analyses of porous bioactive titanium implants. Biomaterials 2006;27:5892-900.

[31] Hulbert SF, Young FA, Matthews RS, Klawitter JJ, Talbert CD. Potential of ceramic materials as permanently implantable skeletal prostheses. J Biomed Mater Res 1970;4:433-56.

[32] Karageorgiou V, Kaplan D. Porosity of 3D biomaterial scaffolds and osteogenesis. Biomaterials 2005;26:5474-91.

[33] Gosain AK, Santoro TD, Song LS, Capel CC, Sudhakar PV, Matloub HS. Osteogenesis in calvarial defects: contribution of the dura, the pericranium, and the surrounding bone in adult versus infant animals. Plast Reconst Surg 2003;112:515-27.

[34] Fu Q, Rahaman MN, Day DE. Accelerated conversion of silicate bioactive glass (13-93) to hydroxyapatite in aqueous phosphate solution containing polyanions. J Am Ceram Soc 2009;92:2870-6.

[35] Radin S, Ducheyne P, Falaize S, Hammond A. In vitro transformation of bioactive glass granules into Ca-P shells. J Biomed Mater Res 2000;49:264-72.

[36] Schepers EJ, Ducheyne P. Bioactive glass particles of narrow size range for the treatment of oral bone defects: a 1-24 month experiment with several materials and particle sizes and size ranges. J Oral Rehabil 1997;24:171-81.

[37] Alexander GB, Heston WM, Iler RK. The solubility of amorphous silica in water. The J Phys Chem 1954;58:453-5.

[38] Kim SR, Lee JH, Kim YT, Riu DH, Jung SJ, Lee YJ, Chung SC, Kim YH. Synthesis of Si, Mg substituted hydroxyapatites and their sintering behaviors. Biomaterials 2003;24:1389-98.

[39] Woodard JR, Hilldore AJ, Lan SK, Park CJ, Morgan AW, Eurell JA, Clark SG, Wheeler MB, Jamison RD, Wagoner Johnson AJ. The mechanical properties and osteoconductivity of hydroxyapatite bone scaffolds with multi-scale porosity. Biomaterials 2007;28:45-54.

[40] Chen QZ, Boccaccini AR. Poly(D,L-lactic acid) coated 45S5 Bioglass®-based scaffolds: processing and characterization. J Biomed Mater Res A 2006;77:445-57.

[41] Peroglio M, Gremillard L, Gauthier C, Chazeau L, Verrier S, Alini M, Chevalier J. Mechanical properties and cytocompatibility of poly(ε-caprolactone)-infiltrated biphasic calcium phosphate scaffolds with bimodal pore distribution. Acta Biomater 2010;6:4369-79.

[42] Martinez-Vazquez FJ, Perera FH, Miranda P, Pajares A, Guiberteau F. Improving the compressive strength of bioceramic robocast scaffolds by polymer infiltration. Acta Biomater 2010;6:4361-8.

[43] Bretcanu O, Misra S, Roy I, Renghini C, Fiori F, Boccaccini AR, Salih V. In vitro biocompatibility of 45S5 Bioglass®-derived glass–ceramic scaffolds coated with poly(3-hydroxybutyrate). J Tissue Eng Regen Med 2009;3:139-48.

[44] Kim HW, Knowles JC, Kim HE. Hydroxyapatite porous scaffold engineered with biological polymer hybrid coating for antibiotic vancomycin release. J Mater Sci Mater Med 2005;16:189-95.

[45] Baino F, Verne E, Vitale-Brovarone C. Feasibility, tailoring and properties of polyurethane/bioactive glass composite scaffolds for tissue engineering. J Mater Sci Mater Med 2009;20:2189-95.

Table 1 Characteristics of silicate 13-93 bioactive glass scaffolds with oriented and trabecular microstructure

Scaffold	Porosity (%)	Pore size (μm)	Compressive strength (MPa)	Elastic modulus (GPa)	Fabrication method
Oriented	50 ± 4	50–150	47 ± 5	11 ± 3	Unidirectional freezing of suspensions
Trabecular	80 ± 5	100–500	11 ± 1	3 ± 0.5	Polymer foam replication

Table 2 EDS data for the Ca/P atomic ratio in different regions of 13-93 bioactive glass scaffold with an oriented microstructure after implantation for 12 and 24 weeks in rat calvarial defects. (The regions of the scaffold examined are shown in Fig. 5a, e).

Time (weeks)	Bone (B)	HA-like layer[1] (H)	SiO_2-rich layer/core (S)	Glass core (G)
12	1.72 ± 0.03	1.75 ± 0.04	2.6 ± 0.2	6.4 ± 0.4
24	1.52 ± 0.06	1.68 ± 0.03	1.9 ± 0.1	–

[1]Ca/P atomic ratio for stoichiometric HA = 1.67

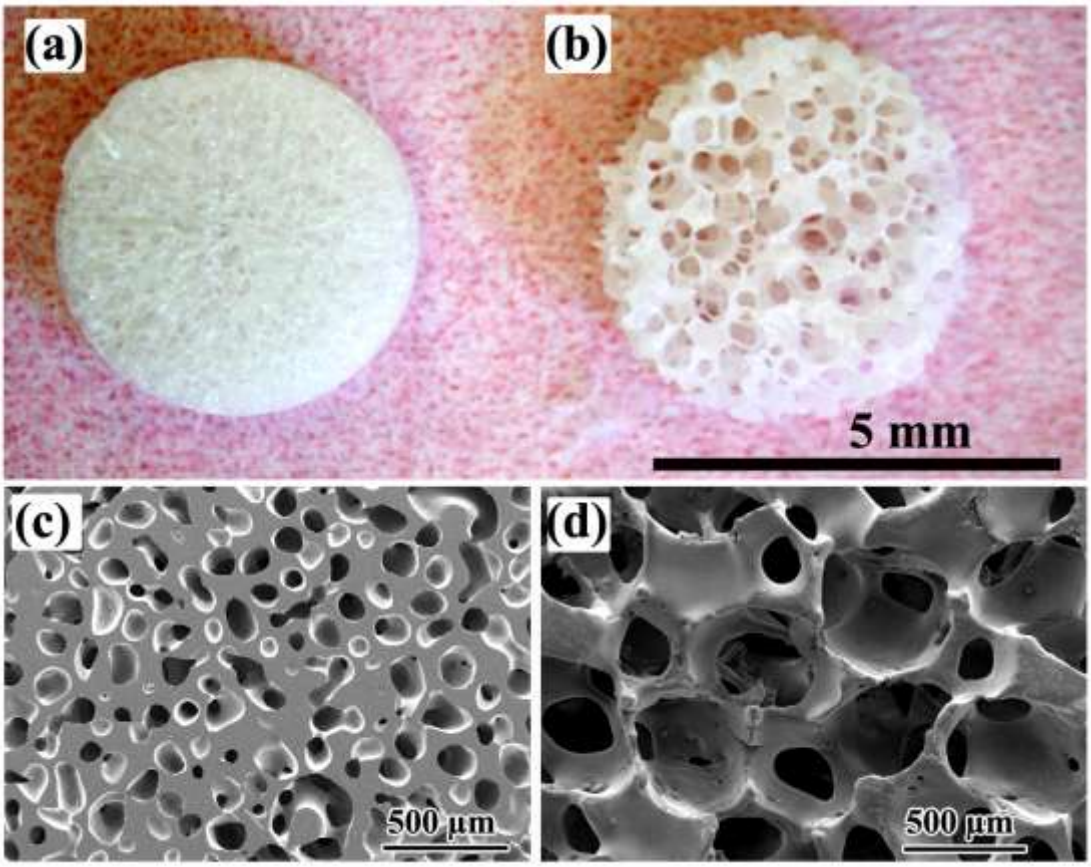

Fig. 1. Optical images of disc-shaped bioactive glass (13-93) scaffolds with (a) an oriented microstructure and (b) a trabecular microstructure (positive control). SEM images of cross-sections of the oriented and trabecular scaffolds are shown in (c) and (d), respectively. The cross-section in (c) is perpendicular to the pore orientation direction.

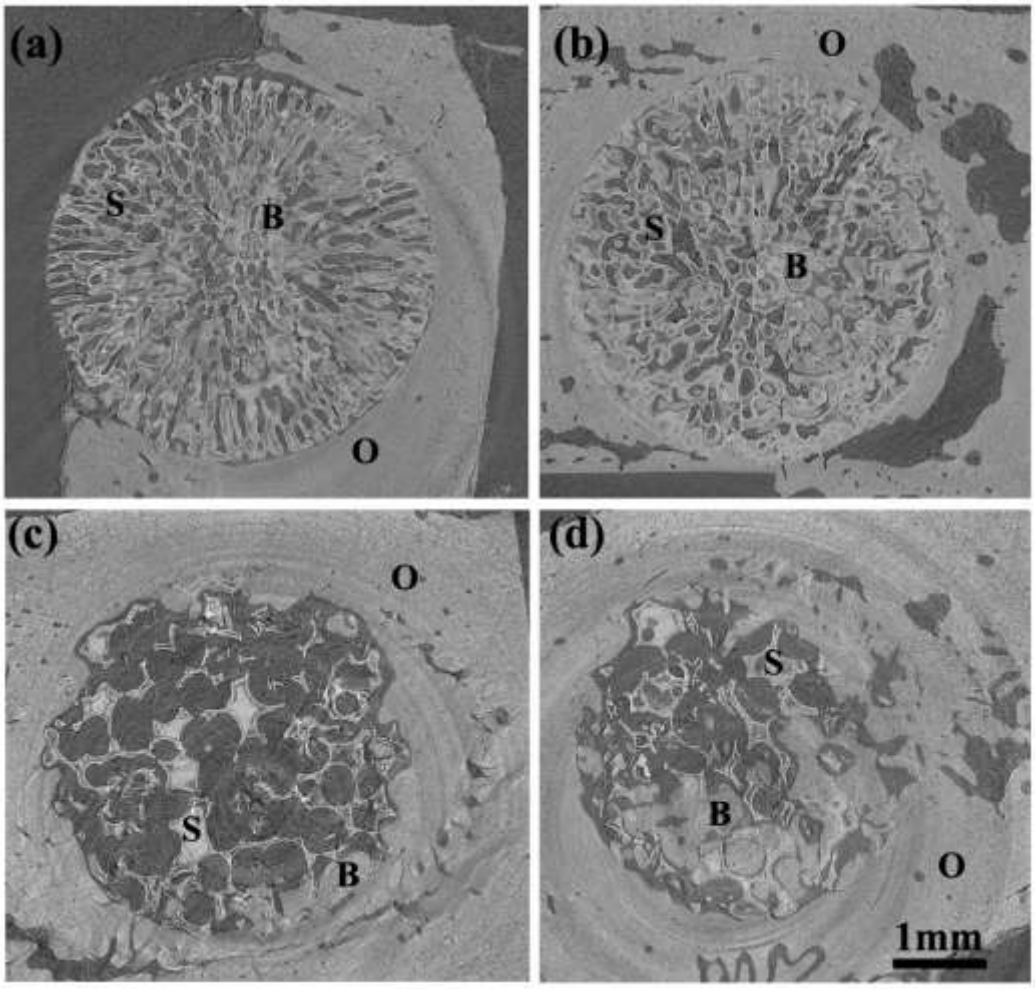

Fig. 2. Synchrotron micro-computerized X-ray tomography (SR microCT) images of oriented scaffold after implantation for 12 weeks (a) and 24 weeks (b), and trabecular scaffold after implantation for 12 weeks (c) and 24 weeks (d). The distribution of old bone (O), new bone formation (B) and the bioactive glass scaffold (S) is shown.

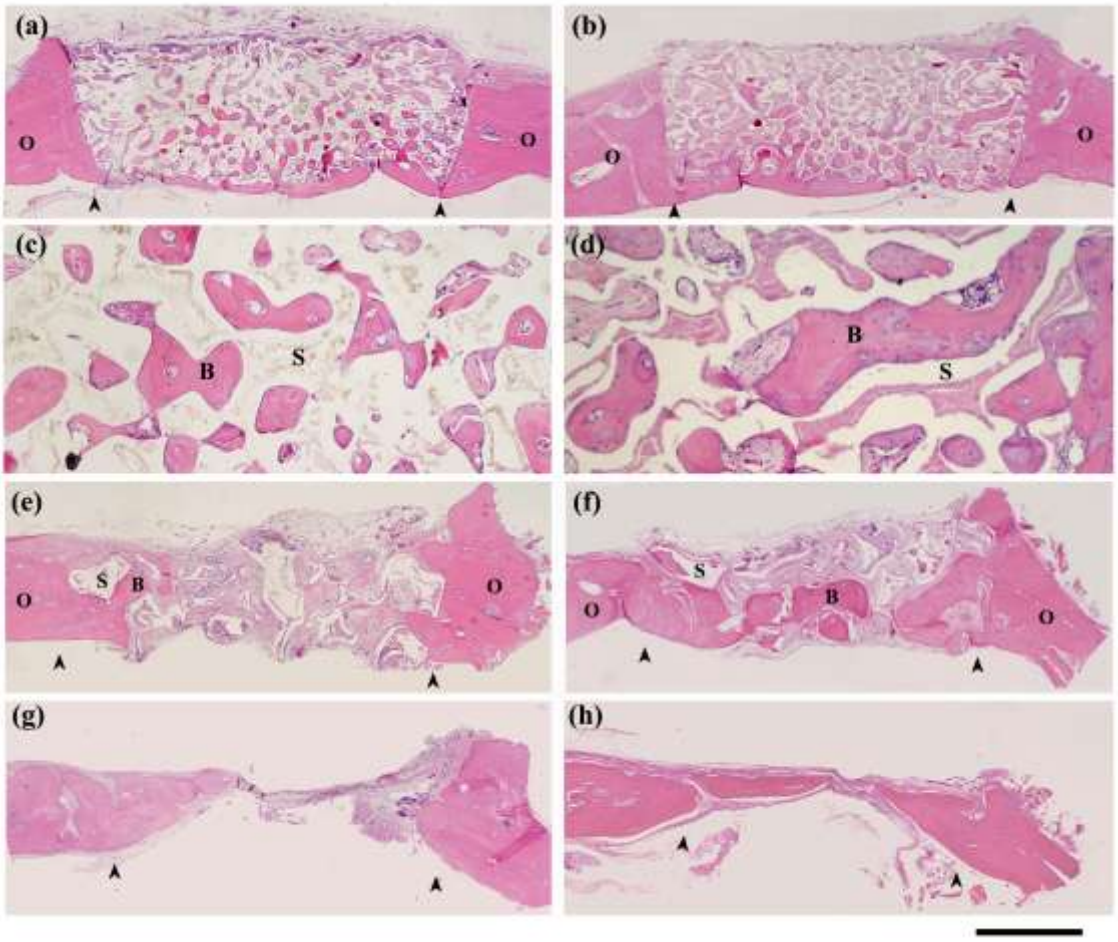

Fig. 3. H&E stained sections of rat calvarial defects implanted with oriented scaffolds at 12 weeks (a, c) and 24 weeks (b, d); defects implanted with trabecular scaffolds at 12 weeks (e) and 24 weeks (f), and untreated defects at 12 weeks (g) and 24 weeks (h). Stained sections at higher magnification (c, d) show new bone (B) in the pores of the oriented scaffolds (S) at 12 weeks and 24 weeks. Arrows indicate the edges of the old bone. Scale bar = 1 mm for (a, b and e-h), and 200 μm for (c, d).

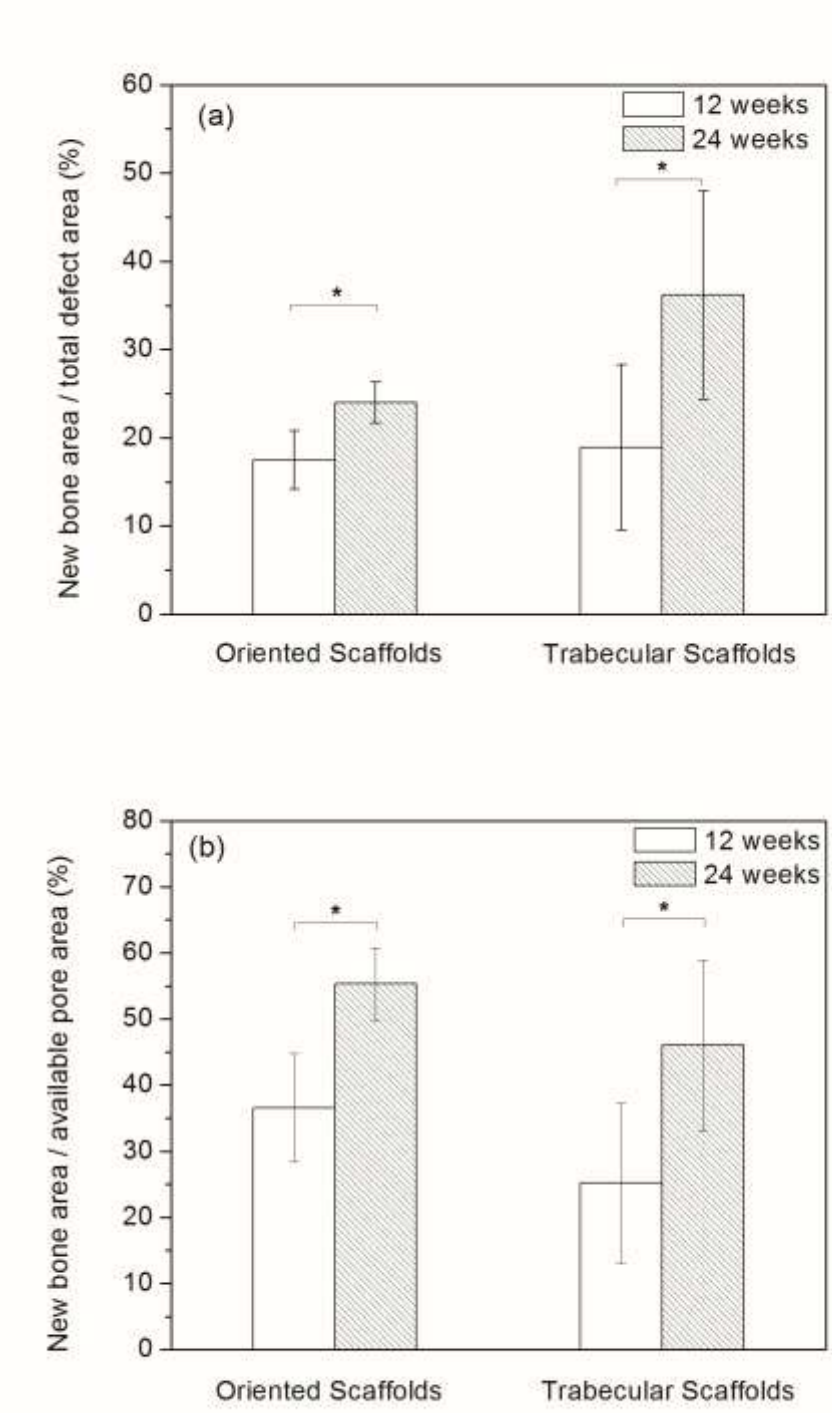

Fig. 4. Histomophometric analysis of H&E stained sections showing total bone regeneration in rat calvarial defects implanted with oriented and trabecular scaffolds at 12 and 24 weeks: (a) normalized to the total defect area; (b) normalized to the available pore area of the scaffolds (*significant difference between scaffolds: $p<0.05$).

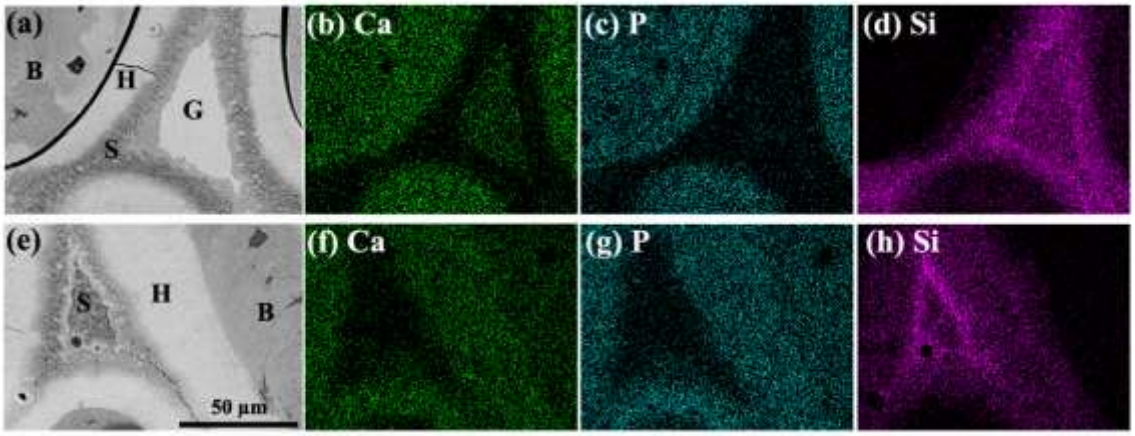

Fig. 5. SEM backscattered electron images and X-ray maps for Ca (K), P(K) and Si(K) for oriented bioactive glass scaffolds after implantation for 12 weeks (a–d) and 24 weeks (e–h) in rat calvarial defects. Mineralized tissue (B) was formed adjacent to the hydroxyapatite (HA)-like layer (H) formed on the surface of the glass. G denotes the unconverted glass, and S the SiO_2-rich layer or SiO_2-rich core.

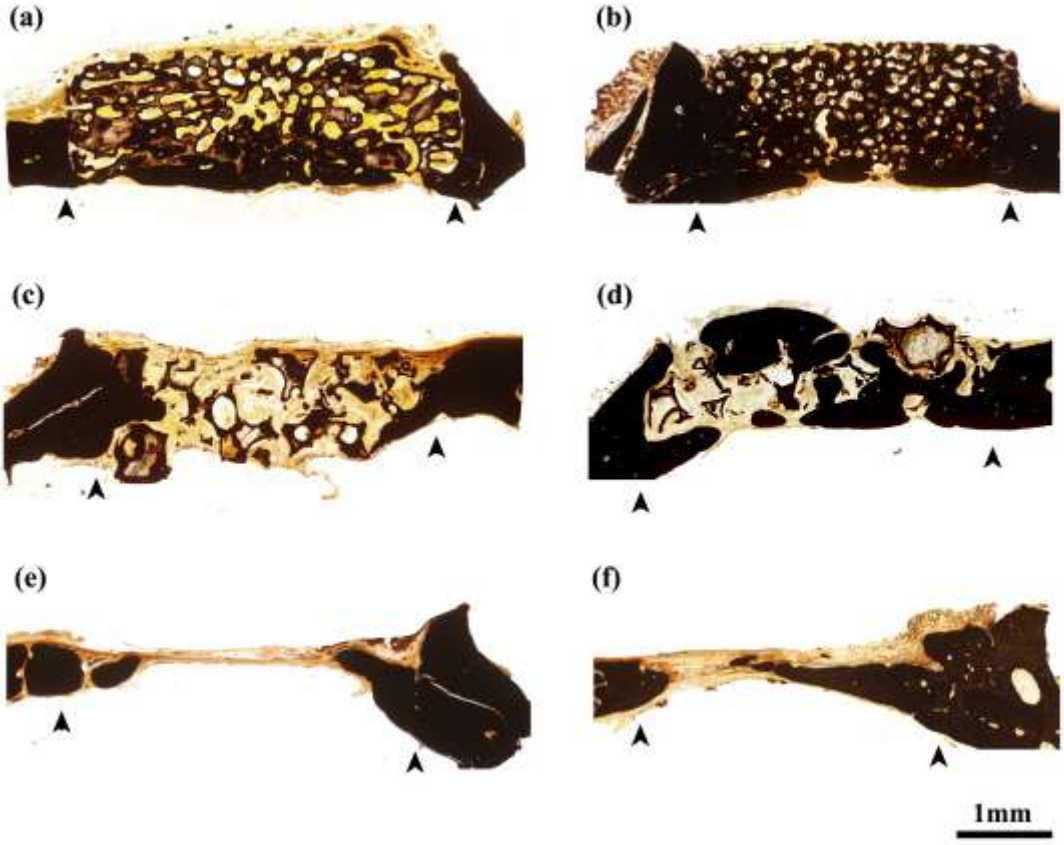

Fig. 6. Von Kossa stained sections of rat calvarial defects implanted with oriented scaffolds at 12 weeks (a) and 24 weeks (b), defects implanted with trabecular scaffolds at 12 weeks (c) and 24 weeks (d), and empty defects at 12 weeks (e) and 24 weeks (f). Arrows indicate the edges of the old bone.

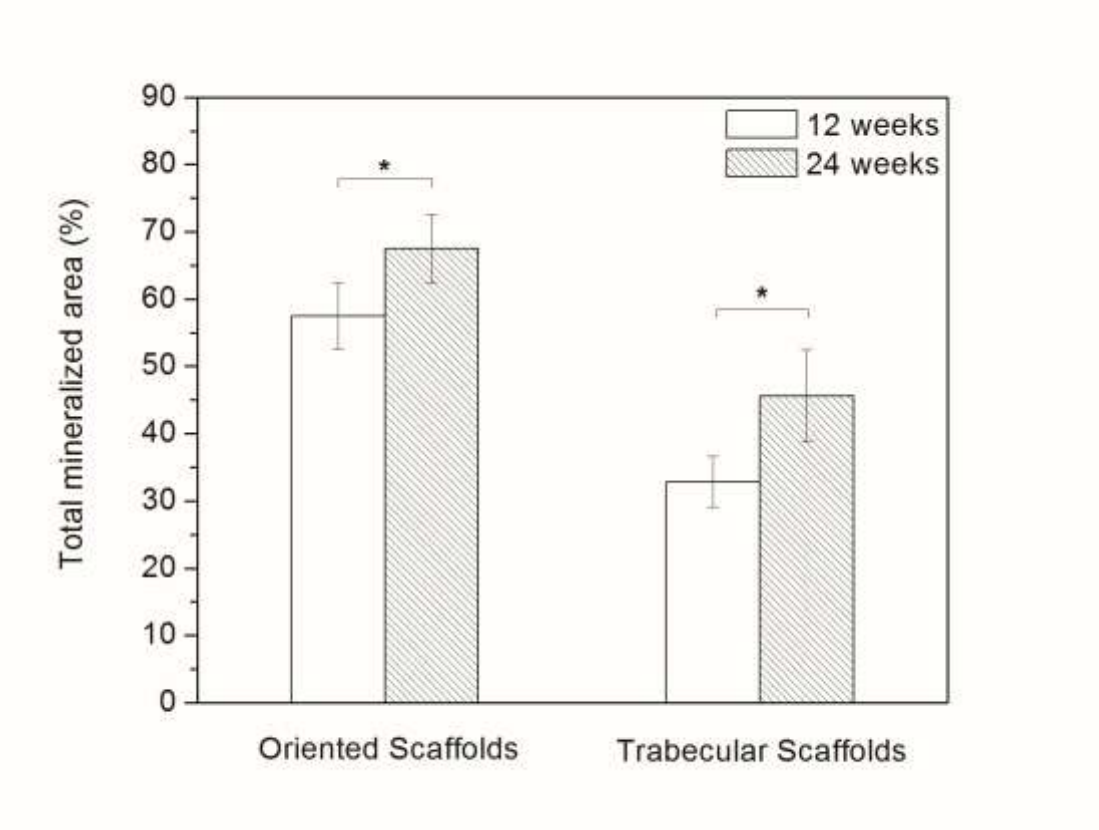

Fig. 7. Histomophometric analysis of von Kossa positive area (total mineralized area of new bone and HA-like layer of scaffold) in rat calvarial defects implanted with oriented and trabecular scaffolds 12 weeks and 24 weeks postimplantation (*significant difference between scaffolds: $p<0.05$).

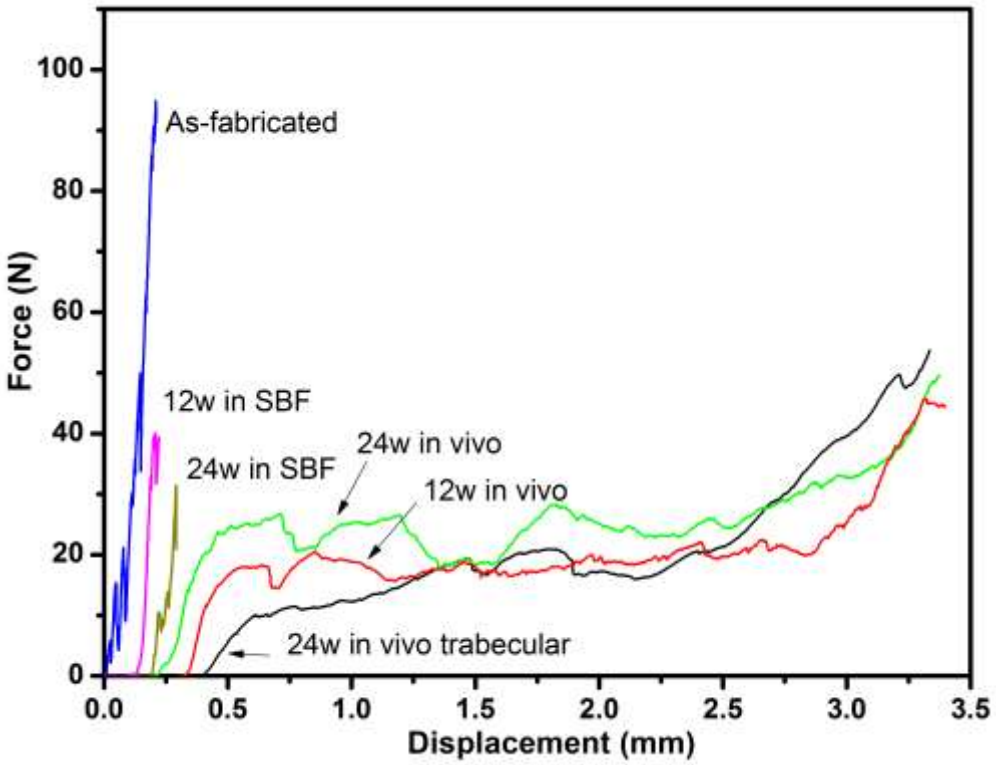

Fig. 8. Force vs. displacement response for oriented scaffolds as fabricated, after immersion in SBF for 12 and 24 weeks, and after implantation in rat calvarial defects for 12 and 24 weeks. The response of trabecular scaffolds (positive control) after implantation for 24 weeks is also shown. (The curves were arbitrarily shifted along the x-axis to maintain clarity)

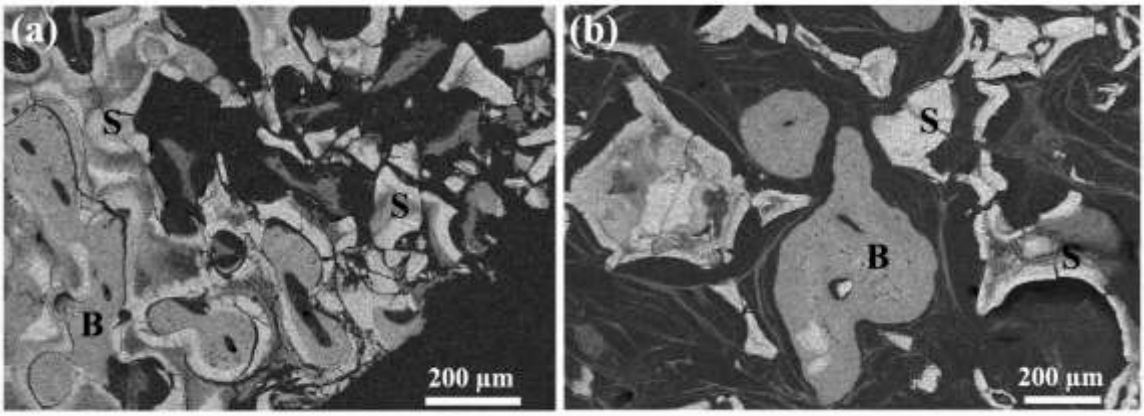

Fig. 9. SEM backscattered images showing the cross-sections of (a) oriented scaffolds and (b) trabecular scaffolds after implantation in rat calvarial defects for 24 weeks and testing in the diametral compression test. (S: converted bioactive glass scaffold; B: mineralized tissue)

IV. MECHANICAL PROPERTIES OF BIOACTIVE GLASS (13-93) SCAFFOLDS FABRICATED BY ROBOTIC DEPOSITION FOR STRUCTURAL BONE REPAIR

Xin Liu[1,2], Mohamed N. Rahaman[1,2], Gregory E. Hilmas[1], B. Sonny Bal[3]

[1]Department of Materials Science and Engineering, [2]Center for Bone and Tissue Repair and Regeneration, Missouri University of Science and Technology, Rolla, MO 65409, USA

[3]Department of Orthopaedic Surgery, University of Missouri-Columbia, Columbia, MO 65212, USA

ABSTRACT

There is a need to develop synthetic scaffolds for repairing large defects in load-bearing bones. Bioactive glasses have attractive properties as a scaffold material for bone repair, but data on their mechanical properties are limited. The objective of the present study was to comprehensively evaluate the mechanical properties of strong porous scaffolds of silicate 13-93 bioactive glass fabricated by robocasting. As-fabricated scaffolds with a grid-like microstructure (porosity = 47%; filament diameter = 330 μm; pore width = 300) were tested in compressive and flexural loading to determine their strength, elastic modulus, Weibull modulus, fatigue resistance, and fracture toughness. Scaffolds were also tested in compression after they were immersed in simulated body fluid (SBF) in vitro or implanted in a rat subcutaneous model in vivo. As fabricated, the scaffolds had a strength = 86 ±9 MPa, elastic modulus = 13 ±2 GPa, and a Weibull modulus = 12 when tested in compression. In flexural loading, the strength, elastic modulus, and Weibull modulus were 11 ± 3 MPa, 13 ±2 GPa, and 6, respectively. In compression, the as-fabricated scaffolds had a mean fatigue life of ~10^6 cycles when tested in air at room temperature or in phosphate-buffered saline at 37 °C under cyclic stresses of 1−10 MPa or 2−20 MPa. The compressive strength of the scaffolds decreased markedly during the first 2 weeks of immersion in SBF or implantation in vivo, but more slowly thereafter. The brittle mechanical response of the scaffolds in vitro changed to an elasto-plastic response after implantation for longer than 2−4 weeks in vivo. In addition

to providing critically needed data for designing bioactive glass scaffolds, the results are promising for the application of these strong porous scaffolds in loaded bone repair.

1. Introduction

Contained bone defects are repairable with commercially-available, osteoconductive and osteoinductive filler materials [1, 2]. However, no ideal biological solution exists to reconstitute structural bone loss, such as segmental defects in the limbs. The available treatments used to repair large bone defects, such as bone allografts, autografts, porous metals, and bone cement, have limitations related to costs, availability, longevity, donor site morbidity, and uncertain healing to host bone. Consequently, there is a great need for porous biocompatible implants that can replicate the strength, morphology, porosity, bioactivity, and load-bearing ability of living bone.

Scaffolds made of synthetic and natural polymers such as poly(lactic acid), poly(glycolic acid), polycaprolactone, and collagen degrade in vivo, and are replaced by new bone matrix synthesized by tissue-forming cells [3, 4]. These materials have proven useful for filling contained bone defects, but their use in structural bone repair is challenging because of their inherently low strength [5, 6]. Calcium phosphate bioceramics such as hydroxyapatite (HA), beta-tricalcium phosphate (β-TCP), and biphasic calcium phosphate (BCP) are logical bone repair materials since they are composed of the same ions as the mineral constituent of bone. However, synthetic HA degrades too slowly to allow osseous repair, while porous β-TCP scaffolds are typically not strong enough to survive physiologic loading.

Bioactive glasses have attractive properties as a scaffold material for bone repair. In vivo, bioactive glass converts to hydroxyapatite (HA), the main mineral constituent of bone, which promotes osseous healing [7−9]. Calcium ions and soluble silicon released during the bioactive glass conversion further promote osteogenesis [10, 11] and activate osteogenic gene expression [12, 13]. Bioactive glass can be doped, during manufacture, with trace amounts of elements such as copper (Cu), zinc (Zn), and strontium (Sr) that are known to promote angiogenesis and healthy bone growth [9, 14]. As the bioactive glass degrades during conversion to HA in vivo, those elements are released at therapeutically acceptable rates.

Most previous studies have targeted glass compositions, such as silicate 45S5 and 13-93, and three-dimensional (3D) scaffold architectures with relatively low-strength, such as compressive strengths in the range of values reported for human trabecular bone [15-18]. Attempts have been made to prepare glass or glass−ceramic scaffolds with higher strength using methods such as sintering particles that were compacted with a pore-forming phase [19] and unidirectional freezing of suspensions [20]. However, the range of pore sizes and the interconnectivity of the pores were difficult to control, which could limit the capacity of the scaffolds to support bone infiltration. Recent studies have shown that silicate 13-93 and 6P53B glass scaffolds fabricated by robocasting, a solid freeform fabrication technique, have compressive strengths comparable to those of human cortical bone [21−25] as well as a highly interconnected porous microstructure that is known to be favorable for supporting bone infiltration. Those strong porous bioactive glass scaffolds could provide promising implants for loaded bone repair.

Although the mechanical properties of bioactive glass scaffolds have been widely reported in the literature, most studies have focused on evaluating the strength and elastic modulus in compression of the as-fabricated scaffolds or scaffolds that were immersed in an aqueous phosphate solution such as a simulated body fluid (SBF) [15]. Load-bearing bones, such as long limb bones, are subjected to multiple loading modes as well as cyclic loading. Consequently, the development of bioactive glass scaffolds for repairing structural bone loss requires a comprehensive evaluation of their mechanical response. As the bioactive glass converts to HA, its properties change with time. Data for the time-dependent mechanical response in vitro and in vivo are also critically important for the design of bioactive glass scaffolds for loaded bone repair.

The objective of the present study was to comprehensively characterize the mechanical response of strong porous scaffolds of silicate 13-93 bioactive glass which were fabricated with a grid-like microstructure by robocasting. The selection of 13-93 glass was based on its proven bioactivity [9] and on our previous studies which showed that scaffolds of this glass can be created with compressive strengths comparable to cortical bone by solid freeform fabrication techniques [21-23]. The strength, elastic modulus, Weibull modulus in compression and flexure, fatigue resistance and fracture toughness of the as-fabricated scaffolds were evaluated. The mechanical response in

compression was also evaluated as a function of immersion time of the scaffolds in SBF in vitro and implantation time in rat subcutaneous sites in vivo.

2. Materials and methods

2.1. Fabrication of bioactive glass scaffolds

Melt-derived bioactive glass frits with the composition designated 13-93 ($53SiO_2$, $6Na_2O$, $12K_2O$, 5MgO, 20CaO, $4P_2O_5$, wt %), provided by Mo-Sci Corp., Rolla, MO, USA, were crushed in a steel shatterbox (8500 Shatterbox®, Spex SamplePrep LLC., Metuchen, NJ, USA) to form particles of size smaller than ~50 μm. Then the particles were ground for 2 h in an attrition mill using water as the liquid medium and ZrO_2 grinding media (3 mm in diameter) to give particles of size ~1 μm. A slurry (ink) for robotic deposition (robocasting) was prepared using a solution with reverse thermal behavior, as described in detail elsewhere [25]. Briefly, the glass particles (40 vol %) were mixed with a 20 wt % aqueous Pluronic® F-127 solution, previously cooled in a refrigerator, using a planetary centrifugal mixer (ARE-310; THINKY, Laguna Hills, CA, USA) and placed for 12 h in a refrigerator at 10 ^oC.

The ink was warmed to room temperature, loaded into a robotic deposition device (RoboCAD 3.0, 3-D Inks, Stillwater, OK, USA) and deposited on an Al_2O_3 substrate immersed in a reservoir of lamp oil (Florasense, Charleston, SC, USA). Scaffolds with a grid-like microstructure were formed by extruding the ink through a 410 μm nozzle (EFD Precision Tips, East Providence, RI, USA) with a line spacing (center-to-center distance between the filaments) of 910 μm. After forming, the scaffolds were dried for 24 h in air at room temperature, heated slowly (0.5 ^oC/min with a few isothermal holds) to 600 ^oC in flowing O_2 gas to burn out the processing additives, and sintered in air for 1 h at 700 ^oC (heating rate = 5 ^oC/min) to densify the glass filaments.

Scaffolds were coated with Au/Pd and examined in a scanning electron microscope (SEM) (S-4700; Hitachi, Tokyo, Japan) at an accelerating voltage of 15 kV and a working distance of 12 mm. Quantification of the microstructure (average pore width and glass filament diameter) was performed using image analysis (ImageJ; National Institutes of Health, USA), while the volume of the macropores in the scaffold was measured using the Archimedes method according to ASTM C830-00.

2.2. Mechanical testing in compression and flexure

The as-fabricated scaffolds were tested in compression and flexure using an Instron testing machine (Model 5881; Norwood, MA, USA). The compressive strength of scaffolds with a cubic shape (6 mm × 6 mm × 6 mm) was measured at a cross-head speed of 0.5 mm min^{-1}, using a 10 kN load cell. The deformation of the sample was determined from the movement of the cross-head. Prior to testing, the contact surfaces of the scaffolds were ground using a surface grinder (FSG-618, Chevalier Machinery Inc., Santa Fe Springs, CA, USA) to produce parallel surfaces. The elastic modulus was determined from the linear region of the stress vs. strain response. The load was applied to the samples in the z direction of the as-formed scaffolds, perpendicular to the plane of deposition (xy plane) shown in Fig. 1a. This loading direction was used because it would match the compressive loading direction of the scaffolds in a segmental bone defect.

Four-point flexural testing was performed on a fully articulated fixture (outer span = 20 mm; inner span = 10 mm) at a crosshead speed of 0.2 mm min^{-1}, using a 2 kN load cell. The stress was applied in the z direction of the scaffolds (the same direction used for the compression tests). The as-fabricated scaffolds (3 mm × 5 mm × 25 mm) were tested according to the procedure described in ASTM C1674-11, and the flexural strength was determined from the equation

$$\sigma = \frac{3Pl}{4bd^2} \tag{1}$$

where P is the applied load, l is the outer span, and b is the sample width and d is the thickness of the sample. The flexural modulus of the samples was determined from the stress and the deflection recorded using a linear variable differential transformer (LVDT) at the mid-span of the sample.

Thirty samples each were tested in compression and in flexure, and the strength and modulus were expressed as a mean ± standard deviation (SD). The Weibull modulus in each loading mode was determined according to ASTM C1239-07 by fitting the strength data with the equation

$$\ln\ln\left(\frac{1}{1-P_f}\right) = m\ln\left(\frac{\sigma}{\sigma_o}\right) \tag{2}$$

where P_f is the probability of failure at a stress σ, and σ_o is the Weibull scale parameter determined from the intercept of the fit to the data and Weibull modulus, m. The value σ_o is also the stress at which the probability of failure is 63%. P_f was evaluated using the equation

$$P_f = \frac{i - 0.5}{n} \quad (3)$$

where n is the total number of specimens tested and i is the specimen rank in ascending order of failure stresses.

After testing, the fractured surfaces of samples with the highest and lowest flexural strengths were coated with Au/Pd, and examined in the SEM (Hitachi; S-4700). Particular attention was paid to the lower region of the fractured surface (which was subjected to a tensile stress during the four-point bending test) and the upper region of the fractured surface (subjected to a compressive stress) to determine differences in the morphology of the fractured surfaces.

2.3. Fracture toughness testing

The fracture toughness of the as-fabricated scaffolds was measured by the single-edge notched beam (SENB) technique using samples of size 3 mm × 5 mm × 25 mm according to the procedure described in ASTM C1421-10. A notch of width <100 μm and depth of ~1.5 mm was machined at the midpoint of the 3 millimeter-wide plane using a dicing saw (ACCU-CUT 5200, AREMCO Products Inc., Ossining, NY). The notch depth (a few times the cell size of the scaffold) was chosen to satisfy the conditions for applicability of linear elastic fracture mechanics (K-dominance at the crack tip) [26]. The fracture toughness K_c was determined using the equation [26]

$$K_C = \sigma\sqrt{\pi a}\,Y F(a/H) \quad (4)$$

where σ is the fracture stress, *a* is the depth of the notch, *H* is the thickness of the sample, *F(a/H)* is a geometrical factor [27], and the dimensionless parameter *Y* is ~1 for the microstructure of the samples tested [26]. Five samples were tested in four-point bending as described earlier, and the fracture toughness was determined as an average ± SD.

2.4. Fatigue testing

Fatigue testing of the as-fabricated scaffolds was performed in cyclic compression using an ElectroForce 3330 testing system (Bose Corp., Eden Prairie, MN, USA).

Samples (6 mm × 6 mm × 6 mm) were tested in air at room temperature and in phosphate-buffered saline (PBS) at 37 ^{o}C using load-control actuation, at a frequency of 5 Hz. Three cyclic compressive stresses of 1−10 MPa, 2−20 MPa and 3−30 MPa were used in the study, with the minimum to maximum stress ratio kept constant at 0.1. The tests were conducted until failure or until 10^6 cycles were reached. The fatigue testing conditions were based on the estimated number of gait cycles (10^6) in one year for patients after joint replacement [28] and the recommended stress levels (10-15 MPa) in ASTM F2118-10. Six samples were tested at each cyclic stress. The fatigue life (mean ± SD) was determined using a logarithmic transformation of the cycles to failure as recommended in ASTM F2118-10. Statistical analysis of the mean fatigue life was performed using one-way analysis of variance (ANOVA) with Tukey's post hoc test; differences were considered significant for $p<0.05$.

2.5. Degradation of compressive strength in vitro and in vivo

The degradation of the compressive strength and elastic modulus of the scaffolds (6 mm × 6 mm × 6 mm) in vitro and in vivo was evaluated in compression using the testing conditions described earlier. The samples were tested after immersion in SBF at 37 ± 0.5 ^{o}C in an incubator (Model CCC 0.5d, Boekel Industries Inc., Feasterville, PA) or after implantation in rat subcutaneous sites for 2, 4, 6 and 12 weeks. For each time point, six samples were tested, and the compressive strength (average ± SD) was plotted as a function of time. In vitro, the ratio of the scaffold mass to the SBF volume was kept constant at 1 g per 100 cm^3, and the SBF was not changed during the immersion period. The samples were tested immediately after removal from the SBF (without drying).

A rat subcutaneous model was used for the in vivo study based on the ease of the implantation surgery and the need to implant scaffolds with an appropriate size for subsequent mechanical testing. Six-month old male Sprague Dawley rats were used. All animal experimental procedures were approved by the Animal Care and Use Committee, Missouri University of Science and Technology, in compliance with the NIH Guide for Care and Use of Laboratory Animals. The rats were anesthetized with a combination of ketamine (50 mg/kg) and xylazine (4 mg/kg). Six scaffolds were implanted into subcutaneous pockets at six sites in the dorsum of each rat. After each implantation

period, the animals were sacrificed by CO_2 inhalation. The samples were harvested, wrapped in gauze wetted with PBS, and tested.

After immersion in SBF or implantation in rat subcutaneous sites, the thickness of the converted layer of the glass filaments in the scaffolds, composed mainly of a porous HA-like material, was measured. The samples were freeze-dried (Freezezone 4.5; Labconco Corp., Kansas City, MO, USA), mounted in epoxy resin, sectioned, and polished. The polished cross-sections were coated with carbon and examined in an SEM (Hitachi; S-4700) in the backscattered electron (BSE) mode at an accelerating voltage of 15 kV and a working distance of 13 mm. At least 15 filaments were examined and the thickness of the converted layer was determined as an average ± SD.

3. Results

3.1. Mechanical properties of as-fabricated scaffolds

The as-fabricated scaffolds had a uniform grid-like microstructure (Fig. 1), with glass filaments of diameter 330 ± 10 μm, a pore width of 300 ± 10 micron in the plane of deposition (xy plane) and a pore width of 150 ± 10 μm in the direction of deposition (z direction). The glass filaments were almost fully dense (relative density = 98 ± 1%, as determined by the Archimedes method) and they appeared to be well bonded to the filaments in the adjacent plane. The total open porosity of the scaffolds, as determined by the Archimedes method was 47 ± 1%.

The mechanical properties of the as-fabricated scaffolds in compression and in flexure are summarized in Table 1. In compression, the scaffolds had a strength = 86 ± 9 MPa and an elastic modulus = 13 ± 2 GPa, whereas the flexural strength and flexural modulus were 11 ± 3 MPa and 13 ± 2 GPa, respectively. The fracture toughness of the scaffolds was 0.48 ± 0.04 MPa $\sqrt{m}$$^{1/2}$.

Figure 2 shows Weibull plots of the compressive and flexural strength data. The plots were approximately linear over most of the stress range, but deviations from a linear relationship were apparent at the low and high stress values. Least-squares fitting of a straight line through the data points gave a Weibull modulus of 12 in compression and 6 in flexure. For each loading mode, an alternative might be to fit two straight lines through the strength data, one for the lower strength values, and the other for the remaining

values. However, SEM images of the fractured surfaces of scaffolds with a higher flexural strength (15 MPa) and a lower flexural strength (8 MPa) showed no marked difference in fracture morphology (Fig. 3). Features such as hackle lines (indicated by arrows) and smooth mirror areas (starred symbols) [30] were found on the fractured surfaces of both samples. The fractured glass filaments near the top region (Fig.3c, f) of the sample (subjected to a compressive stress during four-point bending) showed cantilever curls (curve lines indicated by arrowheads), typically found near the region of compression in flexural testing of brittle solids [30]. However, the origin of failure, typically found in the tensile region (near the lower region in four-point bending) was difficult to determine.

The fatigue life of the as-fabricated scaffolds when tested in compression in air and in PBS is shown in Fig. 4. Of the 6 samples tested under each condition, the number that survived the 10^6 cycles of testing is also indicated. In air, all 6 samples tested under a cyclic stress of 1−10 MPa survived, showing that the samples had a fatigue life greater than 10^6 cycles. As the cyclic stress amplitude was increased to 2−20 MPa and 3−30 MPa, 4 and 3 samples, respectively, survived the 10^6 cycles of testing. Although the mean fatigue life decreased with the increase in the stress amplitude, the difference was not significant.

Under a cyclic stress of 1−10 MPa, testing in PBS did not have a significant effect on the mean fatigue life when compared to the samples tested in air; 5 samples survived the 10^6 cycles of testing. However, testing under the higher cyclic stresses of 2−20 MPa and 3−30 MPa resulted in a significant decrease in the mean fatigue life. In PBS, the mean fatigue life was $10^{5.9}$, $10^{5.3}$, and $10^{4.2}$ cycles at the cyclic stresses of 1−10, 2−20 and 3−30 MPa, respectively. Together, the data indicated that for the cyclic stresses used, the mean fatigue life was independent of the stress when the samples were tested in air, whereas testing in PBS resulted in a significant reduction in the mean fatigue life with increasing stress.

3.2. Degradation of compressive strength in vitro and in vivo

The compressive strength and elastic modulus of the scaffolds after immersion in SBF in vitro or implantation in rat subcutaneous sites in vivo are shown in Fig. 5 as a function of immersion time or implantation time. The strength and modulus decreased

rapidly during the first 2 weeks but more slowly thereafter. This trend was independent of the in vitro or the in vivo environment, but the decrease in vivo was larger than that in vitro. The strength decreased from the as-fabricated value of 86 ± 9 MPa to 58 ± 5 MPa after 2 weeks in SBF and to 35 ± 4 MPa after the same time in vivo (Fig. 5a). After 12 weeks, the strength of the scaffolds immersed in SBF was 52 ± 10 MPa, whereas the strength of the scaffolds implanted in vivo was 16 ± 4 MPa. The elastic modulus of the scaffolds decreased from the as-fabricated value of 13 ± 2 GPa to 11 ± 1 GP after 2 weeks in SBF and to 6 ± 2 GPa after 2 weeks in vivo (Fig. 5b). The modulus of the scaffolds was 9 ± 2 GPa and 2 ± 1 GPa, respectively, after 12 weeks in SBF and in vivo.

Figure 6 shows the mechanical response of the scaffolds in compression after they were immersed in SBF or implanted in rat subcutaneous sites. (The curves were shifted arbitrarily along the x-axis to maintain clarity). After an initial transient, the scaffolds that were immersed in SBF showed a mechanical response typical of porous brittle materials; the stress increased almost linearly with the deformation, followed by failure (Fig. 6a). At failure, the scaffolds fractured into several pieces. In comparison, the scaffolds that were implanted in vivo showed a markedly different response: the brittle response changed to an elasto−plastic response after 2−4 weeks (Fig. 6b). Instead of fracturing into several pieces, the samples maintained their integrity after the mechanical test and became more deformable (Fig. 7). SEM backscattered electron images of the cross-section of the filaments showed that a surface layer of the glass was converted after immersion in vitro or implantation in vivo (Fig. 8a, b).

4. Discussion

The present study provided a comprehensive evaluation of the mechanical properties of strong porous bioactive glass (13-93) scaffolds with a well-controlled microstructure which were fabricated by robocasting. The mechanical properties of the as-fabricated scaffolds in the relevant loading modes of compression and flexure were evaluated, as well as the fatigue resistance and fracture toughness. Since the mechanical properties of bioactive glass change as the glass converts to HA, the mechanical response of the as-fabricated scaffolds in compression was compared with their response after immersion in SBF in vitro or after implantation in a rat subcutaneous model in vivo.

4.1. Mechanical properties of as-fabricated bioactive glass scaffolds

The as-fabricated scaffolds with a uniform grid-like microstructure (porosity = 47 ± 1%; filament diameter ~330 μm; pore width ~300 μm in the xy plane) had a compressive strength of 86 ± 9 MPa when tested in the z direction, a value that is close to the lower end of the values reported for human cortical bone (100−150 MPa). Modifications of this uniform microstructure, as described in previous work [21−23], have resulted in compressive strengths similar to human cortical bone. The elastic modulus of the as-fabricated scaffolds was 13 ± 2 GPa, which is in the range of values reported for cortical bone (10−20 GPa).

The Weibull modulus determined from the strength data for a large number of identical samples (typically 20−30 or more) is commonly used as a measure of the mechanical reliability or the probability of failure of brittle materials [30]. The mechanical response of brittle materials is sensitive to microstructural flaws such as pores and microcracks. Commonly, the strength and Weibull modulus are used to evaluate the probability of failure of brittle materials under a given stress. The Weibull modulus of dense or nearly dense ceramics and glasses has been reported in the range 5−20 [31]. Data for the Weibull modulus of bioactive glasses are limited. The Weibull modulus of porous bioceramic scaffolds, such as HA, beta-tricalcium phosphate (β-TCP), and calcium polyphosphate (CPP), has been reported in the range 3−10 for testing in compression [15, 32−34].

In this study, the Weibull modulus of the scaffolds in compression was 12. A possible reason for this high value is the uniform microstructure composed of dense glass filaments (relative density = 98 ± 1%) that are mainly free from large flaws. Figure 9 shows a comparison of the Weibull plots for the bioactive glass scaffolds in this study with plots taken from the literature for calcium phosphate scaffolds tested in compression [32, 33]. Under the same allowable failure probabilities, the bioactive glass scaffolds showed a compressive failure strength that is higher than that for the HA scaffolds, and far higher than that for the β-TCP scaffolds. Based on the strength and the Weibull modulus data, when subjected to a compressive stress of 50 MPa, the failure probability of the bioactive glass scaffolds, P_f, is equal to 10^{-3} (1 in 1000 scaffolds is predicted to

fail). The average stress on a hip stem is reported as 3−11 MPa [35, 36], well below the stress (50 MPa) for a failure probability of 10^{-3}.

The flexural modulus (13 ± 2 GPa) of the bioactive glass scaffolds measured in four-point bending was similar to the elastic modulus in compression. However, the flexural strength (11 ± 3 MPa) was only 10−15% of the compressive strength, and the Weibull modulus in flexure was half that in compression. The flexural strength of HA scaffolds with a porosity of 30−50% has been reported in the range 2−12 MPa [37]. In comparison, human cortical bone has a flexural strength comparable to its compressive strength (Table 1).

Finite element analysis of a cubic scaffold (2 mm in length) of HA or β-TCP with a grid-like microstructure (filament diameter = 220 μm; pore width = 80 μm in the deposition plane and 120 μm in the z direction) showed that under an applied compressive load of 250 N (stress = 63 MPa), the maximum tensile stress in the scaffold was ~ 80 MPa, generated at the middle of the unsupported filaments. In comparison, under an applied tensile load of 250 N (stress = 63 MPa), the maximum tensile stress was almost 4 times higher (~400 MPa), generated around the joint of two neighboring filaments [38]. The analysis indicated that when applying the same load on a grid-like microstructure, the maximum local tensile stress generated in the glass filaments was much higher in tensile loading than in compressive loading, and the distribution of the stress was very different between the two loading modes [38]. Since brittle materials such as glass typically fail in tension, and assuming that the scaffolds failed when the maximum local tensile stress exceeded the tensile strength of the glass filament, then the compressive strength is expected to be far superior to the tensile strength [38]. The flexural strength found in this study (11 ± 3 MPa) was much lower than the compressive strength (86 ± 9 MPa), which is in general agreement with the predictions of the finite element modeling.

One approach to enhance the flexural strength of the bioactive glass scaffolds is through microstructural modification. As described earlier, the scaffolds used in the present study had a uniform grid-like microstructure. Preliminary results of our ongoing research showed that the flexural strength of the bioactive glass scaffolds can be markedly improved by creating a “gradient” microstructure, similar to the topography of

human long bone. The “gradient” microstructure consisted of a more porous inner region with the same grid-like microstructure used in the present study (porosity ~50%), and an outer region with a grid-like microstructure of lower porosity (15−20%) in which the glass filaments had the same diameter but were more closely spaced.

The fracture toughness of the bioactive glass scaffolds used in the present study (0.48 ± 0.04 MPa $m^{1/2}$) is much lower than the value for human cortical bone (2−12 MPa $m^{1/2}$) [39], but in the range of values for dense glass (0.5−1 MPa·$m^{1/2}$), porous HA (0.3 MPa $m^{1/2}$) [40], and porous phosphate glass−ceramics (0.2−0.6 MPa·$m^{1/2}$) [41]. The toughness of weak bioactive glass or bioceramic scaffolds (compressive strength = 1−20 MPa) can be improved by coating or infiltrating the porous scaffold with a biodegradable synthetic polymer [32, 42, 43]. However, a polymer coating might reduce the bioactivity of the scaffolds, particularly at early implantation times when the coating limits the interaction of cells and tissues with the bioactive glass surface.

Because long limb bones undergo cyclic loading, the fatigue resistance of scaffolds designed for bone substitution is relevant. The results of the present study provide for the first time, information on fatigue resistance of strong porous bioactive glass scaffolds. When the bioactive glass scaffolds were tested in air at room temperature, the fatigue life decreased as the maximum cyclic compressive stress was increased from 10 MPa to 30 MPa, but the decrease was not significant. However, in PBS at 37 °C, the mean fatigue life showed a significant decrease from $10^{5.9}$ cycles to $10^{4.2}$ cycles for the same increase in the stress amplitude. The observed trend for the effect of stress and aqueous environment on the fatigue of silicate 13-93 bioactive glass scaffolds is compatible with the stress corrosion crack growth mechanisms for bioactive and conventional silicate glasses [44] which is generally attributed to the stress corrosion of Si−O−Si bonds at the crack tip [45]. In normal walking, the compressive load on the human femur is estimated to be smaller than 4 times the body weight [46]. Assuming a uniform load distribution, a femoral bone cross-sectional area of ~4 cm^2 [47], and a body weight of 70 kg, the stress on an implant in a segmental femoral defect is <2 MPa. The results of the present study therefore indicate that the bioactive glass scaffolds have excellent fatigue resistance at stresses far higher than normal physiological stresses.

4.2. Degradation of compressive strength in vitro and in vivo

The strength of bioactive glass scaffolds decreases with time as the glass converts to HA.Typically the conversion starts at the surface and moves inward [48]. To account for the strength degradation observed in the present study, the thickness of the converted layer of the bioactive glass filaments in the scaffolds was measured from SEM images of the cross-sections (Fig. 8). The thickness was measured as a function of immersion time in SBF or implantation time in rat subcutaneous sites. As described in previous studies [8, 9], the converted layer in silicate bioactive glass consists of an HA-like outer layer and a thin SiO_2-rich inner layer. As shown in Fig. 8, at 6 weeks, the converted layer in vivo (34 ± 6 μm) was much larger than that in vitro (~5 μm). The faster conversion in vivo has been explained in terms of the more dynamic environment and the presence of electrolytes, proteins and biological polymers in vivo [49, 50].

As shown in Fig. 10a, the thickness *y* of the converted layer in vivo increased with time *t*, and can be well fitted by a parabolic growth equation

$$y^2 = kt \tag{5}$$

where *k* is constant, equal to 12.7 μm^2/week. The basic load-bearing units of the porous scaffolds are the glass filaments of the grid-like microstructure. The newly formed HA-like layer and SiO_2-rich layer formed as a result of the glass conversion were porous and presumably much weaker than the glass phase [51]. Therefore the decrease in strength was expected to correlate with the reduction in the diameter (or cross-sectional area) of the unconverted glass filaments. Using this assumption, the compressive strength σ_t of the scaffold at time *t* has been described in terms of a power-law relation [52, 53]:

$$\sigma_t = \sigma_o \left(1 - \frac{y}{a}\right)^n \tag{6}$$

where σ_o = 86 MPa is the compressive strength of the as-fabricated scaffold, *a* is the radius of the glass filaments, *y* is the thickness of the converted layer, and *n* is a fitting parameter. Substituting for y from Equation (5), and the radius of the glass filaments (*a* = 165 μm) measured in the present study, Equation (6) gives

$$\sigma_t = \sigma_o \left(1 - \frac{12.7\sqrt{t}}{165}\right)^n \tag{7}$$

The best fit to the compressive strength data of the scaffolds implanted in vivo gave n = 6.1 (Fig. 10b). These results show that the degradation of the compressive strength of the bioactive glass scaffolds in vivo is predictable if the conversion rate of the bioactive glass to HA is known.

A challenge in the design of bioactive glass scaffolds for the regeneration of loaded bone is to match the degradation of scaffold mechanical properties with the rate of new bone infiltration. We are currently studying the rate of new bone formation in osseous defects implanted with these scaffolds with grid-like microstructure. By combining those bone infiltration data with the results for the mechanical degradation of the scaffolds obtained in this study, the overall mechanical strength of the implants could be predicted as a function of implantation time.

5. Conclusion

Scaffolds of 13-93 bioactive glass with a grid-like microstructure (porosity = 47%; pore width = 300 μm in the xy plane and 150 in the z direction) were fabricated by robocasting. When tested in the z direction, the scaffolds had a compressive strength of 86 ± 9 MPa, elastic modulus of 13 ± 2 GPa, and a Weibull modulus of 12. In flexural loading (load applied in the z direction), the strength, elastic modulus, and Weibull modulus were 11 ± 3 MPa, 13 ± 2 GPa, and 6, respectively. When tested in compression in air at room temperature or in phosphate-buffered saline at 37 °C, the as-fabricated scaffolds had a mean fatigue life of ~10^6 cycles under cyclic stresses of 1−10 MPa or 2−20 MPa. When compared to similar scaffolds immersed in a simulated body fluid (SBF) in vitro, scaffolds implanted in rat subcutaneous sites in vivo showed a more rapid degradation in compressive strength as a result of faster conversion to HA in vivo. Whereas the scaffolds showed a brittle mechanical response after immersion for up to 12 weeks in SBF, the response changed from brittle to elasto−plastic within 2−4 weeks of implantation in rat subcutaneous sites. The degradation of the compressive strength of the scaffolds as a function of time in vivo can be predicted from the conversion of the bioactive glass to hydroxyapatite. In addition to providing critically needed data for designing bioactive glass scaffolds, the results are promising for the application of these strong porous scaffolds in loaded bone repair.

Acknowledgement

This work was supported by the National Institutes of Health, National Institute of Arthritis, Musculoskeletal and Skin Diseases (NIAMS), Grant # 1R15AR056119-01, and by the U.S. Army Medical Research Acquisition Activity, under Contract No. W81XWH-10-1-0799. The authors thank Mo-Sci Corp., Rolla, MO, USA, for the bioactive glass used in this work, and Dr. J. Watts for assistance with designing a fixture for flexural mechanical testing.

References

[1] Giannoudis PV, Dinopoulos H, Tsiridis E. Bone substitutes: an update. Injury 2005;36S;S20−37.

[2] Laurencin C, Khan Y, El-Amin SF. Bone graft substitutes. Expert Rev Med Devices 2006;3:49−57.

[3] Griffith LG. Polymeric biomaterials. Acta Mater 2000;48:263−77.

[4] Agrawal CM, Ray RB. Biodegradable polymer scaffolds for musculoskeletal tissue engineering. J Biomed Mater Res 2001;55:141−50.

[5] Goldstein SA, Patil PV, Moalli MR. Perspectives on tissue engineering of bone. Clin Orthop Rel Res 1999;357:S419−23.

[6] Kneser U, Schaefer DJ, Munder B, Klemt C, Andree C, Stark GB. Tissue engineering of bone. Minim Invasiv Ther 2002;11:107−16.

[7] Hench LL. Bioceramics. J Am Ceram Soc 1998;81:1705−28.

[8] Hench LL. The story of Bioglass®. J Mater Sci Mater Med 2006;17:967−78.

[9] Rahaman MN, Day DE, Bal BS, Fu Q, Jung SB, Bonewald LF, Tomsia AP. Bioactive glass in tissue engineering. Acta Biomater 2011;7:2355−73.

[10] Wheeler DL, Stokes KE, Park HM, Hollinger JO. Evaluation of particulate Bioglass in a rabbit radius ostectomy model. J Biomed Mater Res 1998;35:249−54.

[11] Wheeler DL, Stokes KE, Hoellrich RG, Chamberland DL, McLoughlin SW. Effect of bioactive glass particle size on osseous regeneration of cancellous defects. J Biomed Mater Res 1998;41:527−33.

[12] Xynos ID, Edgar AJ, Buttery LD, Hench LL, Polak JM. Ionic products of bioactive glass dissolution increase proliferation of human osteoblasts and induce insulin-like growth factor II mRNA expression and protein synthesis. Biochem Biophys Res Commun 2000;276:461−5.

[13] Xynos ID, Edgar AJ, Buttery LD, Hench LL, Polak JM. Gene-expression profiling of human osteoblasts following treatment with ionic products of Bioglass 45S5 dissolution. J Biomed Mater Res 2001;55:151−7.

[14] Hoppe A, Guldal NS, Boccaccini AR. A review of the biological response to ionic dissolution products from bioactive glasses and glass-ceramics. Biomaterials 2011;32:2757−74.

[15] Fu Q, Saiz E, Rahaman MN, Tomsia AP. Bioactive glass scaffolds for bone tissue engineering: state of the art and future perspectives. Mater Sci Eng C 2011;31:1245−56.

[16] Gerhardt LC, Boccaccini AR. Bioactive glass and glass-ceramic scaffolds for bone tissue engineering. Materials 2010;3:3867−910.

[17] Baino F, Vitale-Brovarone C. Three-dimensional glass-derived scaffolds for bone tissue engineering: current trends and forecasts for the future. J Biomed Mater Res A 2011; 97:514−35.

[18] Jones JR. Review of bioactive glass: from Hench to hybrids. Acta Biomater 2013;9:4457−86.

[19] Baino F, Vern é E, Vitale-Brovarone C. 3-D high strength glass-ceramic scaffolds containing fluoroapatite for load-bearing bone portions replacement. Mater Sci Eng C 2009;29:2055−62.

[20] Liu X, Rahaman MN, Fu Q, Tomsia AP. Porous and strong bioactive glass (13-93) scaffolds prepared by unidirectional freezing of camphene-based suspensions. Acta Biomater 2012;8:415-423.

[21] Doiphode ND, Huang TS, Leu MC, Rahaman MN, Day DE. Freeze extrusion fabrication of 13-93 bioactive glass scaffolds for bone repair. J Mater Sci Mater Med 2011;22:515−23.

[22] Huang TS, Doiphode ND, Rahaman MN, Leu MC, Bal BS, Day DE. Porous and strong bioactive glass (13-93) scaffolds prepared by freeze extrusion fabrication. Mater Sci Eng C 2011;31:1482−9.

[23] Deliormanli A, Rahaman MN. Direct-write assembly of silicate and borate bioactive glass scaffolds for bone repair. J Eur Ceram Soc 2012;32:3637−46.

[24] Fu Q, Saiz E, Tomsia AP. Bioinspired strong and highly porous glass scaffolds. Adv Funct Mater 2011;21:1058−63.

[25] Fu Q, Saiz E, Tomsia AP. Direct ink writing of highly porous and strong glass scaffolds for load-bearing bone defects repair and regeneration. Acta Biomater 2011;7:3547−54.

[26] Quintana-Alonso I, Mai SP, Fleck NA, Oakes DCH, Twigg MV. The fracture toughness of a cordierite square lattice. Acta Mater 2010;58:201−7.

[27] Tara H, Paris PC, Irwin GR. The stress analysis of cracks handbook, 2nd edition. St. Louis, MO: Productions, Inc.; 1985.

[28] Schmalzried TP, Szuszczewicz ES, Northfield MR, Akizuki KH, Frankel RE, Belcher G, Amstutz HC. Quantitative assessment of walking activity after total hip or knee replacement. J Bone Joint Surg Am 1998;80:54−9.

[29] Lewandrowski KU, Wise DL, Yaszemski MJ, Gresser JD, Trantolo DJ, Altobelli DE, Tissue engineering and biodegradable equivalents, scientific and clinical applications. New York, NY: Marcel Dekker Inc.; 2002.

[30] Wachtman JB, Cannon WR, Matthewson MJ. Mechanical properties of ceramics, 2nd edition. New York, NY: Wiley; 2009.

[31] Carter C, Norton M. Ceramic materials. New York, NY: Springer; 2007.

[32] Martínez-Vázquez FJ, Perera FH, Miranda P, Pajares A, Guiberteau F. Improving the compressive strength of bioceramic robocast scaffolds by polymer infiltration. Acta Biomater 2010;6:4361−8.

[33] Miranda P, Pajares A, Saiz E, Tomsia AP, Guiberteau F. Mechanical properties of calcium phosphate scaffolds fabricated by robocasting. J Biomed Mater Res A 2008;85:218−27.

[34] Shanjani Y, Hu Y, Pilliar RM, Toyserkani E. Mechanical characteristics of solid-freeform-fabricated porous calcium polyphosphate structures with oriented stacked layers. Acta Biomater 2011;7:1788−96.

[35] Verdonschot N, Huiskes R. Creep behavior of hand-mixed simplex P bone cement under cyclic tensile loading. J Appl Biomater 1994;5:235−43.

[36] Crowninshield RD, Brand RA, Johnston RC, Milroy JC. The effect of femoral stem cross-sectional geometry on cement stresses in total hip reconstruction. Clin Orthop Relat Res 1980:71-7.

[37] Wagoner Johnson AJ, Herschler BA. A review of the mechanical behavior of CaP and CaP/polymer composites for applications in bone replacement and repair. Acta Biomater 2011;7:16−30.

[38] Miranda P, Pajares A, Guiberteau F. Finite element modeling as a tool for predicting the fracture behavior of robocast scaffolds. Acta Biomater 2008; 4:1715−24.

[39] Bonfield W. Elasticity and viscoelasticity of cortical bone. In: Hastings GW, Ducheyne P, editors, Natural and living biomaterials. Boca Raton, FL: CRC Press, 1985.

[40] Zhang Y, Xu H, Takagi S, Chow L. In-situ hardening hydroxyapatite-based scaffold for bone repair. J Mater Sci Mater Med 2006;17:437−45.

[41] Pernot F, Etienne P, Boschet F, Datas L. Weibull parameters and the tensile strength of porous phosphate glass−ceramics. J Am Ceram Soc 1999;82:641−8.

[42] Chen QZ, Boccaccini AR. Poly(D,L-lactic acid) coated 45S5 Bioglass®-based scaffolds: Processing and characterization. J Biomed Mater Res A 2006;77:445−57.

[43] Peroglio M, Gremillard L, Gauthier C, Chazeau L, Verrier S, Alini M, Chevalier J. Mechanical properties and cytocompatibility of poly(e-caprolactone)-infiltrated biphasic calcium phosphate scaffolds with bimodal pore distribution. Acta Biomater 2010;6:4369–79.

[44] Bloyer DR, McNaney JM, Cannon RM, Saiz E, Tomsia AP, Ritchie RO. Stress–corrosion crack growth of Si–Na–K–Mg–Ca–P–O bioactive glasses in simulated human physiological environment. Biomaterials 2007;28:4901−11.

[45] Michalske TA, Freiman SW. A molecular mechanism for stress corrosion in vitreous silica. J Am Ceram Soc 1983;66:284−8.

[46] Duda GN, Schneider E, Chao EYS. Internal forces and moments in the femur during walking. J Biomech 1997;30:933−41.

[47] Rittweger J, Beller G, Ehrig J, Jung C, Koch U, Ramolla J, Schmidt F, Newitt D, Majumdar S, Schiessl H, Felsenberg D. Bone-muscle strength indices for the human lower leg. Bone 2000;27:319−26.

[48] Renghini C, Komlev V, Fiori F, Verne E, Baino F, Vitale-Brovarone C. Micro-CT studies on 3-D bioactive glass-ceramic scaffolds for bone regeneration. Acta Biomater 2009;5:1328−37.

[49] Fu Q, Rahaman MN, Day DE. Accelerated conversion of silicate bioactive glass (13-93) to hydroxyapatite in aqueous phosphate solution containing polyanions. J Am Ceram Soc 2009;92:2870−6.

[50] Radin S, Ducheyne P, Falaize S, Hammond A. In vitro transformation of bioactive glass granules into Ca-P shells. J Biomed Mater Res 2000;49:264−72.

[51] Renghini C, Giuliani A, Mazzoni S, Brun F, Larsson E, Baino F, Vitale-Brovarone C. Microstructural characterization and in vitro bioactivity of porous glass-ceramic scaffolds for bone regeneration by synchrotron radiation X-ray microtomography. J Eur Ceram Soc 2012; DOI:10.1016/j.jeurceramsoc.2012.10.016

[52] Fu Q, Rahaman MN, Fu H, Liu X. Silicate, borosilicate, and borate bioactive glass scaffolds with controllable degradation rate for bone tissue engineering applications. I. Preparation and in vitro degradation. J Biomed Mater Res A 2010;95:164−71.

[53] Liu X, Huang W, Fu H, Yao A, Wang D, Pan H, Lu WW, Jiang X, Zhang X. Bioactive borosilicate glass scaffolds: in vitro degradation and bioactivity behaviors. J Mater Sci Mater Med 2009;20:1237−43.

Table 1 Mechanical properties of as-fabricated 13-93 bioactive glass scaffolds with a grid-like microstructure in compression and flexure (four-point bending). (The load was applied in the z direction, perpendicular to the plane of deposition (xy plane) of the scaffolds).

	Compression			Flexure			
	Strength (MPa)	Elastic modulus (GPa)	Weibull modulus	Strength (MPa)	Flexural modulus (GPa)	Weibull modulus	Fracture toughness (MPa $m^{1/2}$)
Scaffold	86 ± 9	13 ± 2	12	11 ± 3	13 ± 2	6	0.48 ± 0.04
Cortical bone [15, 29]	100−150	10−20		135−193	9−16		2−12
Trabecular bone [15]	2−12	0.1−5		10−20			0.1−0.8

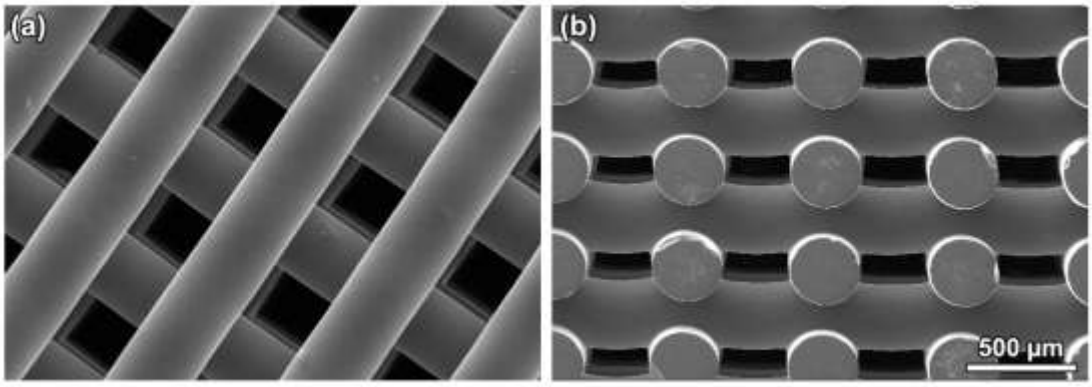

Fig.1. SEM images of silicate 13-93 bioactive glass scaffolds prepared by robotic deposition (robocasting): (a) plane of deposition (xy plane); (b) perpendicular to the deposition plane (z direction).

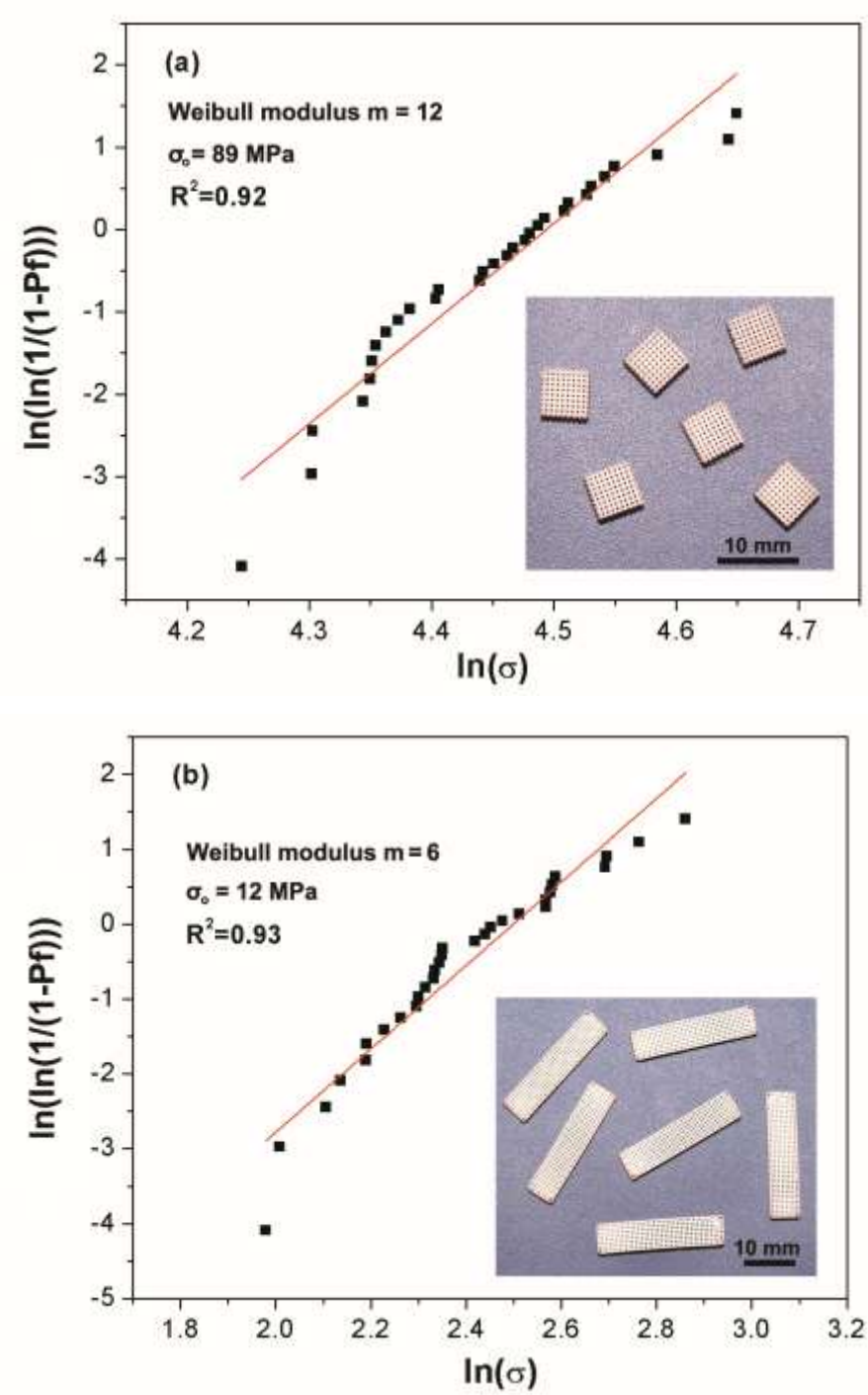

Fig. 2. Weibull plots of (a) compressive strength and (b) flexural strength for silicate 13-93 bioactive glass scaffolds with a grid-like microstructure. (Inset: optical images showing the shape of the samples used in each test).

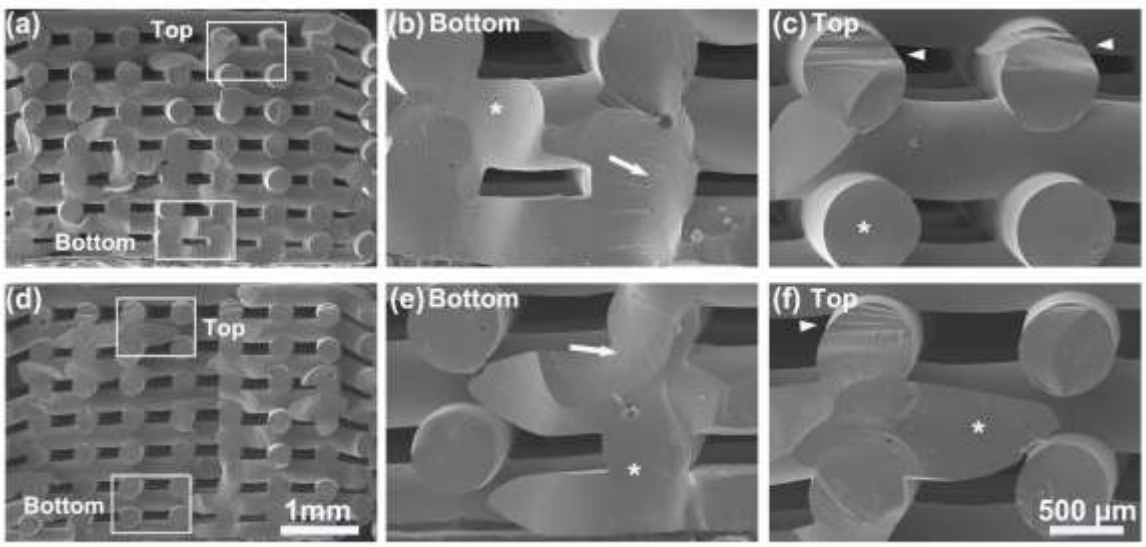

Fig. 3. SEM of images of the fractured surfaces of bioactive glass scaffolds tested in flexure (four-point bending): (a−c) scaffold with a flexural strength of 15 MPa; and (d−f) scaffold with flexural strength of 8 MPa. Higher magnification images of the fractured surface near the bottom surface of the sample (in tension during the test) and near the top surface (compression) are shown in (b, e) and (c, f), respectively. Arrows point to the hackle lines; stars show the mirror area and arrowheads point to the cantilever curls.

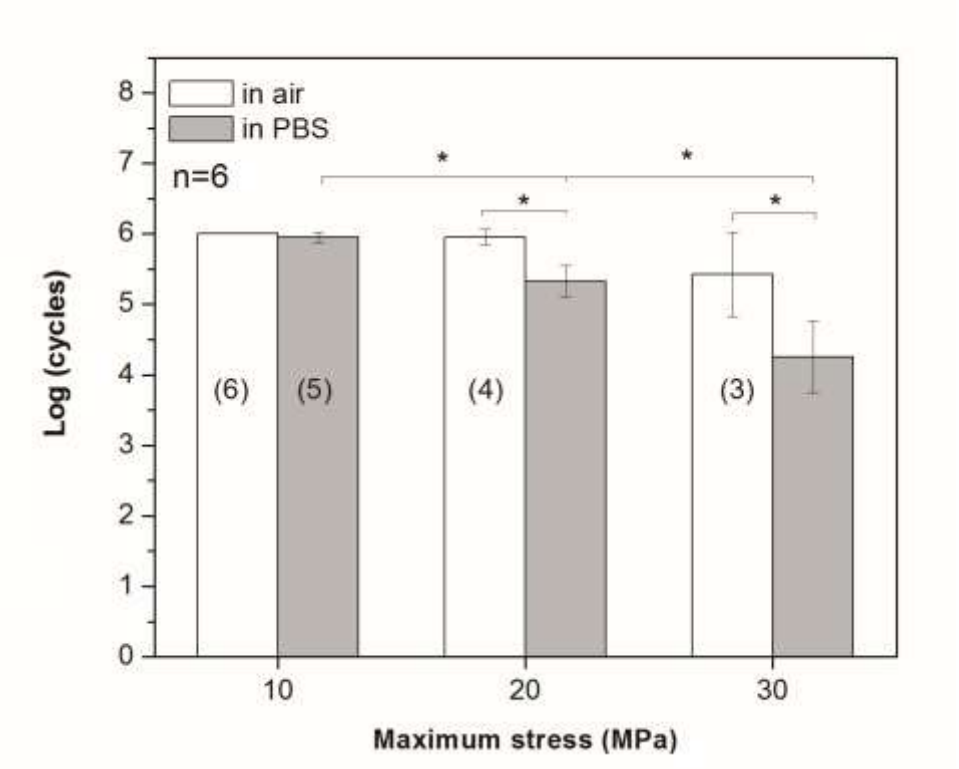

Fig. 4. Fatigue life (average number of cycles to failure) of 13-93 bioactive glass scaffolds tested in air and in phosphate-buffered saline (PBS) under cyclic compressive stresses. The stresses shown are the maximum applied stress in the cyclic loading. (*significant difference between groups, $p < 0.05$). The number in the bar indicates the number of samples that survived 10^6 cycles when the test was terminated.

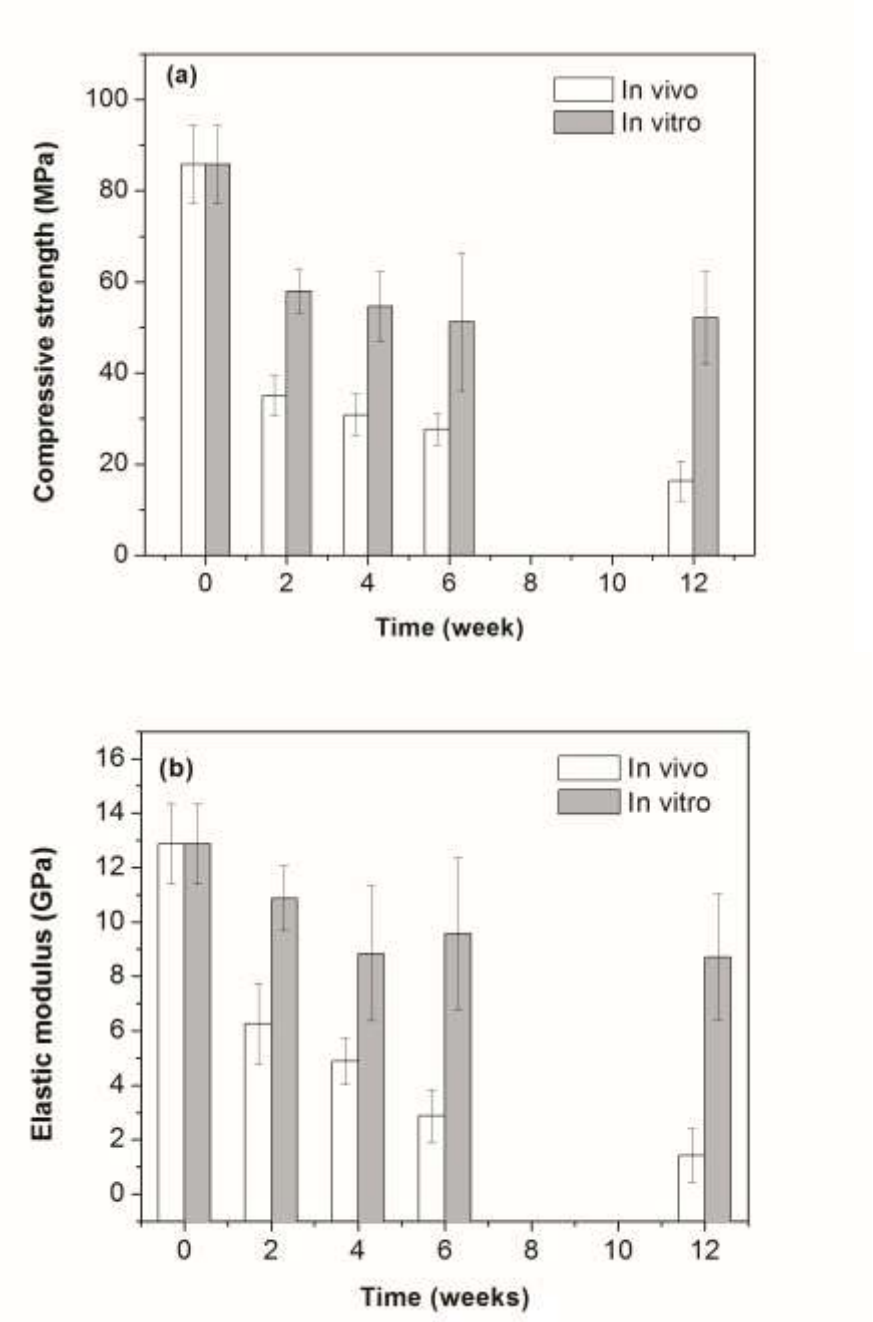

Fig. 5. (a) Compressive strength and (b) elastic modulus as a function of time for 13-93 bioactive glass scaffolds after immersion of the scaffolds in simulated body fluid (SBF) in vitro and after implantation in rat subcutaneous sites in vivo for the times shown.

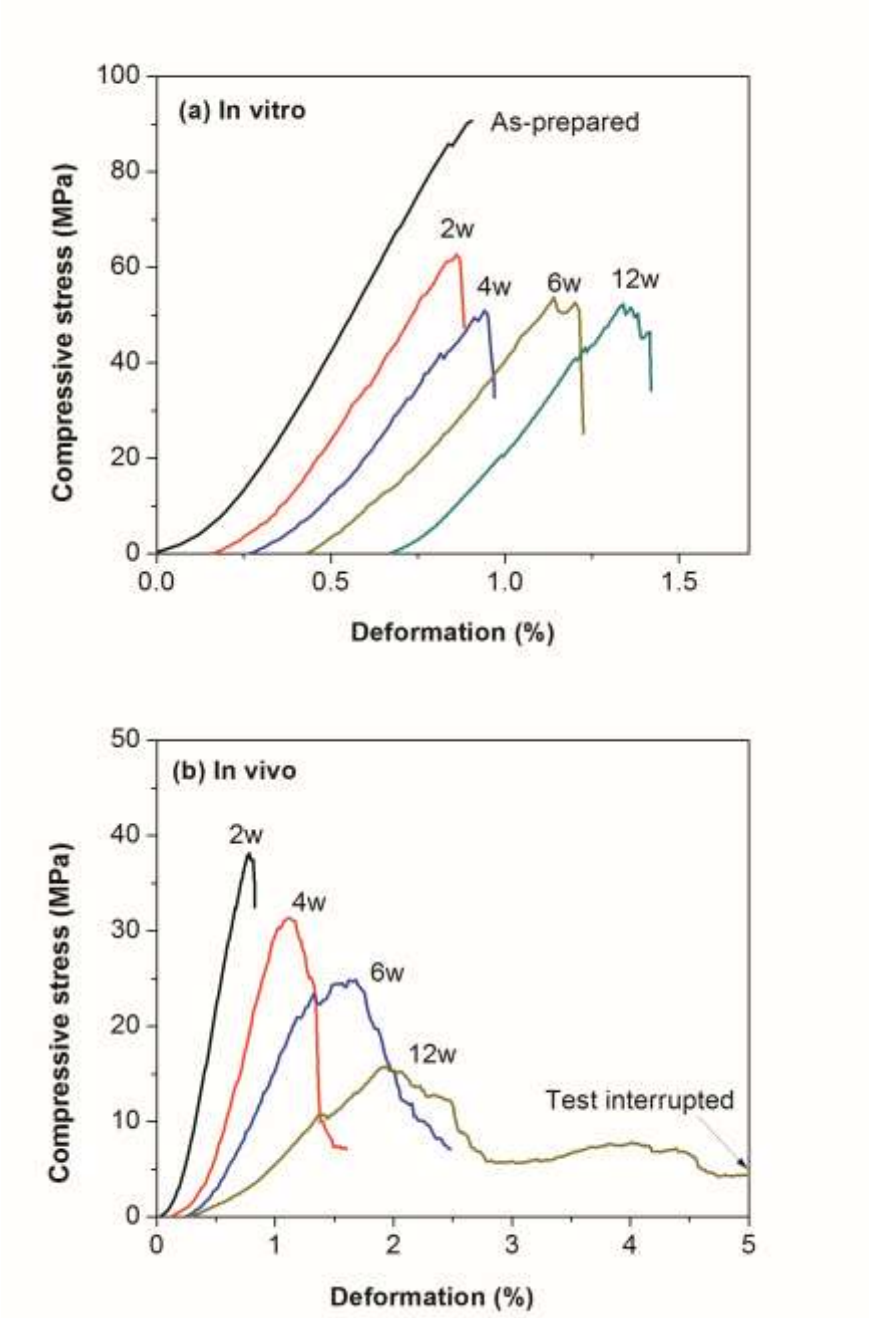

Fig. 6. Mechanical response (compressive stress vs. deformation) of 13-93 bioactive glass scaffolds after immersion of the scaffolds in simulated body fluid (SBF) in vitro and after implantation in rat subcutaneous sites in vivo for the times shown.

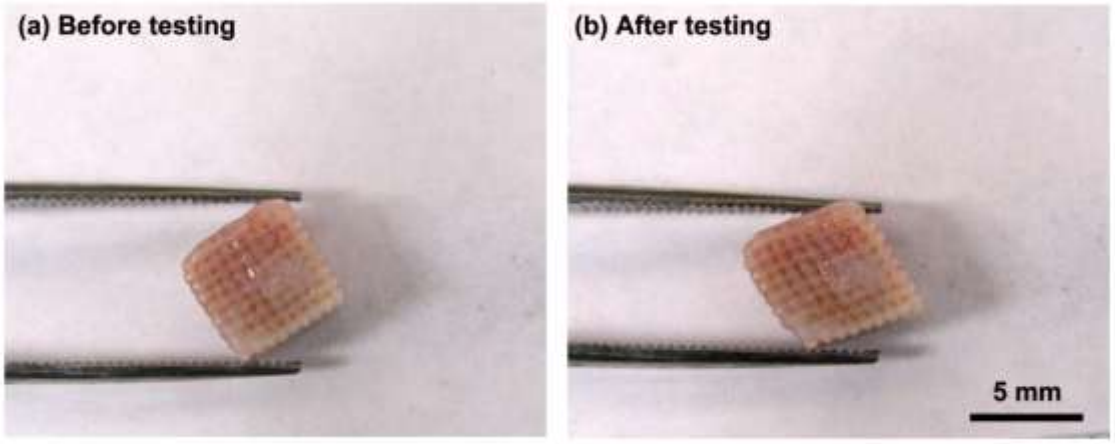

Fig. 7. Optical micrograph showing 13-93 bioactive glass scaffolds after implantation in rat subcutaneous sites for 4 weeks: (a) prior to mechanical testing; (b) after mechanical testing in compression. The scaffolds became highly deformable after the mechanical testing.

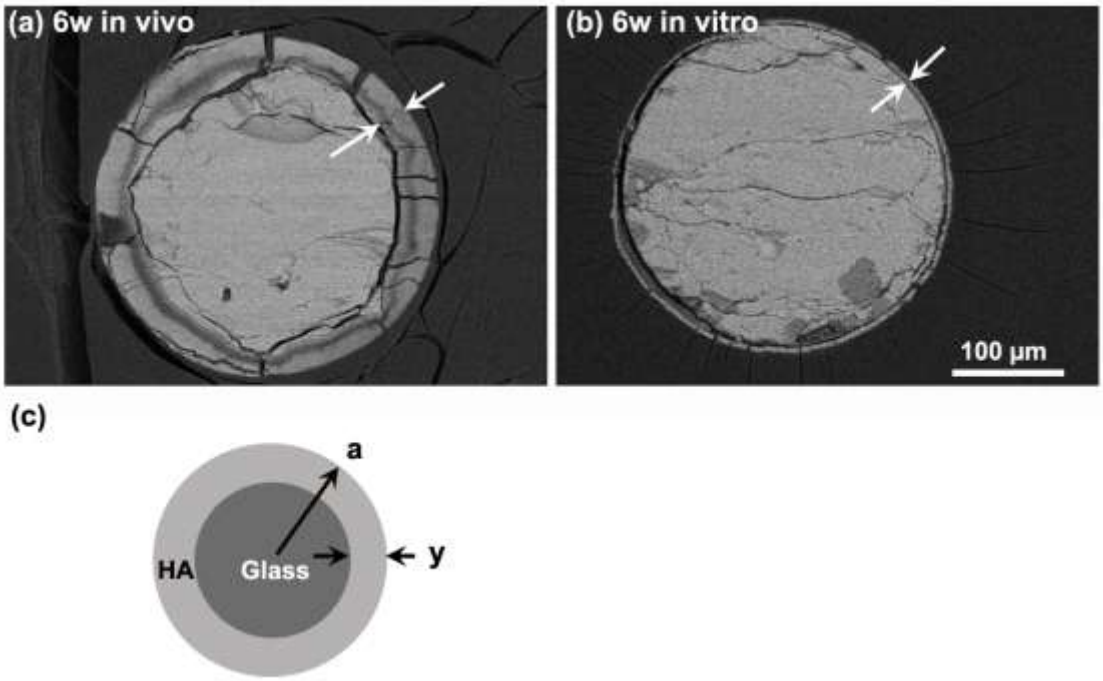

Fig. 8. SEM backscattered electron images showed the cross-sections of the glass filament in 13-93 bioactive glass scaffolds after (a) implantation for 6 weeks in vivo and (b) after immersion for the same time in SBF in vitro. (c) Sketch showing the parameters of the converted glass filament: a = initial radius of the glass filament; y = thickness of the converted layer at time t.

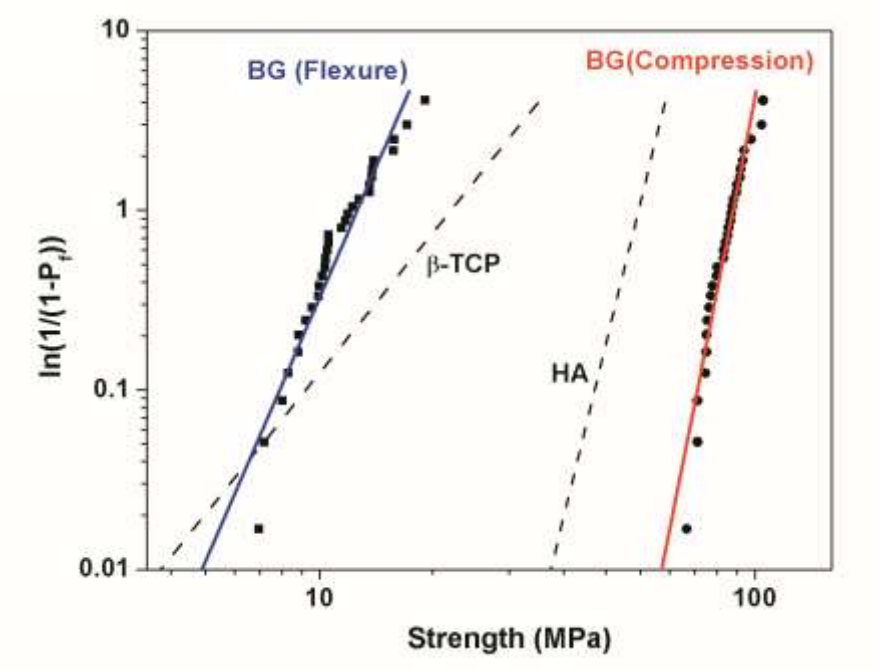

Fig. 9. Weibull plots of the compressive and flexural strength data from the present study for bioactive 13-93 glass (BG). For comparison, Weibull plots of the compressive strength data from the literature [32, 33] for beta-tricalcium phosphate (β -TCP) and hydroxyapatite (HA) scaffolds fabricated by robocasting are also shown for comparison (dashed lines).

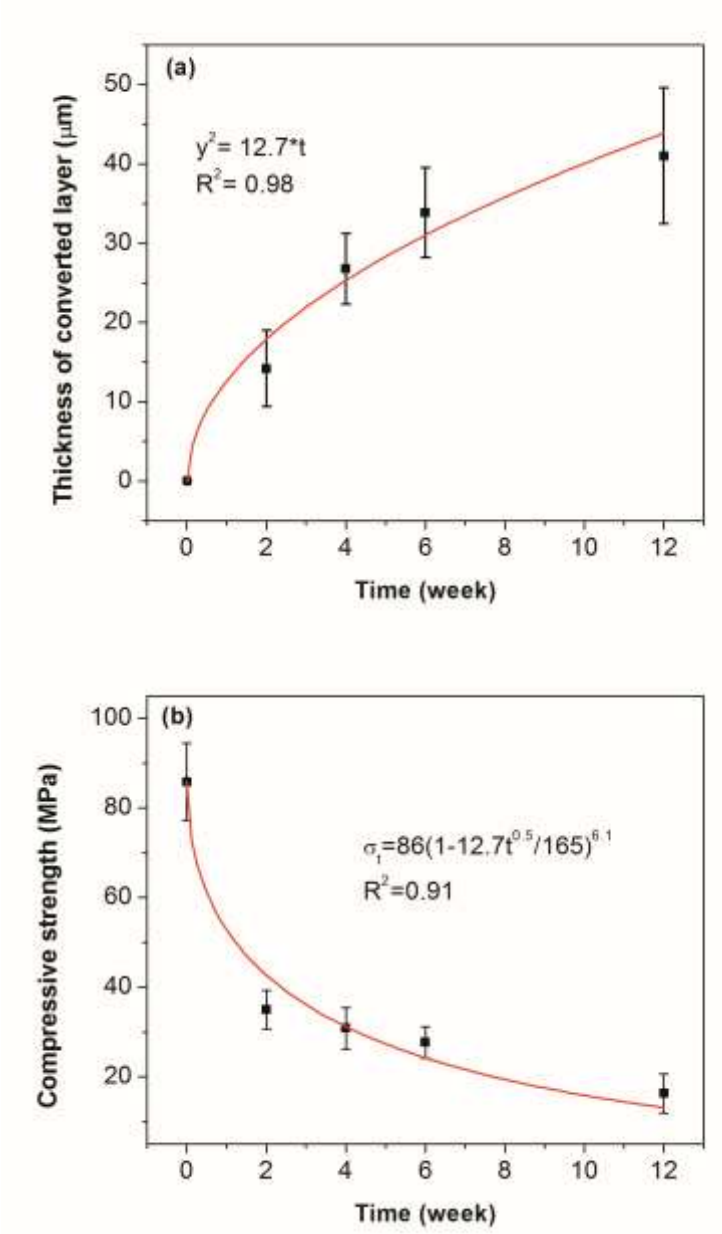

Fig. 10. (a) Data for the thickness of the converted layer of the bioactive glass filaments as a function of implantation time in rat subcutaneous sites in vivo; the data can be fitted by a parabolic curve; (b) data for the compressive strength of the bioactive glass scaffolds as a function of implantation time in vivo; the curve shows the predicted compressive strength based on the conversion data in (a).

V. ENHANCED BONE REGENERATION IN RAT CALVARIAL DEFECTS IMPLANTED WITH SURFACE-MODIFIED AND BMP-LOADED BIOACTIVE GLASS (13-93) SCAFFOLDS

Xin Liu[1], Mohamed N. Rahaman[1], Yongxing Liu[1], B. Sonny Bal[2], Lynda F. Bonewald[3]

[1]Department of Materials Science and Engineering and Center for Bone and Tissue Repair and Regeneration, Missouri University of Science and Technology, Rolla, MO 65409, USA

[2]Department of Orthopedic Surgery, University of Missouri−Columbia, Columbia, MO 65212, USA

[3]Department of Oral and Craniofacial Sciences, School of Dentistry, University of Missouri–Kansas City, Kansas City, MO 64108, USA

ABSTRACT

The repair of large bone defects, such as segmental defects in the long bones of the limbs, is a challenging clinical problem. Our recent work has shown the ability to create porous scaffolds of silicate 13-93 bioactive glass by robocasting which have compressive strengths comparable to human cortical bone. The objective of this study was to evaluate the capacity of those strong porous scaffolds with a grid-like microstructure (porosity = 50%; filament width = 330 μm; pore width = 300 μm) to regenerate bone in a rat calvarial defect model. Six weeks postimplantation, the amount of new bone formed within the implants was evaluated using histomorphometric analysis. The amount of new bone formed in implants composed of the as-fabricated scaffolds was 32% of the available pore space (area). Pretreating the as-fabricated scaffolds in an aqueous phosphate solution for 1, 3, and 6 days, to convert a surface layer to hydroxyapatite prior to implantation, enhanced new bone formation to 46%, 57%, and 45%, respectively. New bone formation in scaffolds pretreated for 1, 3, and 6 days and loaded with bone morphogenetic protein-2 (BMP-2) (1 μg/defect) was 65%, 61%, and 64%, respectively. The results show that converting a surface layer of the glass to hydroxyapatite or loading the surface-treated scaffolds with BMP-2 can significantly improve the capacity of 13-93 bioactive glass scaffolds to regenerate bone in an osseous

defect. Based on their mechanical properties evaluated previously and their capacity to regenerate bone found in this study, these 13-93 bioactive glass scaffolds, pretreated or loaded with BMP-2, are promising in structural bone repair.

1. Introduction

The repair of large bone defects is a challenging clinical problem [1]. While contained bone defects are repairable with commercially-available, osteoconductive and osteoinductive filler materials [2,3], there is no ideal biological solution to reconstitute structural bone loss, such as segmental defects in the long bones of the limbs. Available treatments such as bone allografts, autografts, porous metals, and bone cement have limitations related to costs, availability, longevity, donor site morbidity, and uncertain healing to host bone. Consequently, there is a great need for porous biocompatible implants that can replicate the structure and function of bone and have the requisite mechanical properties for reliable long-term cyclical loading during weight bearing.

As described previously [4−6], bioactive glasses have several attractive properties as scaffold materials for bone repair, such as their biocompatibility, ability to convert in vivo to hydroxyapatite (the mineral constituent of bone), and ability to bond strongly to hard tissue. Some bioactive glasses, such as the silicate glass designated 45S5, also have the ability to bond to soft tissue [5, 6]. Most previous studies have targeted bioactive glass scaffolds with relatively low strength three-dimensional (3D) architectures, such as strengths in the range of human trabecular bone (2−12 MPa) [7]. Recent studies have shown that silicate bioactive glass scaffolds (13-93 and 6P53B) created by solid freeform fabrication techniques such as freeze extrusion fabrication [8] and robocasting [9, 10] have compressive strengths (~140 MPa) comparable to human cortical bone (100−150 MPa) [7].

Our recent work showed that strong porous bioactive glass (13-93) scaffolds created using robocasting had excellent mechanical reliability (Weibull modulus = 12) and promising fatigue resistance under cyclic stresses far greater than normal physiological stresses [11], but the capacity of those strong porous bioactive glass (13-93) scaffolds to regenerate bone has not yet been studied. Our recent studies also showed that the elastic (brittle) mechanical response of the 13-93 bioactive glass scaffolds in vitro

changed to an "elasto−plastic" response after implantation for longer than 2−4 weeks in vivo, as a result of soft and hard tissue growth into the pores of the scaffolds [11, 12]. However, concerns still remain about the low fracture toughness, flexural strength and torsional strength of the as-fabricated bioactive glass scaffolds.

In addition to material composition and microstructure [13], scaffold healing to bone in vivo can be markedly affected by other variables, such as surface composition and structure, the release of osteoinductive growth factors, and the presence (or absence) of living cells. Interconnected pores of size ~100 μm are recognized as the minimum requirement for supporting tissue ingrowth [14], but pores of size ~300 μm or larger may be required for enhanced bone ingrowth and capillary formation [15]. Surface modification of macroporous bioactive glass scaffolds has targeted the creation of fine pores (nanometers to a few microns in size) to modify the surface roughness and increase the surface area of the scaffolds [16−18]. Conversion of a surface layer to HA, by reaction in an aqueous phosphate solution, has been shown to improve the capacity of borate and silicate bioactive glass to support cell proliferation and differentiation in vitro [19]. Treatment of B_2O_3-doped silicate bioactive glass scaffolds with a fibrous microstructure in simulated body fluid (SBF) to create a rough surface layer of carbonated HA was shown to improve the capacity of the scaffolds to support cell proliferation in vitro and to enhance bone formation in vivo [20].

Osteoinductive growth factors such as bone morphogenetic protein-2 (BMP-2) and BMP-7 are well known to stimulate bone formation [21, 22]. However, the use of porous 3D bioactive glass scaffolds as delivery devices for growth factors has so far received little attention. In a recent study [23], the surfaces of three silicate bioactive glasses were functionalized by a silanization technique using 3-amino-propyl-triethoxysilane; then BMP-2 was immobilized on the glass surfaces. However, the release of the BMP-2 and the effect of the BMP-2 on bone regeneration in vivo were not studied.

Particles of 13-93 glass have a lower tendency to crystallize prior to appreciable sintering when compared to 45S5 glass [4]. Consequently, 13-93 glass particles can be more readily sintered into a dense and strong network. As described earlier, our recent work showed that strong porous 3D scaffolds of 13-93 glass, prepared with a grid-like microstructure using robocasting, had promising mechanical properties for loaded bone

repair. The bioactivity of 13-93 glass and the capacity of 13-93 glass scaffolds with a "trabecular" and an "oriented" microstructure to support bone ingrowth in vivo were shown in our previous studies [12, 24].

The objective of the present study was to evaluate the capacity of those strong porous 13-93 bioactive glass scaffolds fabricated by robocasting to regenerate bone in an osseous defect model. The effects on bone regeneration of pretreating the scaffolds for various times in an aqueous phosphate solution, to convert the glass surface to hydroxyapatite (HA) prior to implantation, and loading the pretreated scaffolds with BMP-2 were studied. After implantation for 6 weeks in rat calvarial defects, new bone formation in the implants was evaluated using histomorphometric techniques and scanning electron microscopy.

2. Experiments

2.1. Preparation of bioactive glass (13-93) scaffolds

Scaffolds of 13-93 bioactive glass (composition $6Na_2O$, $12K_2O$, 5MgO, 20CaO, $53SiO_2$, $4P_2O_5$; wt %) with a grid-like microstructure were prepared using a robotic deposition (robocasting) method, as described in our previous work [11]. Briefly, a slurry was prepared by mixing 40 vol% glass particles (~1 μm) with a 20 wt % aqueous Pluronic® F-127 solution in a planetary centrifugal mixer (ARE-310, THINKY U.S.A. Inc, Laguna Hills, CA, USA). Then the slurry was loaded into a robotic deposition device (RoboCAD 3.0, 3-D Inks, Stillwater, OK) and extruded through a syringe (tip diameter = 410 μm) onto an Al_2O_3 substrate to form a 3D scaffold. The extruded filaments were deposited at right angles to the filaments in the adjacent layer, with a center-to-center spacing between the filaments of 910 μm in the plane of deposition. After forming, the scaffolds were dried for 24 h at room temperature, and heated for 2 h at 100 °C to remove any residual water. Then the scaffolds were heated slowly in flowing oxygen to 600 °C (heating rate = 0.5 °C/min, with isothermal holds for 2 h each at 150 °C, 200 °C, 250 °C and 300 °C) to burn out the polymer processing aids, and sintered in air for 1 h at 700 ^{o}C (heating rate = 5 ^{o}C/min) to densify the glass filaments. The as-fabricated constructs were sectioned and ground into thin discs (4.6 mm in diameter × 1.5 mm), washed twice with

deionized water and twice with ethanol, dried in air, and then sterilized by heating for 12 h at 250 °C.

2.2. Surface modification of scaffolds

Some of the as-fabricated scaffolds were modified prior to implantation by reacting them in an aqueous phosphate solution to convert a surface layer of the glass to an amorphous calcium phosphate (ACP) or hydroxyapatite (HA) material. In the surface modification process, the scaffolds were immersed for 1, 3, and 6 days in 0.25 M K_2HPO_4 solution at 60 ^oC and a starting pH = 12.0 (obtained by adding the requisite amount 2 M NaOH solution). The mass of the glass scaffolds to the volume of the K_2HPO_4 solution was kept constant at 1 g per 200 ml, and the system was stirred gently each day. These reaction conditions were based on our previous studies on the conversion of bioactive glasses to HA [25, 26] and the ability to enhance the dissolution rate of the silicate glass network at higher pH [27]. In general, the reaction conditions were selected to accelerate the conversion of 13-93 glass to HA because of the slow conversion of the glass in simulated body fluid (SBF) at the body temperature (~37 ^oC) [4, 24]. After each reaction time, the scaffolds were removed from the solution, washed twice with deionized water, and twice with anhydrous ethanol to displace residual water from the scaffolds. The scaffolds were removed from the ethanol, dried for at least 24 h at room temperature, and stored in desiccator.

2.3. Characterization of converted surface layer

The surface-treated scaffolds were sputter-coated with Au/Pd and examined in a scanning electron microscope, SEM (S-4700; Hitachi, Tokyo, Japan), using an accelerating voltage of 15 kV and a working distance of 8 mm. Some surface-treated scaffolds were also mounted in epoxy resin, sectioned, polished to expose the cross-sections of the glass filaments, and examined in the SEM (S-4700; Hitachi). The thickness of the converted surface layer was determined from more than 15 measurements in the SEM images using the ImageJ software (National Institutes of Health, USA), and expressed as a mean value ± standard deviation (SD).

The converted surface layer was removed by vigorously shaking the scaffolds and used in determining its surface area and phase composition. Surface area measurements were made using nitrogen gas adsorption (Nova 2000e; Quantachrome, Boynton Beach,

FL, USA). The volume of nitrogen adsorbed and desorbed at different gas pressures was measured and used to construct adsorption–desorption isotherms. Eleven points of the adsorption isotherm, which initially followed a linear trend implying monolayer formation of adsorbate, were fitted by the Brunauer–Emmett–Teller equation to determine the surface area.

The presence of crystalline phases in the converted surface layer was determined using X-ray diffraction (XRD) (D/mas 2550 v; Rigaku, The Woodlands, TX, USA). The material was ground into a powder and analyzed using Cu K_α radiation ($\lambda = 0.15406$ nm) at a scanning rate of 1.8 ^{o}/min in the 2θ range 10−80^o.

2.4. Loading the pretreated scaffolds with BMP-2

Some of the pretreated scaffolds were loaded with BMP-2 prior to implantation. In the process, a solution of BMP-2 (Shenandoah Biotechnology Inc., PA, USA) in citric acid was prepared by dissolving 10 μg of BMP-2 in 100 μl sterile citric acid (pH = 3.0). Then 10 μl of the BMP-2 solution was pipetted on to each bioactive glass scaffold (4.6 mm in diameter × 1.5 mm). The amount of BMP-2 loaded into the scaffolds was equivalent to 1 μg per bone defect (or per implant) in the animal model. The BMP-loaded scaffolds were kept for ~24 h in a refrigerator at 4 °C to dry them prior to implantation. For comparison, some of the as-fabricated scaffolds (no pretreatment in the phosphate solution) were also loaded with BMP-2 using the same procedure. The BMP-2 solution was totally incorporated within the pores of the scaffolds, and there was no visible evidence for any of the solution flowing out of the scaffolds.

2.5. Release profile of BMP-2 from the scaffolds in vitro

The release of BMP-2 from the scaffolds into a medium composed of equal volumes of fetal bovine serum (FBS) and phosphate-buffered saline (PBS) plus 1vol% penicillin was measured as a function of time in vitro. Each scaffold was immersed in 500 μl of the solution in a 2.0 ml microtube and kept at 37 ^{o}C in an incubator. Three replicates were used for each group at each time point. At selected times (1h, 8h, 1d, 3d, 7d, 14d), the solution was completely removed and replaced with fresh solution. The amount of BMP-2 released into the solution was measured using by an enzyme-linked immunosorbent assay (ELISA) kit (Pepro Tech, Rocky Hill, NJ, USA) according to the manufacturer's instructions.

2.6. Animals and surgical procedure

All animal experimental procedures were approved by the Animal Care and Use Committee, Missouri University of Science and Technology, in compliance with the NIH Guide for Care and Use of Laboratory Animals (1985). Seven groups of scaffolds, described in Table 1, were implanted in rat calvarial defects for 6 weeks. This implantation time was used because our previous studies had shown considerable bone regeneration in rat calvarial defects implanted with BMP-loaded hollow HA microspheres for the same time [28]. The implants were assigned randomly to the defects, but scaffolds with and without BMP-2 were not mixed in the same animal.

Thirty male Sprague Dawley rats (3 months old; weight = 350–400 g, Harlan Laboratories Inc., USA) were maintained in the animal facility for 2 weeks to become acclimated to diet, water and housing. The rats were anesthetized with a combination of ketamine (72 mg/kg) and xylazine (6 mg/kg) and maintained under anesthesia with isoflurane gas in oxygen. The surgical site was shaved, scrubbed with iodine and draped. Using sterile instruments and aseptic technique, a cranial skin incision was sharply made in an anterior to posterior direction along the midline. The subcutaneous tissue, musculature and periosteum were dissected and reflected to expose the calvarium. Bilateral full-thickness defects 4.6 mm in diameter were created in the central area of each parietal bone using a saline-cooled trephine drill. The dura mater was not disturbed. The sites were constantly irrigated with sterile PBS to prevent overheating of the bone margins and to remove the bone debris. The bilateral defects were randomly implanted with 5 or 10 implants per group. The periosteum and skin were repositioned and closed using wound clips. All animals were given a dose of ketoprofen (3 mg/kg) intramuscularly and ~200 μl penicillin subcutaneously post-surgery. The animals were monitored daily for condition of the surgical wound, food intake, activity and clinical signs of infection. After 6 weeks, the animals were sacrificed by CO_2 inhalation, and the calvarial defect sites with surrounding bone and soft tissue were harvested for subsequent evaluation.

2.7. Histologic processing

The calvarial samples, including the surgical sites with surrounding bone and tissue, were fixed in 10% buffered formaldehyde for 3 days, then transferred into 70%

ethyl alcohol, and cut in half. Half of each sample was for paraffin embedding and the other half for methyl methacrylate embedding. The samples for paraffin embedding were de-siliconized by immersion for 2 h in 10% hydrofluoric acid, decalcified in 14% ethylenediaminetetraacetic acid (EDTA) solution for 4 weeks, dehydrated in a series of graded ethanol, and embedded in paraffin using routine histological techniques. Then the specimens were sectioned to 5 μm and stained with hematoxylin and eosin (H&E). The undecalcified samples were dehydrated in ethanol and embedded in PMMA. Sections were affixed to acrylic slides and ground down to 40 μm using a surface grinder (EXAKT 400CS, Norderstedt, Germany), and stained using the von Kossa technique. Transmitted light images of the stained sections were taken with an Olympus BX 50 microscope connected with a CCD camera (DP70, Olympus, Japan).

2.8. Histomophometric analysis

Histomorphometric analysis was carried out using optical images of the stained sections and the ImageJ software. The percent new bone formed in the defects was evaluated from the H&E stained sections. The entire defect area was determined as the area between the two defect margins, including the entire glass scaffold and the tissue within. The available pore area within the scaffold was determined by subtracting the area of the bioactive glass scaffold from the total defect area. The newly formed bone, fibrous tissue, and bone marrow-like tissue within the defect area were then outlined and measured. The area of each tissue was expressed as a percentage of the total defect area as well as a percentage of the available pore area within the scaffold.

2.9. Scanning electron microscopy

Unstained sections of the implants in PMMA were coated with carbon and examined using a field-emission scanning electron microscope (SEM) (S-4700; Hitachi) operating in the backscattered electron (BSE) mode. The specimens were examined at an accelerating voltage of 15 kV and a working distance of 12 mm.

2.10. Statistical analysis

The data are presented as a mean ± SD. Analysis for differences in new bone, fibrous tissue, and bone marrow-like tissue between groups was performed using one-way ANOVA with Tukey's post hoc test [29]. Differences were considered significant for $p < 0.05$.

3. Results

3.1. Characteristics of bioactive glass scaffolds and converted surface layer

As fabricated, the scaffolds implanted in the rat calvarial defects had a grid-like microstructure (Fig. 1a), composed of almost fully dense bioactive glass filaments of diameter 330 ± 10 μm and pores of width 300 ± 10 μm in the plane of deposition (xy plane) and 150 ± 10 μm in the direction perpendicular to the deposition plane (z direction) (Fig. 1b). The porosity of the scaffolds, as measured using the Archimedes method, was 47 ± 1%.

After reaction of the scaffolds in the K_2HPO_4 solution, the smooth dense surface of the glass filaments became rough and porous (Fig. 2a), with a fine particulate morphology that was dependent on the reaction time. After reaction for 1 day, the converted surface layer consisted mainly of nearly spherical nanoparticles with some fine needle-like particles (Fig. 2b). With an increase in the reaction time to 3 days, the amount of needle-like particles increased (Fig. 2c), whereas after reaction for 6 days, the surface consisted predominantly of needle-like particles (Fig. 2d). The thickness of the converted layer on the surface of the glass was determined from the cross-section of the glass filaments in the scaffold (Fig. 2a inset). As the reaction time increased from 1 day to 6 days, the thickness of the converted layer increased from 2 μm to 13 μm, while the surface area increased from 19 m^2/g to 47 m^2/g (Table 2).

Figure 3 shows XRD patterns of the as-fabricated bioactive glass scaffold and the converted surface layer of the scaffolds after reaction times of 1, 3, and 6 days in the K_2HPO_4 solution. The pattern of the as-fabricated scaffold showed no measurable peaks; instead, it contained a broad band centered at ~30^o 2θ, typical of an amorphous glass. In comparison, the pattern of the converted surface layer on the scaffold reacted for 1 day showed small peaks that corresponded to those of a reference HA (JCPDS 09-0423); as the reaction time increased from 1 day to 6 days, the number and intensity (height) of the peaks increased.

The XRD pattern of the converted layer formed after the one-day reaction also showed a broad bump at ~22^o 2θ in the vicinity of the major peak for the cristobalite phase of silica. The height of the bump gradually weakened with increasing reaction time. A similar bump has been observed in the XRD pattern of silicate 45S5 and 13-93

bioactive glass, and it has been attributed to the polymerization of silanol groups during the early stage of the conversion process, leading to the formation of a silica gel phase [30]. Apparently after the initial formation of a silica-rich layer on the glass, an ACP layer was formed which continued to grow and crystallize to HA with increasing reaction time, as described in detail elsewhere [4−6, 31].

3.2. Release profile of BMP-2 in vitro

Figure 4a shows the amount of BMP-2 released from the scaffolds into the medium at each time interval. The amount of BMP-2 released from the as-fabricated scaffolds was small at all of the time intervals, and there was no significant difference among the values except for the three-day interval. The reason for the lower BMP-2 concentration at the three-day interval is currently unclear but it may be related to difficulties in measuring the low BMP-2 concentrations. The data in Fig. 4a were used to determine the cumulative amount of BMP-2 released into the medium as a function of time, which was expressed as a percent of the total amount of BMP-2 initially loaded into the scaffolds (Fig. 4b). The BMP-2 release profile from the pretreated scaffolds showed the same trend: a rapid burst release during day 1 was followed by a much slower release rate. However, at a given time, the amount of BMP-2 released into the medium increased with the duration of the pretreatment time (1−6 days) in the phosphate solution. In comparison, there was little release from the as-fabricated scaffolds (no surface treatment) that were loaded with BMP-2. After 14 days, the cumulative amount of BMP-2 released from the scaffolds that had been pretreated for 6 days (~30%) was significantly higher than the amount released from the scaffolds pretreated for 3 days (~10%) or for 1 day (~7%). The amount of BMP-2 released from the as-fabricated scaffolds after the fourteen-day period was only ~1%.

3.3. Assessment of bone regeneration and integration of the implanted scaffolds

H&E and von Kossa stained sections of implants composed of the as-fabricated bioactive glass scaffolds and the scaffolds pretreated in the K_2HPO_4 solution for 1 day, 3 days, and 6 days which were implanted for 6 weeks in rat calvarial defects are shown in Fig. 5. The von Kossa positive area (dark stain) within the defect showed the presence of mineralized bone as well as HA (or calcium phosphate material) resulting from the pretreatment of the scaffolds or conversion in vivo. Because of the limited amount of

hydroxyapatite formed in the pretreatment process and the slow conversion of the bioactive glass in vivo, the von Kossa positive area corresponded generally to the H&E stained areas.

All implants showed the formation of new bone into the edges (periphery) of the implants (adjacent to the old bone), indicating good integration of the implants with the surrounding bone. New bone formation was observed mainly within the pores of the implants, and the amount of new bone formed was dependent on the pretreatment in the aqueous phosphate solution. Implants composed of the as-fabricated scaffolds showed a limited amount of new bone within the pores of the implants, predominantly in the form of "islands" (Fig. 5a1−a3). In comparison, the implants composed of the pretreated scaffolds, particularly the scaffolds pretreated for 3 days, showed a better capacity to support new bone formation (Fig. 5b1−d3). Blood vessels were observed within all of the implanted scaffolds in the defects (Fig. 5a3−d3).

Figure 6 shows H&E and von Kossa stained sections of the implants composed of scaffolds that were pretreated for 1day, 3 days, and 6 days, loaded with BMP-2 (1 μg per defect), and implanted for 6 weeks in the rat calvarial defects. A considerable amount of new bone infiltrated the scaffolds and completely bridged the interface with old bone. When compared to the pretreated scaffolds described above (no BMP-2), these BMP-loaded implants showed a markedly larger amount of bone marrow-like tissue that was surrounded by new bone within the pore space of the implants (Fig.6a3−c3).

Since all the scaffolds had the same microstructure, the capacity of the scaffolds to regenerate bone was compared by normalizing the amount of new bone formed to the total pore space (area) of the scaffolds (Fig. 7, Table 3). The amount of new bone formed in the as-fabricated scaffolds after the six-week implantation was 32 ± 13%. In comparison, the percent new bone formed in the scaffolds pretreated in the K_2HPO_4 solution for 1 day, 3 days, and 6 days was 46 ± 10%, 57 ± 14%, and 45 ± 11%, respectively. The amount of new bone formed in the scaffolds pretreated for 3 days was significantly higher than that in the as-fabricated scaffolds ($p < 0.05$). The amount of new bone in formed in the scaffolds pretreated for 1 day, 3 days, and 6 days and loaded with BMP-2 was 65 ± 7%, 61 ± 8%, and 64 ±11%, respectively; these values were

significantly higher than the amount of new bone formed in the as-fabricated scaffolds and in the scaffolds pretreated for 1 and 6 days.

3.4. Assessment of bone marrow and fibrous tissue formation

The amount of bone marrow-like tissue formed in the implants composed of the pretreated scaffolds loaded with BMP-2 was significantly higher than that in the scaffolds without BMP-2 (as-fabricated or pretreated in the phosphate solution) (Fig. 8a), but the amount of fibrous (soft) tissue was significantly lower (Fig. 8b). An interesting observation is that while the amount of new bone formed in the scaffolds pretreated for 3 days (57%) was not significantly different from that in the BMP-loaded scaffolds (61−65%), the type of tissue in the remainder of the pore space was very different. The remaining pore space in the scaffolds pretreated for 3 days was filled mainly with fibrous tissue whereas the remaining pore space in the BMP-loaded scaffolds was filled mainly with bone marrow-like tissue.

3.5. SEM evaluation of implants

Figure 9 shows back-scattered SEM images of the rat calvarial defects implanted with the bioactive glass scaffolds at 6 weeks. The contrast in the gray-scale images is an indication of differences in the calcium content [12]. The unconverted glass, the ACP/HA layer resulting from the pretreatment in the K_2HPO_4 solution and/or from the conversion of the glass in vivo, and new bone, all with a high calcium content, had a light-gray color, while the silica-rich layer formed in the early stage of the conversion of the glass was dark-gray. Lacunae within the bone, fibrous tissue, and bone marrow-like tissue were almost black. The glass filaments of the scaffolds consisted of three regions after implantation: an unconverted glass core (light-gray), a silica-rich layer (dark-gray) on the unconverted glass, and an ACP/HA surface layer (light-gray). The cracks in the scaffolds and the delamination of the ACP/HA layer from the scaffolds presumably resulted from capillary drying stresses during the sample preparation for SEM examination.

New bone formed during the six-week implantation did not appear to bond to the as-fabricated scaffolds (Fig. 9a, b). Instead, the new bone formed islands within the pores of the scaffolds and there were large gaps between the newly formed bone and the ACP/HA surface of the scaffold. In comparison, new bone appeared to bond firmly to the surface of the pretreated scaffolds and the pretreated scaffolds loaded with BMP-2 (Fig.

9c−f). The firm bonding to the surface of the pretreated scaffolds and the BMP-loaded scaffolds was found for all three pretreatment times (1 day, 3 days, and 6 days), but the images for the scaffolds pretreated for 1 day and 6 days are not included for the sake of brevity. Because of differences in new bone formation among scaffolds within the same group, the section in Fig. 9c (pretreated scaffold without BMP-2) showed a larger amount of new bone when compared to the section in Fig. 9e (pretreated scaffold with BMP-2). However, when all the sections within each group were considered, there was no significant difference in new bone formation between the two groups (Fig. 7).

For the scaffolds pretreated for 3 days in the K_2HPO_4 solution prior to implantation (without or with BMP-2) (Fig. 9d, f), the thickness of the HA layer (~6 μm) after the six-week implantation was almost similar to the thickness (~5 μm) prior to implantation (Table 2). In comparison, the thickness of the HA layer formed on the as-fabricated scaffold during the six-week implantation was (~20 μm), indicating that the conversion of the as-fabricated scaffold in vivo was much faster than that for the pretreated scaffold.

4. Discussion

Silicate 13-93 bioactive glass scaffolds similar to those used in this study were previously shown to have promising mechanical properties for the repair of loaded bone [11]. This study showed that pretreatment of those bioactive glass scaffolds in an aqueous phosphate solution to form an ACP or HA surface layer, or loading the pretreated scaffolds with BMP-2 markedly enhanced the capacity of the scaffolds to regenerate bone in an osseous defect. When compared to bioactive glass scaffolds with a variety of composition and microstructure reported in the literature, these pretreated or BMP-loaded scaffolds also showed the capacity to support faster bone regeneration in the same osseous defect model.

4.1. Bone regeneration in the as-fabricated bioactive glass scaffolds

The amount of new bone formed in the as-fabricated bioactive glass (13-93) scaffolds used in this study, determined as a fraction of the available pore area, was 32 ± 13% after the six-week implantation in the rat calvarial defects. For the same glass composition and in vivo model, the amount of new bone formed in scaffolds with an

oriented microstructure (porosity = 50%; pore diameter = 100−150 μm) was 37 ± 8% at 12 weeks, while the amount of new bone formed in scaffolds with a trabecular microstructure (similar to dry human trabecular bone) (porosity = 80%; pore size = 100−500 μm) was 25 ± 12% at 12 weeks [12] (Table 4). Scaffolds with a fibrous microstructure, composed of thermally bonded short fibers (porosity = 50%; pore size = 50−500 μm), showed new bone formation equal to 8.5% of the total defect area at 12 weeks [32]. Since the porosity of the fibrous scaffolds was 50%, the amount of new bone estimated as a fraction of the pore area was ~17%. These results indicate that the grid-like microstructure of the scaffolds used in this study has a better capacity to support bone regeneration when compared to the oriented, trabecular, and fibrous microstructures. The amount of new bone formed at 6 weeks in vivo was approximately the same or greater than that in the oriented, trabecular, or fibrous microstructure at for 12 weeks.

The greater capacity of the grid-like microstructure to support bone infiltration may result from the uniform microstructure of interconnected pores with a favorable size. As described earlier, while interconnected pores of size ~100 μm are recognized as the minimum requirement for supporting tissue ingrowth [14], pores of size ~300 μm or larger may be required for enhanced bone ingrowth and capillary formation [15]. In the grid-like microstructure used in this study, the pores are all interconnected, have the same size (width = 300 μm), and are not constricted at their necks. In comparison, the columnar pores in the oriented scaffolds had a diameter of only 100−150 μm and the interconnectivity between adjacent pores was limited [12], while the necks between adjacent pores in the trabecular and fibrous microstructures are commonly constructed. The greater capacity of the grid-like microstructure to support bone regeneration appeared to result from the better interconnectivity and uniformity of its pores and a pre size that is considered to be favorable for bone ingrowth.

The path of new bone infiltration into the grid-like scaffolds was also different from that in silicate 13-93 and borate bioactive glass scaffolds with the oriented and fibrous microstructures implanted in the same in vivo model. New bone infiltrated the grid-like scaffolds mainly from the edge (adjacent to old bone), indicating that new bone formation was mainly osteoconductive in nature, but some “islands” of new bone were also observed within the interior pores of the scaffold (Fig. 5a2). In comparison, while

bone formation in the oriented and fibrous scaffolds was also mainly osteoconductive, new bone formed mainly on the dural side of the implant with little infiltration into the edge [12]. New bone infiltration into trabecular 13-93 bioactive glass scaffolds was found predominantly at the periphery of the defect. Differences in the path of the new bone infiltration into the scaffolds appear to be dependent on the size and interconnectivity of the pores. Larger pores with better pore interconnectivity, such as those in the grid-like microstructure used in this study, appear to support greater bone infiltration from the edge of the scaffold.

4.2. Bone regeneration in pretreated bioactive glass scaffolds

Although the grid-like microstructure created in this study showed a greater capacity to support new bone formation than the trabecular, oriented or fibrous microstructure, the as-fabricated state of the glass may not be the most ideal condition for optimum bone regeneration. As-fabricated, bioactive glass scaffolds prepared by sintering melt-derived glass particles often have a dense smooth surface (Fig. 1) which provides a low surface area for adsorption of proteins and limits the amount of proteins that can be loaded into the scaffolds by adsorption. The surface of silicate bioactive glass such as 13-93, hydrated in aqueous media, commonly has a high density of negatively-charged silanol ($Si{-}O^{-}$) groups which can form strong electrostatic interactions and hydrogen bonds with adsorbed proteins. Desorption of proteins from the glass surface can be difficult [33−35], and denaturing of the proteins can be significant [34, 36]. In the present study, these problems associated with the as-fabricated glass were overcome by converting a thin surface layer of the glass to ACP or HA in an aqueous phosphate solution. The ACP/HA surface layer, with a high-surface-area mesoporous structure, could better support the adsorption and delivery of proteins such as BMP-2 [28,37].

A remarkable finding of the present study was that when compared to the as-fabricated scaffolds, the surface-treated scaffolds significantly enhanced new bone formation without any additional osteogenic factors. New bone formation in the implanted scaffolds that had been pretreated for 3 days in the phosphate solution (57%) was approximately twice that in the as-fabricated scaffolds (32%), and the new bone almost completely bridged the defect within 6 weeks (Fig. 5). Apparently the

pretreatment conferred superior osteoconductivity or osteoinductive-like properties to the scaffold, but the mechanism is at present unclear.

It is known that an HA surface layer with a chemical and structural similarity to the surface layer of the pretreated scaffold can also form on the as-fabricated bioactive glass scaffold upon implantation in vivo. However, a major difference is that while the HA surface layer is present immediately upon implantation of the pretreated scaffold, it takes some time before the HA layer is formed on the as-fabricated scaffold [4−6]. Thin-film XRD showed the formation of an HA surface layer on 13-93 glass within 7 days in SBF [24]. While the conversion is faster in vivo [4], a time period of a few days might still be required for the formation of the HA layer on the as-fabricated scaffold. Consequently, the pretreated scaffold might be able to play an active role at the defect site, by interacting with cells, tissues, and biomolecules such as endogeneous BMP-2, immediately upon implantation whereas the as-fabricated scaffold might not. Important initial interactions might not occur at the defect site implanted with the as-fabricated scaffolds, and it is possible that the outcome might be less successful later when the HA layer is formed. A dependence of the healing outcome on the intervention treatment time has also been observed in other studies [38,39]. For example, the time at which exogenous BMP-2 is administered was shown to markedly influence bone healing at a fracture site [38]. Administration of BMP-2 at day 0 or at day 4 post-facture resulted in the augmentation of periosteal callus formation, bone mineral content, and superior biomechanical properties when compared to the administration of BMP-2 at a later time (day 8).

A possible interaction that could have an important influence on bone healing is that between the surface of the implant and the exogenous BMP-2 released by the local cells. Upon implantation, the surface of the as-fabricated bioactive glass reacts with the physiological fluid to initially form a silica-gel surface layer [4−6]. It is possible that this silica-gel layer could irreversibly denature proteins such as BMP-2, resulting in a loss of protein bioactivity [40]. A higher amount of the silica-gel, with a negative charge at the physiological pH, could lower the release of BMP-2 or increase the tendency for denaturing the BMP-2. The results for the BMP-2 release profile from the scaffolds in vitro (Fig. 3) appear to support this suggestion, but further studies are required to provide

a clearer understanding. The scaffold pretreated for 6 days in the phosphate solution, showing little evidence for a silica-gel phase in the XRD pattern (Fig. 3), released a significantly larger amount of BMP-2 when compared to the scaffolds pretreated for 1 day or 3 days and the as-fabricated scaffold.

Another factor that could have an effect on the capacity of the scaffolds to support new bone formation in vivo is their degradation (or conversion) rate to HA (or ACP). The presence of the converted HA surface layer on the pretreated scaffolds lead to a reduction in their degradation rate and in the release of ions from the glass phase into the medium when compared to the as-fabricated scaffolds [26,41]. SEM images of the pretreated implants showed little change in the thickness of the HA layer during the six-week implantation in vivo (Fig. 9b, c). In comparison, the thickness of HA layer on the as-fabricated implants grew to ~20 μm (Fig. 9a). Degradation and conversion of the as-fabricated glass is initially rapid, resulting in a marked change in the local pH and osmolarity [26,42,43]. Cell viability could be adversely affected initially [44], and this could have an effect on subsequent cellular and tissue reactions, and eventually on bone formation.

4.3. Bone regeneration in the pretreated bioactive glass scaffolds loaded with BMP-2

Loading the pretreated scaffolds with BMP-2 (1 μg/defect) significantly enhanced new bone formation in the defects when compared to the as-fabricated scaffold (Fig. 7). The percent new bone formed in the BMP-loaded implants was not affected by their different surface treatments despite the large difference in the BMP-2 release profile in vitro between the scaffolds pretreated for 1 day and 3 days and the scaffolds pretreated for 6 days (Fig. 4b). While the release of BMP-2 from the scaffolds in vivo is expected to be different from that in vitro, it is possible that the amount of BMP-2 released from all three pretreated scaffolds might be above the threshold required to stimulate bone formation in vivo.

The amount of new bone formed in the BMP-loaded implants was not significantly greater than that in the implants pretreated for 3 days (no BMP-2) but it was significantly greater than that in implants pretreated for 1 day and 6 days (Fig. 7). Presumably because of the effectiveness of the three-day pretreatment alone in enhancing bone formation, little effect of the BMP-2 loading can actually be seen. Comparing the

tissue formed in the defects, the new bone formed in the implants pretreated for 3 days appeared to be more lamellar, while the new bone in the BMP-loaded implants appeared to be more woven. Furthermore, there was significantly more bone marrow-like tissue and less fibrous tissue in the BMP-loaded implants when compared to pretreated implants (Fig. 8). Marrow-rich bone is known to be a typical outcome of BMP-2 induced bone growth [45−47], but the mechanism of formation is unclear. The lack of mature and hypertrophic cartilage-like tissue is an indication that the bone was formed by a membraneous mechanism.

The BMP-2 loading (1 μg/defect) used in this study was based on the results of previous studies reported in the literature for the use of BMP-2 in stimulating bone healing [48,49]. While that amount of BMP-2 was effective for enhancing bone regeneration in the bioactive glass scaffolds used in this study, the optimum amount is not clear. In a previous study to evaluate the effect of BMP-2 loading on the capacity of three-dimensional poly (lactic-co-glycolic acid) (PLGA) scaffolds to regenerate bone in rat calvarial defects (5 mm in diameter), a BMP-2 dose greater than 120 ng/mm^3 was required for bridging the defect after a six-week implantation period [50]. In comparison, the amount of BMP-2 used in this study (1 μg/defect) was equivalent to a loading of ~ 60 ng/mm^3, which indicates that a much lower concentration of BMP-2 was required to bridge a similar defect using the pretreated bioactive glass scaffolds.

The BMP-loaded bioactive glass scaffolds appear to be more appropriate for treating larger critical sized bone defects. Nevertheless, based on the significant bone formation in the defects implanted with the pretreated scaffolds without BMP-2, it is also reasonable to consider the use of the pretreated scaffolds, particularly the scaffolds pretreated for 3 days, in some bone repair situations. Taking into account the mechanical properties of similar scaffolds observed in a recent study [11], these bioactive glass scaffolds could be considered for applications in loaded bone repair. The scaffolds are currently being evaluated for their capacity to repair segmental bone defects in animal models.

5. Conclusion

Scaffolds of 13-93 bioactive glass prepared with a grid-like microstructure by robocasting (porosity ~50%; filament width = 330 μm; pore width = 300 μm) showed the capacity to support the formation of new bone in rat calvarial defects. Pretreatment of the as-fabricated scaffolds for 3 days in a K_2HPO_4 solution (60 °C; pH = 12), to convert a thin surface layer (~5 μm) of the glass to a high-surface-area hydroxyapatite or amorphous calcium phosphate material prior to implantation, significantly enhanced the capacity of the scaffolds to support new bone formation. Loading the pretreated scaffolds with BMP-2 (1 μg/defect) was also effective for enhancing new bone formation. The capacity of the BMP-loaded scaffolds to enhance bone regeneration was independent of the pretreatment time (1−6 days) in the K_2HPO_4 solution. Pretreatment of silicate bioactive glass scaffolds in an aqueous phosphate solution or loading the pretreated scaffolds with BMP-2 can provide an effective approach for enhancing the capacity of the scaffolds to support bone regeneration and integration in osseous defects. Taking into account the mechanical properties of similar scaffolds observed in a previous study, these 13-93 scaffolds, pretreated or loaded with BMP-2, are promising in structural bone repair.

Acknowledgement

This work was supported by the National Institutes of Health, National Institute of Arthritis, Musculoskeletal and Skin Diseases (NIAMS), Grant # 1R15AR056119-01. The authors thank Mo-Sci Corp., Rolla, MO for the bioactive glass used in this work.

References

[1] Cancedda R, Giannoni P, Mastrogiacomo M. A tissue engineering approach to bone repair in large animal models and in clinical practice. Biomaterials 2007;28:4240-50.

[2] Giannoudis PV, Dinopoulos H, Tsiridis E. Bone substitutes: An update. Injury 2005;36:S20-S7.

[3] Laurencin C, Khan Y, El-Amin SF. Bone graft substitutes. Expert Rev Med Devices 2006;3:49-57.

[4] Rahaman MN, Day DE, Bal BS, Fu Q, Jung SB, Bonewald LF. Bioactive glass in tissue engineering. Acta Biomater 2011;7:2355-73.

[5] Hench LL. Bioceramics. J Am Ceram Soc 1998;81:1705-28.

[6] Hench LL. The story of Bioglass®. J Mater Sci Mater Med 2006;17:967-78.

[7] Fu Q, Saiz E, Rahaman MN, Tomsia AP. Bioactive glass scaffolds for bone tissue engineering: state of the art and future perspectives. Mater Sci Eng C 2011;31:1245-56.

[8] Huang TS, Rahaman MN, Doiphode ND, Leu MC, Bal BS, Day DE, Liu X. Porous and strong bioactive glass (13–93) scaffolds fabricated by freeze extrusion technique. Mater Sci Eng C 2011;31:1482-9.

[9] Deliormanlı AM, Rahaman MN. Direct-write assembly of silicate and borate bioactive glass scaffolds for bone repair. J Euro Ceram Soc 2012;32:3637-46.

[10] Fu Q, Saiz E, Tomsia AP. Direct ink writing of highly porous and strong glass scaffolds for load-bearing bone defects repair and regeneration. Acta Biomater 2011;7:3547-54.

[11] Liu X, Rahaman MN, Hilmas GE. Mechanical properties of bioactive glass (13-93) scaffolds fabricated by robotic deposition for structural bone repair. Acta Biomater 2013; doi: 10.1016/j.actbio.2013.02.026.

[12] Liu X, Rahaman MN, Fu Q. Bone regeneration in strong porous bioactive glass (13-93) scaffolds with an oriented microstructure implanted in rat calvarial defects. Acta Biomater 2013;9:4889-98.

[13] Place ES, Evans ND, Stevens MM. Complexity in biomaterials for tissue engineering. Nat Mater 2009;8:457-70.

[14] Hulbert SF, Young FA, Mathews RS, Klawitter JJ, Talbert CD, Stelling FH. Potential of ceramic materials as permanently implantable skeletal prostheses. J Biomed Mater Res 1970;4:433-56.

[15] Karageorgiou V, Kaplan D. Porosity of 3D biomaterial scaffolds and osteogenesis. Biomaterials 2005;26:5474-91.

[16] Marques A, Jain H, Kiely C, Song K, Kiely C, Almeida R. Nano/macroporous monolithic scaffolds prepared by the sol–gel method. J Sol-Gel Sci Technol 2009;51:42-7.

[17] Moawad HMM, Jain H. Creation of nano–macro-interconnected porosity in a bioactive glass–ceramic by the melt-quench-heat-etch method. J Am Ceram Soc 2007;90:1934-6.

[18] Chen QZ, Rezwan K, Armitage D, Nazhat SN, Boccaccini AR. The surface functionalization of 45S5 Bioglass®-based glass-ceramic scaffolds and its impact on bioactivity. J Mater Sci Mater Med 2006;17:979-87.

[19] Marion NW, Liang W, Reilly GC, Day DE, Rahaman MN, Mao JJ. Borate glass supports the in vitro osteogenic differentiation of human mesenchymal stem cells. Mech Adv Mater Struct 2005;12:239-46.

[20] Miguel BS, Kriauciunas R, Tosatti S, Ehrbar M, Ghayor C, Textor M, Weber FE. Enhanced osteoblastic activity and bone regeneration using surface-modified porous bioactive glass scaffolds. J Biomed Mater Res A 2010;94A:1023-33.

[21] Bessa PC, Casal M, Reis RL. Bone morphogenetic proteins in tissue engineering: the road from the laboratory to the clinic, part I (basic concepts). J Tissue Eng Regen Med 2008;2:1-13.

[22] Bessa PC, Casal M, Reis RL. Bone morphogenetic proteins in tissue engineering: the road from laboratory to clinic, part II (BMP delivery). J Tissue Eng Regen Med 2008;2:81-96.

[23] Verne E, Vitale-Brovarone C, Bui E, Bianchi CL, Boccaccini AR. Surface functionalization of bioactive glasses. J Biomed Mater Res A 2009;90:981-92.

[24] Fu Q, Rahaman MN, Brown RF, Bal BS, Day DE. Mechanical and in vitro performance of 13-93 bioactive glass scaffolds prepared by a polymer foam replication technique. Acta Biomater 2008;4:1854-64.

[25] Fu H, Rahaman MN, Day DE. Effect of process variables on the microstructure of hollow hydroxyapatite microspheres prepared by a glass conversion method. J Am Ceram Soc 2010;93:3116-23.

[26] Yao A, Wang D, Huang W, Fu Q, Rahaman MN, Day DE. In vitro bioactive characteristics of borate-based glasses with controllable degradation behavior. J Am Ceram Soc 2007;90:303-6.

[27] Bunker BC. Molecular mechanisms for corrosion of silica and silicate glasses. J Non-Cryst Solids 1994;179:300-8.

[28] Fu H, Rahaman MN, Brown RF, Day DE. Evaluation of bone regeneration in implants composed of hollow HA microspheres loaded with transforming growth factor β1 in a rat calvarial defect model. Acta Biomater 2013;9:5718-27.

[29] Montgomery DC. Design and analysis of experiments. 7th ed., New York, Wiley, 2009.

[30] Filgueiras MRT, La Torre G, Hench LL. Solution effects on the surface reactions of three bioactive glass compositions. J Biomed Mater Res 1993;27:1485-93.

[31] Martin RA, Twyman H, Qiu D, Knowles JC, Newport RJ. A study of the formation of amorphous calcium phosphate and hydroxyapatite on melt quenched Bioglass® using surface sensitive shallow angle X-ray diffraction. J Mater Sci Mater Med 2009;20:883-8.

[32] Bi L, Jung S, Day D, Neidig K, Dusevich V, Eick D, Bonewald L. Evaluation of bone regeneration, angiogenesis, and hydroxyapatite conversion in critical-sized rat calvarial defects implanted with bioactive glass scaffolds. J Biomed Mater Res A 2012;100A:3267-75.

[33] Messing RA. Molecular inclusions. Adsorption of macromolecules on porous glass membranes. J Am Chem Soc 1969;91:2370-1.

[34] Lobel KD, Hench LL. In vitro protein interactions with a bioactive gel–glass. J Sol-Gel Sci Tech 1996;7:69-76.

[35] Lobel KD, Hench LL. In vitro adsorption and activity of enzymes on reaction layers of bioactive glass substrates. J Biomed Mater Res 1998;39:575-9.

[36] Snyder LR. Principles of Adsorption Chromatography. New York, Marcel Dekker, 1968.

[37] Fu H, Rahaman MN, Day DE, Brown RF. Hollow hydroxyapatite microspheres as a device for controlled delivery of proteins. J Mater Sci Mater Med 2011;22:579-91.

[38] Murnaghan M, McIlmurray L, Mushipe MT, Li G. Time for treating bone fracture using rhBMP-2: a randomised placebo controlled mouse fracture trial. J Orthop Res 2005;23: 625-31.

[39] Chao EY, Inoue N. Biophysical stimulation of bone fracture repair, regeneration and remodelling. Eur Cell Mater 2003;6:72-85.

[40] Messing RA. Insoluble papain prepared by adsorption on porous glass. Enzymologia 1970; 38:39-42.

[41] Brown RF, Rahaman MN, Dwilewicz AB, Huang W, Day DE, Li Y, Bal BS. Conversion of borate glass to hydroxyapatite and its effect on proliferation of MC3T3-E1 cells. J Biomed Mater Res Part A 2009;88A:392-400.

[42] Huang W, Day DE, Kittiratanapiboon K, Rahaman MN. Kinetics and mechanisms of the conversion of silicate (45S5), borate, and borosilicate glasses to hydroxyapatite in dilute phosphate solutions. J Mater Sci Mater Med 2006;17:583-9.

[43] Fu Q, Rahaman MN, Fu H, Liu X. Silicate, borosilicate, and borate bioactive glass scaffolds with controllable degradation rates for bone tissue engineering applications, I: preparation and in vitro degradation. J Biomed Mater Res Part A 2010;95A:164-71.

[44] Mather JP, Roberts PE. Introduction to cell and tissue culture: theory and technique. New York, Plenum Press; 1998.

[45] Hayashi C, Hasegawa U, Saita Y, Hemmi H, Hayata T, Nakashima K, Ezura Y, Amagasa T, Akiyoshi K, Noda M. Osteoblastic bone formation is induced by using nanogel-crosslinking hydrogel as novel scaffold for bone growth factor. J Cell Physiol 2009;220:1-7.

[46] Hong S-J, Kim C-S, Han D-K, Cho I-H, Jung U-W, Choi S-H, Kim CK, Cho KS. The effect of a fibrin-fibronectin/β-tricalcium phosphate/recombinant human bone morphogenetic protein-2 system on bone formation in rat calvarial defects. Biomaterials 2006;27:3810-6.

[47] Chung Y-I, Ahn K-M, Jeon S-H, Lee S-Y, Lee J-H, Tae G. Enhanced bone regeneration with BMP-2 loaded functional nanoparticle–hydrogel complex. J Control Release 2007;121:91-9.

[48] Lee J-H, Kim C-S, Choi K-H, Jung U-W, Yun J-H, Choi S-H, Cho KS. The induction of bone formation in rat calvarial defects and subcutaneous tissues by recombinant human BMP-2, produced in Escherichia coli. Biomaterials 2010;31:3512-9.

[49] Marden LJ, Hollinger JO, Chaudhari A, Turek T, Schaub RG, Ron E. Recombinant human bone morphogenetic protein-2 is superior to demineralized bone matrix in repairing craniotomy defects in rats. J Biomed Mater Res A 1994;28:1127-38.

[50] Cowan CM, Aghaloo T, Chou YF, Walder B, Zhang X, Soo C, Ting K, Wu B. MicroCT evaluation of three-dimensional mineralization in response to BMP-2 doses in vitro and in critical sized rat calvarial defects. Tissue Eng 2007;13:501-12.

Table 1 Bioactive glass (13-93) scaffold groups used in this study

Scaffold group	Pretreatment time in K_2HPO_4 solution (day)	BMP-2 loading	Number of Defects
As fabricated (0d)	-	-	10
1d	1	-	5
3d	3	-	10
6d	6	-	5
1d+BMP	1	1 μg/defect	5
3d+BMP	3	1 μg/defect	5
6d+BMP	6	1 μg/defect	5

Table 2 Thickness and specific surface area of the converted layer formed by reacting silicate (13-93) bioactive glass scaffolds for the times shown in 0.25 M K_2HPO_4 solution at 60°C and starting pH = 12.0.

Immersion time (day)	Thickness (μm)	Specific surface area (m^2/g)
1	2 ± 1	19 ± 2
3	5 ± 2	30 ± 3
6	13 ± 2	47 ± 1

Table 3 Amount of new bone, fibrous tissue, and bone marrow-like tissue formed in bioactive glass (13-93) scaffolds implanted for 6 weeks in rat calvarial defects. The amount of each tissue is expressed as a percent of the available pore space (area) in the scaffolds and the total defect area.

Scaffold group	New bone (%)		Fibrous tissue (%)		Bone marrow-like tissue (%)	
	Available area	Total area	Available area	Total area	Available area	Total area
As fabricated (0d)	32 ± 13	18 ± 8	62 ± 14	34 ± 8	1 ± 1	1 ± 1
1d	46 ± 10	25 ± 5	45 ± 12	25 ± 7	2 ± 1	1 ± 1
3d	57 ± 14	33 ± 10	35 ± 13	19 ± 7	3 ± 2	2 ± 1
6d	45 ± 11	26 ± 8	48 ± 13	28 ± 8	2 ± 1	1 ± 1
1d+BMP	65 ± 7	38 ± 4	14 ± 12	8 ± 7	13 ± 6	8 ± 3
3d+BMP	61± 8	35 ± 3	7 ± 7	4 ± 4	22 ± 8	12 ± 4
6d+BMP	64 ± 11	38 ± 6	15 ± 19	10 ± 12	16 ± 8	10 ± 5

Table 4 Comparison of new bone formed in scaffolds composed of silicate 13-93 glass with different microstructures after implantation in rat calvarial defects (4.0−4.6 mm in diameter × 1.5 mm). The amount of new bone is shown as a percent of the available pore space (area) in the scaffolds and the total defect area.

Microstructure of scaffolds	Porosity (%)	Pore size (μm)	New bone (%)		Implantation time (weeks)	Reference
			Available pore area	Total area		
Grid-like	47	300 × 300 × 150	32 ± 13	18 ± 8	6	This study
Trabecular	80	100−500	25 ± 12	19 ± 9	12	[12]
Oriented	50	100−150	37 ± 8	18 ± 3	12	[12]
Fibrous	50	50−500	~17*	8.5 ± 2	12	[32]

* Estimated from the total defect area

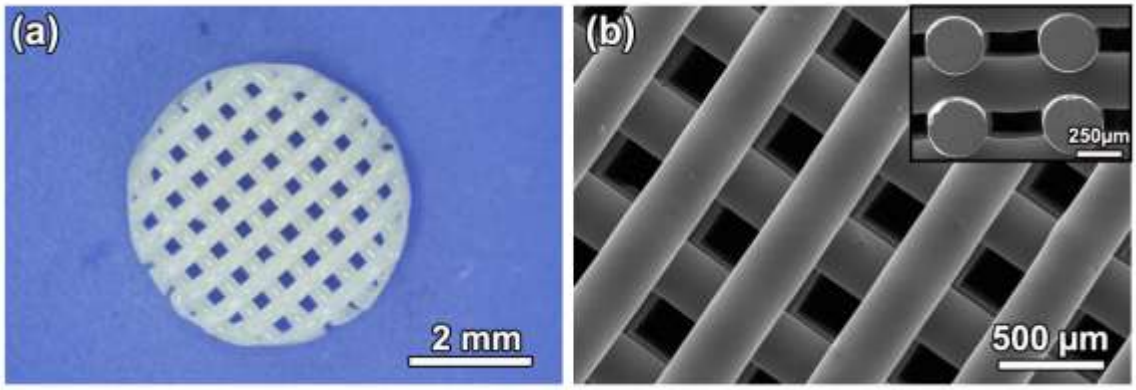

Figure 1. (a) Optical image of 13-93 bioactive glass scaffold prepared by robocasting for implantation in rat calvarial defect. (b) Higher magnification SEM image of the scaffold showing the dense glass filaments and porous architecture in the plane of deposition (xy plane). Inset: SEM image in a plane perpendicular to the xy plane. The scaffolds had a porosity of 47 ± 1%, a pore width of 300 ±10 µm in the plane of deposition (xy plane) and 150 ± 10 µm in z direction.

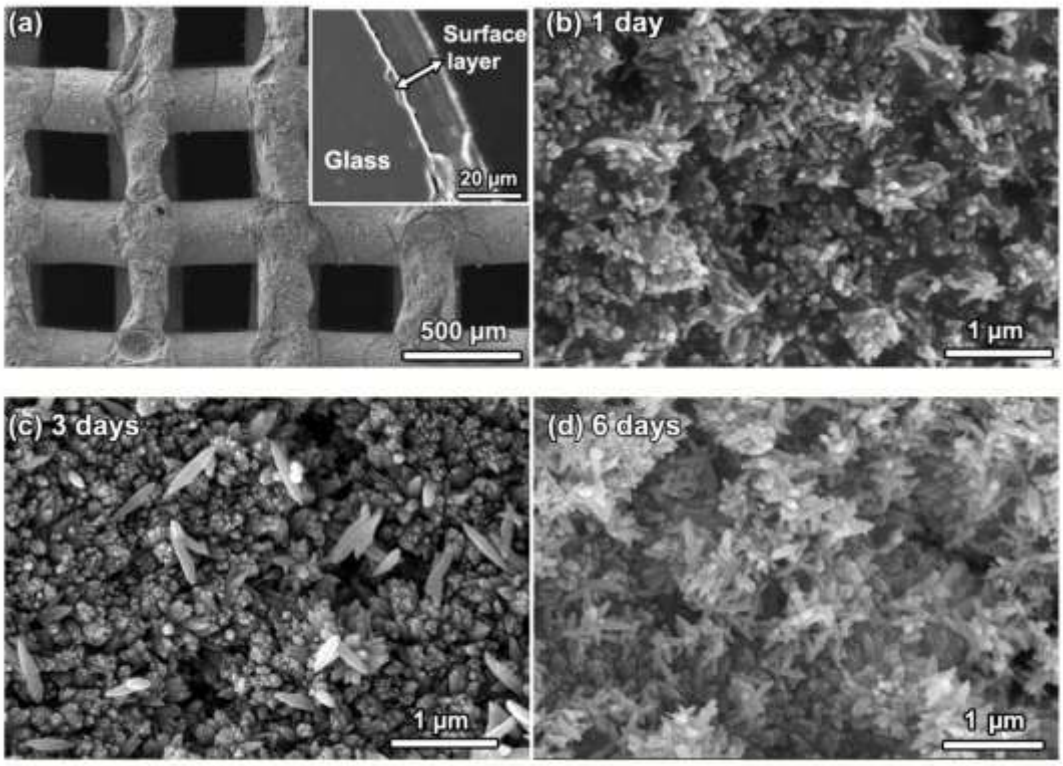

Figure 2. (a) SEM image of a bioactive glass scaffold after reaction for 6 days in 0.25 M K_2HPO_4 solution (60°C; pH = 12.0). Inset: cross-section of a bioactive glass filament showing the thickness of the converted surface layer. (b)−(d) Higher magnification SEM images of the surface of the converted layer formed by reaction for (b) 1 day, (c) 3 days, and (d) 6 days in the phosphate solution.

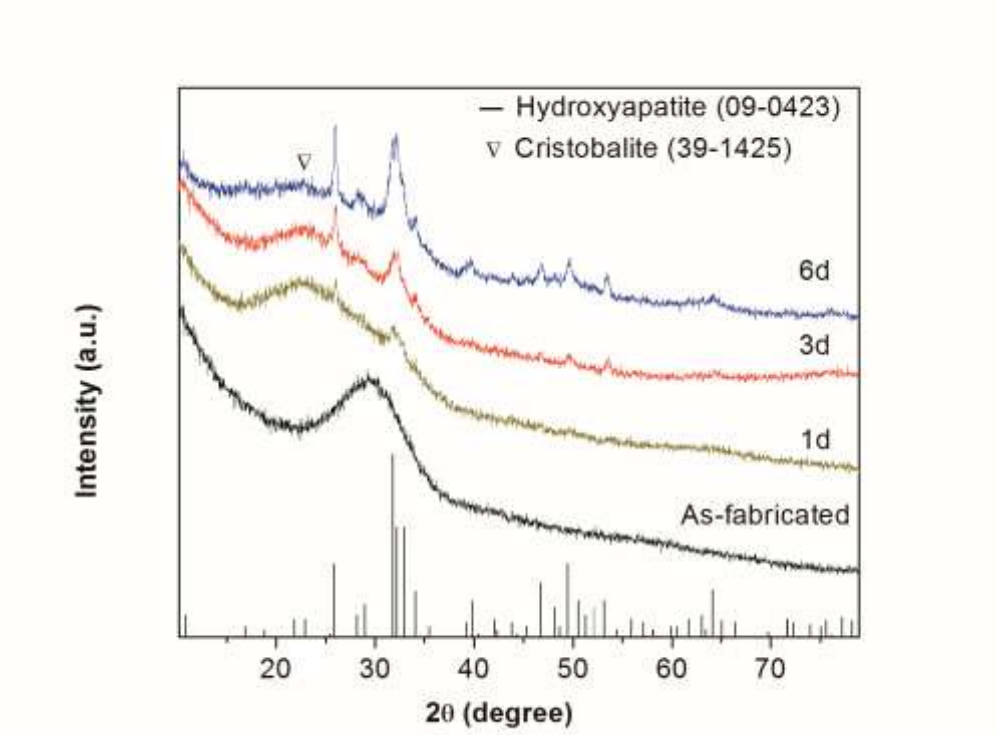

Figure 3. X-ray diffraction patterns of the as-fabricated bioactive glass (13-93) scaffold, and the converted surface layer formed by reacting the bioactive glass for 1 day, 3 days, and 6 days in 0.25 M K_2HPO_4 solution (60°C; pH = 12.0). The diffraction peaks corresponding to a reference hydroxyapatite (JCPDS 09-0423) and the main cristobalite peak (JCPDS 39-1425) are indicated.

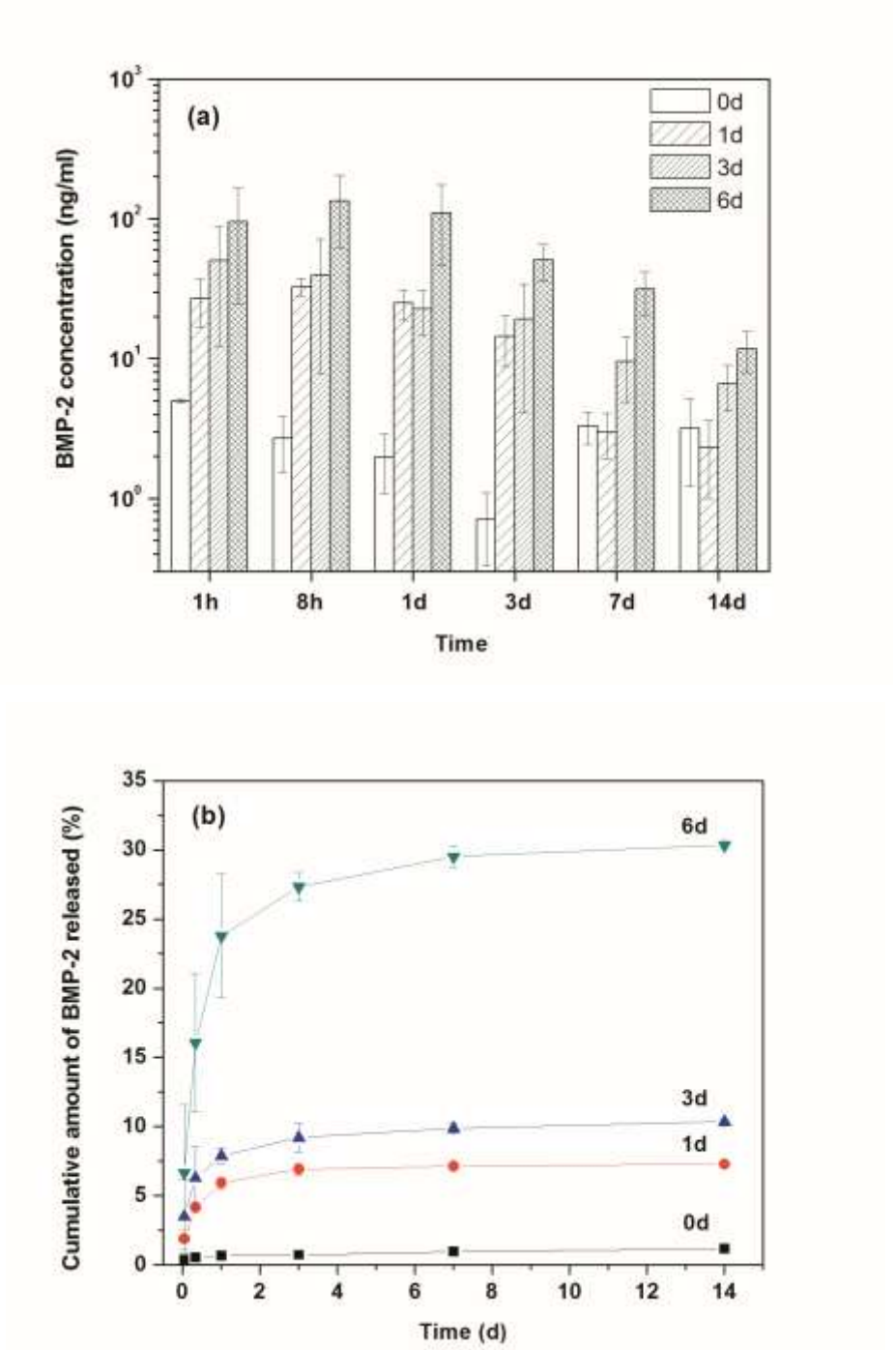

Figure 4. (a) Amount of BMP-2 released a different time intervals from the as-fabricated scaffold (0d) and the scaffolds pretreated for 1day, 3 day and 6 days (1d; 3d; 6d; respectively) into a medium composed of FBS/PBS. Each scaffold was initially loaded with 1 μg of BMP-2. (b) Cumulative amount of BMP-2 released from the scaffolds (as a fraction of the amount of BMP-2 initially loaded into the scaffolds) versus time.

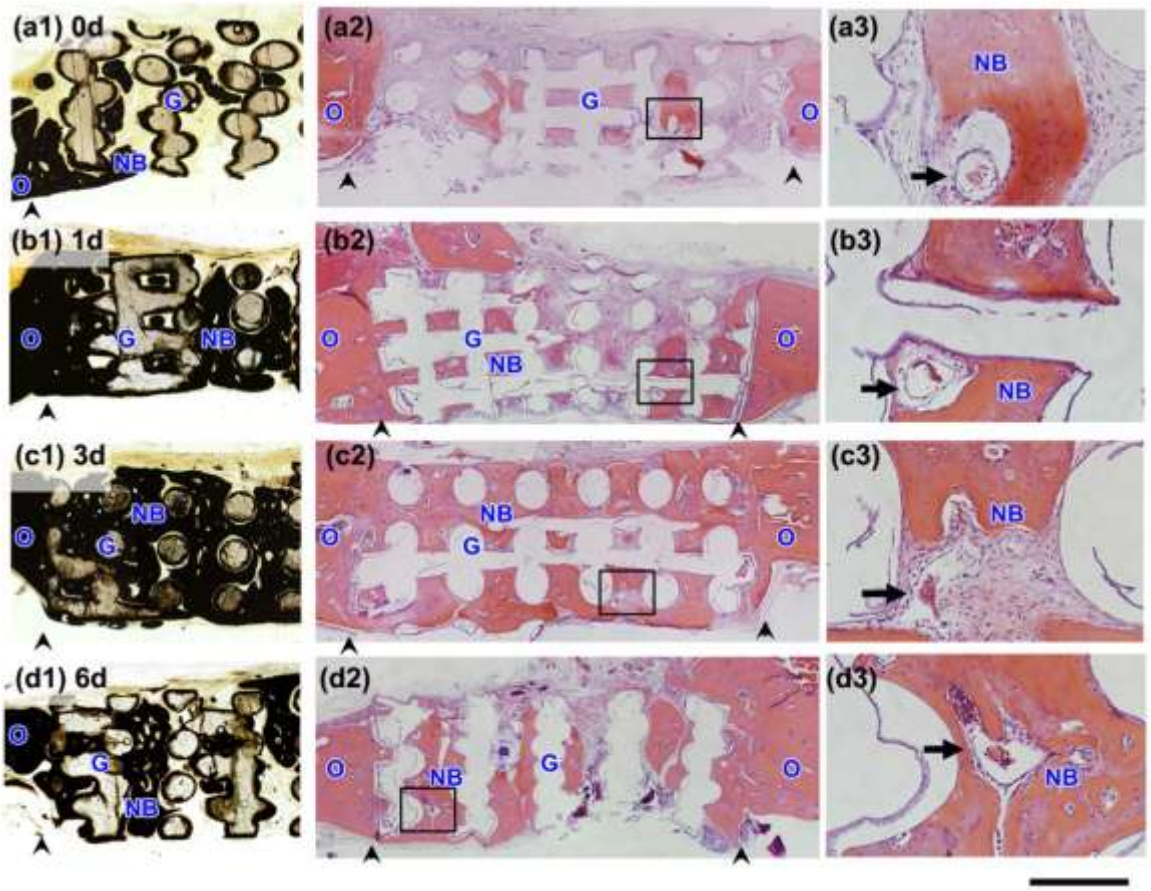

Figure 5. Von Kossa stained sections (a1−d1) and H&E stained sections (a2−d3) of rat calvarial defects implanted for 6 weeks with bioactive scaffolds as fabricated (0d) and pretreated for 1 day, 3 days, and 6 days in aqueous phosphate solution (1d; 3d; 6d; respectively). (a3)−(d3) are higher magnification images of the boxed areas in (a2)−(d2). Scale bar =1 mm for (a1−d2) and 200 μm for (a3−d3). G = bioactive glass; NB = new bone; O = old bone; arrows indicate blood vessels, arrowheads indicate the edges of old bone.

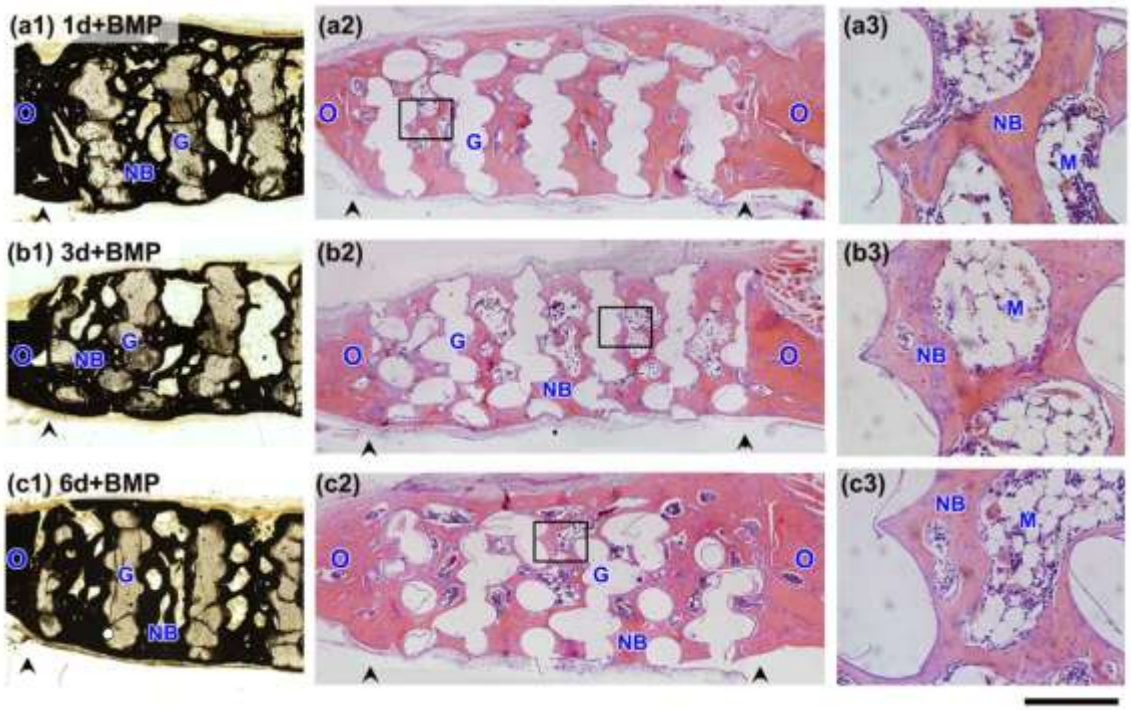

Figure 6. Von Kossa stained sections (a1−c1) and H&E stained sections (a2−c3) of rat calvarial defects implanted for 6 weeks with bioactive scaffolds pretreated for 1 day, 3 days, and 6 days in aqueous phosphate solution and loaded with BMP-2 (1 μg/defect) (denoted 1d + BMP; 3d+BMP; 6d+BMP, respectively). (a3)−(c3) are higher magnification images of the boxed areas in (a2)−(c2). Scale bar =1 mm for (a1−c2) and 200 μm for (a3−c3). G = bioactive glass; NB = new bone; O = old bone; M = bone marrow-like tissue, arrowheads indicate the edges of old bone.

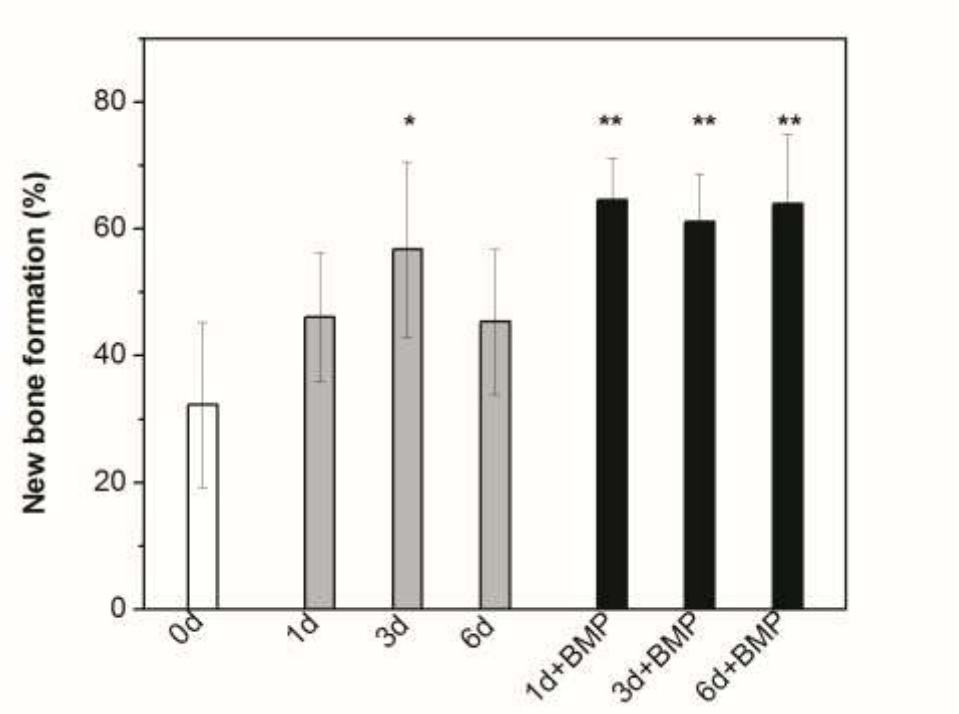

Figure 7. Percent new bone formed in rat calvarial defects implanted with scaffolds of 13-93 glass at 6 weeks postimplantation: as fabricated (0d); pretreated for 1 day, 3 days, and 6 days in aqueous phosphate solution (1d; 3d; 6d; respectively); pretreated 1 day, 3 days, and 6 days and loaded with BMP-2 (1 μg/defect) (1d+BMP; 3d+BMP; 6d+BMP, respectively). The new bone formed is shown as a percent of the available pore space in the scaffolds. (*significant difference compared to 0d; **significant difference compared to 0d, 1d, and 6d; $p < 0.05$).

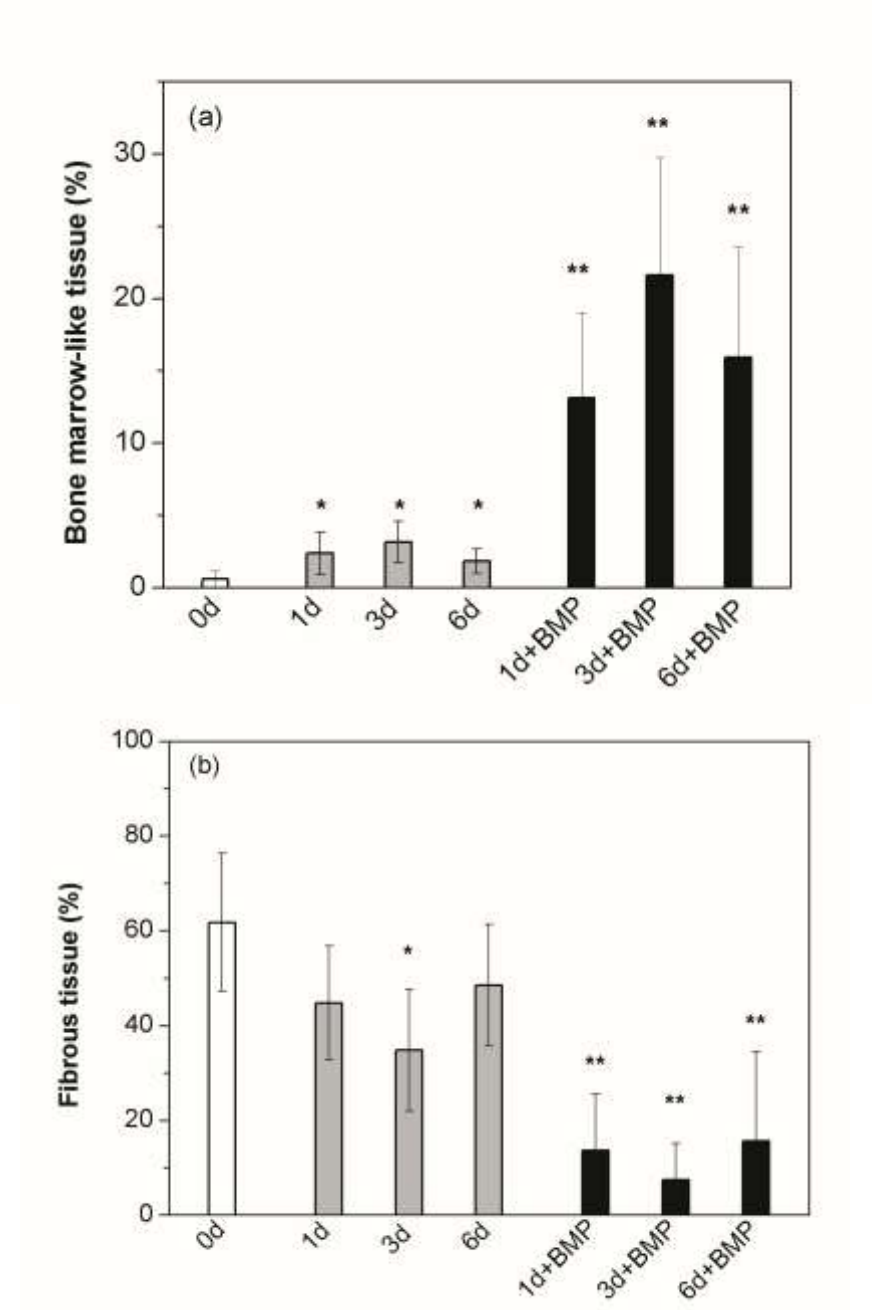

Figure 8. Percent bone marrow-like tissue (a) and fibrous tissue (b) formed in rat calvarial defects implanted with scaffolds of 13-93 glass at 6 weeks postimplantation: as fabricated (0d); pretreated for 1 day, 3 days, and 6 days in aqueous phosphate solution (1d; 3d; 6d; respectively); pretreated 1 day, 3 days, and 6 days and loaded with BMP-2 (1 μg/defect) (1d+BMP; 3d+BMP; 6d+BMP, respectively). (*significant difference compared to 0d; **significant difference compared to 0d, 1d, 3d and 6d; $p < 0.05$).

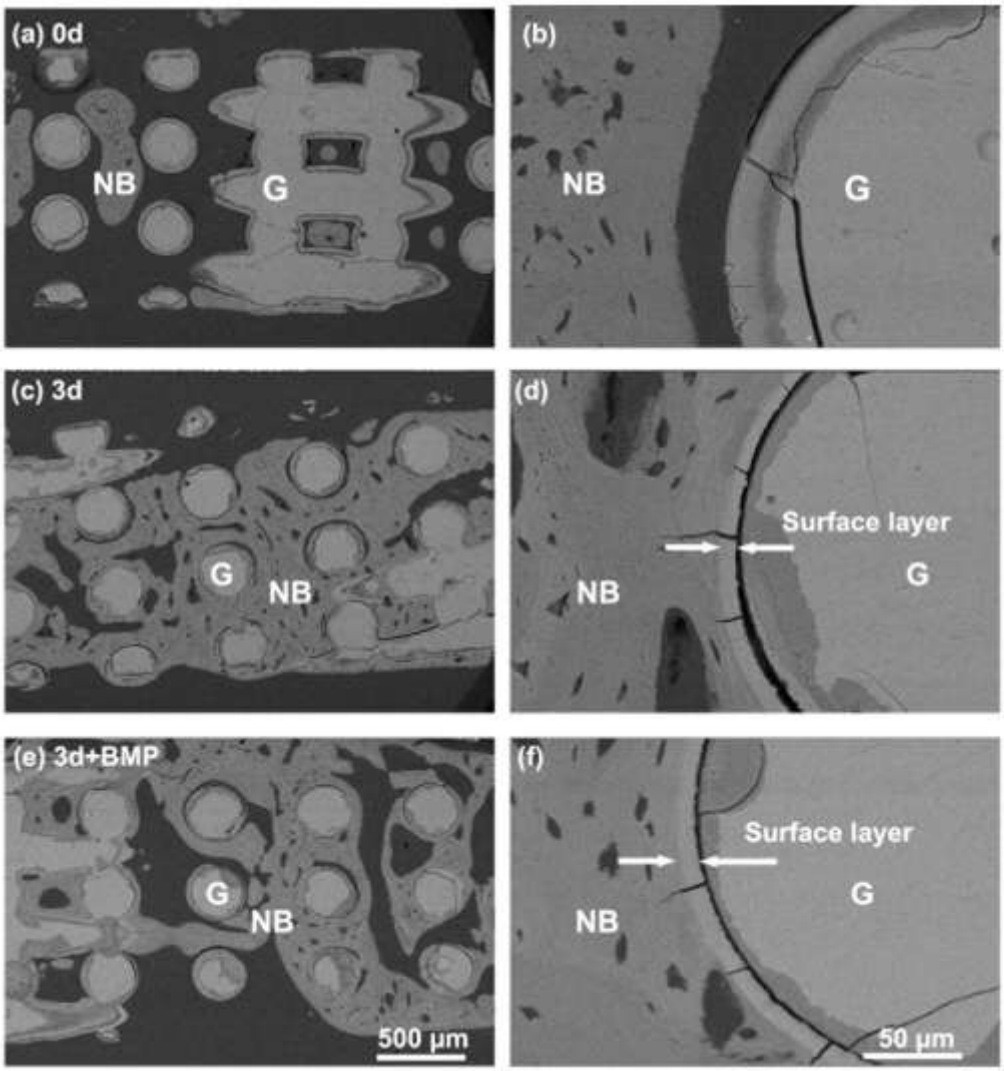

Figure 9. Back-scattered SEM images of rat calvarial defects implanted with bioactive glass scaffolds at 6 weeks postimplantation: (a), (b) as-fabricated scaffolds; (c), (d) scaffolds pretreated for 3 days in aqueous phosphate solution; (e), (f) scaffolds pretreated for 3 days in aqueous phosphate solution and loaded with BMP-2. (NB = new bone; G = bioactive glass). The approximate thickness of the HA surface layer on the pretreated scaffolds prior to implantation is shown in (d) and (f).

SECTION

2. CONCLUSIONS

1. Bioactive glass scaffolds with an oriented microstructure of columnar pores can be prepared by a two-step forming process consisting of unidirectional freezing of camphene-based suspensions followed by thermal annealing at 34 °C, sublimation of the camphene at room temperature and sintering. The use of the organic (camphene)-based suspensions and the two-step processing methods can provide the following benefits when compared to the use of aqueous suspensions:

(a) A reduction in the degradation of the bioactive glass, particularly for borate-based bioactive glasses that typically have a higher degradation rate than silicate-based bioactive glasses;

(b) A wider range of average pore size (diameter) in the as-formed scaffolds (15−160 μm for annealing times of 0−72 h at 34 °C) compared to the lamellar pores of width 10−40 μm typically obtained in the unidirectional freezing of aqueous suspensions. The larger pore size (diameter) of the scaffolds is known to be more conducive to tissue infiltration in vivo.

2. For scaffolds formed from suspensions with a given particle concentration, the alignment of the columnar pores and the homogeneity of the microstructure are dependent primarily on the freezing conditions. Freezing at a constant rate and at higher freezing rates (e.g., 7 °C/min) using a controlled freezing apparatus resulted in better pore alignment and a more homogeneous microstructure when compared to freezing at variable rate on a cold substrate (kept at 3 °C).

3. Optimized silicate 13-93 bioactive glass scaffolds with an oriented microstructure (porosity = 50%; average pore diameter = 100 μm) had a compressive strength of 47 ± 5 MPa and elastic modulus of 11 ± 3 GPa when tested in the orientation direction. These values are much higher than those for scaffolds of the same glass with a trabecular microstructure (porosity = 80 %; pore size = 100−500 μm) or a fibrous microstructure

(porosity = 50%; pore size = 100−500 μm) with compressive strength in the range 2−12 MPa and elastic modulus of 2−4 GPa.

4. When implanted in rat calvarial defects, the oriented scaffolds (porosity = 50%; pore size = 50−150 μm) showed the ability to support infiltration of bone into the pores of the scaffolds which was comparable to that of trabecular scaffolds with higher porosity (80%) and pore size (100−500 μm). New bone formation, evaluated as a percent of the available pore space in the scaffold, increased form 37% at 12 weeks to 55% at 24 weeks in the defects implanted with the oriented scaffolds, compared to values of 25% (12 weeks) and 46% (24 weeks) for the trabecular scaffolds.

5. The use of a robotic deposition (robocasting) method provided better control of the scaffold architecture when compared to the methods such as unidirectional freezing of suspensions, polymer foam replication, and thermal bonding of particles or short fibers used in earlier phases of this work.

6. In comparison to most previous work in which the strength and elastic modulus of bioactive glass scaffolds were evaluated in compression only, this study provided a more comprehensive evaluation of the mechanical properties of silicate 13-93 bioactive glass scaffolds prepared by robocasting.

7. Silicate 13-93 bioactive glass scaffolds with a grid-like microstructure (porosity = ~50%; pore width = ~300 μm in the deposition or xy plane and ~150 μm in z direction) prepared by robocasting showed mechanical properties that were superior to those of scaffolds of the same glass prepared by more conventional methods described above.

(a) The compressive strength (86 ± 9 MPa) and elastic modulus (13 ± 2 GPa) of the scaffolds in the z direction were comparable to the values for cortical bone;

(b) The Weibull modulus of the scaffolds in compression (equal to 12) was higher than the values of 3−10 reported for porous bioactive ceramic scaffolds such as hydroxyapatite;

(c) The scaffolds had good fatigue resistance in compression when tested under cyclic stresses far greater than normal physiological loads.

8. The elastic modulus of the scaffolds in flexure (13 ± 2 GPa) was comparable to that of human cortical bone. However, the flexural strength of the scaffolds (11 ± 3 MPa), while comparable to the highest values reported for hydroxyapatite scaffolds with a similar porosity, was far smaller than the values reported for human cortical bone.

9. The brittle mechanical response of the bioactive glass scaffolds in vitro changed markedly to an elasto-plastic response after implantation of the scaffolds in rat subcutaneous sites in vivo for longer than 2−4 weeks.

10. Conversion of the 13-93 bioactive glass scaffolds to hydroxyapatite in vivo (rat subcutaneous sites or rat calvarial defects) was faster than in simulated body fluid in vitro.

11. The degradation in the compressive strength of 13-93 bioactive glass scaffolds in vivo can be predicted from the conversion rate of the glass to hydroxyapatite.

12. When implanted in rat calvarial defects, as-fabricated scaffolds of 13-93 glass with a grid-like microstructure showed a better capacity to support bone infiltration than oriented, trabecular, and fibrous scaffolds described earlier.

13. The capacity of 13-93 bioactive glass scaffolds with a grid-like microstructure to support new bone formation in rat calvarial defects can be significantly improved by converting a thin surface layer of the glass in an aqueous phosphate solution prior to implantation.

14. Conversion of a thin surface layer of the glass in 13-93 bioactive glass scaffolds can provide substrate for loading and controlled release of a growth factor such as bone morphogenetic protein-2.

15. When loaded with BMP-2 (1 μg/defect), surface-treated bioactive glass (13-93) scaffolds with a grid-like microstructure have the capacity to significantly enhance new bone formation in rat calvarial defects.

16. Based on their mechanical properties and their capacity to support bone regeneration in an osseous defect, silicate 13-93 bioactive glass scaffolds with a grid-like microstructure are promising in structural bone repair.

3. SUGGESTIONS FOR FUTURE WORK

Based on the results of the present work, there are several interesting possibilities for the future work.

1. Evaluation of bioactive glass scaffolds in loaded bone defect model:

As described above, scaffolds with a grid-like microstructure (prepared by robocasting) have shown a promising combination of mechanical properties and capacity to support bone regeneration in a non-loaded bone defect model (rat calvarial defect model). The as-fabricated scaffolds, the surface-treated scaffolds, and the surface-treated scaffolds loaded with BMP-2, described in this thesis, should be tested in an appropriate in vivo model to evaluate their capacity to repair loaded bone. The rat femoral segmental defect model and the rabbit tibial segmental defect model are examples of widely-used small animal models.

2. Optimizing the microstructure of scaffolds prepared by robotic deposition:

The results showed that scaffolds with a grid-like microstructure prepared by robocasting had promising mechanical properties in compression, but their flexural strength was much lower than the reported values for cortical bone. Because long bones are subjected to flexural loading, the flexural strength of scaffolds designed for segmental bone repair is relevant. This study used scaffolds with a simple grid-like microstructure. Future work should consider the design and modeling of porous scaffolds for optimum mechanical properties in compression as well as flexure. An example is the design of scaffolds with a “gradient” microstructure, composed of a less porous outer region and a more porous inner region, to mimic human long bones.

3. Measuring and modeling the mechanical properties of bioactive glass implants in vivo:

The results of the present study showed that changes in the compressive strength of silicate 13-93 bioactive glass scaffolds as a function of implantation time in rat subcutaneous sites can be predicted from the conversion rate of the bioactive glass to hydroxyapatite in vivo. If data for bone formation in vivo and for the properties of the

new bone are also available, then a model could be developed to predict the compressive strength of the implants using computational simulation.

There is little data on the mechanical properties of bioactive glass scaffolds as a function of implantation time in an osseous defect site in vivo. Implants used in the rat calvarial defect model, a widely used assay, are too small for reliable mechanical testing. Bioactive glass scaffolds implanted in rat femoral segmental defects or, better still, rabbit tibial segmental defects, should be tested in multiple loading modes (compression; flexure; torsion; fatigue) as a function of implantation time to generate the much-needed data.

4. Optimizing the surface treatment of the bioactive glass scaffolds:

The results of the present study showed that pretreating the bioactive glass scaffolds (grid-like microstructure prepared by robocasting) in an aqueous phosphate solution to convert a thin surface layer to a calcium phosphate material significantly enhanced new bone formation in vivo. In the experiments, the properties of the starting phosphate solution were fixed (0.25 M K_2HPO_4, pH=12 at 60 ^oC). It is not clear whether those pretreatment conditions were the optimum conditions for enhancing bone regeneration in vivo or for controlling the release of BMP-2 from the scaffolds. Other immersion conditions should be investigated to vary the composition and microstructure of the surface layer, and test their effects on BMP-2 release in vitro and bone regeneration in vivo.

5. Determine the optimum dose of BMP-2 in the pretreated bioactive glass scaffolds:

The results showed that loading the pretreated scaffolds with BMP-2 significantly enhanced bone regeneration when compared to the as-fabricated scaffolds (no pretreatment). It is not clear whether the amount used in this study is the optimum amount for bone regeneration. The amount of BMP-2 loading (1 μg/defect) used in this study was based on data in the literature. BMP-2 is expensive, and large amounts of BMP-2 can have adverse effects in vivo. Pretreated scaffolds loaded with different amounts of BMP-2 should be evaluated in rat calvarial defects to determine the optimum BMP-2 dose for bone regeneration.

6. Long-term evaluation of bone quality

In the present study, the scaffolds were implanted for 6 weeks. While considerable new bone was formed in the pretreated scaffolds and the pretreated scaffolds loaded with BMP-2, it is not clear whether the bone healing is transient or not. Longer implantation times (e.g., 12 and 24 weeks) should also be used.

7. Doping of trace elements in the bioactive glass composition:

Silicate 13-93 bioactive glass was used in all of the experiments in the present study. Recent studies have shown that doping bioactive glass with trace amount of elements such as Cu and Zn can stimulate angiogenesis in the implants which is considered to be beneficial for bone regeneration. Scaffolds made from 13-93 bioactive glass doped with elements such as Cu and Zn should be studied to evaluate the ability of those elements to enhance bone regeneration and angiogenesis in osseous defects, such as rat calvarial defects.

8. Fabricating scaffolds with complex anatomical geometry:

As one of the solid freeform fabrication techniques, robocasting has the potential to build scaffolds with customized external shape and pre-designed internal architecture from computer generated models. In this work, scaffolds with an external geometry of a cube, a cylinder, and a disc were prepared. Developing the process to prepare scaffolds with complex shape to match the anatomical geometry of the tissue to be replaced would be beneficial for the future application of the scaffolds.

APPENDIX

CONVERSION OF MELT-DERIVED MICROFIBROUS BORATE (13-93B3) AND SILICATE (45S5) BIOACTIVE GLASS IN AS SIMULATED BODY FLUID

Xin Liu, Mohamed N. Rahaman, Delbert E. Day

Department of Materials Science and Engineering and Center for Bone and Tissue Repair and Regeneration, Missouri University of Science and Technology, Rolla, MO 65409, USA

ABSTRACT

Microfibrous bioactive glasses are showing a considerable capacity to heal soft tissue wounds, but little information is available on the mechanism of healing. In the present study, the conversion of microfibrous borate bioactive glass (diameter = 0.2−5 μm) with the composition designated 13-93B3 (5.5 Na_2O, 11.1 K_2O, 4.6 MgO, 18.5 CaO, 3.7 P_2O_5, 56.6 B_2O_3, wt%) was evaluated in vitro as a function of immersion time in a simulated body fluid (SBF) at 37 °C using structural and chemical analysis. Silicate 45S5glass microfibers (45 SiO_2, 24.5 Na_2O, 24.5 CaO, 6 P_2O_5, wt%) were also studied for comparison. Microfibrous 13-93B3 glass degraded almost completely and converted to a calcium phosphate material within 7−14 days in SBF, whereas >85% of the silica remained in the 45S5 microfibers, forming a silica-gel phase. An amorphous calcium phosphate (ACP) product that formed on the 13-93B3 microfibers crystallized at a slower rate to hydroxyapatite (HA) when compared to the ACP that formed on the 45S5 fibers. For immersion times >3 days, the 13-93B3 fibers released a higher concentration of Ca into the SBF than the 45S5 fibers. The fast and more complete degradation, slow crystallization of the ACP product, and higher concentration of dissolved Ca in SBF could contribute to the capacity of the microfibrous borate 13-93B3 glass to heal soft tissue wounds.

1 Introduction

Bioactive glasses have been widely researched over the last few decades for applications in bone repair, and they are now receiving increasing interest for applications in soft tissue repair [1]. Bioactive glass has a well-recognized ability to enhance bone formation and to form a strong bond with hard and soft tissues [1, 2]. When implanted in the body, bioactive glass reacts with the body fluids, releasing ions into the fluids, and converts to hydroxyapatite (HA), the main mineral constituent of bone, which is responsible for the formation of the firm bond with hard and soft tissues [1, ,2].

Since its discovery nearly 40 years ago [2], the silicate bioactive glass designated 45S5, sometimes referred to by its commercial name Bioglass®, has been the most widely researched glass for biomedical applications. Melt-derived silicate bioactive glasses based on the 45S5 composition, as well as other silicate-based glasses prepared by sol−gel processing have also been investigated for biomedical applications [1]. Recent work has shown that certain compositions in other glass forming systems are also bioactive, such as borate glass [3-5] and phosphate glass [6]. In particular, some borate glasses, because of their lower chemical durability, react faster and convert more completely to an HA-like material, when compared to silicate 45S5 glass [7-9]. Studies have shown the ability of borate bioactive glasses to support cell proliferation and differentiation in vitro, as well as soft tissue infiltration and bone regeneration in vivo [1].

The ions released from some bioactive glasses have been reported to be beneficial for soft or hard tissue repair. Studies have shown that soluble silicon, dissolved from silicate bioactive glass presumably as silicic acid, $Si(OH)_4$, promoted osteogenesis [10] and activated osteogenic gene expression [11]. Boric acid, $B(OH)_3$, dissolved from borate bioactive glass, is considered to be an effective antiseptic component in wound management [12]. In addition to its key role as a major mineral source for bone growth, calcium is required in epidermal cell migration and regeneration patterns in the later stages of wound healing [13]. Although the mechanism is unclear, the calcium concentration at the wound site should be consistent with events in the healing cascade [14]. As a result, controlling the calcium concentration is essential in wound healing.

Recent work has shown the ability of bioactive glass to promote angiogenesis (formation of blood vessels), which is critical to numerous applications in hard tissue

regeneration and the healing of soft tissue wounds. The ability of a bioactive glass to induce angiogenesis could provide a robust alternative approach to the use of expensive growth factors for stimulating neovascularization of engineered tissues. The beneficial effects of small concentrations of 45S5 bioactive glass for stimulating angiogenesis have been shown in several recent studies, as reviewed recently [15]. Other bioactive glasses are under investigation for their ability to promote angiogenesis. In a recent study, borate bioactive glass (13-93B3) scaffolds have shown promising results for promoting angiogenesis in a rat subcutaneous implantation model [16].

Because of their attractive properties such as high surface area, rapid degradation and conversion to hydroxyapatite (HA), easy handling, and shape flexibility [17−20], nanofibrous and microfibrous bioactive glass composed of fibers with diameters smaller than a few microns have been attracting growing interest for potential applications in hard and soft tissue repair [21, 22]. In particular, microfibrous borate bioactive glass with the composition designated 13-93B3, has shown remarkable success in treating slowly healing or non-healing wounds [22]. However, there is little information on the mechanism of healing.

This study is the first of its kind, with the objective of providing a comprehensive evaluation of the degradation and conversion behavior of microfibrous bioactive glasses in vitro. Compositions from two different glass-forming systems, a borate glass designated 13-93B3 used previously to heal soft tissue wounds [22] and the widely researched silicate 45S5 glass, were used in the present study. The microfibrous glasses, prepared from conventionally-formed melt-derived glasses, were immersed in a simulated body fluid, and the conversion was characterized as a function of time using structural and analytical techniques.

2 Materials and methods

2.1 Starting materials

The microfibrous bioactive glasses used in this study, provided by Mo-Sci Corp., Rolla, MO, USA, were prepared from melt-derived glasses. They had the overall appearance and feel of cotton wool. Two glass compositions were used: a borate glass designated 13-93B3, with the composition 5.5 Na_2O, 11.1 K_2O, 4.6 MgO, 18.5 CaO, 3.7

P_2O_5, 56.6 B_2O_3 (wt%) and the widely-known silicate 45S5 glass with the composition 45 SiO_2, 24.5 Na_2O, 24.5 CaO, 6 P_2O_5 (wt%). The as-received glass microfibers were cleaned by washing in ethanol in an ultrasonic bath, and dried in air prior to use.

2.2 Assessment of in vitro degradation and conversion

Assessment of the in vitro degradation and conversion of the microfibrous glasses was performed by immersing the materials in a simulated body fluid (SBF) and characterizing the structural and compositional changes as a function of immersion time. The SBF, with an ionic composition similar to that of human blood plasma (Table 1), was prepared as described in detail elsewhere [23]. Briefly, the requisite amounts of Reagent grade sodium chloride, sodium bicarbonate, potassium chloride, calcium chloride, dibasic potassium phosphate, and magnesium chloride (Sigma-Aldrich; St. Louis, MO, USA) were dissolved in deionized water, and the solution was buffered at pH = 7.4 at 37 ^oC using hydrochloric acid and Tris buffer. Samples of each microfibrous glass were immersed at a ratio of 1 g of glass per 500 ml SBF for up to 14 days in a sealed polyethylene bottle at 37 ^oC, with the system shaken once every day. After immersion in the SBF, the reacted glasses were gently washed twice with deionized water and then twice with ethanol, dried overnight at room temperature, and finally dried for 24 h at 60 ^oC. The experiments for each glass composition at each time point were performed in duplicate.

2.3 Characterization of microfibrous glasses and reaction products

Samples of the as-received and reacted microfibrous glasses were sputter-coated with Au/Pd and examined in a scanning electron microscope, SEM (S-4700, Hitachi, Tokyo, Japan), using an accelerating voltage of 15 kV and a working distance of 8 mm. The fibers were ground to a powder for compositional analysis using Fourier transform infrared (FTIR) spectroscopy (NEXUS 670 FTIR; Thermo Nicolet, Madison, WI, USA) and X-ray diffraction, XRD (X'Pert Pro; PANalytical, Almelo, the Netherlands). A mass of 2 mg of the powder was mixed with 198 mg KBr, and pressed to form pellets for FTIR analysis, performed in the wavenumber range 400−2,000 cm^{-1} at a resolution of 4 cm^{-1}. The XRD was performed using Cu K_α radiation (λ = 0.15406 nm) at a scan rate of 1.8 ^{o}/min in the 2θ range 10−80^o.

Samples for transmission electron microscopy (TEM) were prepared by dispersing the glass fibers in ethanol and placing a few drops of the suspension on nickel grids coated with a carbon film. TEM (Tecnai G^2 F20; FEI Co., Hillsboro, OR, USA) was performed at 200 kV. Selected area diffraction (SAD) patterns were recorded by using a selected-area aperture allowing observation of a circular area of diameter 200 nm. The composition of thin sections of the fibers was measured using energy-dispersive X-ray (EDS) spectroscopy performed in the TEM using an atmospheric thin-window energy-dispersive X-ray system (INCA; Oxford Instruments, UK). Calcium to phosphorus ratios and the percentage of magnesium normalized to the calcium content were calculated using INCA software. Three randomly selected regions were analyzed and the data were expressed as a mean ± standard deviation. TEM images of the as-received microfibrous glasses at low magnification were analyzed using NIH Image J software to determine the diameter of the fibers. At least 100 fibers were counted, and the diameter was expressed as a mean ± standard deviation.

At selected immersion times of the microfibrous bioactive glass in SBF, the pH of the solution was measured using a pH meter, while the ionic concentration of Ca, P, B and Si ions in the SBF was measured using inductively-coupled plasma optical emission spectrometry, ICP-OES (Optima 2000DV; Perkin Elmer, Waltham, MA). The measurements were made in duplicate, and the data were expressed as a mean ± standard deviation.

3 Results

3.1 As-received microfibrous 13-93B3 and 45S5 bioactive glasses

Figures 1a, b shows lower magnification SEM images of the as-received borate 13-93B3 and silicate 45S5 bioactive glass fibers. The diameters of the borate 13-93B3 fibers were in the range ~200 nm to 3 μm, with an average value of 1.2 ± 0.7 μm, while the diameter of the silicate 45S5 glass fibers ranged from 500 nm to 5 μm, with an average of 2.3 ± 1.8 μm. SEM and TEM images at higher magnification (Figs. 1c, e) showed that the 13-93B3 fibers had a typical smooth glass surface. In comparison, the uneven surface of the 45S5 fibers (Fig. 1d) suggested the presence of crystal-like particles embedded in the glass surface, which was confirmed by the rough surface seen

in the TEM image (Fig. 1f). SAD patterns in the TEM indicated no measurable crystallinity in the 13-93B3 fibers, but a small amount of crystallinity was detected in the 45S5 glass fibers, presumably resulting from the crystal-like particles on their surface.

3.2 Surface morphology of converted fibers

Figure 2 shows SEM images of the surfaces of the borate 13-93B3 and silicate 45S5 fibers after immersion in SBF for 1, 3 and 7 days. After 1 day, the surface of the 13-93B3 fiber appeared to be fairly smooth, consisting of spherulites of diameter <50 nm. The surface of the 45S5 fibers also showed spherical-shaped features, and appeared to be rougher. After 3 days, the surface morphology of the 13-93B3 fiber appeared similar to that at 1 day. In contrast, the appearance of the 45S5 fibers was distinctly different and had become a highly porous surface composed of clusters of plate-like particles. With a longer immersion time (7 d), the 13-93B3 fibers showed a porous surface composed of whisker-like particles, whereas the plate-like structure of the particles on the 45S5 fibers became more evident.

3.3 FTIR analysis of composition

FTIR spectra (Fig. 3) show compositional changes in the glass fibers resulting from their conversion in SBF. For the as-received borate 13-93B3 glass fibers (Fig. 3a), the main resonances are attributed to the glass network; the resonances at 1350−1450 cm^{-1} and at 690−720 cm^{-1} are assigned to the B−O stretching mode and bending mode of BO_3 groups respectively, while the resonance at 900−1100 cm^{-1} is assigned to the B−O stretching mode of BO_4 groups [24, 25]. After immersion in SBF for 1 day, the resonances attributed to the glass network weakened markedly, and resonances attributed to vibrations of the phosphate group dominated the spectrum, such as the major resonance at ~1040 cm^{-1} for the $(PO_4)^{3-}$ ν3 resonance and the weak resonance at ~600 cm^{-1} for the $(PO_4)^{3-}$ ν4 resonance [26]. These two resonances became more intense with longer immersion time. The $(PO_4)^{3-}$ ν4 resonance at ~600 cm^{-1} started to split into two peaks (at ~605 and 560 cm^{-1}) within an immersion time of 3 days, which became more intense after 7 days. Resonances corresponding to the $(CO_3)^{2-}$ ν3 vibration in the region of 1400−1650 cm^{-1} and the $(CO_3)^{2-}$ ν2 vibration at 873 cm^{-1} were present in the spectra for the fibers immersed for 3 days or longer, revealing the formation of a carbonate-substituted phosphate product [27].

The primary resonances in the spectrum for the as-received silicate 45S5 glass fibers (Fig. 3b) consisted of the vibrational modes of the Si−O−Si bond in the glass network, such as the stretching vibration at 1030 cm^{-1} and the bending vibration at 460 cm^{-1} [28]. The broad resonances in the range 850−950 cm^{-1} corresponded to Si−O−2NBO (non-bridging oxygen) vibrational modes associated with the Ca^{2+} and Na^{+} ions in the glass network [28]. Similar to the results for borate 13-93B3 glass fibers, resonances corresponding to the phosphate and carbonate groups started to appear in the spectrum after immersion of the fibers in SBF. In addition, after a one-day immersion, the NBO vibration mode of Si−O bond weakened, indicating ion exchange and hydrolysis of the silica network. The resonance at ~800 cm^{-1} assigned to the tetragonal Si−O−Si group was present in the spectrum for the fibers immersed for 3 days, and it intensified after 7 days, revealing the polymerization of silanol groups [28]. Compared to the spectra for the borate 13-93B3 fibers, the splitting of the $(PO_4)^{3-}$ ν4 resonance at ~605 and 560 cm^{-1} became more evident at an earlier immersion time (1 day compared to 3 days).

The crystallinity of the calcium phosphate reaction product resulting from the conversion of the fibers in SBF can be evaluated from the extent of the splitting of the $(PO_4)^{3-}$ ν4 resonance at 560−600 cm^{-1} [29]. The splitting factor (SF) was calculated by dividing the sum of the intensities of the two peaks (A1 and A2) by the intensity of the valley (A3), as illustrated in Fig. 3a (inset) [30, 31]. The calculated SF values were higher for the 45S5 fibers (2.9 at 3 days and 3.1 at 7 days) than for the 13-93B3 fibers (2.2 at 3 days and 2.6 at 7 days), indicating better crystallinity of the calcium phosphate product formed on the 45S5 glass fibers at a given immersion time.

3.4 XRD analysis of crystalline phases

Figure 4 shows XRD patterns of the microfibrous 13-93B3 and 45S5 glasses as-received and after conversion in SBF. The patterns for the as-received 13-93B3 and 45S5 fibers showed no measurable amount of a crystalline phase. After immersion of the borate 13-93B3 fibers in SBF, the patterns of the reacted fibers showed no measurable amount of a crystalline phase after 3 days, but after 7 days, they showed peaks corresponding to the (002) and (211) planes in crystalline HA. In comparison, the patterns of the silicate 45S5 fibers showed peaks corresponding to the (002) and (211) planes in HA after 3 days in SBF. In addition, a broad bump (~22° 2θ) in the vicinity of

the major peak for cristobalite was present, which became more evident after the seven-day immersion. This bump may be attributed to the polymerization of silanol groups in the 45S5 glass during the conversion process, leading to the formation of a silica gel phase [32].

In general, the XRD results are in accordance with the FTIR observations that showed the presence of a crystalline calcium phosphate phase at a shorter immersion time and with better crystallinity for the silicate 45S5 fibers.

3.5 TEM characterization of microstructure, composition and phases

TEM images of the borate 13-93B3 and silicate 45S5 glass fibers immersed in SBF for 3 and 7 days are shown in Fig. 5. After the three-day immersion, the 13-93B3 fibers showed a smooth surface with some whisker-like particles present at a few places on the surface (Fig. 5a1). Higher magnification images showed that the reacted fibers were composed of spherulites of diameter <20 nm (Fig. 5a2), which was in good agreement with SEM observations of the surface morphology described previously (Fig. 2c). With increasing immersion time (7 days), the surface of the 13-93B3 fibers became completely covered with a whisker-like material. In comparison, the 45S5 fibers were covered with a wavy surface layer after the three-day immersion (Fig. 5c1, c2), which changed to a fine elongated morphology after 7 days (Fig. 5d1, d2).

The SAD pattern for 13-93B3 glass fibers immersed for 3 days in SBF showed a single diffuse halo (Fig. 5a3), an indication of an amorphous phase. With an increase in the immersion time to 7 days, the diffuse halo sharpened to a weak diffraction ring corresponding to the (211) plane in HA (Fig. 5b3). In the case of the 45S5 fibers, the SAD patterns showed the presence of a strong (211) ring and a weak (002) ring, characteristic of a weakly crystallized HA, after the three-day immersion (Fig. 5c3), which increased in sharpness with an increase in the immersion time to 7 days (Fig. 5d3). High resolution TEM showed isolated nanocrystalline regions in the surface region of silicate 45S5 glass fibers that were immersed for 3 days in SBF, as observed from the presence of lattice fringes (Fig. 6a). With an increase in the immersion time to 7 days, the lattice fringes became more evident and the crystalline regions became larger (Fig. 6b). In general, the TEM observations were consistent with the SEM, XRD, and FTIR results described previously.

Figure 7 shows EDS spectra of the borate 13-93B3 and silicate 45S5 glass fibers, as-received and after immersion for 3 and 7 days in SBF. The intensity of each peak was normalized to the intensity of the calcium peak, and the spectra have been displaced vertically for clarity. The spectra for the as-received fibers contained peaks corresponding to the elements in the borate 13-93B3 and silicate 45S5 glass. No detectable amount of Na and K was found in the spectra for the 13-93B3 and 45S5 fibers at an immersion time of 3 or 7 days; however, a small amount of Mg was present in the 13-93B3 fibers reacted for 3 and 7 days. The intensity of the P peak increased markedly at 3 days, but it changed little as the immersion time was increased to 7 days. For the 45S5 glass fibers, the intensity of the Si peak relative to that of Ca decreased after the immersion, but a Si peak was still observed at 7 days. The Ca/P atomic ratios of the reacted glass fibers (Table 2), determined from the EDS spectra, were close to the value for stoichiometric HA (1.67).

3.6 Ionic concentration of microfibrous glass dissolution product

The pH of the SBF in which the glass fibers were immersed had a starting value of 7.4. Upon immersion of the 45S5 fibers, the pH increased to ~8.3 after 3 days and showed little change thereafter (Fig. 8). In comparison, upon immersion of the borate 13-93B3fibers, the pH increased to a nearly steady value of ~8.0 after 7 days. The increase in the pH of the SBF was presumably due to rapid release of the alkali ions (Na; K) from the glass. Figure 9 shows the concentration of the ions released from the bioactive glass fibers into the SBF as a function of immersion time. For the borate 13-93B3 fibers, the Ca concentration increased in an approximately linear manner with immersion time up to 7 days, but then increased more slowly at longer times, to a value of ~5 mM at 14 days (Fig. 9a). In comparison, the Ca concentration resulting from the 45S5 dissolution increased more rapidly up to ~3 days but then decreased to ~3 mM at 7 days or longer. The concentration of P in the SBF decreased rapidly with immersion time for both the 13-93B3 and the 45S5 fibers, but the decrease was steeper for the 45S5 fibers (Fig. 9b). Within 3 days, the concentration of P decreased to <0.1 mM for the 45S5 fibers. For the 13-93B3 fibers, the concentration of P appeared to decrease in two steps: a steep decrease during the first day, followed by another steep decrease between days 3 to 7.

Figures 9c, d show the concentrations of B and Si, respectively, in the SBF as a function of immersion time of the 13-93B3 and 45S5 fibers. The percentage of B and Si

released was also found by normalizing the measured ionic concentration to the total concentration of those ions which would result from complete dissolution of the glass in SBF (Table 1). The concentration of B increased steeply with time, and it appeared to increase in two steps: a steep increase during day 1, followed by another steep increase between days 3 to 7. Approximately 80% of the boron in the glass was dissolved in SBF by day 7, and almost complete dissolution of the boron occurred by day 14. The Si concentration initially increased rapidly, but within 3 days it reached a nearly steady value of ~2 mM which was equivalent to the dissolution of only ~14% of the Si in the starting glass (Table 1).

4 Discussion

The results of the present study provide the first detailed information on the degradation of microfibrous borate 13-93B3 and silicate 45S5 bioactive glasses in vitro and their conversion to a calcium phosphate product. While differences exist between the in vitro medium (SBF) used in the present study and the in vivo environment, these results should nevertheless be useful in providing a basis for understanding the role of these microfibrous bioactive glasses in the healing of hard and soft tissues.

4.1 Degradation of bioactive 13-93B3 and 45S5 glass fibers

Both types of bioactive glass fibers degraded rapidly and converted to a calcium phosphate product in SBF within 3 to 7 days, but there were differences in their behavior. The silicate 45S5 fibers degraded more slowly than the borate 13-93B3 fibers, as determined from the percentage of total B and Si released from the two types of fibers into SBF (Figs. 9c, 9d). Despite this slower overall degradation rate, the 45S5 fibers immersed in SBF initially (at day 1) released a slightly higher Ca^{2+} concentration (3.4 mM) than the 13-93B3 fibers; the Ca^{2+} concentration was 3.4 mM and 2.7 mM, respectively, for the 45S5 and 13-93 fibers (Fig. 9a). This higher Ca^{2+} concentration could result from more rapid ion-exchange reactions between the network modifying ions (Ca^{2+}; Na^{+}) of the 45S5 glass and hydrogen (or hydronium) ions from the SBF which lead to the formation of a silica-rich layer on the 45S5 fibers in the early stages of the degradation process [40].

Later (immersion times >3 days), as the ACP starts to form on the silica-rich layer of the 45S5 fibers and crystallize to HA, the Ca^{2+} concentration decreased to ~2.7 mM. In comparison, the Ca^{2+} concentration in SBF resulting from the dissolution of the borate 13-93B3 fibers continued to increase, reaching a value of ~5 mM after 7 to 14 days. This increase in the Ca^{2+} concentration might result from the congruent dissolution of the 13-93B3 fibers, which is believed to occur for borate glass in neutral solution, leading to the release of boron and the network modifiers such as Na^{+} and Ca^{2+} [4, 41]. In addition, the ACP product formed on the borate 13-93B3 fibers crystallized more slowly than the ACP product on the 45S5 fibers, as described previously.

The potential for HA formation on the surface of $CaO{-}SiO_2$ and $CaO{-}P_2O_5$ glasses in SBF has been discussed in terms of the degree of supersaturation of the SBF, taken as the ratio of the ionic activity product (IP) to the solubility product (K_{sp}) of HA in the solution [42]. The IP of HA in the solution is given by

$$IP = \left(a_{Ca^{2+}}\right)^{10}\left(a_{PO_4^{3-}}\right)^{6}\left(a_{OH^-}\right)^{2} \quad (1)$$

where *a* is the activity of the ion. Putting the activity of each ion equal to its activity coefficient γ times its concentration (in square brackets), Equation (1) can be written

$$IP = \left(\gamma_{Ca^{2+}}\right)^{10}\left(\gamma_{PO_4^{3-}}\right)^{6}\left(\gamma_{OH^-}\right)^{2}\left[Ca^{2+}\right]^{10}\left[PO_4^{3-}\right]^{6}\left[OH^-\right]^{2} \quad (2)$$

Taking the activity coefficients of the Ca^{2+}, $(PO_4)^{3-}$, and OH^- ions as equal to their values at the physiological ionic strength, 0.36, 0.06, and 0.72, respectively [42], and the concentration of the ions from the data in Figs. 8, 9, the IP of HA in SBF due to the dissolution of the borate 13-93B3 and silicate 45S5 fibers is shown in Fig. 10. As shown, the IP has values of $\sim 10^{-98}$ to 10^{-91} over the two-week immersion period.

Since K_{sp} for HA in aqueous solution at 37 ^{o}C is reported to be 5.5×10^{-118} [42], the degree of the supersaturation IP/K_{sp} is much higher than unity even in the starting SBF. The results in Fig.10 show that, initially, there is a steep increase in the IP due to the dissolution of both the 13-93B3 and 45S5 fibers, but the IP for the 45S5 fibers ($\sim 10^{-91}$) is higher than the value for the 13-93B3 fibers (10^{-93}–10^{-92}) after an immersion time of 1 day. This higher IP coupled with the formation of a silica gel layer on the surface could contribute to the faster formation of HA on the silicate 45S5 fibers. Thereafter, the IP due to the dissolution of the 45S5 fibers decreases markedly to $\sim 10^{-98}$

at day 7, as a result of the consumption of Ca^{2+} and $(PO_4)^{3-}$ ions in the formation of HA. In comparison, the IP due to the dissolution of the 13-93B3 fibers is has a much higher value for immersion times >2 days (Fig. 10), presumably because of the absence of a silica gel layer and the higher solubility product of ACP [43−45].

The ICP results (Fig. 9c) showed that when immersed in SBF, the borate glass network in the 13-93B3 fibers degraded continuously with time, releasing B, presumably as boric acid, $B(OH)_3$, into the solution. The glass network was almost completely degraded within 14 days. In comparison, the Si released from the silicate 45S5 fibers, presumably as silicic acid, $Si(OH)_4$, initially increased rapidly, but then reached a nearly steady value of ~2.0 mM after 3 days. This value is close to the Si concentration for the saturation concentration of silica in water (1.7−2.0 mM at 25 ^oC) [46]. Approximately 85% of the silica in the original silicate glass network remained in the 45S5 fibers, forming a silica gel phase (Figs. 3, 4). It has been suggested that the overall dissolution rate of silicate glass is controlled by the dissolution of the silica gel [47]. Presumably after the saturation concentration of silica in SBF is reached, further degradation of the silicate glass network could occur by a solution−precipitation process in which the silica gel phase dissolves and re-precipitates in the fibers.

4.2 Conversion of bioactive 13-93B3 and 45S5 glass fibers to hydroxyapatite

The ACP product formed on the silicate 45S5 fibers crystallized to HA at a faster rate than the ACP formed on the borate 13-93B3 fibers. This difference in crystallization rate may result from morphological differences accompanying the conversion process and from compositional differences resulting from the ionic dissolution products of the fibers. Conversion of silicate 45S5 bioactive glass in aqueous phosphate solution (such as SBF) is widely believed to follow a sequence of reactions, as described in detail elsewhere [1, 2]. Rapid ion exchange reactions between the glass network modifiers (e.g., Na^+; Ca^{2+}) and hydrogen (or hydronium) ions from the medium, followed by condensation and polymerization of the resulting silanol groups, lead to the formation of a silica-rich layer on the glass. Further dissolution of the glass, coupled with the reaction between the Ca^{2+} ions and the phosphate ions from the medium, leads to the formation of an amorphous calcium phosphate (ACP) layer that grows with time and subsequently crystallizes to HA. Conversion of the borate 13-93B3 glass follows a similar process but

without the initial formation of a silica-rich layer. It has been suggested that the silica-rich layer formed on 45S5 glass provides sites for rapid nucleation and crystallization of the ACP [33, 34].

Crystallization of the ACP formed on borate glass fibers has been found to be similar to that of the ACP formed by chemical precipitation from a solution containing calcium and phosphate ions [35]. Initially, the ACP that was formed by precipitation from solution had a nearly spherical morphology, and the surface of the spherulites was believed to provide the primary sites for nucleation of HA. The conversion was marked initially by a period of apparent stability of the ACP, followed by rapid conversion to HA [36]. The absence of a silica-rich layer in the conversion process could be a factor in the slower crystallization of the ACP formed on borate 13-93B3 fibers.

ACP is prone to substitution by cations and anions during its formation by precipitation reactions. Ions such as $(CO_3)^{2-}$, Mg^{2+} and $(P_2O_7)^{4-}$ even in small concentrations have been found to increase the stability of ACP [37]. ACP is considered to be a precursor to the formation of bone mineral in vertebrates [31]. It has been suggested that ions such as Mg^{2+} and $(P_2O_7)^{4-}$ could possibly play an important role in maintaining the presence of ACP in skeletal tissue [38, 39]. The presence of 0.7 mM and 1.5 mM Mg^{2+} ions in SBF has been reported to reduce the crystallization rate of the HA product on 45S5 glass by 2 and 3 times, respectively [28], and a high enough value of Mg^{2+} could prevent the formation of HA. In the present study, Mg^{2+} ions in SBF (1.5 mM) plus Mg^{2+} ions dissolving from the 13-93B3 glass fibers could lead to a total Mg^{2+} concentration in SBF of 4.0 mM, assuming complete dissolution of the glass (Table 1). EDS analysis of the converted glass fibers indicated a higher percentage of magnesium (normalized to the calcium concentration) in the converted 13-93B3 fibers than in the converted 45S5 fibers (Table 2). With an increase in the immersion time from 3 to 7 days, the Mg content in the 45S5 fibers decreased, presumably due to a greater amount of calcium phosphate formation. However, the converted 13-93B3 fibers showed a stable Mg content of ~5%, which could be due to a continuous release of Mg^{2+} ions during the degradation of the glass fibers and incorporation into the ACP product. The higher amount of Mg incorporated into the calcium phosphate product could also play a role in reducing the crystallization rate of the ACP formed on the 13-93B3 fibers.

As described previously, the reaction system consisted of 1 g of glass fibers immersed in 500 ml of SBF. Since both glasses contained P_2O_5 (6.0 wt% and 3.7 wt% for 45S5 and 13-93B3 glass, respectively), the total phosphate content of the SBF used in the immersion process is equal to the phosphate content of the SBF itself plus the phosphate content resulting from the degradation of the glass fibers. Assuming that each glass is dissolved completely in SBF without any reaction, the theoretical concentration of P in SBF is 2.7 mM and 2.1 mM, respectively, for 45S5 and 13-93B3 glass (Table 1). Assuming further that these theoretical phosphate concentrations are available for conversion of the glass fibers to a calcium phosphate material with the HA composition, then ~50% of each glass can be converted. A higher fraction of the glass fibers cannot be converted because the phosphate concentration in SBF is exhausted. The ICP results (Fig. 9b) showed that the phosphate ion concentration in the SBF was almost exhausted after an immersion time of 3 days for the 45S5 fibers and after 7 days for the 13-93B3 fibers. However, it is not clear whether the conversion reaction ceased after those immersion times. Slow degradation of the glass fibers, leading to release of Ca and P, could lead to further conversion of the fibers coupled with low concentrations of Ca and P in the SBF. In fact, the P content of the 45S5 and 13-93B3 fibers used in the conversion process was 1 to 1.7 times the P content of the as-prepared SBF.

The results of the present work showed a continuous degradation of the microfibrous 13-93B3 fibers, with release of boron and the network modifiers (e.g., Ca^{2+}). In addition, a more slowly crystallizing ACP product phase was formed in the conversion of the 13-93B3 glass fibers which may have a higher solubility in aqueous media when compared to HA. These results, coupled with the potential antibacterial and angiogenic effect of boron [12, 16], may provide a basis for understanding the success of microfibrous 13-93B3 glass in healing soft tissue wounds [22].

5 Conclusions

Melt-derived microfibrous bioactive glasses with the silicate 45S5 and borate 13-93B3 compositions degraded rapidly and converted to a calcium phosphate product when immersed in a simulated body fluid (SBF) at 37 °C, but there were differences in their behavior. The borate glass network in the 13-93B3 fibers degraded faster than the silicate

network in the 45S5 fibers, releasing almost all of the boron into the medium within 7−14 days. In comparison, degradation of the silicate glass fibers resulted in a nearly stable Si concentration after ~3 days, approximately equal to the value for the saturation concentration of silica in aqueous media near room temperature. While both groups of fibers converted to an amorphous calcium phosphate (ACP) phase which subsequently crystallized to hydroxyapatite (HA), the ACP product formed on the 13-93B3 fibers crystallized more slowly. For immersion times >3 days, the 13-93B3 fibers released a higher concentration of Ca into the SBF than the 45S5 fibers. The rapid degradation coupled with the more slowly crystallizing ACP phase and the higher Ca concentration released into the SBF may partly account for the success of microfibrous 13-93B3 bioactive glass in healing soft tissue wounds as observed elsewhere.

6 Acknowledgement

The authors thank Mo-Sci Corp., Rolla, Missouri, for providing the microfibrous glass used in this work, Yetunde Oladapo for assistance with FTIR and XRD sample preparation, and Dr. Kai Song for assistance with TEM.

7 References

[1] Rahaman MN, Day DE, Sonny Bal B, Fu Q, Jung SB, Bonewald LF, Tomsia AP. Bioactive glass in tissue engineering. Acta Biomater 2011;7:2355-73.

[2] Hench LL. The story of Bioglass. J Mater Sci Mater Med 2006;17:967-78.

[3] Day DE, White JE, Brown RF, McMenamin KD. Transformation of borate glasses into biologically useful materials. Glass Technol 2003;44:75-81.

[4] Han X, Day DE. Reaction of sodium calcium borate glasses to form hydroxyapatite. J Mater Sci Mater Med 2007;18:1837-47.

[5] Day DE, Erbe EM, Richard M, Wojcik JA. Bioactive materials. US Patent No. 6709,744 (2004)

[6] Ahmed I, Lewis M, Olsen I, Knowles JC. Phosphate glasses for tissue engineering: Part 1. Processing and characterisation of a ternary-based P_2O_5-CaO-Na_2O glass system. Biomaterials 2004;25:491-9.

[7] Huang W, Day DE, Kittiratanapiboon K, Rahaman MN. Kinetics and mechanisms of the conversion of silicate (45S5), borate, and borosilicate glasses to hydroxyapatite in dilute phosphate solutions. J J Mater Sci Mater Med 2006;17:583-96.

[8] Yao A, Wang D, Huang W, Fu Q, Rahaman MN, Day DE. In vitro bioactive characteristics of borate-based glasses with controllable degradation behavior. J Am Ceram Soc 2007;90:303-6.

[9] Fu Q, Rahaman MN, Fu H, Liu X. Silicate, borosilicate, and borate bioactive glass scaffolds with controllable degradation rate for bone tissue engineering applications. I. Preparation and in vitro degradation. J Biomed Mater Research A 2010;95:164-71.

[10] Wheeler DL, Stokes KE, Hoellrich RG, Chamberland DL, McLoughlin SW. Effect of bioactive glass particle size on osseous regeneration of cancellous defects. J Biomed Mater Research 1998;41:527-33.

[11] Xynos ID, Edgar AJ, Buttery LDK, Hench LL, Polak JM. Gene-expression profiling of human osteoblasts following treatment with the ionic products of Bioglass® 45S5 dissolution. J Biomed Mater Research 2001;55:151-7.

[12] Irion G. Comprehensive wound management. 2 ed. Thorofare, NJ, USA: SLACK Incoporated; 2010.

[13] Lansdown ABG. Calcium: a potential central regulator in wound healing in the skin. Wound Repair Regen 2002;10:271-85.

[14] Barnett SE, Varley SJ. The effects of calcium alginate on wound healing. Ann Roy Coll Surg 1987;69:153-5.

[15] Gorustovich AA, Roether JA, Boccaccini AR. Effect of bioactive glasses on angiogenesis: a review of in vitro and in vivo evidences. Tissue Eng Pt B-Rev 2010;16:199-207.

[16] Jung SB. Borate based bioactive glass scaffolds for hard and soft tissue engineering: University of Missouri Science and Technology; PhD thesis, 2010.

[17] Quintero F, Pou J, Comesaña R, Lusquiños F, Riveiro A, Mann AB, Hill RG, Wu ZY, Jones JR. Laser spinning of bioactive glass nanofibers. Adv Funct Mater 2009;19:3084-90.

[18] Kim HW, Kim HE, Knowles JC. Production and potential of bioactive glass nanofibers as a next-generation biomaterial. Adv Funct Mater 2006;16:1529-35.

[19] Xia W, Zhang D, Chang J. Fabrication and in vitro biomineralization of bioactive glass (BG) nanofibres. Nanotechnology 2007;18:135601.

[20] Gao C, Gao Q, Bao X, Li Y, Teramoto A, Abe K. Preparation and in vitro bioactivity of novel mesoporous borosilicate bioactive glass nanofibers. J Am Ceram Soc 2011;94:2841-5.

[21] Jo J-H, Lee E-J, Shin D-S, Kim H-E, Kim H-W, Koh Y-H, Jang JH. In vitro/in vivo biocompatibility and mechanical properties of bioactive glass nanofiber and poly(ε-caprolactone) composite materials. J Biomed Mater Res B 2009;91B:213-20.

[22] Wray P. 'Cotton candy' that heals? Borate glass nanofibers look promising. Am Ceram Soc Bull 2011;90:25-9.

[23] Kokubo T, Kushitani H, Sakka S, Kitsugi T, Yamamuro T. Solutions able to reproduce in vivo surface-structure changes in bioactive glass-ceramic A-W. J Biomed Mater Res 1990;24:721-34.

[24] Verhoef AH, den Hartog HW. Structure and dynamics of alkali borate glasses: a molecular dynamics study. J Non-Cryst Solids 1995;182:235-47.

[25] Kamitsos EI, Karakassides MA, Chryssikos GD. Vibrational spectra of magnesium-sodium-borate glasses. 2. Raman and mid-infrared investigation of the network structure. J Phys Chem 1987;91:1073-9.

[26] Kim CY, Clark AE, Hench LL. Early stages of calcium-phosphate layer formation in bioglasses. J Non-Cryst Solids 1989;113:195-202.

[27] Rehman I, Bonfield W. Characterization of hydroxyapatite and carbonated apatite by photo acoustic FTIR spectroscopy. J Mater Sci Mater Med 1997;8:1-4.

[28] Filgueiras MR, La Torre G, Hench LL. Solution effects on the surface reactions of a bioactive glass. J Biomed Mater Res 1993;27:445-53.

[29] Termine JD, Posner AS. Infra-red determination of the percentage of crystallinity in apatitic calcium phosphates. Nature 1966;211:268-70.

[30] Reiche I, Vignaud C, Menu M. The crystallinity of ancient bone and dentine: new insights by transmission electron microscopy. Archaeometry 2002;44:447-59.

[31] Mahamid J, Sharir A, Addadi L, Weiner S. Amorphous calcium phosphate is a major component of the forming fin bones of zebrafish: Indications for an amorphous precursor phase. P Natl Acad Sci 2008;105:12748-53.

[32] Varshneya AK. Fundamentals of inorganic glasses. San Diego, CA: Academic Press; 1994.

[33] Pereira MM, Clark AE, Hench LL. Effect of texture on the rate of hydroxyapatite formation on gel-silica surface. J Am Ceram Soc 1995;78:2463-8.

[34] Hayakawa S, Tsuru K, Ohtsuki C, Osaka A. Mechanism of apatite formation on a sodium silicate glass in a simulated body fluid. J Am Ceram Soc 1999;82:2155-60.

[35] Eanes ED, Termine JD, Nylen MU. An electron microscopic study of the formation of amorphous calcium phosphate and its transformation to crystalline apatite. Calc Tiss Res 1973;12:143-58.

[36] Eanes ED, Gillessen IH, Posner AS. Intermediate states in the precipitation of hydroxyapatite. Nature 1965;208:365-7.

[37] Dorozhkin SV. Amorphous calcium (ortho)phosphates. Acta Biomater 2010;6:4457-75.

[38] Bilezikian JP, Raisz LG, Rodan Ga. Principles of bone biology. San Diego, CA, USA: Academic Press; 2002.

[39] Heinonen JK. Biological role of inorganic pyrophosphate. London, UK: Kluwer Academic Publishers; 2001.

[40] Bunker BC. Molecular mechanisms for corrosion of silica and silicate glasses. J Non-Cryst Solids 1994;179:300-8.

[41] Liu X, Huang W, Fu H, Yao A, Wang D, Pan H, Lu WW, Jiang X, Zhang X. Bioactive borosilicate glass scaffolds: in vitro degradation and bioactivity behaviors. J Mater Sci Mater Med 2009;20:1237-43.

[42] Nelson DG. The influence of carbonate on the atomic structure and reactivity of hydroxyapatite. J Dent Res 1981;60 Spec No C:1621-9.

[43] LeGeros RZ. Calcium phosphates in oral biology and medicine. Monogr Oral Sci 1991;15:1-201.

[44] Fulmer MT, Ison IC, Hankermayer CR, Constantz BR, Ross J. Measurements of the solubilities and dissolution rates of several hydroxyapatites. Biomaterials 2002;23:751-5.

[45] Alexander GB, Heston WM, Iler RK. The solubility of amorphous silica in water. J Phys Chem 1954;58:453-5.

[46] Clark DE, Pantano CG, Jr., Hench LL. Corrosion of glass. New York, NY: Books for Industry and The Glass Industry; 1979.

Table 1. Ionic concentration of the as-prepared simulated body fluid (SBF), and the theoretical ionic concentration of SBF which would result from complete dissolution of borate 13-93B3 and silicate 45S5 glass fibers without any reaction and with formation of a stoichiometric HA reaction product (values in brackets).

Concentration (mM)	Na	K	Mg	Ca	P	Si	B
SBF (initial)	142.0	5.0	1.5	2.5	1.0	0	0
13-93B3	145.9	10.1	4.0	9.6 (6.1)	2.1 (0)	0	30.5
45S5	157.8	5.0	1.5	11.2 (6.7)	2.7 (0)	15.0	0

Table 2. EDS analysis in the TEM for the Ca/P atomic ratio, and the Mg concentration normalized to the Ca concentration, for borate 13-93B3 and silicate 45S5 fibers after immersion for 3 and 7 days in SBF.

Immersion	Ca/P ratio		Mg/Ca ratio (%)	
time (days)	45S5	13-93B3	45S5	13-93B3
3	1.7 ± 0.1	1.7 ± 0.1	3.3 ± 1.1	5.2 ± 1.5
7	1.7 ± 0.1	1.7 ± 0.1	0.8 ± 0.4	5.0 ± 1.6

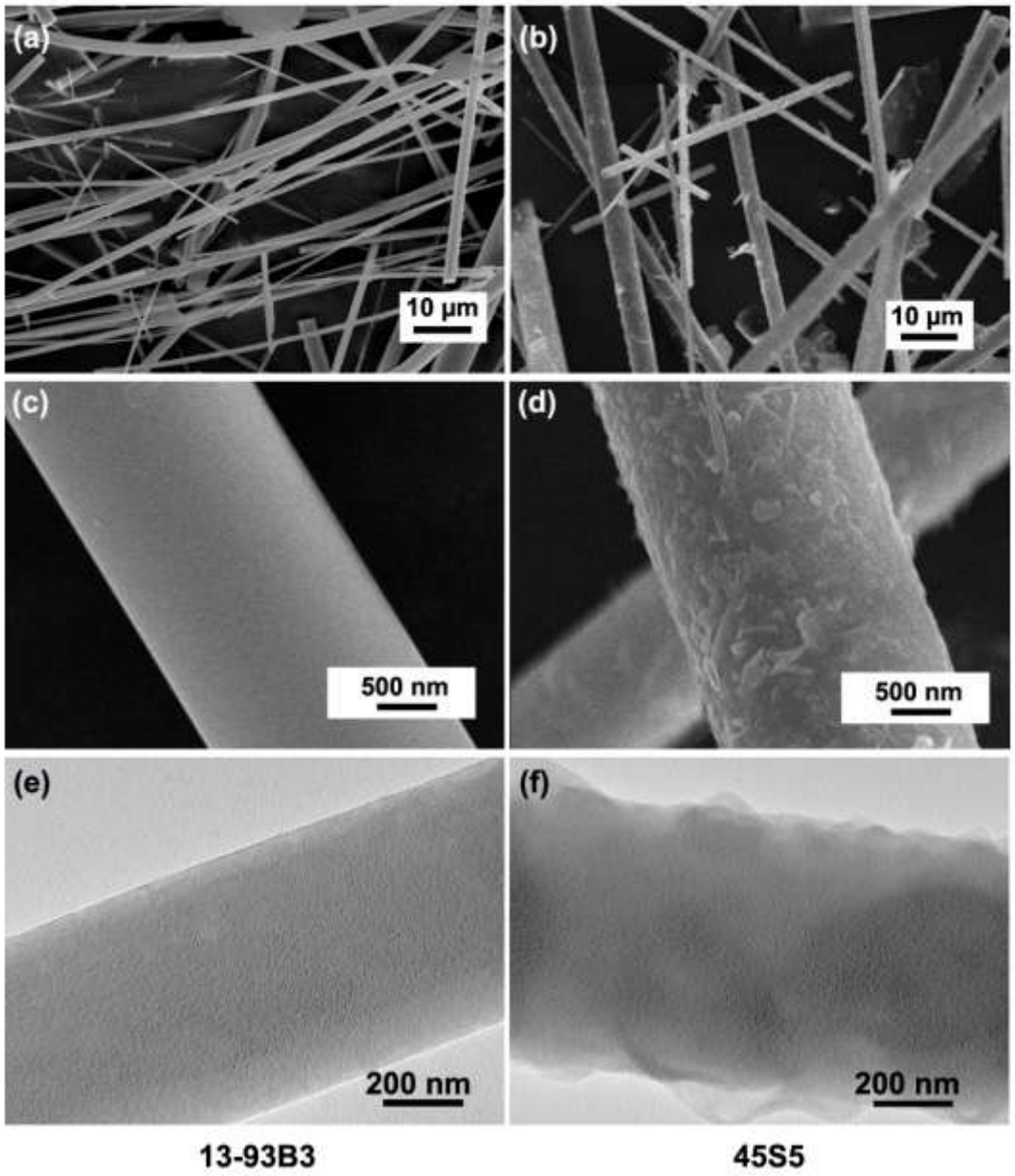

Fig. 1. SEM images of the as-received borate 13-93B3 glass fibers (a, c), and the silicate 45S5 glass fibers (b, d); TEM images of the as-received 13-93B3 fiber (e) and the 45S5 fiber (f).

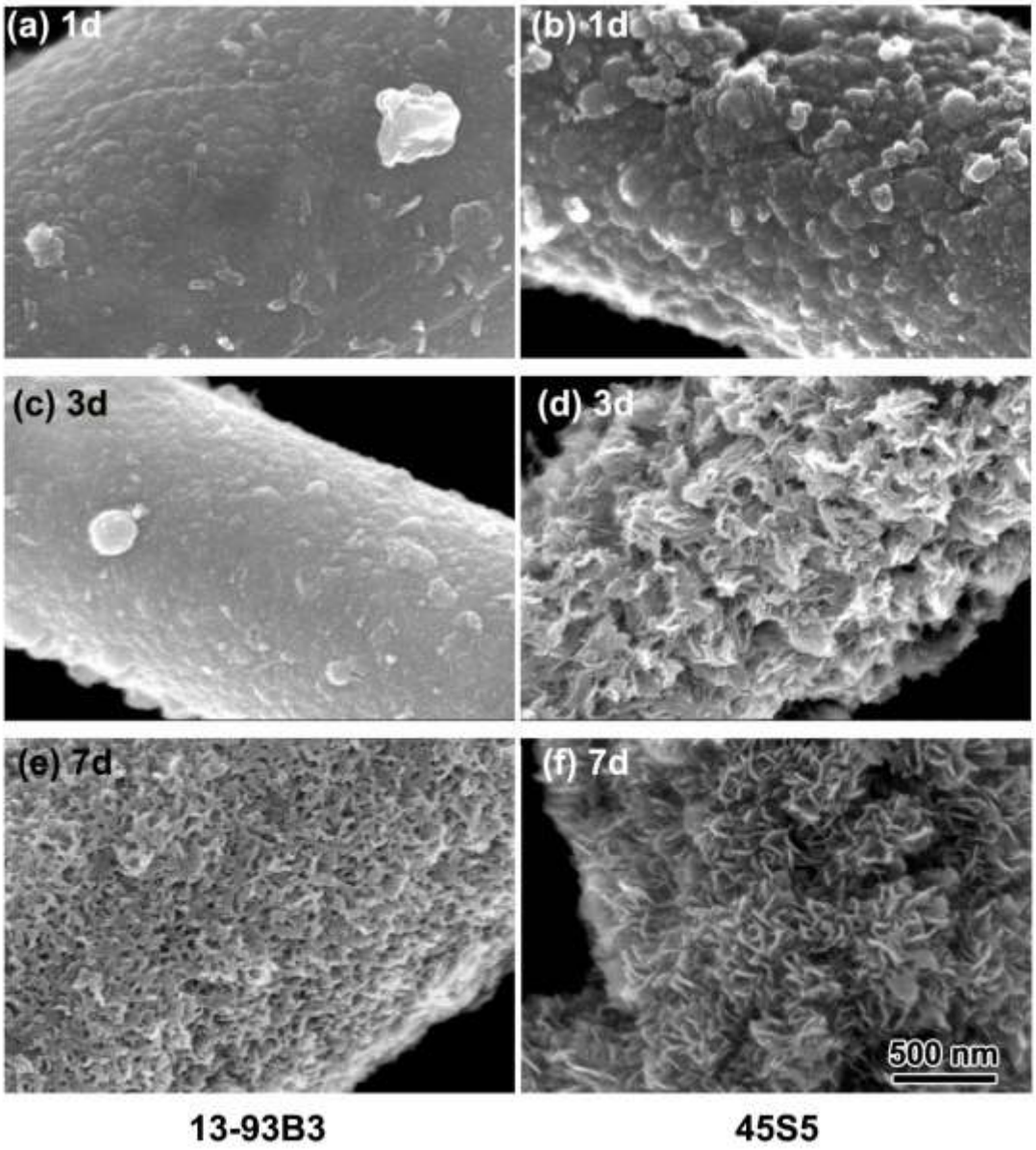

Fig. 2. SEM images of the surface of 13-93B3 glass fibers (a, c, e) and 45S5 glass fibers (b, d, f) after immersion in simulated body fluid (SBF) at 37 °C for 1 day (a, b); 3 days (c, d); 7 days (e, f).

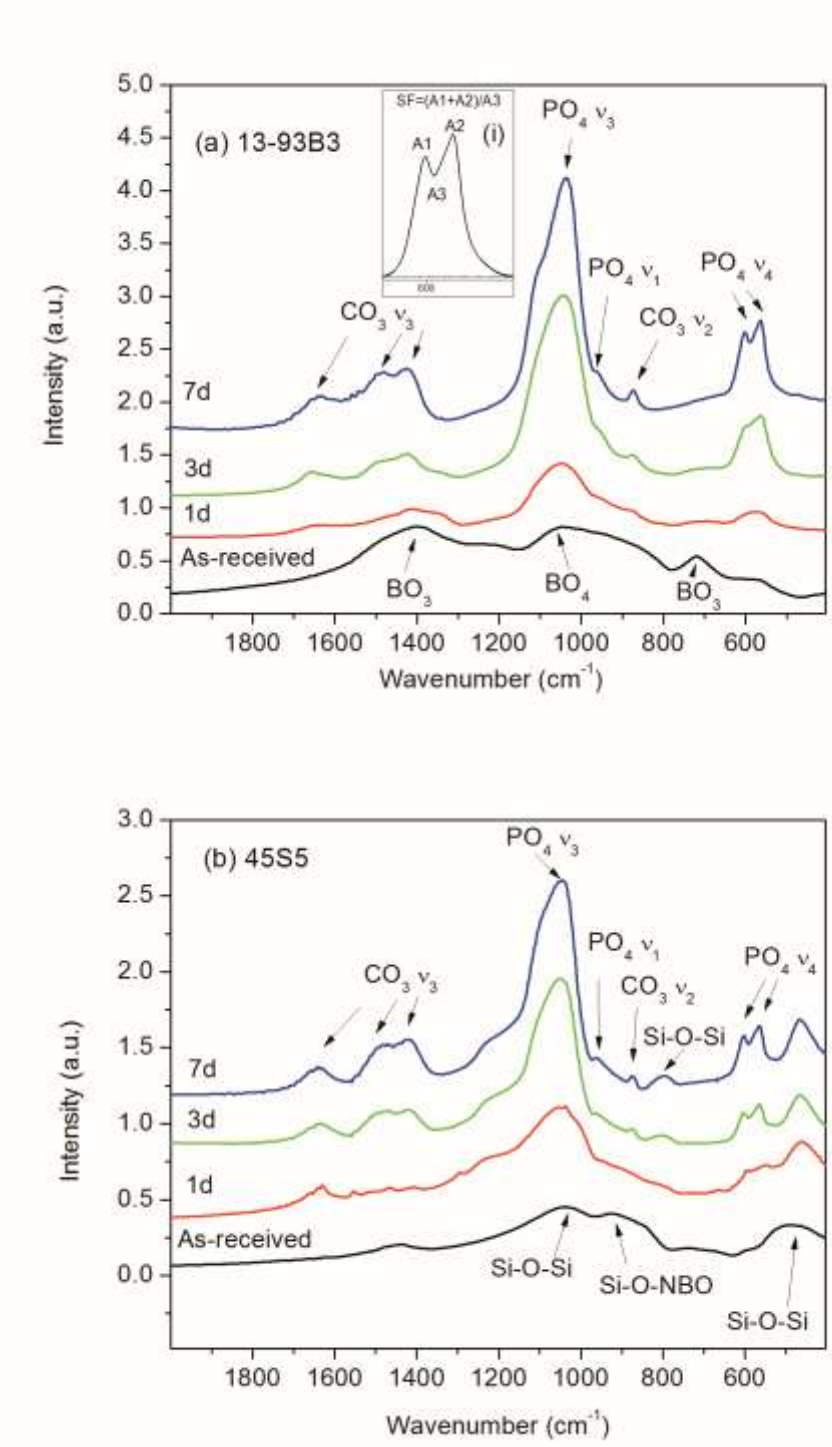

Fig. 3. FTIR spectra of (a) borate 13-93B3 glass fibers and (b) silicate 45S5 glass fibers as-received and after immersion in SBF at 37 ^{o}C for the times indicated. Inset (i) in (a) shows the method of determining the splitting factor for the phosphate $(PO_4)^{3-}$ ν_4 resonance.

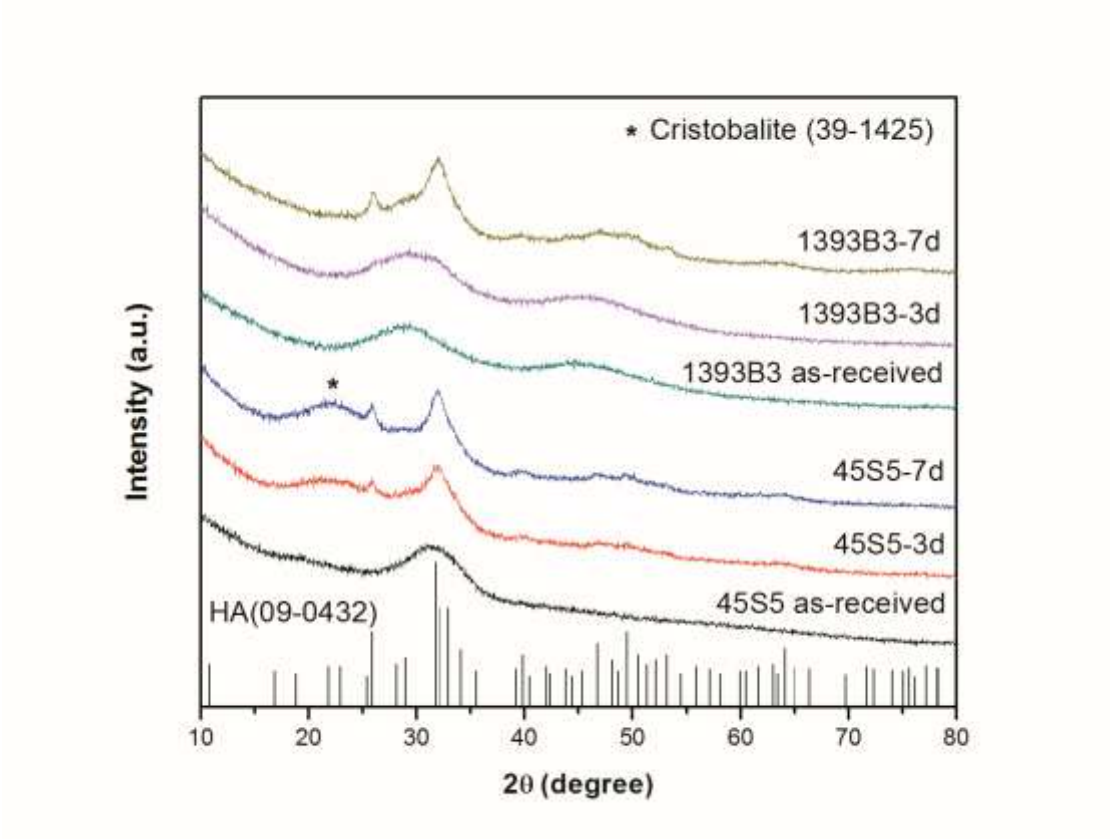

Fig. 4. XRD patterns of borate 13-93B3 and silicate 45S5 glass fibers as-received and after immersion in SBF at 37 ^{o}C for the times indicated. (⋆ denotes the position of the main peak in cristobalite)

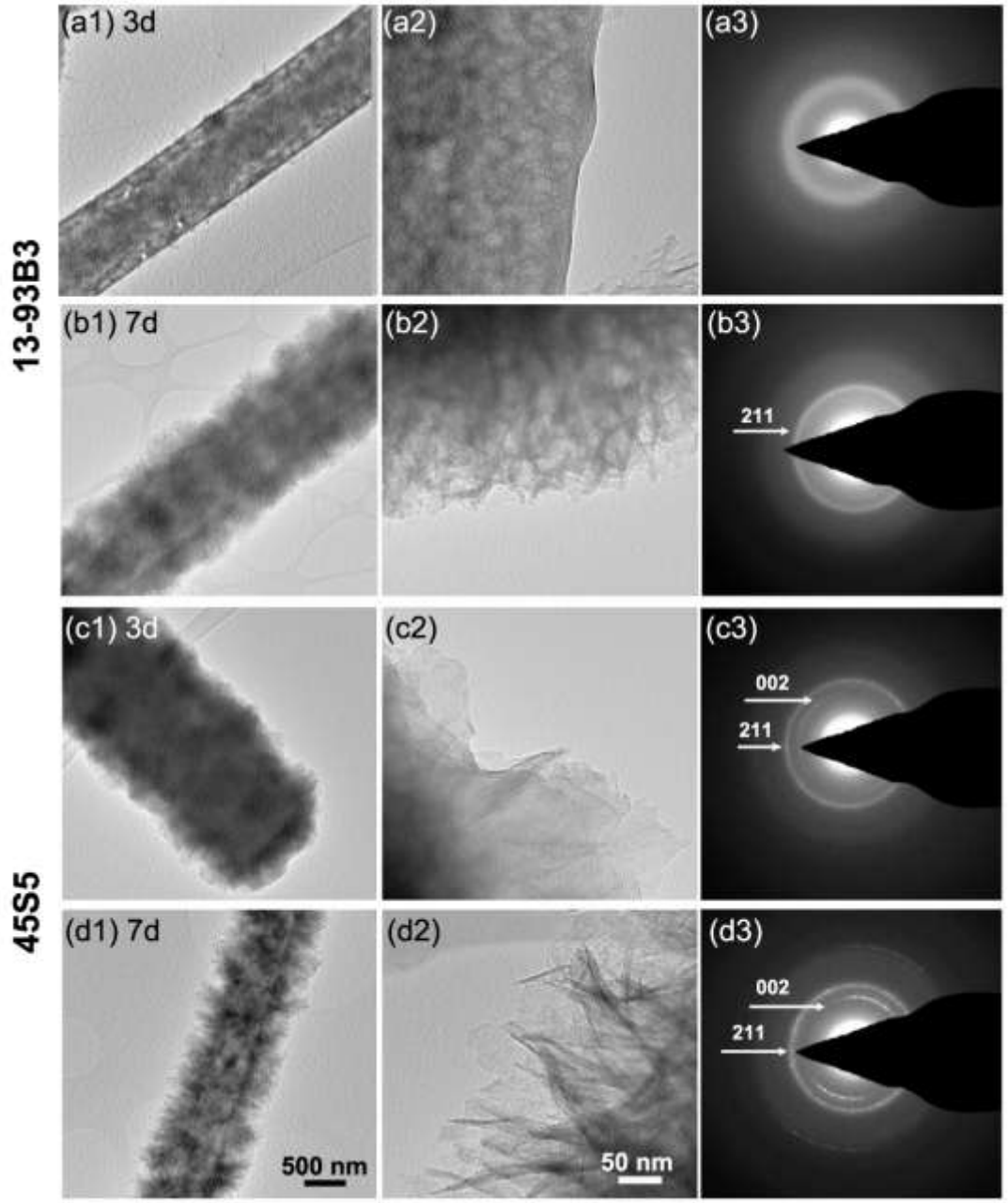

Fig. 5. TEM images and selected area diffraction (SAD) patterns of borate 13-93B3 glass fibers immersed in SBF at 37 °C for (a1−a3) 3 days and (b1−b3) 7 days, and silicate 45S5 glass fibers immersed under the same conditions for (c1−c3) 3 days and (d1−d3) 7 days.

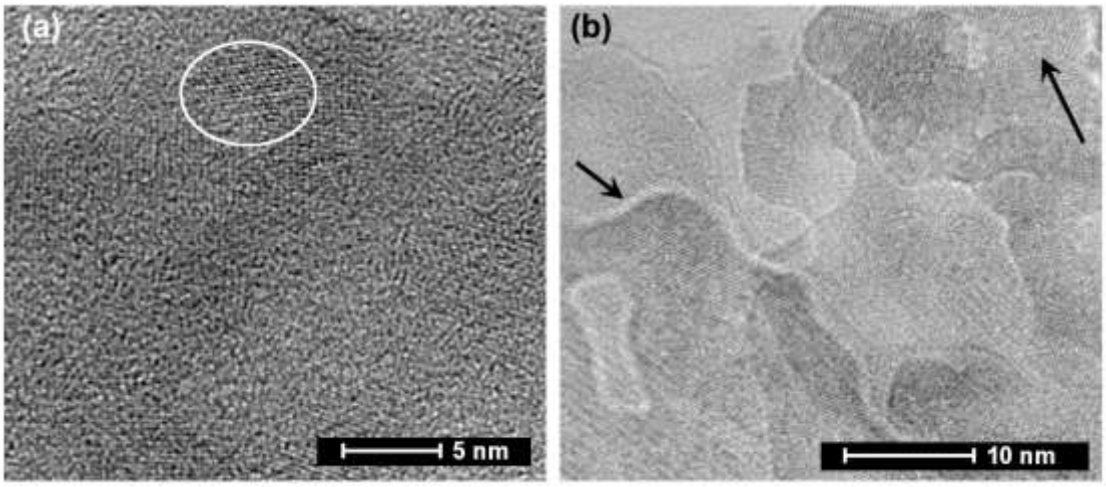

Fig. 6. High resolution TEM images of the surface region of silicate 45S5 glass fiber after immersion in SBF at 37 ^{o}C for (a) 3 days and (b) 7 days. Lattice fringes representative of crystalline regions are indicated by a circle in (a) and by arrows in (b).

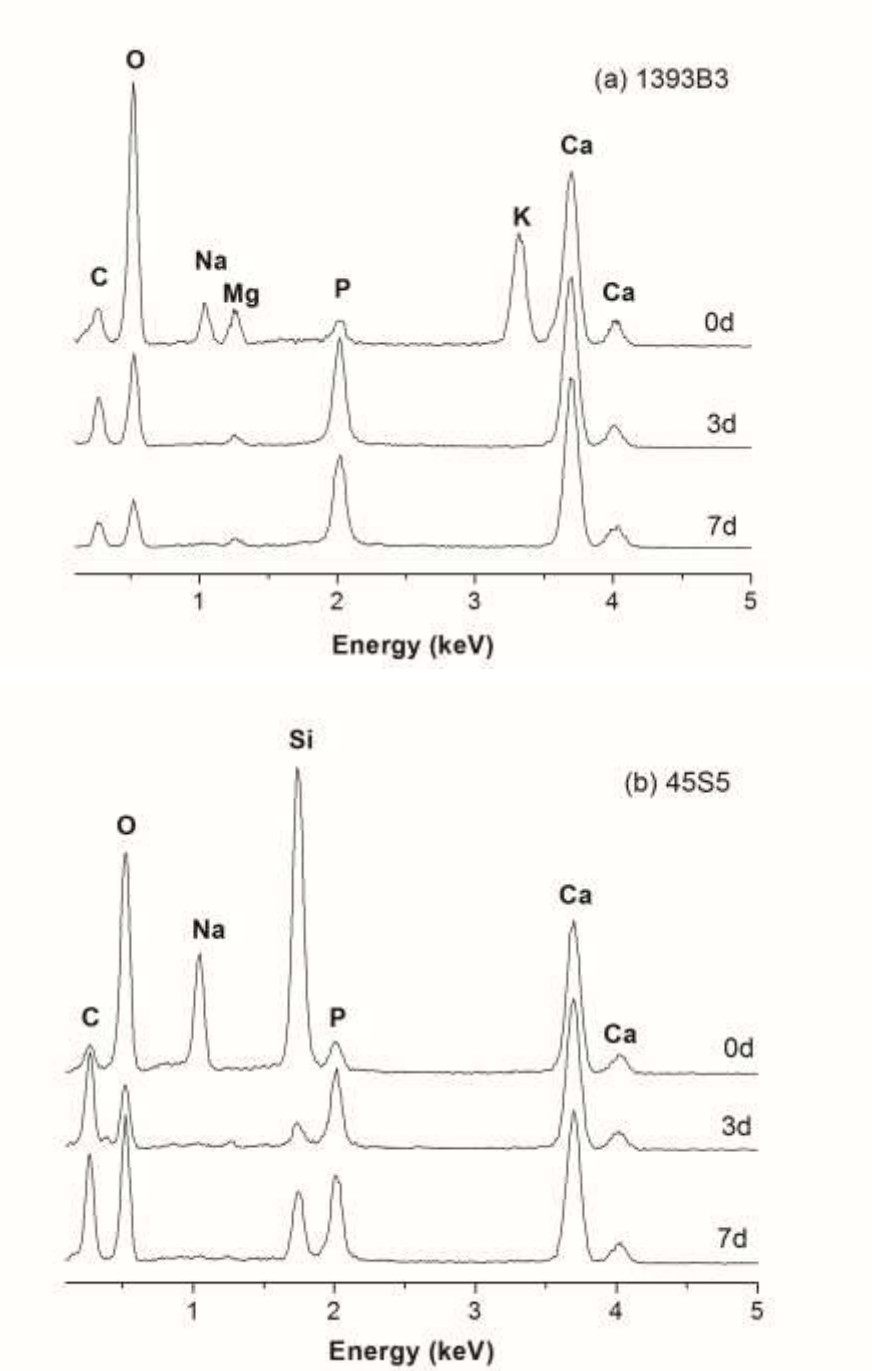

Fig. 7. EDS spectra of (a) 13-93B3 glass fibers and (b) 45S5 glass fibers as-received (0 days) and after immersion in SBF for the times indicated (3 days; 7 days).

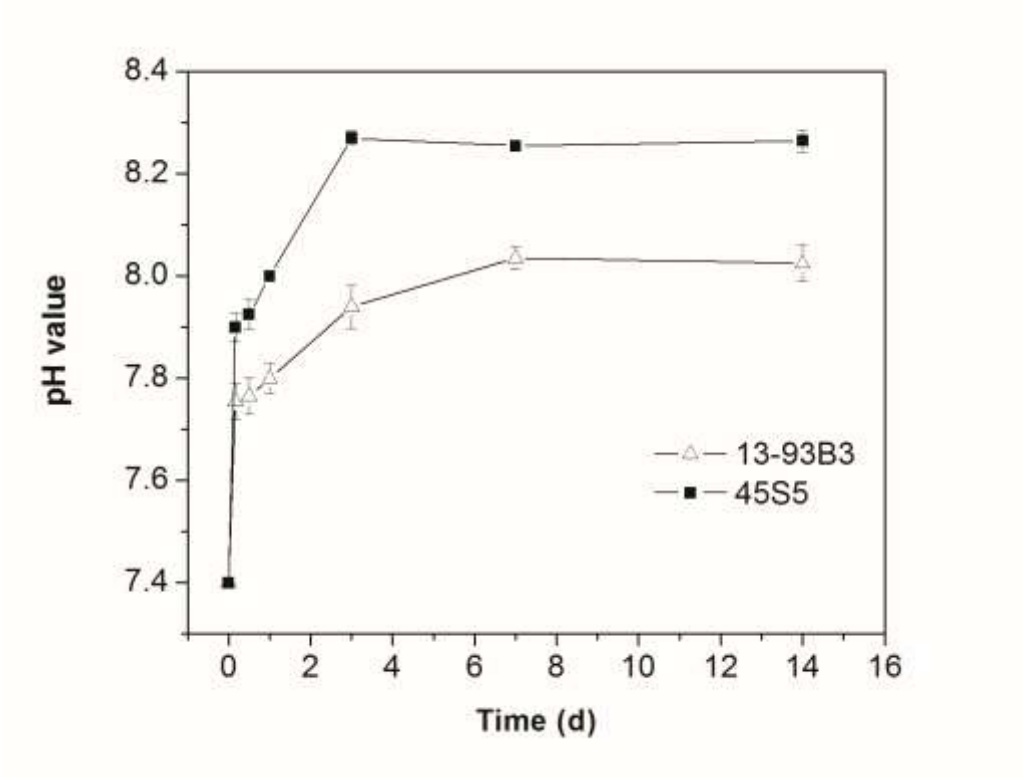

Fig. 8. pH of simulated body fluid (SBF) as a function of immersion time of the borate 13-93B3 and silicate 45S5 bioactive glass fibers.

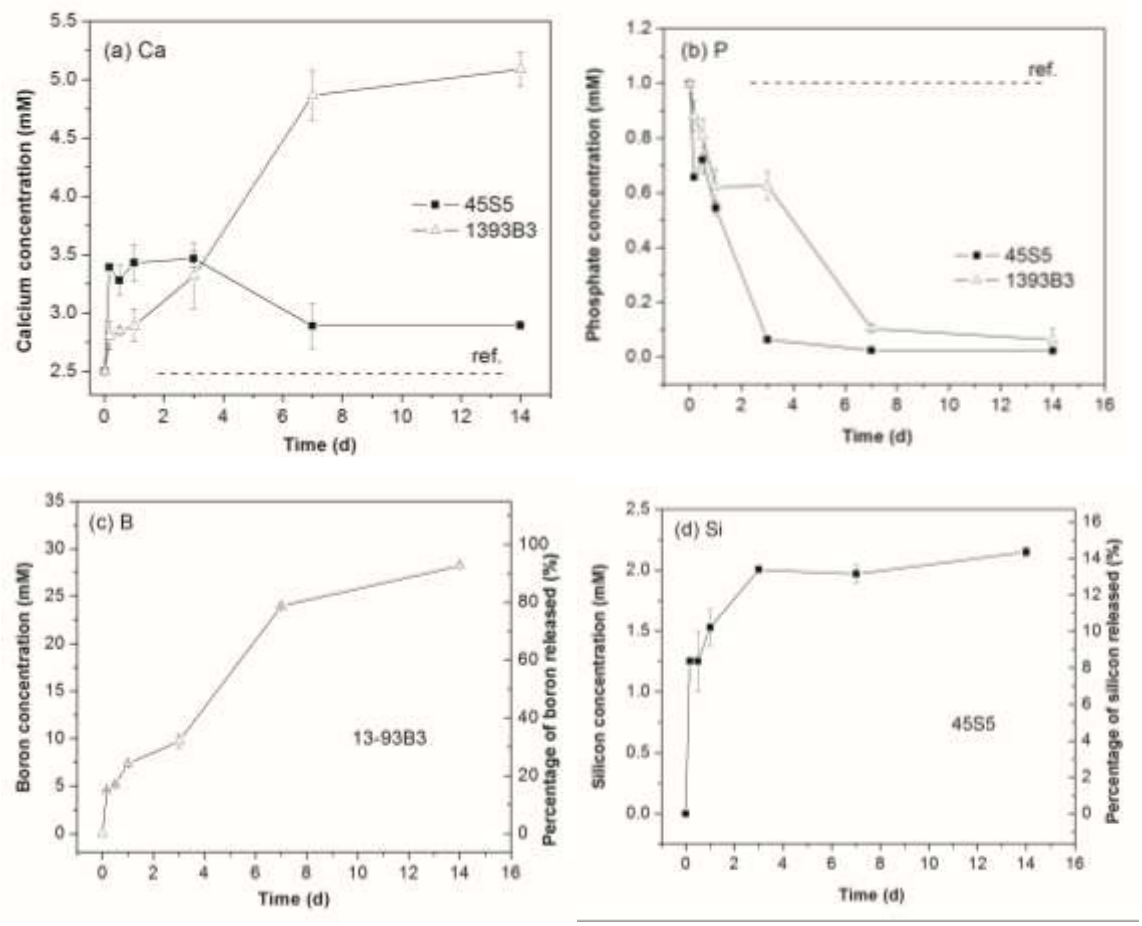

Fig. 9. Concentration of ions released from the borate 13-93B3 and silicate 45S5 bioactive glass fibers into SBF at 37 °C as a function of immersion time: (a) calcium, (b) phosphate, (c) boron, and (d) silicon. The dashed reference line in (a) and (b) shows the ionic concentration in the as-prepared SBF.

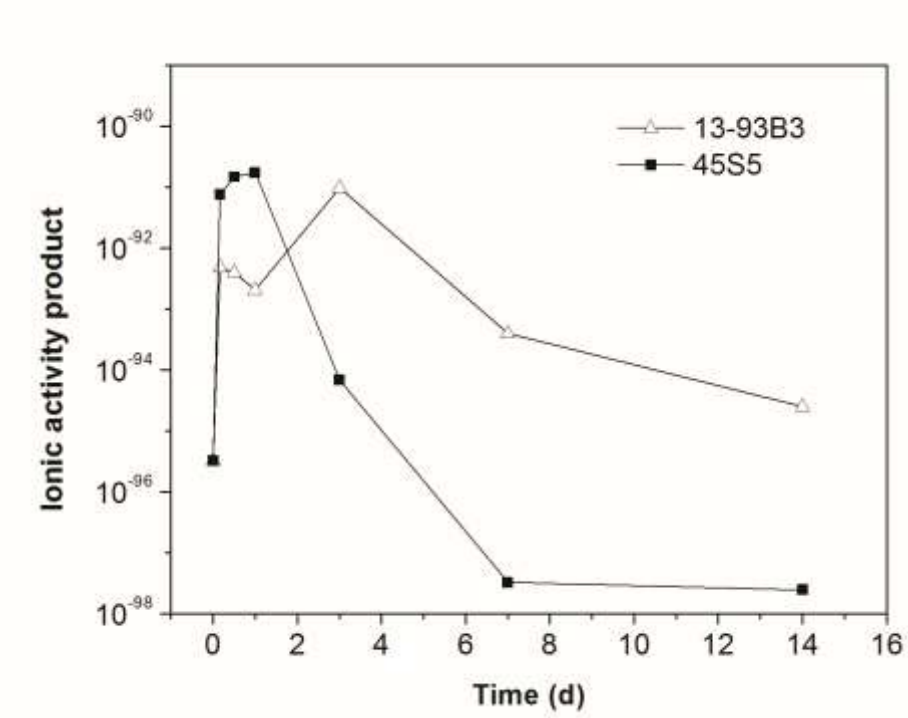

Fig. 10. Ionic activity product (IP) of hydroxyapatite in simulated body fluid (SBF) versus immersion time of borate 13-93B3 and silicate 45S5 bioactive glass fibers.

VITA

Xin Liu was born in 1985 in Jingdezhen, Jiangxi Province, China. In August 2002, Xin started her undergraduate education at Tongji University in Shanghai. With her enthusiasm for materials science, Xin completed her B.S. degree majoring in Materials Science and Engineering in 2006, and received Outstanding Graduating Student Award of Tongji University. She developed her interests in research during her senior design project on bioactive glass. After graduation, she continued the master program in Materials Science and Engineering at Tongji University under the supervision of Dr. Wenhai Huang. She completed her M.S. degree in 2008, and received the Shanghai Outstanding Master's Thesis Award.

Driven by her desire for more fundamental understanding in materials science, Xin started her Ph.D. study in Spring 2009, under the supervision of Dr. Mohamed N. Rahaman at Missouri University of Science and Technology. During her doctoral work, she published 11 journal papers (10 already published and one accepted), 8 of which she is the first author, 2 conference proceedings and 5 presentations at international conferences in the United States.